High Temperature Heat Flux Measurement: Sensor Design, Calibration, and Applications

Clayton A. Pullins

Dissertation submitted to the Faculty of the
Virginia Polytechnic Institute and State University
in partial fulfillment of the requirements for the degree of

Doctor of Philosophy
in
Mechanical Engineering

Thomas E. Diller, Chair
Srinath V. Ekkad
Scott T. Huxtable
Roger L. Simpson
Brian Vick

May 18, 2011
Blacksburg, Virginia

Keywords: heat flux sensor, high temperature, calibration, gage sensitivity

High Temperature Heat Flux Measurement: Sensor Design, Calibration, and Applications

Clayton A. Pullins

Abstract

This effort is focused on the design, calibration, and implementation of a high temperature heat flux sensor for thermal systems research and testing. The High Temperature Heat Flux Sensor (HTHFS) was designed to survive in the harsh thermal environments typically encountered in hypersonic flight, combustion and propulsion research, and large-scale fire testing. The sensor is capable of continuous use at temperatures up to 1000 °C. Two methods for steady-state calibration of the HTHFS at elevated temperatures have been developed as a result of this research. The first method employs a water-cooled heat flux sensor as a reference standard for the calibration. The second method utilizes a blackbody radiant source and a NIST calibrated optical pyrometer as the calibration standard. The HTHFS calibration results obtained from both methods compare favorably with the theoretical sensitivity versus temperature model.

Implementation of the HTHFS in several types of transient thermal testing scenarios is also demonstrated herein. A new data processing technique is used to interpret the measurements made by the HTHFS. The Hybrid Heat Flux (HHF) method accounts for the heat flow through the sensor and the heat storage in the sensor, and thus renders the HTHFS virtually insensitive to the material on which it is mounted. The calibrated output of the HTHFS versus temperature ensures accuracy in the measurements made by the sensor at high operating temperatures.

This work received support from NASA Graduate Student Researchers Program and Virginia Space Grant Consortium graduate fellowships.

Acknowledgments

I would like to extend my deepest gratitude to the following for help and guidance throughout the course of this research:

- My research advisor Dr. Tom Diller for his patience and guidance
- My dissertation committee members: Dr. Srinath Ekkad, Dr. Scott Huxtable, Dr. Roger Simpson, and Dr.Brian Vick
- My mentors at NASA DFRC: Larry Hudson and Craig Stephens
- My collaborators: Dave Hubble, Andy Gifford, Arun Mangalam, Matt Moholt, and Al Stewart
- My family and friends for their unconditional love and support
- My loving girlfriend Erin for always providing kind words of encouragement

Contents

1 Introduction **1**

1.1 Motivation 1

1.2 Dissertation Structure 1

2 In-situ High Temperature Heat Flux Sensor Calibration **3**

2.1 Abstract 4

2.2 Nomenclature 4

2.3 Introduction 6

2.4 Background: Heat Flux Sensor Calibration 6

2.5 Virginia Tech's High Temperature Heat Flux Sensor 8

2.5.1 HTHFS Design 8

2.5.2 Theoretical HTHFS Sensitivity 8

2.6 High Temperature Calibration System 10

2.6.1 Conceptual Design: Cylindrical Radiation Cavity 11

2.6.2 Physical Design 12

2.6.3 Experimental Setup 13

2.6.4 System Characterization 15

2.6.5 Calibration Results 19

2.6.6 Uncertainty Analysis 21

2.7 Discussion and Future Work 23

2.8 Conclusions 24

2.9 Acknowledgments 24

3 Uncertainty Reduction in the Transfer Calibration Method for High Temperature Heat Flux Sensors 25

3.1 Abstract 26

3.2 Nomenclature 26

3.3 Introduction 28

3.4 Experimental Setup and Procedure 30

3.4.1 Calibration System Physical Design 31

3.4.2 Calibration Procedure and Data Acquisition 37

3.5 Heat Flux Model of the Calibration System 38

3.5.1 Calibrated Sensitivity 38

3.5.2 Analytical Model Equations 38

3.5.3 Enclosure Discretization 40

3.5.4 Sidewall Heat Flux Model 40

3.5.5 Surface Temperatures and Properties 42

3.5.6 Calibration Correction Factor 43

3.6 Experimental Results 44

3.6.1 System Characterization: Initial DWHFS Calibrations 44

3.6.2 System Optimization: HTHFS Calibrations 46

3.6.3 Reduced Pressure Tests 49

3.7 Uncertainty Analysis 50

3.8 Discussion 52

3.9 Conclusions 55

3.10 Acknowledgments 55

4 Adaptation of the In-Cavity Calibration Method for High Temperature Heat Flux Sensors 56

4.1 Abstract 57

4.2 Nomenclature 57

4.3 Introduction 59
4.4 Experimental Setup 61
4.4.1 Facility Description 61
4.4.2 High Temperature Heat Flux Sensor (HTHFS) 63
4.4.3 Calibration Procedure and Data Acquisition 66
4.5 Heat Flux Model of the Sensor in the Blackbody Cavity 67
4.5.1 Model Equations 68
4.5.2 Enclosure Discretization 69
4.5.3 Surface Temperatures and Properties 70
4.6 Experimental Results 71
4.6.1 Coated HTHFS Initial Testing 71
4.6.2 Oxidized HTHFS High Temperature Testing 73
4.7 Uncertainty Analysis 76
4.8 Discussion 78
4.9 Conclusions 81
4.10 Acknowledgments 81

5 On the Use of High Temperature Heat Flux Sensors in Thermal Research 82
5.1 Abstract 83
5.2 Nomenclature 83
5.3 Introduction 84
5.4 Heat Flux Measurement 84
5.4.1 Sensor Measurement Principles 85
5.4.2 Hot-Wall vs. Cold-Wall Heat Flux Measurement 86
5.4.3 Hot-Wall Measurement Challenges and Advancements 87
5.5 Experimental Setup and Procedure 88
5.5.1 Water-Cooled Gardon Sensor 89
5.5.2 High Temperature Heat Flux Sensor (HTHFS) 89
5.5.3 Experimental Setup 93

5.5.4 Experimental Procedure 94
5.6 Experimental Results 95
5.6.1 Case 1: Actively Cooled HTHFS 95
5.6.2 Case 2: Passively Cooled HTHFS on Efficient Heat Sink 97
5.6.3 Case 3: Passively Cooled HTHFS on Thermal Insulator 98
5.7 Conclusions 99
5.8 Acknowledgments 99

6 Conclusions and Recommendations for Future Work 100
6.1 Research Conclusions 100
6.2 Recommendations for Future Work 101

A HTHFS Construction 106
A.1 Thermopile Construction 107
A.2 Strain Relief Tube Preparation 110
A.3 Lead Wire Preparation: Thermopile End 113
A.4 Thermopile Installation 115
A.5 Sensor Potting 119
A.6 Lead Wire Preparation: Connector End 121
A.7 Painting 123

B High Temperature Transfer Calibration Procedure 124
B.1 Hot Plate Preparation 125
B.2 Cold Plate Preparation 129
B.3 Sidewall Tube Preparation 129
B.4 Calibration Setup 129
B.5 Calibration Procedure 130

C MATLAB Code 134
C.1 Secondary Transfer Calibration 135

C.1.1 Stand-Alone Files 135
C.1.2 Function M-Files 150
C.2 Primary In-Cavity Calibration 163
C.2.1 Stand-Alone Files 163
C.2.2 Function M-Files 175
C.3 HTHFS Applications 178
C.3.1 Stand-Alone Files 178
C.3.2 Function M-Files 195

D Copyright Permission **199**

List of Figures

2.1 HTHFS secured in inconel housing. 9

2.2 (a) Element thermal conductivity and (b) sensitivity of HTHFS thermopile. . 10

2.3 High temperature calibration system schematic. 11

2.4 High temperature calibration system CAD model. 13

2.5 Stainless steel hot plate housing flush mounted HTHFS with (a) initial and (b) heavy surface oxidation. 14

2.6 (a) Emissivity parameter estimation and (b) SB heat flux comparison. 18

2.7 HTHFS calibrated sensitivity versus sensor temperature. 20

2.8 HTHFS calibrated sensitivity showing expanded uncertainty (95 %CI). . . . 23

3.1 High temperature calibration system model drawings: (a) Trimetric exploded view of calibration system assembly with labeled components. (b) Trimetric view (no explosion). (c) Top view. (d) Side view of the $L = 1.27$ cm plate separation system configuration (notice the gravitational vector). 32

3.2 High temperature calibration system parts: (a) Cold plate with $L = 1.27$ cm sidewall in place. (b) DWHFS mounted in the hot plate with the surface painted prior to heating. (c) HTHFS mounted in the hot faceplate prior to painting. (d) HTHFS mounted in the hot plate, as shown after painting and heating. 33

3.3 Schematic cross-section of the calibration system showing the control volume used in the heat flux model. The control volume enclosure (shown in two dimensions) is formed by three primary control surfaces: (1) hot plate surface, (2) cylindrical sidewall, and (3) cold plate surface. 40

3.4 DWHFS calibrated sensitivity versus average temperature: (a) Sensitivity determined using the adiabatic sidewall heat flux model; the sensitivity increases significantly with increasing plate separation distance, L, due to heat loss through the cylindrical sidewall. (b) Sensitivity determined using the radial heat loss sidewall model. 45

3.5 Sidewall heat flux model comparison for the $L = 1.27$ cm calibration configuration; results are for one individual thermal event: (a) Measured and modeled sidewall control surface temperatures. (b) Calculated radiosity distribution and calibration correction factor for each sidewall model. 47

3.6 HTHFS calibration results for two tests at different plate separation distances (Test#1: $L = 1.27$ cm; Test#6: $L = 2.54$ cm): (a) Measured Schmidt-Boelter heat flux. (b) The heat flux correction factor, f, is the ratio of the cold sensor modeled heat flux to the hot sensor modeled heat flux. (c) HTHFS sensitivity showing good agreement between calibrations at two different values of L. . . 48

3.7 Calibrated sensitivity versus average temperature for all tests performed using the HTHFS. The results show good repeatability in the calibration particularly for $T_{\mathrm{t,avg}} \geq 300$ °C. Note: for Test#1-5: $L = 1.27$ cm, and for Test#6-9: $L = 2.54$ cm. 49

3.8 HTHFS averaged calibration results showing expanded uncertainty (95% confidence interval) for two different plate separation distances: (a) Schmidt-Boelter measured and modeled heat flux. (b) HTHFS calibrated sensitivity. Also shown in (b) is the HTHFS theoretical sensitivity versus temperature taken from [1]. 53

4.1 VTBB heater assembly cutaway drawing isometric view. The CAD model is shown with one quarter of the heater assembly cut away to reveal the in-cavity location of the air cooled HTHFS. The HTHFS is positioned in one end of the dual cavity blackbody coaxial to cavity at a distance of $L = 1.27$ cm from the blackbody partion wall. The optical pyrometer measures the partition temperature by sensing radiation from the open end of the dual cavity blackbody. 62

4.2 VTBB heater assembly section view showing system materials, gas flow paths, and location of the air-cooled HTHFS during testing. 63

4.3 Air cooled HTHFS drawing showing labeled components and important dimensions. Clockwise from top left: (a) isometric exploded view of thermopile and stainless steel plug, (b) top view of sensor assembly showing sensing area, (c) side view of plug showing thermopile length (in direction of heat transfer) and plug length, and (d) air cooled HTHFS assembly view showing electrical and cooling tube routing. 64

4.4 HTHFS theoretical sensitivity versus average temperature. 66

4.5 Section view detail of the HTHFS as positioned within the blackbody during testing. The control volume enclosure, shown schematically in two dimensions, is used in the net-radiation analysis. The enclosure is formed by the five control surfaces labeled on the bottom right. 69

4.6 Test #1 results showing a) measured temperatures and b) calculated heat flux for the HTHFS with the carbon black coating. 72

4.7 Test #1-3 results showing a) measured voltages and b) calculated HTHFS sensitivity for the HTHFS with the carbon black coating. 72

4.8 Test #1-3 averaged HTHFS sensitivity versus temperature and quadratic-polynomial fit. 73

4.9 Test #4 oxidized HTHFS surface emissivity estimation: sum of squares minimization. 74

4.10 In-cavity high temperature heat flux sensor calibration results. 75

4.11 HTHFS calibrated sensitivity showing expanded uncertainty (95 %CI). . . . 79

4.12 HTHFS experimental sensitivity comparison. The normalized results are for two similar HTHFS thermopiles, one calibrated using a transfer technique [1], and the other calibrated using the in-cavity technique. 80

5.1 Heat flux sensor control surface schematic. The sensor is shown mounted flush with the surface of the substrate (test article). The total heat transfer through the sensor by conduction is a combination of the net radiation and convection to/from the sensor surface. 86

5.2 HTHFS schematic drawings: (a) $N = 5$ thermopile detail showing materials, important dimensions, and lead wire/surface thermocouple locations. Typical dimensions for the $N = 5$ thermopile shown are: $l = 1.0$ cm, $w = 0.5$ cm, and $\delta = 0.26$ cm. (b) Circular plug housing with $N = 2$ thermopile. (c) Rectangular flat housing with $N = 5$ thermopile. 90

5.3 HTHFS normalized sensitivity versus average temperature. The experimental results span three types of calibrations performed on three different sensors. The high temperature results are taken from [2, 3]. Each experimental data point is normalized by the corresponding sensor's calibrated room temperature sensitivity. The theoretical sensitivity is based on a one-dimensional thermal model of the HTHFS thermopile [2]. 92

5.4 HTHFS Composite specific heat versus temperature. The points represent data taken from [4, 5] while the lines through the points are polynomial fits. Using these polynomials, the HTHFS composite specific heat is calculated from Eq. 5.8. 92

5.5 Flat plate heater system schematic. The radiation heat flux incident on the two sensor surfaces is equal. 93

5.6 Three experimental cases for hot-wall heat flux measurement using the HTHFS: (a) Case 1: HTHFS mounted in an air-cooled stainless steel body. The overhead view of the calibration setup shows the flat graphite heater plate and the water-cooled Gardon sensor. (b) Case 2: HTHFS mounted on a long steel column (hidden) with an insulated perimeter to promote one-dimensional axial conduction. (c) Case 3: HTHFS flush mounted in a fibrous alumina insulation board. 94

5.7 Case 1 heat flux and temperature data. The HTHFS is mounted in an air-cooled cylindrical body. (a) Heat flux versus time. (b) Sensor temperature versus time. 96

5.8 Case 2 heat flux and temperature data. The HTHFS is mounted on the end of a long steel column. (a) Heat flux versus time. (b) Sensor temperature versus time. 97

5.9 Case 3 heat flux and temperature data. The HTHFS mounted in a low thermal conductivity fibrous alumina insulation board. (a) Heat flux versus time. (b) Sensor temperature versus time. 98

A.1 From right to left: chromel, zirconia-toughened alumina (ZTA), unbent alumel, bent alumel, and jig for welding thermopile strip together. 107

A.2 Alumel bending clamps side view (outer guide plates are not installed). The arrow shows the direction for the die to bend the alumel piece. 108

A.3 Alumel bending clamp assembly top view (both dies in place). The arrow shows the unbent piece of alumel. 108

A.4 Left: Bent strip of alumel. Right: Long thermopile (5 bent alumel strips, 6 chromel strips, 10 ZTA strips) assembled in jig for spot welding. 108

A.5 Top view of diced thermopile. 109

A.6 Side view of diced thermopile. 109

A.7 Left: Jig for dicing inconel strain relief tubes. Right: HTHFS inconel housing (1.0 in $\times$ 0.5 in $\times$ 0.125 in). 110

A.8 Inconel strain relief tubes diced to length (0.75 in) with 0.375 in axial slot. . 110

A.9 Strain relief tube showing arms bent to ≈ 45° with needle nose pliers. 111

A.10 Strain relief tube showing arms bent to 90° with vise. 112

A.11 Finished strain relief tubes and inconel housing. 112

A.12 Inconel sheathed dual thermocouple cable stripped to expose conductors. The strain relief tube, four-bore ceramic tube, and four single-bore ceramic tubes are all installed. A magnet (as shown) is used to differentiate between the alumel conductors (magnetic) and the chromel conductors (non-magnetic). . 114

A.13 The lead wire assembly is fed through the hole in the the inconel housing (top face shown). By convention, the "top" thermocouple pair is on the right when viewing the sensor housing top face. 115

A.14 Machine screws (shown) or set screws (preferred) are used to secure the thermopile in the housing; small strips of ZTA are used to electrically insulate the thermopile from the housing. One thermocouple pair is routed to the top side of the thermopile, and the other thermocouple pair is routed to the bottom side of the thermopile. 116

A.15 Tape is used to hold the thermocouple lead wires in place for welding. The excess lengths of lead wire are clipped off after welding. 117

A.16 Sensor assembly after lead wire and strain relief tube spot welding. 118

A.17 Two sensors shown after the potting material (Aremco Ceramacast 675-N) was cured and sanded flush. 120

A.18 Connector end of lead wire cable. The individual conductors are sheathed with Kapton tubes, and the collet and locking nut for the connector mounting bracket is installed. 122

A.19 Connector end of lead wire cable. The mini-plug thermocouple connectors and connector mounting bracket are installed. 122

A.20 Finished HTHFS; the sensing area is coated with Zynolyte high temperature flat black paint. 123

B.1 Custom HTHFS designed to fit in the Mesoscribe hot plate mounting bracket. 125

B.2 HTHFS installed in the hot plate mounting bracket showing the location of the surface thermocouples. 126

B.3 HTHFS hot plate surface prepared for painting. 127

B.4 Hot plate surface (with Mesoscribe DWHFS) after painting, prior to high temperature curing. 127

B.5 Painted hot plate surface (with HTHFS) after high temperature curing. . . . 128

B.6 Cold plate with Schmidt-Boelter reference sensor installed. The surface is coated first with two layers of Zynolyte (as shown), and then with one layer of GE Aerocoat carbon soot (not shown). 129

B.7 $L = 0.5$ in (1.27 cm) stainless steel sidewall tube positioned on the cold plate with stainless steel bearings. The positioning bearings sit in blind holes drilled into the cold plate, hot plate, and sidewall tube surfaces. Five N-type thermocouples are welded at different axial locations along the sidewall tube's inner surface. The cold plate is shown with the GE Aerocoat carbon soot surface coating. 130

B.8 Fibrous insulation is installed on all external surfaces of the calibration system during testing. The bell jar shown is only used for reduced pressure tests. . . 131

B.9 High temperature transfer calibration system components (clockwise from bottom left): computer, data acquisition system, variable transformer, multimeter, calibration test section, vacuum pump, and water reservoir. The bell jar and vacuum pump are only used for reduced pressure tests. 132

List of Tables

2.1 Calculated correction factor, f, for a sample test. 19

2.2 Standard uncertainty values used in calculating $u_c(f)$. 22

2.3 Calibration results and uncertainty as a function HTHFS mean temperature, $T_{\mathrm{t,avg}}$. Results averaged over five test sample. 22

3.1 Standard uncertainty values used in calculating $u_c(f)$. 51

3.2 Calibration results and uncertainty as a function HTHFS mean temperature, $T_{\mathrm{t,avg}}$. Results averaged over the sample of five HTHFS calibrations with the system in the $L = 1.27$ cm configuration. 54

4.1 Average heat flux for the three oxidized HTHFS tests (test #4-6). 75

4.2 Standard uncertainty values used in calculating $u_c(q''_{\mathrm{t}})$. 77

4.3 Calibration results and uncertainty as a function HTHFS mean temperature, $T_{\mathrm{t,avg}}$. Results averaged over the sample of three oxidized tests. 78

B.1 Approximate heater voltage settings for desired steady-state hot plate temperatures. 132

Chapter 1

Introduction

1.1 Motivation

Virtually all physical systems in one way or another involve the transfer of thermal energy. Management of thermal energy transport is a key aspect in numerous engineering applications. Heat transfer measurement is a complex process that requires a thorough understanding of the thermodynamics and physics involved. The number of applications for heat flux sensors is expanding at a rapid pace, particularly in energy management, aerospace engineering, and fire research. Direct measurement of heat flux, often desired in practice, requires careful design and implementation of both sensors and calibration systems to ensure accuracy in the measurements. Heat flux sensor calibration techniques attempt to mimic the measurement environment as closely as possible with high repeatability. This work is focused on the design, calibration, and implementation of Virginia Tech's High Temperature Heat Flux Sensor (HTHFS).

1.2 Dissertation Structure

This dissertation is devoted to the high temperature calibration of heat flux sensors, and the implementation of these sensors in realistic transient testing scenarios. Chapters 2 and 3 document the development of a simple bench top system which uses a secondary calibration method designed specifically for high temperature heat flux sensors. The secondary calibration system is both cheap and relatively straightforward to implement. Chapter 2 presents the conceptual design of the system and preliminary calibration results, and Chapter 3 provides an in-depth characterization study of the system. Chapter 4 introduces a new scheme for the primary calibration of heat flux sensors at high temperature using a blackbody radiant heater system. Chapter 5 is devoted to the implementation of high temperature heat flux

sensors in thermal research. Sensor operational characteristics are demonstrated through transient, high temperature, high heat flux experiments.

Chapter 2

In-situ High Temperature Heat Flux Sensor Calibration

This chapter comprises sections from the International Journal of Heat and Mass Transfer Paper No. HMT_7613 accepted for publication on March 20, 2010. The full-length paper is reprinted here with permission.

2.1 Abstract

Recent advances in heat flux measurement have resulted in the development of a robust thermopile heat flux sensor intended for use in extreme thermal environments. The High Temperature Heat Flux Sensor (HTHFS) is capable of simultaneously measuring thermopile surface temperature and heat flux at sensor temperatures up to 1000 °C. The need for high temperature heat flux calibration of the HTHFS has resulted in the development of a new wide angle radiation calibration system, which operates with the sensor at elevated temperatures. The temperature dependence of the sensor output over the range of 100 °C to 900 °C has been successfully characterized with acceptable uncertainty limits. The calibrated HTHFS sensitivity agrees well with a theoretical sensitivity model, suggesting that the primary cause for the sensor's output temperature dependence is due to the change in thermal conductivity of the sensor elements with temperature.

2.2 Nomenclature

A	area (cm^2)
D	cavity diameter (cm)
F	radiation view factor
f	correction factor applied to sensitivity calculation
$\boldsymbol{g}$	gravitational vector
k	statistical coverage factor
l	characteristic length (cm)
L	cavity length (cm)
q	heat transfer rate (W)
q''	heat flux ($W\ cm^{-2}$)
r	radius (cm)
s	sample standard deviation
S	sensitivity to absorbed heat flux ($\mu V\ W^{-1}\ cm^2$)
Se	relative Seebeck coefficient ($\mu V\ \ ^\circ C^{-1}$)
T	temperature (°C)
u	standard uncertainty

u_c	combined standard uncertainty
u_r	uncertainty in the repeatability of the calibration
U	expanded uncertainty
V	thermoelectric voltage (μV)

Greek Letters

α	hemispherical total absorptivity
δ	Kronecker delta
ϵ	hemispherical total emissivity
κ	thermal conductivity (W cm^{-1} °C^{-1})
ν	number of effective degrees of freedom
σ	Stefan-Boltzmann constant (W cm^{-2} K^{-4})

Subscripts

a	absorbed
avg	average
c	pertaining to the cold plate surface
cond	conduction
conv	conduction
h	pertaining to the hot plate surface
inc	incident
net	calculated net
rad	radiation
s	pertaining to the surface
sb	pertaining to the Schmidt-Boelter sensor
t	pertaining to the HTHFS
w	pertaining to the cavity wall surface

2.3 Introduction

Heat flux measurement is a complex process that requires careful design and implementation of both sensors and calibration systems to ensure accuracy in the measurements. Heat flux is a critical parameter in many engineering systems, such as vehicle thermal protection and propulsion systems. Direct measurement of heat flux can be accomplished with the use of a differential temperature sensor. Differential temperature sensors measure a spatial temperature gradient which is proportional to heat flux. One type of sensor, the thermopile, measures differential temperature directly using a series connection of thermocouples across a thermal resistance. Thermopile measurement principles are summarized in [6]; also provided is a list of commercially available heat flux sensors. All sensors considered in this study are thermopile sensors, which are often referred to as "total" heat flux sensors because they respond to all three modes of heat transfer.

Thermopile heat flux sensors are typically grouped into two categories: flush-mounted insert gages or surface-mounted flat gages; standard test methods for both types are outlined in [7, 8]. The upper temperature limit (continuous use) for both categories of thermopile sensors is typically below 300 °C [6]. Insert gages are often water cooled to maintain their temperature at acceptable levels. Often, direct measurement of heat flux is required, however, the inherent complications associated with a water cooled sensor may not be desired. For such cases, uncooled sensors capable of withstanding a given thermal environment are appropriate. The need for a heat flux sensor capable of operation at high temperatures (> 300 °C) led to the development of the High Temperature Heat Flux Sensor (HTHFS) at Virginia Tech [9]. The present paper introduces a novel method for calibrating the HTHFS and other uncooled differential heat flux sensors at elevated sensor temperatures.

2.4 Background: Heat Flux Sensor Calibration

There are a number of potential problems when using a differential heat flux sensor. One major issue is that calibration obtained under different modes of heat transfer may yield different results. A second problem is that the presence of the heat flux sensor may alter the temperature field and resulting heat flux [10]. To address such issues, sensor calibration techniques attempt to mimic the measurement environment as closely as possible with high repeatability. This is no easy task, as the extreme thermal environments in which the sensors discussed in this paper are intended can be difficult to reproduce. Careful evaluation of the variation between calibration and application is required to ensure appropriate sensor response in practice.

Numerous approaches are employed in the calibration of heat flux sensors. Radiation is the most popular mode of heat transfer utilized in calibrations, because it is typically the easiest mode with which to establish a consistent, known heat flux. Also, radiation calibration

facilities are able to produce a very wide range of heat flux levels [10]. Absolute "accuracy" in heat flux measurements is difficult to assess due to the lack of a national heat flux standard. Two types of radiation calibration procedures are used for total heat flux sensors: either primary or secondary calibrations. A primary calibration procedure is one in which the radiative heat flux is characterized according to established temperature standards using the Stefan-Boltzmann principle. A secondary calibration procedure is one in which the radiative heat flux is characterized by a secondary standard heat flux sensor. The secondary standard sensor's calibration can be traced to temperature or power standards. Examples of some primary and secondary calibration facilities are given in [11].

The National Institute of Standards and Technology (NIST) provides room temperature radiation calibrations for heat flux levels up to 5 W cm^{-2} using an electrical substitution radiometer as a secondary heat flux standard [12]. The electrical substitution radiometer's calibration is traceable to measurements made by a primary standard high-accuracy cryogenic radiometer. The electrical substitution radiometer is placed outside the aperture of a variable-temperature blackbody, receiving incident flux from a narrow viewing angle normal to the sensor surface. Heat flux calibration is then transfered from the electrical substitution radiometer to a candidate sensor by physical substitution.

One issue with this approach is that the incident flux is provided from a narrow viewing angle, whereas in practice, heat flux sensors typically receive radiant heat flux from a large field of view [13]. Variation between calibration conditions and those found in practice can lead to measurement errors due to the angular sensitivity of a particular heat flux sensor [14]. Round robin studies have revealed significant discrepancies between heat flux calibrations performed at wide angle facilities and those performed at narrow angle facilities [11].

In practice, the HTHFS is expected to receive radiant flux from a large field of view, and therefore, it is desired to calibrate the sensor using a wide angle source. The most common wide angle primary calibration facilities use either a cylindrical or spherical blackbody source. The wide angle facility in [11] utilizes a spherical furnace cavity. The "in-cavity" or "plunge" technique [13] utilizes the same cylindrical blackbody source as NIST [12], however, instead of the candidate heat flux sensor being located outside of the blackbody aperture, the sensor is plunged into the heated cavity to receive radiant heat flux over its full field of view. One common wide angle secondary calibration facility uses a heated flat plate to transfer calibration from a secondary standard heat flux sensor to a candidate sensor [15].

Sensors are often desired for test scenarios that require operation at elevated temperature. All of the aforementioned wide angle facilities are designed to calibrate sensors maintained at constant temperature via water cooling. Application of actively cooled sensors in hot structures testing is problematic due to the thermal discontinuity between the cold sensor and the hot structure. Uncooled sensors intended for high temperature in-situ heat flux measurement must be calibrated in facilities capable of producing known heat flux over a wide range of sensor temperatures. To the authors' knowledge, no such system is currently in operation. Development of a wide angle facility for calibrating heat flux sensors at elevated

temperatures is the focus of the present paper.

2.5 Virginia Tech's High Temperature Heat Flux Sensor

The HTHFS is capable of simultaneous measurement of thermopile surface temperature and heat flux. The sensor's upper temperature limit (continuous use) is 1000 °C. A brief description of the sensor is presented in the following sections; a more detailed description of the HTHFS design and operation is given by Gifford et al. [9].

2.5.1 HTHFS Design

Unlike other thermopile sensors, the HTHFS thermocouple elements (K-type) serve as the thermal resistance of the sensor. The elements are welded together to form a durable thermopile. When heat flows through the thermopile, the sensor outputs a voltage, V_{t}, proportional to the temperature difference across the sensor's thermal resistance:

$$V_{\mathrm{t}} = NSe\,(T_1 - T_2) \tag{2.1}$$

Here N is the number of thermocouple junction pairs in the thermopile, and Se is the relative Seebeck coefficient of the thermocouple alloys. The thermopile voltage output is related to heat conduction by Fourier's law (one-dimensional, steady-state):

$$q'' = -\kappa\frac{dT}{dx} = \kappa_{\mathrm{t}}\frac{T_1 - T_2}{l_{\mathrm{t}}} = \frac{\kappa_{\mathrm{t}} V_{\mathrm{t}}}{l_{\mathrm{t}} NSe} \tag{2.2}$$

where l_{t} and κ_{t} are, respectively, the length (in the direction of heat flow) and thermal conductivity of the sensor's thermal resistance layer. The HTHFS has a surface thermocouple (K-type) welded onto both the top and bottom of the thermopile. The positive (chromel) legs of the two surface thermocouples serve as the lead wires for the thermopile bulk output. The thermopile (1.0 cm × 0.5 cm × 0.32 cm) is secured in an inconel housing (2.54 cm × 1.27 cm × 0.32 cm) with set screws and cast aluminum nitride as shown in Fig. 2.1. Because the HTHFS is intended for in-situ measurement in hot structure testing, no active cooling mechanism is built into the sensor.

2.5.2 Theoretical HTHFS Sensitivity

The HTHFS sensitivity, S_{t}, to an applied heat flux is defined as

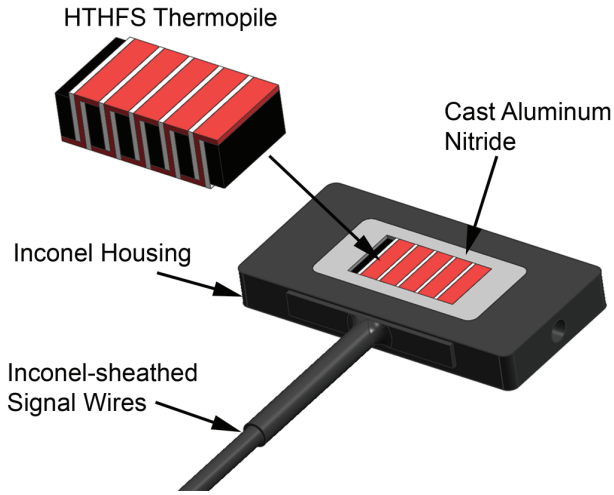

Figure 2.1: HTHFS secured in inconel housing.

$$S_{\mathrm{t}} \equiv \frac{V_{\mathrm{t}}}{q''} \tag{2.3}$$

where q'' is the average heat transfer through the sensor divided by the surface area of the sensor. Combining Eqs. 2.2–2.3, the HTHFS sensitivity can be written as

$$S_{\mathrm{t}} = \frac{l_{\mathrm{t}} N S e}{\kappa_{\mathrm{t}}} \tag{2.4}$$

The HTHFS thermopile is composed of three materials: chromel, alumel, and zirconia toughened alumina (ZTA). Assuming one-dimensional conduction and uniform temperature profiles perpendicular to the direction of heat transfer, the HTHFS composite thermal conductivity, κ_{t}, can be calculated with the use of an equivalent thermal circuit as described in [16]. The calculation of κ_{t} requires knowledge of the geometry and material properties of the sensor components.

Thermal conductivity versus temperature data were taken from [17] for both chromel and alumel, which have nickel mass fractions of 90 % and 95 %, respectively. The ZTA ceramic is made from alumina and zirconia, with respective volume fractions of 85 % and 15 %. The zirconia is assumed to be evenly dispersed in the composite. ZTA composite thermal conductivity versus temperature was calculated using the Maxwell-Eucken method [18] with data taken from [19] and [20] for alumina and zirconia, respectively. A second-order polynomial model is applied to both the chromel and alumel data in order to predict their conductivities at higher temperature than reported in [17]. The polynomial models fit the chromel and alumel data well (Fig. 2.2a), and are consistent with the behavior of nickel in the 500 °C to 900 °C range [16]. Figure 2.2a shows the thermal conductivity of HTHFS components versus temperature, as well as the calculated HTHFS composite thermal conductivity versus

temperature.

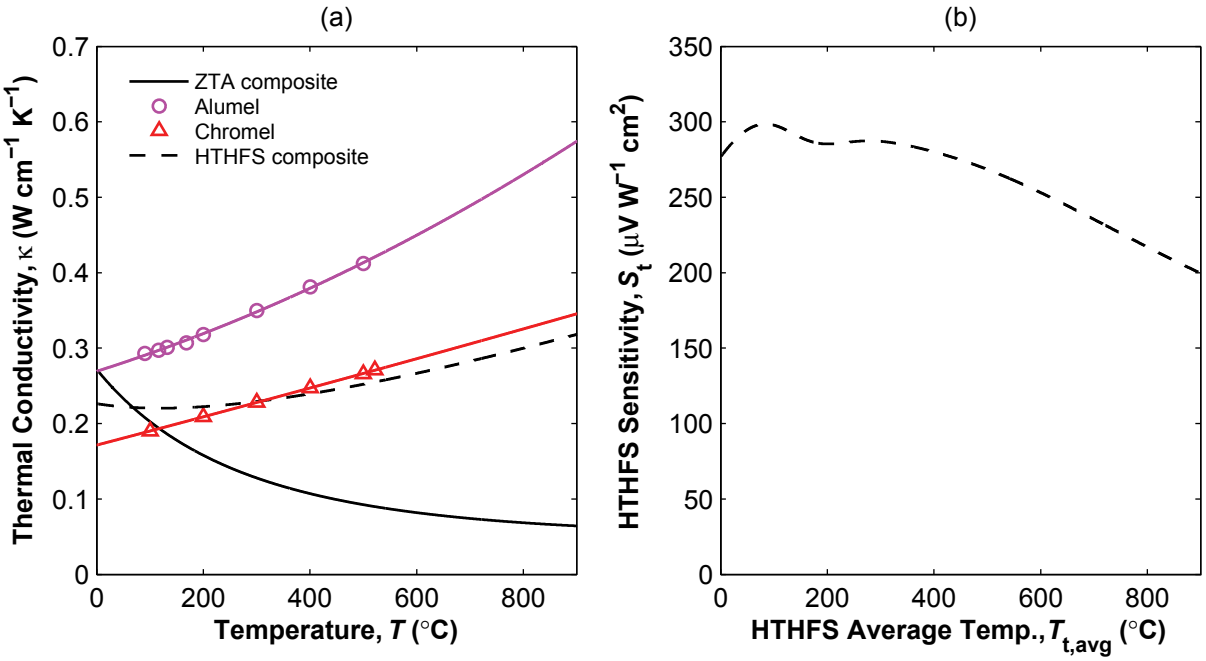

Figure 2.2: (a) Element thermal conductivity and (b) sensitivity of HTHFS thermopile.

Incorporating change in κ_t and Se with temperature allows the prediction of the thermopile's sensitivity versus thermopile average temperature, according to Eq. 2.4. The relative Seebeck coefficient versus temperature for K-type thermocouples is taken from [21]. Applying the $\kappa_t(T)$ and $Se(T)$ trends to the theoretical sensitivity calculation results in the dashed curve shown in Fig 2.2b. For simplicity, the effect of thermal expansion ($L = L(T)$) on sensitivity is considered negligible. The predicted thermopile sensitivity decreases with increasing temperature above 300 °C. The strange trend in the theoretical sensitivity around 100 °C can be attributed to $Se(T)$. A high temperature calibration system, discussed in the following section, was designed and characterized with the goal of experimentally determining HTHFS output temperature dependence.

2.6 High Temperature Calibration System

The primary goal of the proposed calibration system is to produce repeatable, radiative heat flux at elevated sensor temperatures, with minimal uncertainty. The system is specifically designed for high temperature sensors that are not actively cooled. The design and characterization of the system is outlined in the following sections.

2.6.1 Conceptual Design: Cylindrical Radiation Cavity

The cylindrical radiation cavity, shown schematically in Fig. 2.3, consists of two horizontal plates which are separated by a distance, L. The system confines atmospheric air in a cylindrical cavity with diameter, D, and aspect ratio, L/D. It is desired that the inner surfaces of the two horizontal plates are maintained at constant temperature under steady-state operation, where T_{h} and T_{c} are the inner surface temperatures of the hot and cold plates, respectively. The cylindrical sidewall is intended to represent an ideal reradiating surface, characterized by zero net radiation heat transfer ($q_{\mathrm{w}} = 0$). Reradiating surfaces are closely represented by real surfaces that are well insulated on one side and have negligible convective heat transfer on the opposite side [16]. In an effort to combat natural convection effects inside the cavity, the system is oriented such that the hot plate is located above the cold plate, with the gravity vector pointing downward, orthogonal to the horizontal plates (Fig. 2.3).

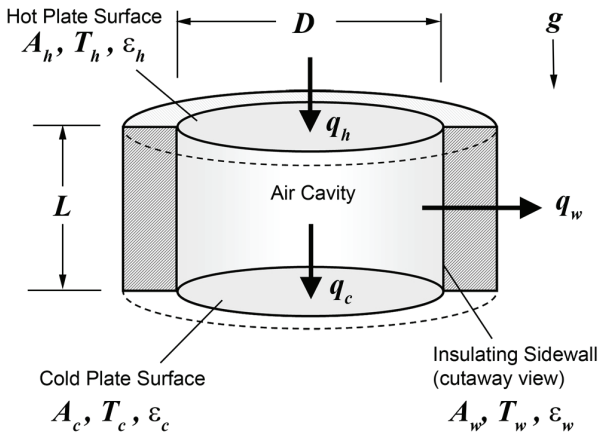

Figure 2.3: High temperature calibration system schematic.

Assuming radiation exchange between diffuse-gray surfaces with uniform radiosities, a simple equation for the heat transfer from the hot plate to the cold plate with the sidewall acting as a reradiating surface has the form [16]

$$\frac{q_{\mathrm{h}}}{A_{\mathrm{h}}} = q''_{\mathrm{h}} = q''_{\mathrm{c}} = \frac{\sigma(T_{\mathrm{h}}^4 - T_{\mathrm{c}}^4)}{\left[\frac{1-\epsilon_{\mathrm{h}}}{\epsilon_{\mathrm{h}}} + \frac{2}{F_{\mathrm{hc}}+1} + \frac{1-\epsilon_{\mathrm{c}}}{\epsilon_{\mathrm{c}}}\right]}. \tag{2.5}$$

where the subscripts represent the surfaces in the enclosure shown in Fig. 2.3: surface (h) is the hot plate inner surface, surface (c) is the cold plate inner surface, and surface (w) is the insulating sidewall inner surface, which is approximated as the reradiating surface. The net heat transfer rate through each control surface, q_{s}, has a direction as shown in Fig. 2.3. The variables T, ϵ, and A of Eq. 2.5 are, respectively, absolute temperature (K),

emissivity, and area of the specified surface (note: $A_h = A_c$). The radiation view factor, F_{12}, is defined as the fraction of radiation leaving surface 1 that is intercepted by surface 2; from the summation of view factors, $F_{cw} = F_{hw} = 1 - F_{hc}$. The Stefan-Boltzmann constant, σ, is equal to 5.67×10^{-12} W cm^{-2} K^{-4}. One thing to note about Eq. 2.5 is that the heat transfer does not depend on the sidewall emissivity, ϵ_w, for an adiabatic sidewall.

From Eq. 2.5 it is apparent that, for a set temperature difference between the hot and cold plates, increasing either ϵ_c, ϵ_h, or F_{hc} increases heat flux. In the limiting case (for a given plate area) as ϵ_h, ϵ_c, and F_{hc} approach their theoretical limit of unity, the radiation exchange between the plates approaches blackbody behavior. The radiation view factor for a given cavity size is calculated as

$$F_{hc} = 1 - 2\left(\frac{L}{D}\right)^2 \left[\sqrt{\left(\frac{D}{L}\right)^2 + 1} - 1\right] \tag{2.6}$$

which approaches unity in the limit as either $D \to \infty$ or $L \to 0$.

2.6.2 Physical Design

With the conceptual cavity design serving as a guideline, a prototype high temperature calibration system has been constructed and tested. The prototype consists of a hot plate and a cold plate in which heat flux sensors are flush mounted (in the center of each plate) and separated by an air cavity. The system is designed to operate with the hot plate on top (with respect to earth gravity vector) to reduce natural convection. A plate diameter of 7.62 cm was chosen to accommodate a wide range of radiation cavity diameters, while limiting the power requirement for the heater system. The sidewall, made from rigid fibrous alumina, is machined accordingly to provide the desired cavity size. For this analysis, the sidewall was machined to form a radiation cavity where $L = 1.27$ cm and $D = 5.08$ cm ($L/D = 0.25$). A resistance heater potted into the hot plate provides heat to the system, while water cooling in the cold plate provides the means of heat removal. The entire system is encased in rigid fibrous alumina insulation to limit heat loss to the surroundings. Figure 2.4 shows a CAD model of the calibration system with labeled components.

The aluminum cold plate houses a reference standard Schmidt-Boelter (SB) heat flux sensor (Medtherm model No. 64-30SB-20K) which is mounted flush with the plate surface. The SB sensor's calibration is traceable to NIST temperature and electrical standards. Both the SB sensor and the cold plate in which it is housed have internal channels for cooling water. The stainless steel hot plate houses one HTHFS which is flush mounted in the plate (Fig. 2.5). An inconel sheathed, flat-spiral coil heater is mechanically fastened to the backside of the hot plate with a stainless steel cap plate. Cast aluminum nitride fills the void areas between the coil and hot plate to reduce contact resistance. The hot and cold plate sandwich the insulating sidewall, forming the cylindrical air cavity in which the radiation exchange

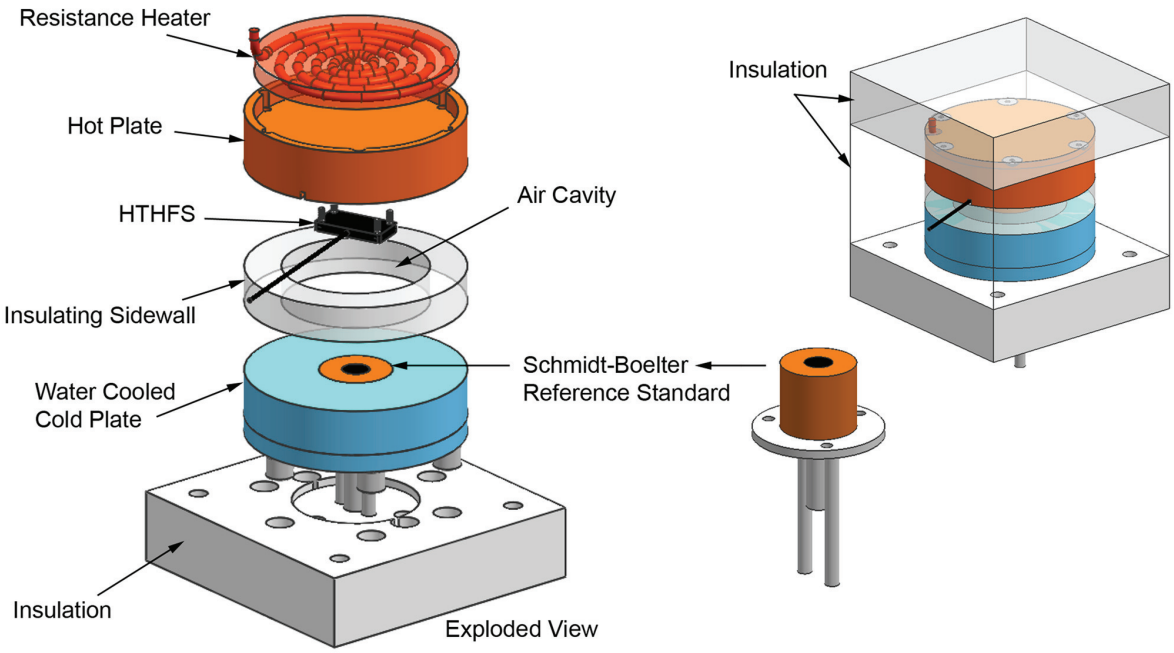

Figure 2.4: High temperature calibration system CAD model.

between the plates takes place. The system is designed to transfer heat flux calibration from the secondary standard SB sensor to the HTHFS.

2.6.3 Experimental Setup

Experimental characterization of the system began with comparing initial measurements from the reference standard SB sensor to the ideal solution (Eq. 2.5). Steady-state heat flux events were physically realized by controlling power to the resistance heater with the use of a single-phase 120 VAC variable transformer. One steady-state thermal event was produced for hot plate temperatures from 100 °C to 900 °C in steps of approximately 100 °C (nine thermal events per test). Room temperature water was circulated through the cold plate and SB sensor using a small submersible pump. Flow rates of 17 mL s^{-1} and 14 mL s^{-1} were maintained for the cold plate and SB sensor, respectively.

In order to characterize system performance, temperature measurements were made with K-type thermocouples at various locations inside the cavity. Cold plate temperatures were measured with a thermocouple in the SB sensor along with two thermocouples spot welded onto the surface of the cold plate. Hot plate temperatures were measured with five thermocouples: two thermocouples built into the HTHFS, one thermocouple built into the heater, and two fine wire thermocouples spot welded onto the hot plate surface (as shown in Fig. 2.5). The surface thermocouples are electrically connected to the plates only at the junction. In

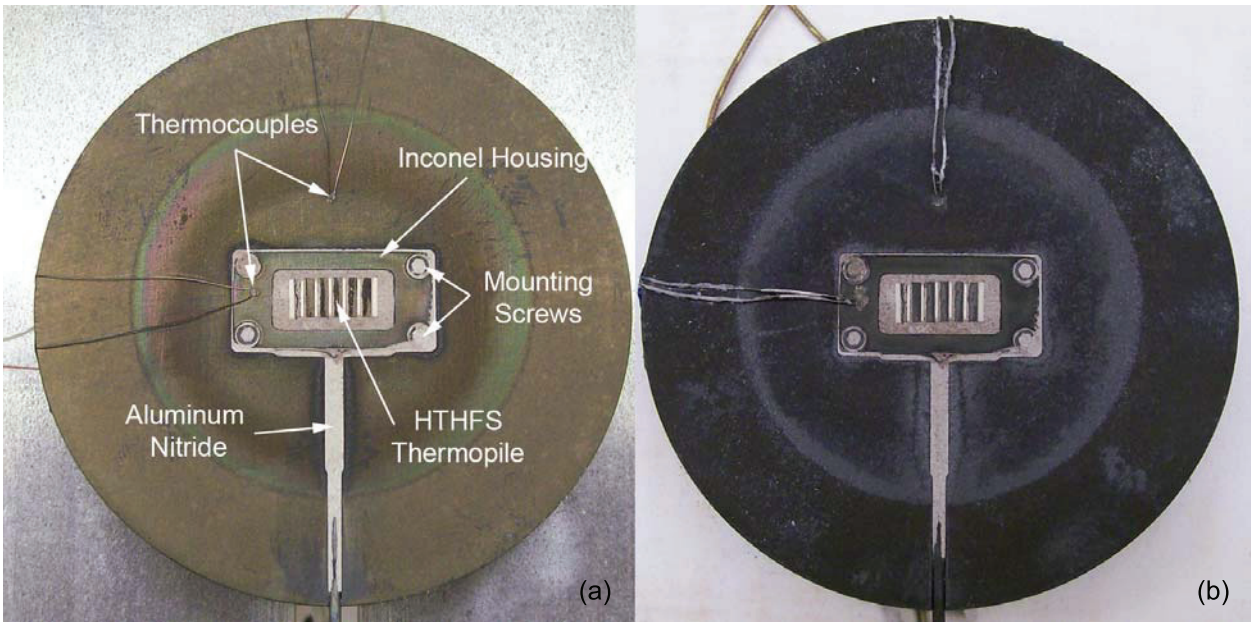

Figure 2.5: Stainless steel hot plate housing flush mounted HTHFS with (a) initial and (b) heavy surface oxidation.

early tests, the wires were electrically isolated from the hot plate surface using ceramic sleeves. Once a heavy oxidation layer formed on the hot plate surface, the ceramic sleeves were no longer necessary to prevent electrical contact between the plate and thermocouple lead wires. Heat conduction from the thermocouple junction through the lead wires is assumed negligible, because the fine wires, routed along the hot plate surface, are assumed to be at approximately the same temperature as the plate surface.

Temperature and heat flux signals were read into 24-bit National Instruments CompactDAQ thermocouple modules as analog differential inputs. Cold-junction temperature was compensated for each channel using on board thermistor measurements. The ±125 mV range of the analog-to-digital converter provides significant resolution for the expected output from the heat flux sensors with a least significant bit of $0.25/2^{24} = 14.9$ nV.

The cold plate surface was painted with flat black paint to match the SB sensor face ($\epsilon_c = \epsilon_{sb} = 0.94$). The hot plate surface was left uncoated: the paint used on the cold plate has an upper temperature limit of approximately 630 °C, which is below the desired upper temperature bound for the hot plate of 900 °C. Preliminary test runs were performed over the full operating range of the system to allow the hot plate surface to oxidize (Fig. 2.5), increasing its emissivity.

2.6.4 System Characterization

To transfer calibration from the reference standard to the HTHFS, the heat flux experienced by each sensor must be well known (ideally equal). Although the ideal solution (Eq. 2.5) provides insight to system operation, a more detailed analysis of system operation is required to characterize the heat flux experienced by each sensor. Small discrepancies in the heat flux experienced by each sensor is expected due to the inherent differences in the sensors' designs. The effect of each sensor's geometry and intrusiveness on the heat flux transfer calibration was considered. Unlike the assumption made in Eq. 2.5, the surface radiosities are not exactly uniform over each plate. Instead, due to the geometrical view factor, the heat flux is highest at the center of the plates. Because of the nonlinear heat flux distribution on each plate, the average heat flux experienced by each sensor will not be exactly the same if the sensing areas are different.

The presence of the sensors in the measurement environment has a small effect on the temperature profile on each plate. Preliminary tests revealed that, although the HTHFS and stainless steel plate thermal properties were well matched, the contact resistance between the plate and sensor results in some plate surface temperature discontinuity. At high operating temperatures, the difference in measured plate surface temperature and HTHFS thermopile surface temperature was as high as 30 °C. For these reasons, it is expected that the heat flux experienced by each sensor is slightly different. To account for such effects, an analytical model was developed, using measured temperatures to calculate the heat flux distribution on each surface of the cavity. The following sections outline the methods used to correct for the small heat flux discrepancies between the two sensors.

Analytical Model

An analytical model was used to characterize the heat flux distribution on the hot and cold plate surfaces. Experimentally measured surface temperatures serve as inputs to the analytical model. The model assumes heat is transferred through air by conduction with no convection, and that the air does not participate in the radiation exchange. Because the top-heated orientation dictates stable stratification of the air within the cylindrical cavity, it is assumed that convection exchange is negligible. Numerical and experimental results in [22, 23] indicate that heat transfer through air in the top-heated cylindrical cavity occurs by conduction only, although inclination of the cavity (cavity centerline axis with respect to gravity vector) can cause weak circulation in the air.

As a conservative approach, correlations from [22, 23] have been used to estimate the potential convection error caused by inclination of the cavity. For an inclination angle of 10°, the maximum predicted augmentation of heat transfer by convection is less than 5 % of the calculated conduction heat transfer for all test conditions. For each steady-state thermal event, a worst-case estimate of the convection error at each surface is $q''_{\mathrm{s,conv}} = 0.05 \times q''_{\mathrm{s,cond}}$.

The effects of convection error on the heat flux calibration are examined in §2.6.6.

Considering radiation and conduction exchange within the cavity (neglecting convection), the net heat flux from each surface, $q''_{\mathrm{s,net}}$, is calculated as

$$q''_{\mathrm{s,net}} = q''_{\mathrm{s,cond}} + q''_{\mathrm{s,rad}} \tag{2.7}$$

where $q''_{\mathrm{s,cond}}$, the conduction component of heat flux out of the surface, and $q''_{\mathrm{s,rad}}$, the radiation component of heat flux out of the surface, are considered uncoupled. Assuming one-dimensional conduction through the air cavity,

$$q''_{\mathrm{s,cond}} = -\kappa_{\mathrm{air}} \frac{dT}{dx} = \kappa_{\mathrm{air}} \frac{T_{\mathrm{h,avg}} - T_{\mathrm{c,avg}}}{L} \tag{2.8}$$

with κ_{air} taken at the film temperature. The temperature gradient is simply the difference in the average measured surface temperature of the hot and cold plate divided by the cavity length, L.

Assuming diffuse-gray radiation exchange between cavity surfaces with uniform radiosities, a general system of equations relating radiative heat flux, $q''_{j,\mathrm{rad}}$, and surface temperature, T_j, for the ith surface is [24]

$$\sum_{j=1}^{N} \left(\frac{\delta_{ij}}{\epsilon_j} - F_{ij} \frac{1-\epsilon_j}{\epsilon_j} \right) q''_{j,\mathrm{rad}} = \sum_{j=1}^{N} \left(\delta_{ij} - F_{ij} \right) \sigma T_j^4 \tag{2.9}$$

where, corresponding to a specific surface, $i = 1, 2, ..., N$. Also, $\delta_{ij} = 1$ when $i = j$ and is zero otherwise. In the case of a three-surface enclosure with an adiabatic sidewall, Eq. 2.9 is equivalent to Eq. 2.5. Higher accuracy in the calculated heat flux distribution may be obtained with Eq. 2.9 compared to Eq. 2.5 by breaking the each cavity surface into discrete sections of uniform temperature and radiosity.

Application of Eq. 2.9 to the present experimental setup, creates one equation for each surface. The hot and cold plates are each broken into three distinct surfaces: one central disk of radius r_{s} representing the heat flux sensing area, and two surrounding rings. The ring immediately surrounding the sensing area represents the sensor body or housing, while the outermost ring represents the plate in which the sensor is mounted. Surface temperature measurements in each section serve as inputs to the load vector (right-hand side of Eq. 2.9). The adiabatic sidewall is broken into five distinct ring sections, all of equal length ($L/5$). A sensitivity analysis revealed that increasing the number of sidewall sections past five has negligible effect on the calculated hot and cold plate radiosities. Because the sidewall sections are considered adiabatic ($q''_{\mathrm{w}} = 0$), a value of 0 W cm^{-2} is input into the degree-of-freedom vector ($q''_{j,\mathrm{rad}}$ of Eq. 2.9) for each sidewall section, leaving $N = 11$ equations for the $N = 11$ unknowns.

Solution of the matrix equations yields the unknown plate surface heat fluxes and sidewall radiosities. The net heat flux over each sensing area is then calculated from Eq. 2.7. It is important to note that for Eqs. 2.7-2.9, q'' is the net heat flux out of the surface (convention for heat flow direction). As with Eq. 2.5, Eq. 2.9 assumes that the air is perfectly translucent and there is negligible convection exchange within the cavity.

Parameter Estimation: Hot Surface Emissivity

Solving the radiosity matrix equations requires knowledge of the emissivity of each surface in the cavity other than the adiabatic sidewall. The cold plate surface and SB sensor surface are coated with flat black paint with an emissivity of $\epsilon_c = \epsilon_{sb} = 0.94$. Unlike the cold surfaces, the hot surfaces (HTHFS and hot plate) are not coated with paint. Instead, they were left uncoated and allowed to oxidize over a series of heating cycles (Fig. 2.5). Heavily oxidized stainless steel and inconel can have surface emissivities in the range of 0.6 to 0.9 [16, 24]. In order to determine the appropriate value for the unknown emissivities, a parameter estimation scheme was developed which utilizes experimental temperature and heat flux measurements. For simplicity, the HTHFS surface emissivity was assumed to be the same as the stainless steel hot plate surface emissivity. This assumption is reasonable because all materials (other than the small amount of ceramic in the HTHFS) in the hot plate and HTHFS are nickel alloys of similar composition. It is also assumed that the surface emissivity is constant, ignoring any spectral or surface temperature dependence.

As described in §2.6.3, each test run consists of nine steady-state thermal events. After each test run, the radiosity matrix equations are solved in a loop with values of the hot surface emissivity, $\epsilon_t = \epsilon_h$ ranging from 0.01 to 0.99, serving as the loop parameter. For each value of ϵ_h, a sum of squares function, X, is calculated as

$$X(\epsilon_h) = \sum_{i=1}^{9} \left(q''_{sb,a}(i) - q''_{sb,net}(\epsilon_h, i) \right)^2 \tag{2.10}$$

where $i = 1, 2, ..., 9$ represents the thermal event number, $q''_{sb,a}$ is the absorbed heat flux measured by the reference standard SB sensor, and $q''_{sb,net}$ is the cold sensor heat flux calculated using Eqs. 2.7-2.9. The best estimate for ϵ_h is the one which minimizes $X(\epsilon_h)$. The use of this sum of squares function for the parameter estimation scheme ensures that the predicted heat flux (cold sensor) matches the measured heat flux (SB reference standard sensor).

Because ϵ_h can only have a value from 0 to 1, the parameter estimation loop does not need any convergence criteria to arrive at the appropriate value. Instead, the best estimate for ϵ_h will correspond to the smallest value for $X(\epsilon_h)$ over the full range of possible emissivities. Several preliminary tests were performed in order to allow the hot plate and HTHFS to become heavily oxidized. After this initial oxidation phase, five tests were run. The results from these five tests are reported in this work. The mean hot plate emissivity and sample

standard deviation for the five tests was found to be 0.728 and 0.005, respectively.

The plots shown in Fig. 2.6, which contain data taken from one specific test, demonstrate the parameter estimation technique and the role it plays in the determination of the heat flux correction factor, f, discussed in the following section. Figure 2.6a shows the sum of squares function versus hot plate emissivity; the minimum value of this function corresponds to the best estimate for ϵ_{h}. Figure 2.6b shows measured (SB sensor) and modeled heat flux (magnitude) versus hot plate temperature for the test. The cold and hot sensor predicted heat flux is calculated using the estimated parameter (ϵ_{h}) and measured surface temperatures applied to Eqs. 2.7-2.9.

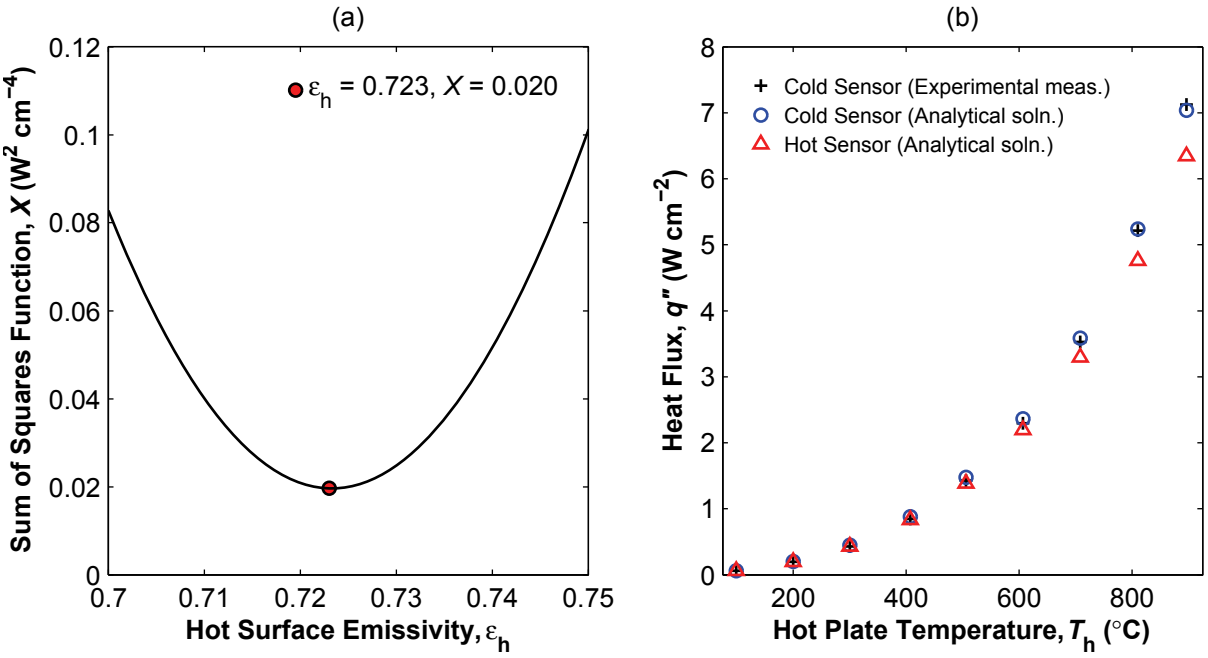

Figure 2.6: (a) Emissivity parameter estimation and (b) SB heat flux comparison.

As shown in Fig. 2.6b, the calculated cold sensor heat flux matches well with the measured heat flux (SB sensor). Because no noticeable trend in the difference between the predicted and measured heat flux is observed, these results appear to support the assumption that the hot plate emissivity is best estimated as a constant value for this experiment. Also shown in Fig. 2.6b is the predicted hot sensor heat flux, which deviates slightly from the cold sensor heat flux as the temperature of the hot plate increases. The trend in the heat flux discrepancy is due to the temperature discontinuity across the hot plate surface caused by the presence of the HTHFS. Because the temperature of the HTHFS is slightly lower than the surrounding hot plate (§2.6.3), the cold sensor receives more heat than that leaving the hot sensor. The effect is more profound in the high temperature range, because the radiative heat flux is proportional to the absolute temperature raised to the fourth power.

Heat Flux Correction Factor

To account for the predicted difference in heat flux experienced by each sensor, a correction factor, f, can be calculated for each steady-state thermal event of a specific test as

$$f = q''_{\mathrm{sb,net}}/q''_{\mathrm{t,net}} \tag{2.11}$$

where $q''_{\mathrm{sb,net}}$ and $q''_{\mathrm{t,net}}$, the SB and HTHFS predicted heat flux (Fig. 2.6), respectively, are calculated using Eqs. 2.7-2.9. The correction factor is then used in the calculation of the HTHFS sensitivity, described in the following section. Calculated correction factors for the data shown in Fig. 2.6 are listed in Table 2.1; also listed are the calculated heat fluxes used to determine f. The largest correction used in the heat flux calibration is 10 % ($f = 1.1$).

Table 2.1: Calculated correction factor, f, for a sample test.

T_{h} / (°C)	$q''_{\mathrm{t,cond}}$ / (W cm^{-2})	$q''_{\mathrm{sb,net}}$ / (W cm^{-2})	$q''_{\mathrm{t,net}}$ / (W cm^{-2})	f
104	0.018	0.065	0.063	1.031
209	0.047	0.219	0.212	1.034
311	0.081	0.487	0.467	1.042
414	0.120	0.917	0.868	1.057
515	0.162	1.554	1.453	1.070
616	0.208	2.473	2.293	1.078
722	0.260	3.810	3.498	1.089
819	0.311	5.457	4.969	1.098
900	0.356	7.198	6.519	1.104

2.6.5 Calibration Results

The heat flux through each sensor's surface can be equated according to

$$q''_{\mathrm{sb,a}} = q''_{\mathrm{t,a}} \cdot f \tag{2.12}$$

where $q''_{\mathrm{sb,a}}$ and $q''_{\mathrm{t,a}}$ are the SB and HTHFS measured absorbed heat flux, respectively, and f is calculated for every steady-state thermal event using the analytical model. In this fashion, the SB sensor's calibration can be transferred to the HTHFS. Note, in Eq. 2.12 and in Fig. 2.6b the heat flux direction is not represented; the HTHFS thermopile is insensitive to direction, and therefore only the heat flux magnitude is presented for simplicity. The HTHFS sensitivity to absorbed heat flux is determined from

$$S_{\mathrm{t,a}} = \frac{V_{\mathrm{t}}}{q''_{\mathrm{t,a}}} \tag{2.13}$$

where V_t is the HTHFS voltage output. Combining Eqs. 2.12–2.13, the HTHFS sensitivity to absorbed heat flux is

$$S_{t,a} = \frac{V_t}{V_{sb}} S_{sb,a} \cdot f \tag{2.14}$$

where $S_{sb,a}$ is the calibrated Schmidt-Boelter sensitivity (to absorbed heat flux) provided by the manufacturer, and the sensor output ratio, V_t/V_{sb}, is directly measured. If desired, the sensitivity of the HTHFS to incident radiation can be determined from

$$S_{t,inc} = \alpha_t S_{t,a} = \epsilon_t S_{t,a}, \tag{2.15}$$

assuming diffuse-gray radiation exchange ($\alpha = \epsilon$). Calibration results from five tests are shown in Fig. 2.7.

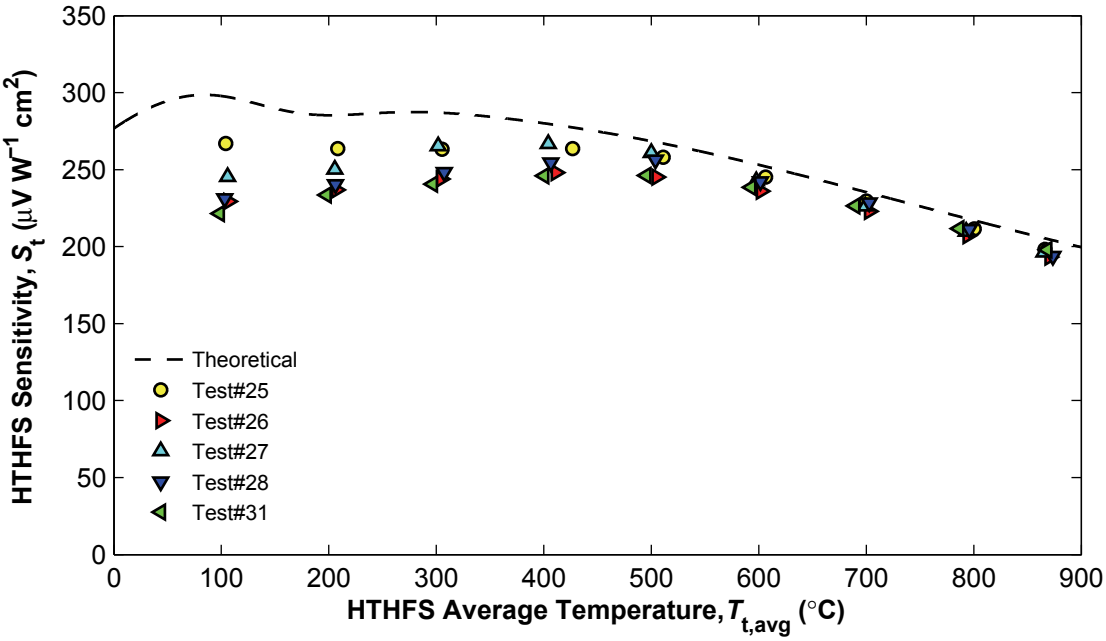

Figure 2.7: HTHFS calibrated sensitivity versus sensor temperature.

The theoretical sensitivity (§2.5.2) is plotted for comparison with experimental results. The calibrated sensitivity follows a similar trend as the theoretical sensitivity with a slightly lower magnitude over the entire temperature range, suggesting that the thermal conductivity of the thermopile is slightly higher than predicted, especially in the low temperature range. The slope in the calibrated sensitivity from 400 °C to 900 °C agrees very well with prediction. The uncertainty in the calibration results appears to be greater in the lower temperature range. A closer examination of the propagation of uncertainty in the experiment is presented in the following section.

2.6.6 Uncertainty Analysis

Each quantity, x_i, used to determine the HTHFS sensitivity has an associated standard uncertainty, $u(x_i)$. The combined standard uncertainty in the resulting HTHFS sensitivity, $u_c(S_{\mathrm{t,a}})$, is determined according to [25] from

$$u_c(S_{\mathrm{t,a}}) = \sqrt{\sum_{i=1}^{4} \left(\frac{\partial S_{\mathrm{t,a}}}{\partial x_i} u(x_i) \right)^2 + (u_r)^2} \tag{2.16}$$

where $\partial S_{\mathrm{t,a}}/\partial x_i$ are the sensitivity coefficients for each quantity on the right-hand side of Eq. 2.14. The uncertainty in the repeatability of the sensitivity calibration, u_r, is taken to be the calculated standard deviation of the mean sensitivity determined from the sample of five tests reported in this work (see Fig. 2.7).

Standard uncertainties are determined using either Type A or Type B evaluation methods. Type A evaluation of standard uncertainty is based on statistical methods, while Type B evaluation is based on scientific judgment using all relevant information available. In the present paper, standard uncertainties have been evaluated using Type A methods wherever possible. In general, $u(x_i)$ is either conservatively estimated or it is represented by a statistically estimated standard deviation. A root-sum-squares technique is used when multiple sources contribute to the standard uncertainty in one quantity, x_i. Instead of using a coverage factor when determining $u(x_i)$, an overall coverage factor, k, for $u_c(S_{\mathrm{t,a}})$ is taken as the Student's t multiplier for 95 % confidence and ν effective degrees of freedom. The effective degrees of freedom for the sensitivity calibration is calculated using the Welch-Satterthwaite formula [25].

The standard uncertainty in V_{t} and V_{sb} is a combination of sensor and measurement system uncertainties. Bias error is measured at the start of each test, when the system is in thermal equilibrium (sensors have zero output), and removed from the data during post-processing. The measurement uncertainty associated with the data acquisition system was determined through calibration using a precision DC power supply. Uncertainty in the sensor outputs is either estimated (HTHFS) or calculated using repeatability and linearity information provided by the manufacturer (SB). The standard uncertainty in the SB sensor's calibrated sensitivity is quoted by the manufacturer to be ± 1.5 %.

The correction factor, f, is calculated using experimental measurements and system properties applied to Eqs. 2.7-2.9 as described in §2.6.4. The combined standard uncertainty in f is calculated from the propagation of uncertainty in the quantities used to calculate the correction factor. Due to the complexity of Eqs. 2.7-2.9, a sequential perturbation numerical technique, outlined in [26], is used to calculate $u_c(f)$. Calibration error caused by convection can affect the correction factor calculation by either introducing a small heat flux bias of equal magnitude between the two sensors, or by introducing a heat flux bias of unequal magnitude between the two sensors. Use of the sequential perturbation technique allowed for

both of these possible scenarios to be considered in the calculation of $u_c(f)$. The standard uncertainty in the quantities used to calculate f are listed in Table 2.2. A summary of the calibration results and associated uncertainties is provided in Table 2.3.

Table 2.2: Standard uncertainty values used in calculating $u_c(f)$.

Quantity	Symbol(s)	$u(x_i)$	Units
Hot surface temperatures	T_t, T_h	2.5	°C
Cold surface temperatures	T_sb, T_c	1.0	°C
Lengths	L, D, r_t, r_sb	0.013	cm
Surface emissivities	$\epsilon_\mathrm{h} = \epsilon_\mathrm{t}$, $\epsilon_\mathrm{c} = \epsilon_\mathrm{sb}$	0.022	–
Air thermal conductivity	κ_air	$0.1 \times \kappa_\mathrm{air}$	W cm^{-1} °C^{-1}
Convective heat flux augmentation	$q''_\mathrm{s,conv}$	$0.05 \times q''_\mathrm{s,cond}$	W cm^{-2}

Table 2.3: Calibration results and uncertainty as a function HTHFS mean temperature, $T_\mathrm{t,avg}$. Results averaged over five test sample.

$T_\mathrm{t,avg}$ / (°C)	$u(V_\mathrm{t})$ / (μV)	$u(V_\mathrm{sb})$ / (μV)	$u(S_\mathrm{sb,a})$ / (μV W^{-1} cm^2)	$u_c(f)$	$U(S_\mathrm{t,a})$ / (μV W^{-1} cm^2)	$S_\mathrm{t,a}$ / (μV W^{-1} cm^2)
104	0.18	0.87	9.7	0.045	30	239
204	0.29	2.8	9.7	0.028	22	245
303	0.57	6.0	9.7	0.022	20	252
408	1.1	12	9.7	0.019	19	256
501	1.8	20	9.7	0.017	17	253
597	2.7	32	9.7	0.015	15	241
696	3.8	49	9.7	0.014	14	227
790	5.2	72	9.7	0.013	12	210
871	6.4	95	9.7	0.012	11	196

The combined standard uncertainty in the HTHFS sensitivity calibration, $u_c(S_\mathrm{t,a})$, is multiplied by the coverage factor, k, to get the expanded uncertainty, $U(S_\mathrm{t,a})$. A coverage factor of $k = 2.03$ is used to provide a 95 % confidence interval about the measurement results (Student's t multiplier for $\nu = 35$). Figure 2.8 shows averaged results from five tests. The average calibration sensitivity is plotted with bars showing the expanded uncertainty in the result, which is approximately ±7 % of the calibrated HTHFS sensitivity for sensor temperatures from 300 °C to 900 °C. The calibrated sensitivity is slightly lower than predicted with the model, suggesting that the actual thermopile has a higher thermal conductivity than the composite model.

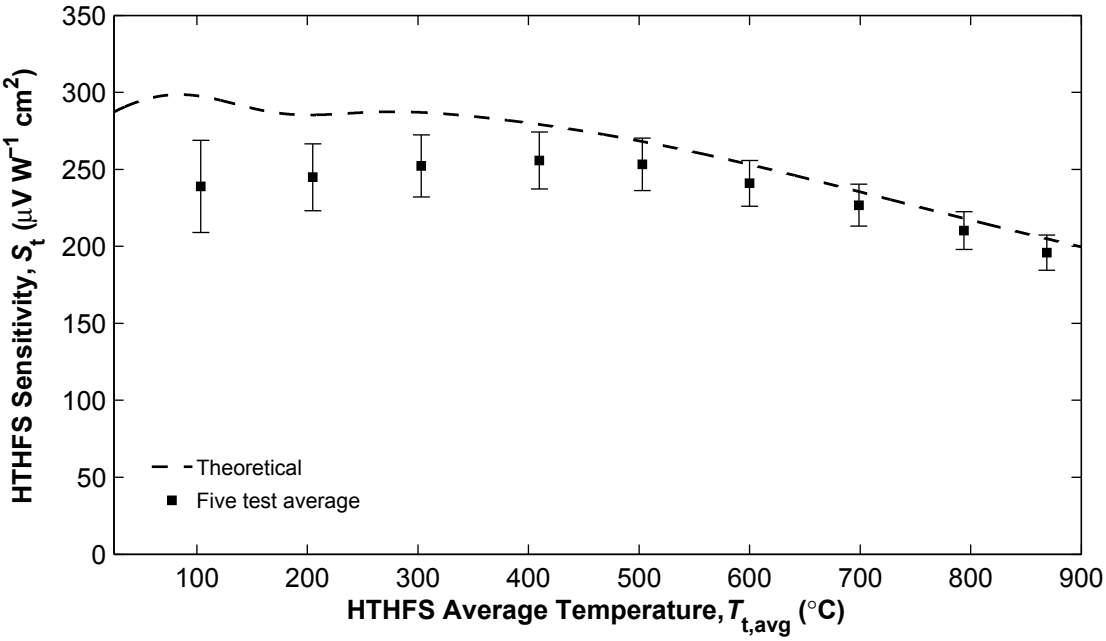

Figure 2.8: HTHFS calibrated sensitivity showing expanded uncertainty (95 %CI).

2.7 Discussion and Future Work

The first prototype high temperature calibration system has successfully characterized Virginia Tech's HTHFS up to 900 °C, improving the sensor's ability to accurately measure heat flux at elevated temperature. The trend in the sensor's sensitivity versus temperature agrees well with the prediction based on thermopile material properties. The bench top calibration system is both cheap and portable.

Initial results have provided useful information for future system improvement. Characterization of the system affirmed that the thermal disturbance caused by the HTHFS located in the stainless steel hot plate is small, but significant. Use of the analytical model shows how correcting for thermal disturbances may be accomplished with reasonable results. A parameter estimation scheme was developed to estimate the total hemispherical emissivity of the hot plate and hot sensor based on calibrated heat flux measurements made by the standard SB sensor. A constant value for this emissivity input into the radiosity matrix yields model results that are consistent with experimental findings.

The uncertainty analysis revealed that the major sources for uncertainty over the entire operating range of the system are in the surface emissivities used in determining f, particularly ϵ_{h}. Although the parameter estimation scheme chooses the most appropriate value for the hot surface emissivity, it is assumed that the emissivity is independent of spectral and surface temperature effects. High temperature coatings with well defined optical properties will be

investigated for future use with the calibration system. The uncertainty analysis also showed that at low temperatures, the primary reason for the increased uncertainty in the result may be attributed to the low heat flux sensor output when compared to the uncertainty in the voltage measurement itself.

The magnitude of convection exchange inside the cavity must also be investigated. Commercial finite element software may prove useful in determining the effect of convection inside the cavity. One solution to eliminating both convection and conduction inside the cavity would be to evacuate the cavity. A cost-benefit analysis will give insight for future improvements aimed at reducing uncertainty in the calibration process.

2.8 Conclusions

HTHFS output temperature dependence over the range of 100 °C to 900 °C has been successfully characterized with acceptable uncertainty limits. The temperature dependency in the HTHFS output is primarily caused by change in thermal conductivity with temperature of the sensor's individual elements. The HTHFS calibrated sensitivity versus temperature has a similar trend as the theoretical sensitivity model, and suggests that the thermopile's composite thermal conductivity is slightly higher than predicted with the sensitivity model. The uncertainty in the calibration is higher in the low temperature range because the radiation heat flux is very low (same order of magnitude as conduction). Analytical modeling is necessary to account for small systematic discrepancies in heat flux experienced by the two sensors.

2.9 Acknowledgments

Funding for this work was provided by NASA through NRA and GSRP grants.

Chapter 3

Uncertainty Reduction in the Transfer Calibration Method for High Temperature Heat Flux Sensors

The material in this chapter was submitted for review in the International Journal of Heat and Mass Transfer on April 18, 2011.

3.1 Abstract

Direct measurement of hot-wall heat flux at temperatures in excess of 300 °C poses an exciting challenge for scientists and engineers in regard to thermal sensor design, implementation, and calibration. A novel method for calibrating heat flux sensors at elevated sensor temperatures is presented in this work. This transfer calibration is based on steady-state heat transfer in a right cylindrical air enclosure with a hot top wall and a cold bottom wall. The primary focus in this work is to achieve the lowest possible expanded uncertainty in the transfer calibration. A detailed analysis is presented demonstrating the appropriate modeling of the heat transfer processes in the calibration enclosure. Experimental characterization of the system was performed to determine the optimal size of the cylindrical enclosure. The high temperature transfer calibration method is demonstrated through the calibration of two high temperature working standard heat flux sensors. An aspect ratio of $L/D = 0.19$ was found to be the optimal configuration for the calibration enclosure, corresponding to an expanded uncertainty in the transfer calibration of $\pm 6\%$ for sensor temperatures ≥ 300 °C.

3.2 Nomenclature

A	area (cm^2)
D	calibration enclosure diameter (cm)
E_b	blackbody emissive power (W cm^{-2})
f	calibration correction factor
F	radiation configuration factor
$\boldsymbol{g}$	gravitational vector
J	radiosity (W cm^{-2})
k	statistical coverage factor
l	length (cm)
L	plate separation distance (cm)
M	total number of discrete surfaces used in the net-radiation analysis
N	number of thermocouple junction pairs in thermopile
p	absolute pressure (Pa)
q''	heat flux (W cm^{-2})
r	radius (cm)

S	heat flux sensor sensitivity (μV W^{-1} cm^2)
S_e	relative Seebeck coefficient (μV °C^{-1})
t	time (s)
T	temperature (°C)
T_f	film temperature (°C)
u	standard uncertainty
u_c	combined standard uncertainty
u_r	uncertainty in the repeatability of the calibration
U	expanded uncertainty in the calibration
V	thermoelectric voltage (μV)
x	distance (cm)

Greek Letters

χ	test variable
δ	Kronecker delta
ϵ	hemispherical total emissivity
κ	thermal conductivity (W cm^{-1} °C^{-1})
ν	number of effective degrees of freedom in the calibration
σ	Stefan-Boltzmann constant (W cm^{-2} K^{-4})

Subscripts

avg	average
b	high temperature flat black paint coating
bot	pertaining to the bottom surface
c	pertaining to the cold plate surface
cb	carbon black coating
cond	conduction
conv	convection
h	pertaining to the hot plate surface
i	index variable

j	index variable
meas	measured
o	oxidation coating
p	paint
rad	radiation
s	surface
sb	pertaining to the Schmidt-Boelter sensor
t	pertaining to the HTHFS
top	pertaining to the top surface
tot	total
v	virtual black surface
w	pertaining to the enclosure sidewall
ws	pertaining to the working standard heat flux sensor

3.3 Introduction

Thermal energy management is a critical factor in the design and operation of engineering systems and processes. The measurement of heat transfer is often required to monitor or control such processes. Numerous types of sensors are used to directly measure heat flux (thermal energy transfer per area), many of which are commercially available [6]. Spatial temperature gradient sensors are among the most widely used types of heat flux sensors. Spatial temperature gradient sensors are generally referred to as "total" heat flux sensors because they respond to all modes of heat transfer: radiation and convection/conduction exchange between the sensor and the surrounding environment. As this heat flows through the sensor's thermal resistance layer (perpendicular to the sensing surface), a temperature difference is created which is proportional to the heat flux by Fourier's law of conduction. The relationship between the measured temperature difference and the heat flux is established by direct calibration. All sensors referred to in the current study are total heat flux sensors.

Various approaches have been used for heat flux sensor calibration, employing all modes of heat transfer. Heat flux calibrations are classified as either primary calibrations or secondary calibrations according to the heat flux standard used. Primary calibration methods utilize blackbody radiant sources that are characterized by either primary standard radiometers or primary standard temperature detectors. Secondary calibration methods use a secondary standard heat flux sensor to characterize the heat output from a chosen source. Calibration

is transferred from the secondary standard heat flux sensor to a working standard heat flux sensor by subjecting the working standard to same heat source. Details of the primary and secondary calibration methods can be found in [27] and [28], respectively.

Radiation is the most common mode of heat transfer used in calibrations, because of the wide range of available heat flux levels and the high repeatability that can be achieved with a radiant source [6]. All calibrations described in [27] and [28] use radiant sources and actively cooled heat flux sensors. Active cooling is used to maintain the sensors at or very near the surrounding environment temperature. When measuring this cold-wall heat flux, it is important that temperature differences between the sensor and its surroundings are kept to a minimum, to limit any unwanted convection or radiation exchange with the surroundings. Consequently, the cold-wall condition allows the sensors to respond to only the radiation incident on the object surface. Guidelines for the accurate measure of cold-wall heat flux using temperature gradient sensors are presented in [29, 7, 8]. Conversely, hot-wall heat flux refers to the heat flux experienced by a body which is at a higher temperature than its surroundings. The hot-wall heat flux is equal to the sum of the net convection to and net radiation absorbed by the object surface. This is generally quite different than the incident incident radiation and is more representative of many practical applications.

When the measurement of hot-wall heat flux is desired, active cooling of heat flux sensors is not appropriate. Instead, the heat flux sensor is desired to inherit the temperature of the test article in which it is mounted. This ensures that the heat flux measured by the sensor is a true representation of the heat flux experienced by the article with no sensor present. While most common heat flux sensors are limited to temperatures below 300 °C, some recent advances in thermal instrumentation design have produced sensors capable of withstanding temperatures much greater than 300 °C. Two examples of such sensors are the High Temperature Heat Flux Sensor (HTHFS) [9] and the Direct Write Heat Flux Sensor (DWHFS) [30], both of which are capable of surviving at temperatures in excess of 1000 °C.

Accurate measurement of hot-wall heat flux requires that sensors, such as the HTHFS and DWHFS, are calibrated over their entire operating temperature range. This is important because the material properties of the sensors change with temperature, and therefore the output is temperature dependent. Currently, there is no standard method for the calibration of heat flux sensors at elevated temperatures. A recent study [2] investigated adapting the in-cavity primary calibration method [13] for calibration of sensors at elevated temperatures. The results in [2] show promise for future improvement, but clearly point out that the inherent complications found in room temperature calibrations are exacerbated by elevated sensor temperatures. Another recent work [1] focused on the design and implementation of a secondary calibration method for high temperature sensors, using a unique transfer technique. Optimization of this high temperature transfer calibration method [1] is the focus of the current study, with the primary goal being improvement in the accuracy of the calibration.

The high temperature transfer calibration technique is similar to other secondary calibration

methods in that a secondary standard and working standard heat flux sensor are subject to the same level of heat flux (magnitude). What is unique in the high temperature transfer calibration is the direction of heat flow for the two sensors is opposite: heat exits the hot sensor's surface, and enters the cold sensor's surface. In this manner, physical substitution of the two sensors is unnecessary. The calibration system is based on the principle of radiation exchange in a right cylindrical enclosure at different end temperatures. The hot end of the enclosure is formed by a heated plate in which a working standard heat flux sensor (to be calibrated) is flush-mounted. The cold end of the enclosure is formed by a cooled plate in which a secondary standard heat flux sensor is flush-mounted. The two horizontal plates are separated by a right cylindrical tube which is well insulated on the outer surface. Atmospheric air is confined in the enclosure which is oriented with the hot plate above the cold plate (the outward normal vector from the hot plate surface is aligned with the gravity vector) to reduce natural convection. The cylindrical enclosure has dimensions L and D defined by the length and inside diameter of the sidewall tube, respectively.

The high temperature transfer scheme was demonstrated in [1] through the calibration of one HTHFS (working standard) using a Schmidt-Boelter heat flux sensor as the secondary standard. An enclosure size of $L = 1.27$ cm and $D = 5.08$ cm was used for all tests performed. Steady-state thermal events were realized at several HTHFS temperatures ranging from $100 - 870$ °C. The calibrated HTHFS sensitivity (voltage output per applied heat flux) agreed well with theoretical sensitivity, and the expanded uncertainty in the calibration was estimated as $13\% - 6\%$ for HTHFS temperatures from $100 - 870$ °C (decreasing uncertainty with increasing HTHFS temperature). The preliminary uncertainty analysis revealed that the primary sources of uncertainty in the calibration are due to (1) temperature discontinuity on the hot plate surface, (2) uncertainty in the hot surface emissivity, and (3) uncertainty in the convection exchange within the enclosure [1].

This study intends to expand upon the work performed in [1] by addressing the previously mentioned issues, as well as investigating factors not considered in the original study. System improvements include new hot plate and sidewall physical designs, the addition of multiple thermocouples within the calibration enclosure, and investigation of high temperature surface coatings. System characterization is performed at four different cavity sizes, and also at reduced air pressure. Three different models describing the heat flux distributions in the enclosure are compared. Finally, a rigorous uncertainty analysis is carried out to determine the optimal configuration of the system. The high temperature transfer technique is demonstrated through the calibration of two different working standard heat flux sensors, the HTHFS and the DWHFS.

3.4 Experimental Setup and Procedure

The proposed calibration system is designed to subject two heat flux sensors simultaneously to equal magnitude heat flux under steady-state operation. Steady-state thermal events

are realized by controlling electrical power input to the system's heater, which is embedded in the hot plate. Heat is removed from the system by cooling water pumped through the cold plate. Details of the physical system design and test procedures are presented in the following sections.

3.4.1 Calibration System Physical Design

The improved high temperature transfer calibration system is shown schematically in Fig. 3.1. The system is composed of three primary parts: the hot plate, the sidewall, and the cold plate. A secondary standard heat flux sensor is flush-mounted in the center of the cold plate, and a working standard heat flux sensor (to be calibrated) is flush-mounted in the center of the hot plate. The two plates are separated by a distance, L, which is governed by the sidewall tube length. The inside diameter of the sidewall tube is held constant for this study, at $D = 6.62$ cm. The entire calibration system is encased in binder-free fibrous alumina insulation (not shown in Fig. 3.1) which has a very low thermal conductivity and can withstand the high temperatures of the calibration system external surfaces during testing. Efficient insulation encourages one-dimensional heat flow from the hot plate to the cold plate by radiation and conduction through the enclosure air. Details of individual system components are discussed in the following sections. Pictures of the components are shown in Fig. 3.2.

Heat Flux Sensors

The secondary standard heat flux sensor employed here is a water-cooled Schmidt-Boelter (SB) heat flux sensor (Medtherm model No. 64-30SB-20K). The SB sensor is a temperature gradient sensor which has a self generating output voltage proportional to the heat flux conducted through the sensing element. Operational characteristics of the SB sensor are discussed at length in [31]. The sensor element is potted into a 2.54 cm diameter copper cooling body. The actual sensing element is very small, and has a diameter of approximately 0.15 cm. A K-type thermocouple measures the cooling body temperature. The SB body temperature is maintained at a constant room temperature value (≈ 25 °C) for all tests via cooling water pumped through the SB cooling body. The SB sensor's calibration is performed by the manufacturer, and is traceable to temperature and electrical power standards defined by the National Institute of Standards and Technology.

The working standards used in this study, the HTHFS and the DWHFS, are both thermopile sensors. A thermopile is a common type of temperature gradient sensor whose output is generated by a series connection of thermocouples across a thermal resistance layer. Thermopile output voltage, V, is proportional to the temperature difference across the sensor's thermal resistance layer:

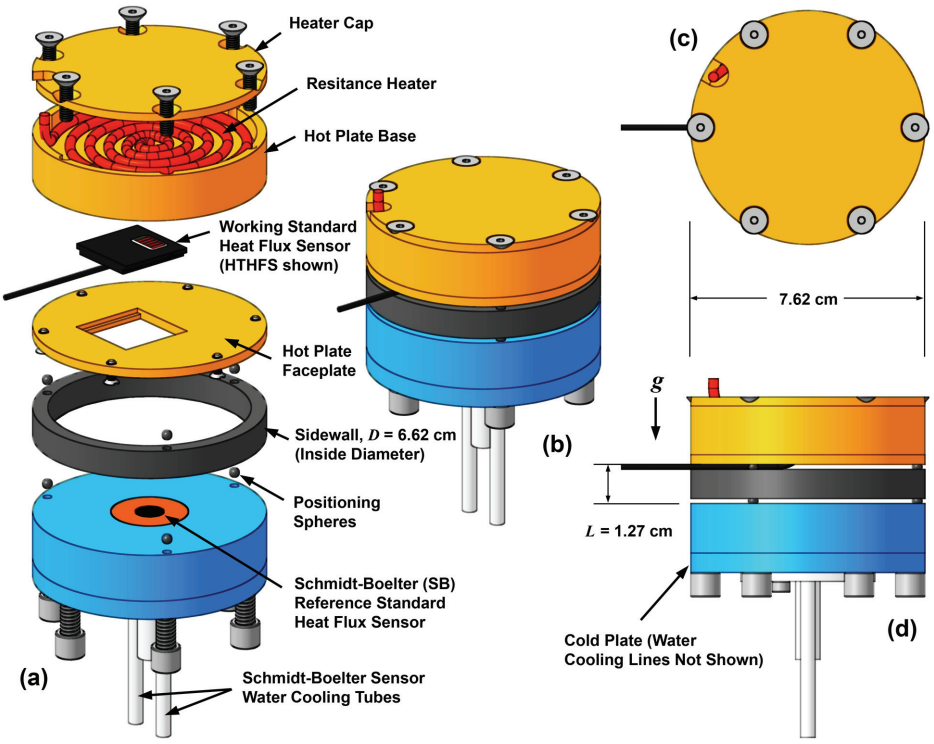

Figure 3.1: High temperature calibration system model drawings: (a) Trimetric exploded view of calibration system assembly with labeled components. (b) Trimetric view (no explosion). (c) Top view. (d) Side view of the $L = 1.27$ cm plate separation system configuration (notice the gravitational vector).

$$V = NS_e\,(T_1 - T_2) \tag{3.1}$$

where N is the number of thermocouple junction pairs, and S_e is the relative Seebeck coefficient of the thermocouple alloys. Assuming one-dimensional, steady-state heat conduction, the thermopile voltage output (Eq. 3.1) is related to heat flux by Fourier's law:

$$q'' = -\kappa\frac{dT}{dx} = \kappa\frac{T_1 - T_2}{l} = \frac{\kappa V}{lNS_e} \tag{3.2}$$

where l and κ are, respectively, the length (in the direction of heat flow) and thermal conductivity of the thermopile's thermal resistance layer. The sensitivity, S, of a heat flux sensor is defined as

$$S \equiv \frac{V}{q''} \tag{3.3}$$

where q'' is the average heat transfer through the sensor (by conduction) divided by the

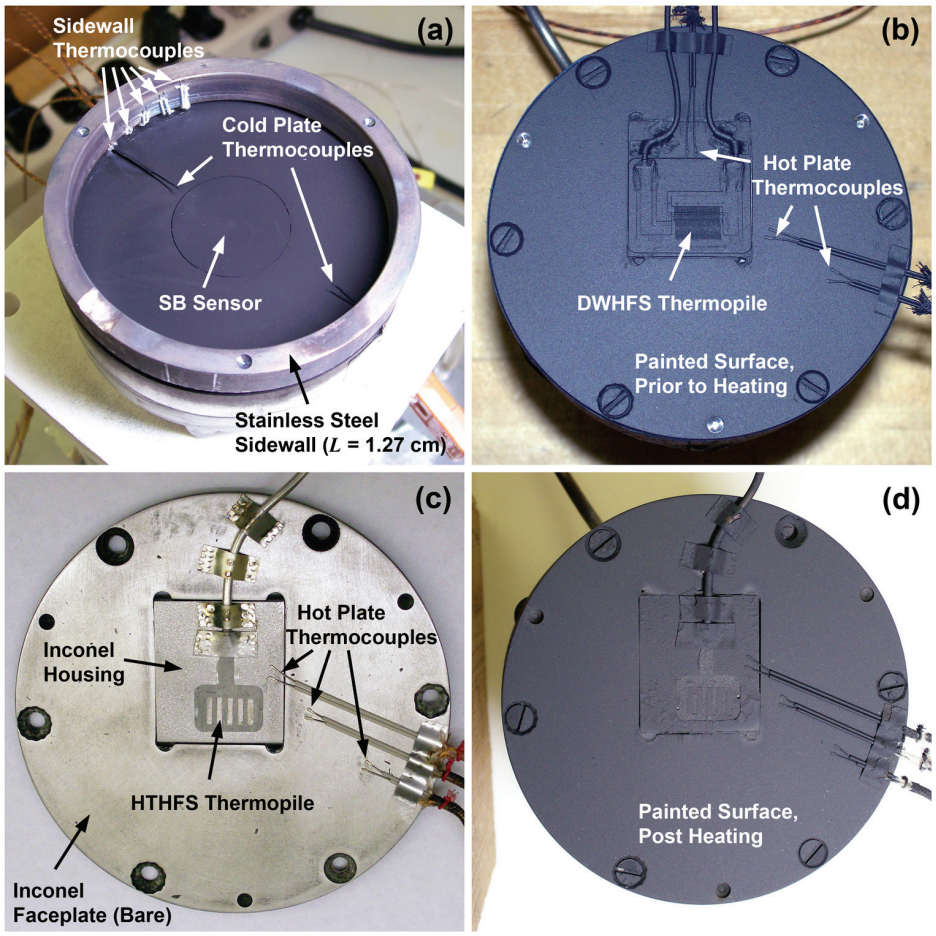

Figure 3.2: High temperature calibration system parts: (a) Cold plate with $L = 1.27$ cm sidewall in place. (b) DWHFS mounted in the hot plate with the surface painted prior to heating. (c) HTHFS mounted in the hot faceplate prior to painting. (d) HTHFS mounted in the hot plate, as shown after painting and heating.

surface area of the sensor. Combining Eqs. 3.2–3.3, the theoretical sensitivity of any general thermopile sensor can be expressed as

$$S_{\text{theory}} = \frac{lNS_e}{\kappa} \tag{3.4}$$

where, for any given thermopile, N is constant, while l, S_e, and κ may all vary with thermopile temperature, that is

$$S_{\text{theory}} = S_{\text{theory}}(T) = \frac{l(T)NS_e(T)}{\kappa(T)} \tag{3.5}$$

Eq. 3.5 indicates the importance of both measuring the thermopile temperature, and cali-

brating the thermopile over its entire operating temperature range.

The two thermopiles used in this work are constructed of similar high temperature materials, but two very different manufacturing processes are used to produce the sensors. The HTHFS thermopile is composed of K-type thermocouple alloys and fired zirconia toughened alumina. Unlike typical thermopile designs which use a dielectric as the thermal resistance layer, the HTHFS thermocouple elements serve as the thermal resistance layer of the sensor, with zirconia toughened alumina used only for electrical isolation of neighboring thermocouple junction pairs. The HTHFS thermopile shown in Fig. 3.2(c,d) is a five junction pair model ($N_\mathrm{t} = 5$) with length $l_\mathrm{t} = 0.32$ cm and surface area $A_\mathrm{t} = 1.0$ cm $\times$ 0.5 cm that is mounted in an inconel housing using a set screw and cast aluminum nitride. Lead wire configuration allows the measurement of the HTHFS output voltage, V_t, as well as the top and bottom surface temperatures (K-type thermocouples), $T_\mathrm{t,top}$ and $T_\mathrm{t,bot}$, respectively. Here the "top" surface of the working standard sensor is the surface that views the secondary standard sensor and calibration enclosure. Details of the HTHFS thermopile design are given in [9]. The theoretical HTHFS sensitivity versus average thermopile temperature is determined in [1].

The DWHFS shown in Fig. 3.2(b) is a typical thermopile, in that the thermal resistance layer of the sensor is a dielectric. The DWHFS uses N-type thermocouples connected in series across a yttria-stabilized zirconia thermal resistance layer. A unique Direct Write (DW) process [30] is used to "print" the thermocouple alloys and the dielectric material onto an inconel substrate. The DWHFS thermopile shown in Fig. 3.2(b) has forty thermocouple junction pairs ($N_\mathrm{d} = 40$) and thermopile length $l_\mathrm{d} \approx 0.01$ cm and surface area $A_\mathrm{d} = 0.8$ cm $\times$ 0.4 cm. Lead wire configuration allows the measurement of the DWHFS output voltage, V_d, as well as the top and bottom surface temperatures (N-type thermocouples), $T_\mathrm{d,top}$ and $T_\mathrm{d,bot}$, respectively.

Hot Plate Design

System heat input is provided by an inconel sheathed, flat-spiral resistance heater. The heater is mechanically fastened to the back of the stainless steel hot plate base with a stainless steel cap and screws, as shown in Fig. 3.1. The void areas between the heater and hot plate are filled with aluminum nitride paste (which hardens after heating) to reduce contact resistance. A K-type thermocouple is built into the heater to monitor the heater temperature. The heater has a continuous use upper temperature limit of 1000 °C.

The original design [1] incorporated a recessed pocket cut out of the stainless steel hot plate face, in which the HTHFS was fastened with four screws. A thin layer of aluminum nitride paste was sandwiched between the HTHFS and the hot plate base to reduce contact resistance. During testing, a significant discrepancy was noticed to exist between the measured HTHFS surface temperature and the measured hot plate surface temperature, which were ideally supposed to be equal (radial heat transfer is undesirable). This hot plate surface

temperature discrepancy, which was as high as 30 °C, resulted in systematic calibration corrections up to 10% and higher than desired calibration uncertainty [1]. In this work, the hot plate has been redesigned to include a mounting plate for the working standard heat flux sensors. Instead of the sensor being screwed into a pocket cut out of the hot plate base as before, the sensor is now fastened to the hot plate base with an inconel faceplate and screws (see Fig. 3.1(a)). Lips on two edges of the square hole in the faceplate apply mechanical pressure on corresponding grooves in the working standard sensor housing as the assembly is bolted to the hot plate base. Thermal contact resistance is reduced with the use of high temperature aluminum nitride adhesive, which forms a thin (≈ 0.01 cm) bond line between the hot plate base and the sensor/faceplate.

The new sensor mounting scheme represents an improvement over the original design both thermally and mechanically. The hot plate is designed for one-dimensional heat conduction from the heater to the hot plate surface. The thermal resistance between the heater and the hot plate face is now nearly uniform radially (same thermal resistance from heater plane to sensor surface and surrounding faceplate surface). This is accomplished by matching the sensor housing/substrate and faceplate materials, and also by using the aluminum nitride adhesive between the hot plate base and sensor/faceplate. Also, the small screws that were formerly used to mount the sensor to the hot plate have been eliminated; although these screws were small, they were located very near the important sensing area, and therefore could locally disturb thermal pathways. Now, the faceplate mounting screws are larger and easier to remove/replace multiple times. They are also located at the edge of the hot plate, shielded from view of the reference standard sensor by the sidewall. The new design discourages two-dimensional conduction in the hot plate, thus improving calibration accuracy. It allows for quick and relatively simple change of the working standard sensor to be calibrated.

Three N-type thermocouples are spot welded to the hot plate surface: one is welded on the working standard heat flux sensor housing/substrate surface at a distance of 1.0 cm from the plate center, and two are welded on the faceplate surface at distances of 1.27 cm and 2.54 cm, respectively, from the plate center. The size 30 AWG wires (0.025 cm conductor diameter) are sheathed with rigid alumina tubes and run along the hot plate surface, as shown in Fig. 3.2(b–d), to reduce conduction losses from the junction through the wires. Each surface thermocouple junction is formed by spot welding the two N-type alloys to the hot plate surface (intermediate metal) at a distance of ≈ 0.2 cm apart; this is done to ensure a good measurement of the actual plate surface temperature. Once the hot plate is fully assembled, the hot plate surface is sanded with P320 grit sandpaper, cleaned with acetone, and painted with three thin coats of high temperature flat black paint. Before calibrations are performed, the paint is cured by scheduled baking at multiple temperatures up to 600 °C for several hours. The final thickness of the cured paint layer is approximately 60 μm. Post baking (see Fig. 3.2(d)), the appearance of the paint is slightly lighter and more dull than it appears prior to baking (Fig. 3.2(b)). For all tests performed in this work, the paint experienced temperatures up to 850 °C without significant cracking or peeling.

Cold Plate Design

The cold plate design is unchanged from the original. The flanged SB sensor is flush-mounted in the cold plate base with screws. The two-piece cold plate base is made out of aluminum, with a channel machined in one of the pieces for cooling water. The two pieces are fastened together with screws, and the water channel surfaces are sealed with low-outgassing epoxy adhesive. The cold plate surface is coated with two thin layers of flat black paint (same paint as hot plate), and one thin layer of high emissivity carbon black soot. During testing, cooling water is pumped through the cold plate base and the SB sensor at flow rates of 17 mL s^{-1} and 14 mL s^{-1}, respectively. Two K-type thermocouples are spot welded to the cold plate surface at distances of 1.5 cm and 2.54 cm, respectively from the plate center, as shown in Fig. 3.2(a).

Cavity Sidewall Design

The sidewall tube used in the initial study [1] was made from rigid fibrous alumina insulation board. Although this material had very low thermal conductivity, the material lost some rigidity over the course of testing. In this study, tests are performed at four different values of the plate separation distance, L, to optimize the system in terms of calibration accuracy and uncertainty reduction. To facilitate quick change in L while maintaining a high level of positioning repeatability (in reference to the location of the two sensors), a modular sidewall system has been developed. The main body of the sidewall is a machined stainless steel tube. Stainless steel was chosen as the sidewall tube material for its availability, low cost, and ease with which nickel-based thermocouples (K-type and N-type) are welded to it. The sidewall is aligned with the hot and cold plate with positioning spheres, and the weight of the hot plate and sidewall lock the components in place. Shallow blind holes are drilled in the two end faces of the sidewall tube and corresponding holes are drilled in the hot plate and cold plate surfaces (see Figs. 3.1-3.2). In total, six stainless steel positioning spheres are used to align the system's components, as shown in Fig. 3.1. The plate separation distance, L, is defined by the diameter of the positioning spheres, the diameter of the blind holes, and the length of the sidewall tube. All pertinent dimensions were chosen to create four different values of $L = 1.27,\ 2.54,\ 5.08,$ and 7.62 cm.

In addition to establishing a highly repeatable positioning procedure for multiple length sidewall configurations, the positioning spheres also separate the hot and cold plates from the stainless steel tube by a thin air gap. This serves two purposes: first, the air gaps provide a convenient space to run all signal wires outside of the calibration enclosure (no need to cut custom channels in each sidewall tube for each signal wire), and second, the air gaps prevent excess heat conduction from the hot plate to the cold plate through the stainless steel sidewall tube. The resistance to axial heat transfer between the sidewall end and either the hot or cold plate is an important factor influencing the steady-state temperature of the sidewall during testing. The high resistance from the air gap (parallel combination of

resistance to conduction and radiation) is especially important since the sidewall tube has been changed from a very low thermal conductivity material to a relatively high thermal conductivity material.

Five N-type thermocouples are spot welded to the interior surface of each sidewall tube. The five glass fiber sheathed thermocouples are evenly spaced along the length of the corresponding sidewall tube. The sidewall tubes are not painted, but instead left bare and allowed to oxidize during preliminary test runs. The $L = 1.27$ cm sidewall is shown in Fig. 3.2(a) with thermocouples as it is positioned on the cold plate during testing.

3.4.2 Calibration Procedure and Data Acquisition

Once the desired sidewall configuration is chosen, the system is assembled using the positioning spheres. The weight of the components lock the parts in place during testing. The system is placed on top of a rigid insulation plate, and 2.54 cm thick fibrous alumina blanket is wrapped around all of the exposed external surfaces. Cooling water is pumped through the SB sensor and the cold plate. The temperature of the SB sensor is maintained at $T_{\mathrm{sb}} = 26 \pm 1.0$ °C for all tests. Electrical power supplied to the heater is regulated with a variable alternating current transformer. Voltage set points are chosen to provide the desired steady-state hot plate temperatures for each calibration test. Tests are run either in ascending or descending order with respect to voltage set points over time. No hysteresis was observed.

The voltage supplied to the heater is monitored with a true root mean square multimeter. All other measurement signals are read into National Instruments Compact–DAQ modules as analog differential inputs, and stored on the data acquisition computer using LabVIEW software. All signals are sampled at a rate of 1 Hz for the entire duration of each test. A higher sampling frequency is unnecessary as the calibration results are for steady-state thermal events. Heat flux sensor voltage signals are acquired using a ±125 mV input range universal analog input module with 24-bit analog-to-digital converter resolution. Thermocouple voltage signals are acquired using a ±80 mV input range thermocouple module with 24-bit analog-to-digital converter resolution. Cold-junction temperature is measured with on-board thermistors. Unless otherwise noted, all thermocouples used in this study are K-type. In total, sixteen thermocouples are used: two in either working standard heat flux sensor (N-type for the DWHFS), one built into the heater, three on the surface of the hot plate (N-type), five on the inner surface of the sidewall (N-type), one in the SB sensor cooling body, two on the cold plate surface, one in the cooling water, and one in ambient air.

3.5 Heat Flux Model of the Calibration System

Secondary transfer calibrations are designed to provide equal levels of heat flux to the secondary standard and working standard heat flux sensors. Sometimes, the working standard sensor differs from the secondary standard sensor in a way that alters the heat flux distribution during calibration. For example, if the two sensors are different in size or shape, the heat flux measured by one sensor is not necessarily the same heat flux measured by the other sensor, depending on the heat source and calibration setup. Any discrepancies must be accounted for and corrected to maintain calibration accuracy. A heat flux model of the calibration system presented in this work was developed in order to calculate any necessary calibration corrections. The heat flux model is explained in the following sections.

3.5.1 Calibrated Sensitivity

For steady-state calibrations the heat flux (magnitude) to each sensor is equated according to

$$q''_{\mathrm{sb}} = q''_{\mathrm{ws}} \cdot f \tag{3.6}$$

where q''_{sb} is the secondary standard SB heat flux magnitude, and q''_{ws} is the working standard heat flux magnitude. The subscript "ws" can be substituted for either "t" for the HTHFS or "d" for the DWHFS, depending on the calibration setup. A small calibration correction factor, f, is applied to compensate for any systematic discrepancy in the heat flux magnitude experienced by the two sensors. Combing Eqs. 3.3 and 3.6, the working standard calibrated sensitivity is calculated from

$$S_{\mathrm{ws}} = \frac{V_{\mathrm{ws}}}{V_{\mathrm{sb}}} S_{\mathrm{sb}} \cdot f \tag{3.7}$$

where S_{sb} is the calibrated Schmidt-Boelter sensitivity constant (cold-wall gage factor) provided by the manufacturer, and the sensor output ratio, $V_{\mathrm{ws}}/V_{\mathrm{sb}}$, is directly measured.

3.5.2 Analytical Model Equations

An analytical heat flux model of the calibration enclosure is used to calculate the calibration correction factor, f, for each steady-state thermal event. The model uses experimentally measured temperatures (steady-state values) to calculate the distribution of heat flux on each surface of the cylindrical calibration enclosure. The model assumes heat is transferred through the enclosure air by conduction, and that the air does not participate in the radiation exchange. Because the enclosure is top-heated, stable stratification of the enclosure air is prescribed, and therefore natural convection effects are assumed negligible at the sensor

locations. This assumption is discussed in more detail in §3.6.3 and §3.7. The model assumes axisymmetric distributions of temperature and heat flux (about the cylindrical enclosure centerline).

Considering radiation and conduction exchange between enclosure surfaces, the modeled total heat flux from each surface, $q''_{\mathrm{s,tot}}$, is calculated as

$$q''_{\mathrm{s,tot}} = q''_{\mathrm{s,cond}} + q''_{\mathrm{s,rad}} \tag{3.8}$$

where $q''_{\mathrm{s,cond}}$ is the conduction component of heat flux, and $q''_{\mathrm{s,rad}}$ is the radiation component of heat flux. This model uses experimental measurements of temperatures to calculate heat fluxes. Assuming one-dimensional steady-state conduction through the air-filled enclosure,

$$|q''_{\mathrm{s,cond}}| = \kappa_{\mathrm{air}} \frac{T_{\mathrm{h}} - T_{\mathrm{c}}}{L} \tag{3.9}$$

where T_{h} and T_{c} are the hot plate and cold plate surface temperatures, respectively, and the thermal conductivity of air, κ_{air}, is evaluated at the film temperature, $T_f = (T_{\mathrm{h}} + T_{\mathrm{c}})/2$. Specific values for $\kappa_{\mathrm{air}}(T_f)$ are determined from a polynomial fit to data in [16].

The term $q''_{\mathrm{s,rad}}$ in Eq. 3.8 represents the net heat flux through a given surface by radiation heat transfer. As in [1], a net-radiation analysis for enclosures is used to determine $q''_{\mathrm{s,rad}}$ for each enclosure surface. As shown schematically in Fig. 3.3, the control volume enclosure used in this analysis is formed by the hot plate surface, the inner surface of the sidewall tube, and the cold plate surface. The thin air gaps between the plates and sidewall are modeled as a virtual black surfaces, with $\epsilon \approx 1$, similar to the approach used in [32] and [2]; this technique is described in more detail in §3.5.5. Assuming diffuse-gray radiation exchange between enclosure surfaces with uniform radiosities, a general system of equations relating radiative heat flux, $q''_{j,\mathrm{rad}}$, and surface temperature, T_j, for the ith surface is [24]

$$\sum_{j=1}^{M} \left(\frac{\delta_{ij}}{\epsilon_j} - F_{i-j} \frac{1-\epsilon_j}{\epsilon_j} \right) q''_{j,\mathrm{rad}} = \sum_{j=1}^{M} \left(\delta_{ij} - F_{i-j} \right) \sigma T_j^4 \tag{3.10}$$

where ϵ_j is the hemispherical total emissivity of surface j, and $\delta_{ij} = 1$ when $i = j$ and is zero otherwise. Eq. 3.10 creates a set of M simultaneous equations for M unknown values of q'', T, or a combination of q'' and T. M is total number of discrete surfaces used in the net-radiation analysis. The radiation view factor, F_{i-j}, is defined as the fraction of radiation leaving surface i that is intercepted by surface j. The assumptions made in the derivation of Eq. 3.10 are (over each discrete surface area): the temperature and surface properties are uniform, the surface properties are independent of wavelength and direction, all energy is emitted and reflected diffusely, and the incident and reflected energy flux is uniform [24]. Higher accuracy is obtained with Eq. 3.10 by using a larger number of discrete surfaces, given the same control volume enclosure.

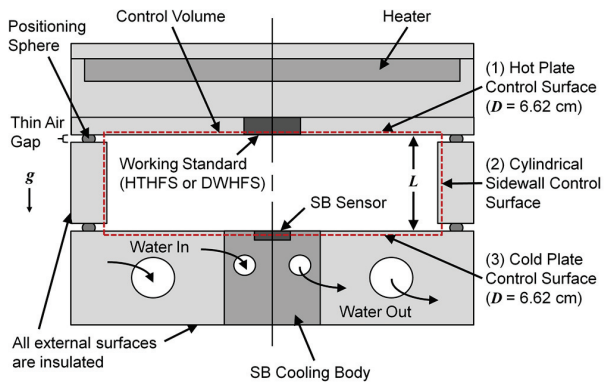

Figure 3.3: Schematic cross-section of the calibration system showing the control volume used in the heat flux model. The control volume enclosure (shown in two dimensions) is formed by three primary control surfaces: (1) hot plate surface, (2) cylindrical sidewall, and (3) cold plate surface.

3.5.3 Enclosure Discretization

The enclosure shown schematically in Fig. 3.3 consists of three primary control surfaces: (1) the hot plate surface, (2) the sidewall tube inner surface, and (3) the cold plate surface. Each of these primary areas are divided into smaller areas to improve the accuracy of the net-radiation analysis (Eq. 3.10). The hot plate surface is is divided into four sections: a central disk of radius $r_{\mathrm{ws}} = 0.36$ cm representing the working standard sensing area, and three annular rings with outer radii of 0.89, 1.91, and 3.31 cm. Similarly, the cold plate surface is is divided into four sections: a central disk of radius $r_{\mathrm{sb}} = 0.08$ cm representing the secondary standard (SB) sensing area, and three annular rings with outer radii of 1.27, 1.91, and 3.31 cm. The sidewall control surface is divided into fifty equal length cylindrical ring segments. Equal length segments are chosen to simplify the calculation of the enclosure configuration factors. The high number of divisions for the sidewall control surface ensures that the small air gaps are represented to scale relative to the stainless tube section; this is important to accurately model the heat transfer phenomena in the calibration enclosure. In total, $M = 58$ discrete areas are used in this analysis.

3.5.4 Sidewall Heat Flux Model

In the first study [1], the sidewall control surface was modeled as a reradiating surface, with zero net radiation heat transfer. A reradiating surface is an idealized surface, which is closely represented by real surfaces that are well insulted on one side, and have negligible convection on the opposite side [16]. In this study, multiple plate separation distances are used, and during initial testing, it was found that significant discrepancies existed between

tests performed with different sidewall lengths (see §3.6.1). This was determined to be caused by radial heat loss through the sidewall section. There are three possible ways to model the sidewall in Eq. 3.10, all of which are compared in this study and explained in the following sections.

Sidewall Model #1: Reradiating Surface

The reradiating surface model is the simplest to implement, and no measurement of the actual sidewall temperature is necessary. Instead of inputing M known temperatures into Eq. 3.10 and solving the system of equations for the M unknown heat fluxes, a combination of known temperatures (hot and cold plate surfaces) and known heat fluxes (sidewall surfaces) are input, and the equations are rearranged and solved accordingly. For each sidewall surface, $q''_{\mathrm{s,rad}} = 0$ is input, and the unknown becomes the surface radiosity, J_{s}, which in the case of zero net radiation heat transfer, is simply the blackbody emissive power, $E_b = \sigma T^4$. One interesting result of modeling the sidewall as a reradiating surface, is that the emissivity of the sidewall, ϵ_{w}, drops out of Eq. 3.10. This is most readily demonstrated considering net radiation heat flux leaving an enclosure surface (Eq. 3.10 assumptions apply):

$$q''_{\mathrm{s,rad}} = \frac{\sigma T_{\mathrm{s}}^4 - J_{\mathrm{s}}}{\left(1 - \epsilon_{\mathrm{s}}\right)/\epsilon_{\mathrm{s}}} \tag{3.11}$$

where, in the case of $q''_{\mathrm{s,rad}} = 0$, $J_{\mathrm{s}} = \sigma T_{\mathrm{s}}^4$, and ϵ_{s} is not needed to relate the surface radiosity to the surface temperature.

Sidewall Model #2: Estimated Radial Heat Loss

The estimated radial heat loss model is similar to the reradiating surface model in that known heat fluxes are input into Eq. 3.10 instead of known temperatures for each sidewall section. Instead of using $q''_{\mathrm{s,rad}} = 0$, however, the net radiative heat loss through the sidewall surface is estimated. Physically, this heat loss is due to two-dimensional conduction in the sidewall and surrounding insulation. The effect of radial heat loss through the sidewall is that the hot plate has to supply more heat than the cold plate receives, which leads to a systematic discrepancy in the transfer calibration.

The radial component of heat transfer out of the control volume shown in Fig. 3.3 is conservatively modeled assuming one-dimensional radial conduction through the sidewall tube and insulation, which is then convected and radiated to the surrounding environment. An iterative procedure involves the determination of an intermediate temperature (insulation external temperature), which couples the sidewall temperature (solved for in Eq. 3.10) to the environment temperature (measured), by equating the sidewall conduction to the external convection and radiation. The associated thermal resistances to conduction, convection, and radiation are estimated using relevant material data, empirical correlations, and the

assumption of diffuse-gray radiation exchange at the outer surface. The end result is that the estimated heat loss model predicts slightly lower sidewall temperatures than those calculated with the reradiating surface model, and this explains the discrepancies observed during initial testing (§3.6.1).

Sidewall Model #3: Known Temperatures

The known surface temperatures model is straightforward, however, measurements of the actual sidewall surface temperatures are necessary. M known temperatures are input into Eq. 3.10 and the system of equations is solved for the M unknown heat fluxes. The radiosity for each surface in the enclosure is calculated from Eq. 3.11.

3.5.5 Surface Temperatures and Properties

The surface temperature of the hot plate is measured at four locations by the working standard sensor top thermocouple and the three hot plate thermocouples, as shown in Fig. 3.2(b-d). The measurement locations correspond to the discrete surface area segments described in §3.5.3. Similarly, the temperature of the cold plate is measured by two surface thermocouples and the SB sensor's body thermocouple, as shown in Fig. 3.2(a). The surface temperature of the SB thermopile and surrounding cooling body (high thermal conductivity copper) are assumed to be at the temperature measured by the body thermocouple. Because the hot and cold plate surfaces are painted, the measured temperatures are slightly different than the true surface temperatures. The true surface temperatures used in Eqs. 3.8-3.11 are therefore calculated from

$$T_{\mathrm{s}} = T_{\mathrm{s,meas}} \pm \frac{q''_{\mathrm{sb}} l_{\mathrm{p}}}{\kappa_{\mathrm{p}}} \tag{3.12}$$

where q''_{sb} is the SB measured total heat flux (magnitude), l_{p} is the measured paint thickness, and κ_{p} is the paint thermal conductivity estimated from data in [33].

The small temperature drop across the paint coating (for the hot and cold plate surfaces only) is calculated from Fourier's law for one-dimensional steady-state conduction, that is $\Delta T = q''_{\mathrm{sb}} l_{\mathrm{p}} / \kappa_{\mathrm{p}}$. Because of the direction of heat transfer, the true surface temperature of the hot plate is less than the measured surface temperature, and the true surface temperature of the cold plate is greater than the measured surface temperature, hence the '$\pm$' sign in Eq. 3.12. For all tests in this study, the calculated temperature drop across the paint is very small (maximum of 0.6% of the measured temperature), and has a minor effect on the calibration. This is done simply to eliminate systematic bias error in the surface temperature measurements, which is important in the calibration uncertainty analysis.

Experimental temperature measurements are required when the known temperatures sidewall model is used for the net-radiation analysis. Sidewall temperature measurements were made by five surface thermocouples welded to the sidewall, as shown in Fig. 3.2(a). The sidewall is divided into fifty equal length sections for the net-radiation analysis. This number of divisions is used to ensure the small gaps between the plates and the sidewall tube ends (see Fig. 3.3) are modeled roughly to scale relative to the stainless steel tube section. The air gaps are modeled as virtual black surfaces, of the same diameter and adjacent to the inner wall of the stainless steel sidewall tube, and an emissivity of $\epsilon_{\mathrm{v}} = 0.999$. The temperature distribution along the sidewall control surface is modeled as: a linear drop from the hot plate to the top edge of the stainless steel tube, a third-order polynomial variation along the stainless steel tube, and a linear drop from the bottom edge of the stainless steel tube to the cold plate. This temperature distribution is based on experimental temperature measurements, and ensures that temperature and radiosity discontinuities are avoided. Modeling the air gaps as virtual black surfaces with the specified temperatures is a good approximation for the net-radiation analysis, as all other surfaces in the enclosure view the small air gaps as cavities; a similar approach is used in [32] and [2].

The cold plate surface is coated with two thin layers of flat black paint and one thin layer of carbon black coating. The flat black paint is applied to the surface first because it adheres to the metallic surfaces well and it is electrically insulating. The electrically conductive carbon black coating is then applied on top of the flat black paint. The carbon black coating has a high emissivity, $\epsilon_{\mathrm{cb}} = 0.98$, which is independent of surface temperature in the range of $25 - 250$ °C [2]. The carbon black coating serves as a reference coating. The emissivity of the cured flat black paint was determined by a simple transfer calibration as $\epsilon_{\mathrm{cb}} = 0.80$. The transfer calibration involves subjecting the HTHFS (maintained at constant room temperature) to an infrared radiation source with two different coatings on the sensor face. The output of the sensor is used to determine the emissivity of one coating in reference to the other coating. The temperature dependent emissivity of the oxidized stainless steel sidewall tube is determined from a polynomial fit to data in [34].

3.5.6 Calibration Correction Factor

After each test, the recorded measurements are processed using MATLAB software. The steady-state values for all measured voltages and temperatures represent the average value of the transient signals over a time interval of 100 s. During testing, the criteria for reaching steady-state is $|(dT/dt)_{\mathrm{avg}}| < 0.005$ °C s^{-1} over a time period of 100 s. The steady-state temperatures are used in Eqs. 3.8-3.12 to determine the total heat flux to/from each surface in the calibration enclosure. The calibration correction factor is calculated for each steady-state thermal event from

$$f = \frac{q''_{\text{sb,tot}}}{q''_{\text{ws,tot}}} \tag{3.13}$$

where $q''_{\text{sb,tot}}$ is the modeled total SB heat flux magnitude, and $q''_{\text{ws,tot}}$ is the modeled total working standard heat flux. Three different sidewall heat flux models can be used in Eq. 3.10, and therefore, for each thermal event three possible calibration corrections can be calculated with Eq. 3.13. The three models are compared in §3.6.1-3.6.2.

3.6 Experimental Results

The experimental study consists of three parts. Initial tests were performed with the DWHFS as the working standard heat flux sensor. The majority of system characterization work was done during this initial phase. The second portion of experiments were performed with the HTHFS as the working standard heat flux sensor. Results from this phase of testing were used in the calibration uncertainty analysis. Finally, the last portion of tests were performed with the entire system operated at atmospheric and reduced pressures, in an effort to justify the assumption of negligible convection exchange between the sensors and the enclosure air.

3.6.1 System Characterization: Initial DWHFS Calibrations

The DWHFS used for initial system testing had a useful upper operating temperature limit of approximately 700 °C. The purpose of the initial tests were to (1) evaluate the performance of surface coatings, (2) investigate the effect of heat loss through the sidewall, (3) and reveal the critical design parameters affecting calibration accuracy. Although twenty calibration runs were performed, only a snapshot of the results are presented here, and the major findings are summarized.

The high temperature black paint has been previously used and was known to survive at temperatures up to approximately 600 °C. An unintentional finding during this phase of testing was that the paint would actually survive and maintain adhesion at temperatures up to 850 °C. Though the paint appeared more dull and lighter after an initial cure (§3.4.1), successive testing at temperatures up to 850 °C produced no noticeable change in the surface appearance. This finding is important, because the surface of the hot plate is desired to have a uniform emissivity which does not vary significantly with temperature.

Calibration results from four tests are shown in Fig. 3.4. Each test consists of five to six thermal events with hot plate temperatures ranging from $100 - 600$ °C. A different plate separation distance was used for each test. The results were initially processed assuming the reradiating surface model for the sidewall, and the DWHFS calibrated sensitivity versus temperature was found to vary significantly with the plate separation distance, as shown

in Fig. 3.4(a). This observation can be explained by conservation of energy in the control volume enclosure. All heat supplied through the hot plate control surface exits through the sidewall and cold plate control surfaces. The more heat leaving through the sidewall, the larger the discrepancy between the total heat supplied by the hot plate and total heat removed by the cold plate.

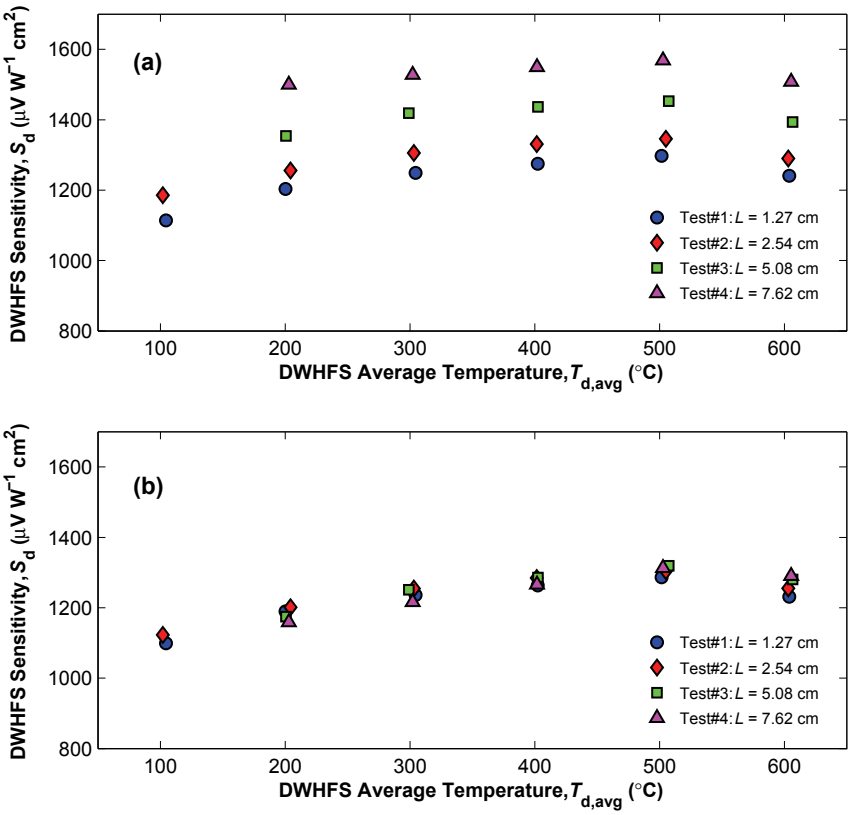

Figure 3.4: DWHFS calibrated sensitivity versus average temperature: (a) Sensitivity determined using the adiabatic sidewall heat flux model; the sensitivity increases significantly with increasing plate separation distance, L, due to heat loss through the cylindrical sidewall. (b) Sensitivity determined using the radial heat loss sidewall model.

The increase in S_{d} with L shown in Fig. 3.4(a) is a result of systematic error in the calibration, which is not accurately accounted for with the correction factor f that is calculated under the assumption that the sidewall acts as an ideal reradiating surface. When f is calculated assuming some radial heat loss through the sidewall (see §3.5.4) the calibration results compare more favorably, as shown in Fig. 3.4(b). The results shown in both Fig. 3.4(a) and Fig. 3.4(b) are from the same set of four tests, the only difference is in the calibration correction factor, which is dependent upon the assumed sidewall heat flux model. One important observation here is that the calibrated sensitivity for the $L = 1.27$ cm and $L = 2.54$ cm

configurations is relatively independent of the sidewall heat flux model (reradiating versus radial heat loss), which is not the case for the $L = 5.08$ cm and $L = 7.62$ cm configurations. This observation suggests the $L = 1.27$ cm and $L = 2.54$ cm configurations show the most promise for the calibration system, and are worthy of further investigation.

3.6.2 System Optimization: HTHFS Calibrations

After the initial testing phase was completed, the HTHFS was mounted in the hot plate. The HTHFS has a continuous use upper temperature limit of 1000 °C, and therefore calibrations were performed up to the maximum operating temperature of the system. Steady-state hot plate surface temperatures of 850 °C were achieved operating with the system heater at 1000 °C (heater continuous use temperature limit). Tests were performed using two different plate separation distances, $L = 1.27$ cm and $L = 2.54$ cm. While the results from the initial DWHFS calibrations showed that the radial heat loss sidewall model improved the calibration, the accuracy of the model was not checked. For this portion of experiments, five sidewall thermocouples were welded to each stainless steel sidewall tube so that the known temperatures sidewall model (§3.5.4) could be used. Comparison of the three models demonstrates the importance of actually measuring the sidewall temperature distribution.

Nine steady-state thermal events were used in each HTHFS calibration, with hot plate temperatures ranging from $100 - 850$ °C. Five tests were run with the system in the $L = 1.27$ cm configuration, and four tests were in the $L = 2.54$ cm configuration. The data presented in Fig. 3.5 are for one specific thermal event in a test of the $L = 1.27$ cm configuration; these data are shown for comparison of the three sidewall thermal models. The thermal event with a hot plate temperature of 500 °C is shown in Fig. 3.5 because this is the representative mid-point for all the HTHFS calibrations.

In Fig. 3.5, $x = 0$ is the location where the sidewall and hot plate control surfaces intersect, and $x = L$ is the location where the sidewall and cold plate control surfaces intersect. The temperature and radiosity of each discrete section of the sidewall are illustrated by points in Fig. 3.5, and the lines connecting the points are simply linear interpolants shown for clarity. The measured hot plate, cold plate, and sidewall temperatures are shown in Fig. 3.5(a) along with the modeled distributions. For both the adiabatic surface and the radial heat loss sidewall models, the temperature distributions are not directly input, but instead are solved for as described in §3.5.4-3.5.4. The known temperatures model, on the other hand, is based directly off of actual measurements as shown in Fig. 3.5(a) and described in §3.5.4. The three modeled radiosity distributions, which are related to the modeled temperature distributions through Eq. 3.11, are shown in Fig. 3.5(b).

Agreement between the known temperatures and radial heat loss models is generally good for all thermal events, specifically in the center region where the stainless steel tube is located. The known temperatures sidewall model captures the large temperature gradients that exist across the air gaps, and thus more accurately describes the physical system. Note,

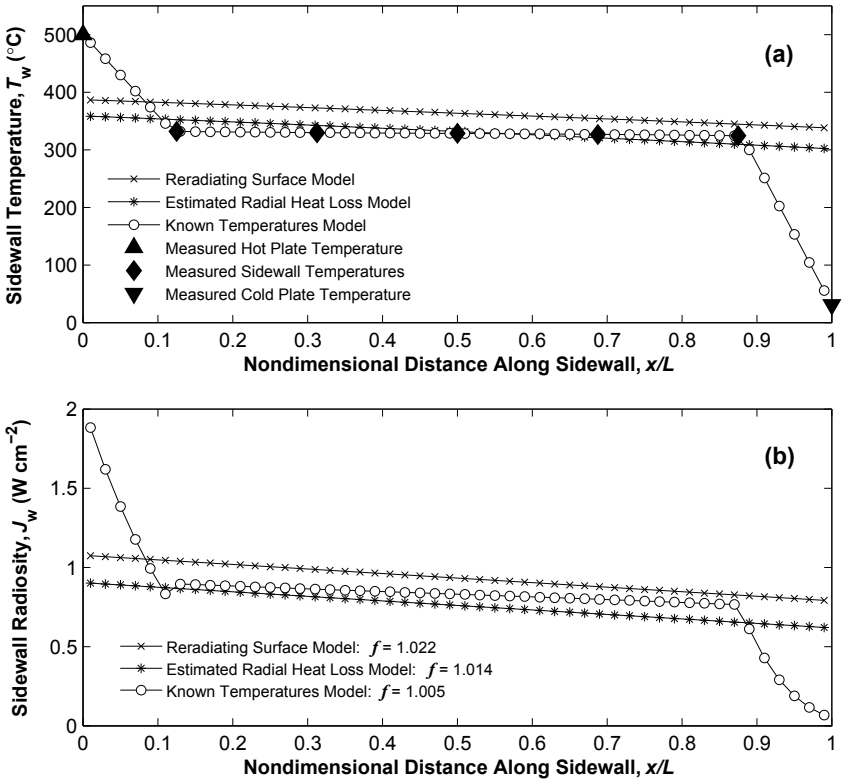

Figure 3.5: Sidewall heat flux model comparison for the $L = 1.27$ cm calibration configuration; results are for one individual thermal event: (a) Measured and modeled sidewall control surface temperatures. (b) Calculated radiosity distribution and calibration correction factor for each sidewall model.

for the $L = 1.27$ cm configuration, the air gaps are located at $0 \leq x/L \leq 0.125$ and $0.875 \leq x/L \leq 1$, as shown in Fig. 3.5. The calibration correction factor for each assumed sidewall model is listed in Fig. 3.5(b). Using the known temperatures sidewall model, which is the most accurate of the available three, the calibration correction factor for this thermal event is $f = 1.012$. Physically this means that the SB heat flux magnitude is predicted to be 1.2% higher than the HTHFS heat flux for this specific thermal event. With f so small, no modeling is actually necessary in practice if the system is built to the specifications detailed in this work. All subsequent test results presented in this work utilize the known temperatures sidewall model in the heat flux analysis to determine the calibration correction factor.

Results from one test for each of the two plate separation distances, $L = 1.27$ cm and $L = 2.54$ cm, are plotted in Fig. 3.6. Figure 3.6(a) shows the SB measured heat flux magnitude for each calibration run. As expected, the measured heat flux is slightly higher

for the shorter L. The calibration correction factors for each test are shown in Fig. 3.6(b); in all cases the predicted discrepancy between the two sensor heat fluxes is less than than 4%. The calibrated sensitivty versus temperature is shown in Fig. 3.6(c). Excellent agreement between the two calibrations, specifically at temperatures above 200 °C, provides confidence in the calibration technique. The results at the low end of the calibration diverge slightly, this is attributed to the very low calibration heat flux levels, where the relative uncertainty is thought to be high. Measuring heat flux at such low levels can be problematic [35], where natural convection effects, among others, could lead to calibration bias error. The calibrated HTHFS sensitivity results from all nine tests performed are shown in Fig. 3.7. The results show high repeatability in the high temperature transfer calibration.

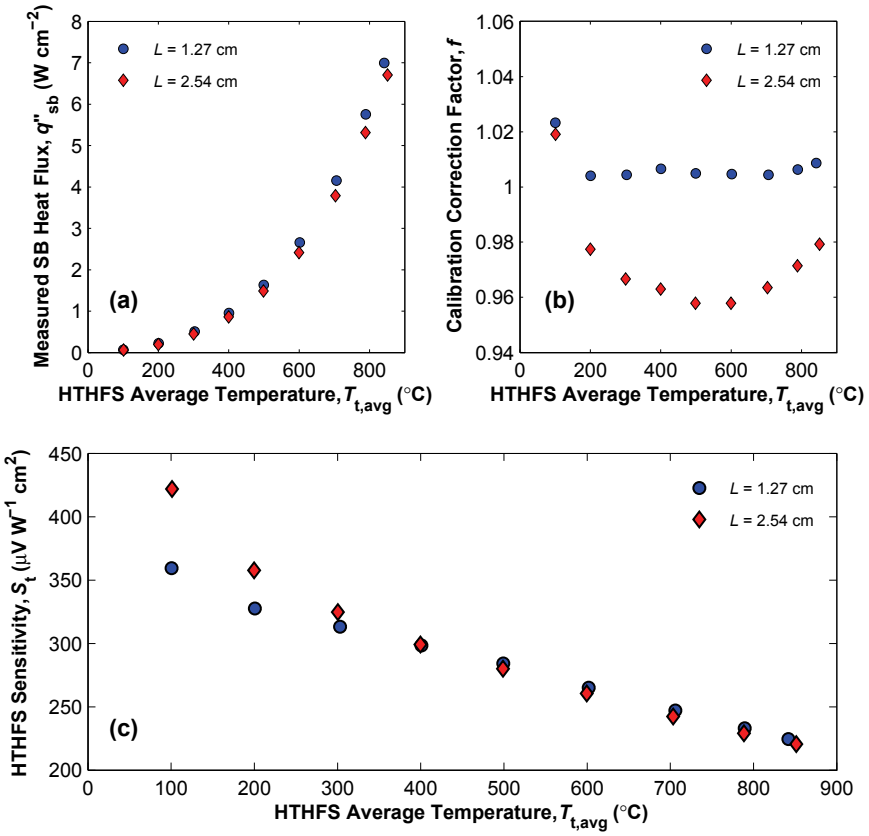

Figure 3.6: HTHFS calibration results for two tests at different plate separation distances (Test#1: $L = 1.27$ cm; Test#6: $L = 2.54$ cm): (a) Measured Schmidt-Boelter heat flux. (b) The heat flux correction factor, f, is the ratio of the cold sensor modeled heat flux to the hot sensor modeled heat flux. (c) HTHFS sensitivity showing good agreement between calibrations at two different values of L.

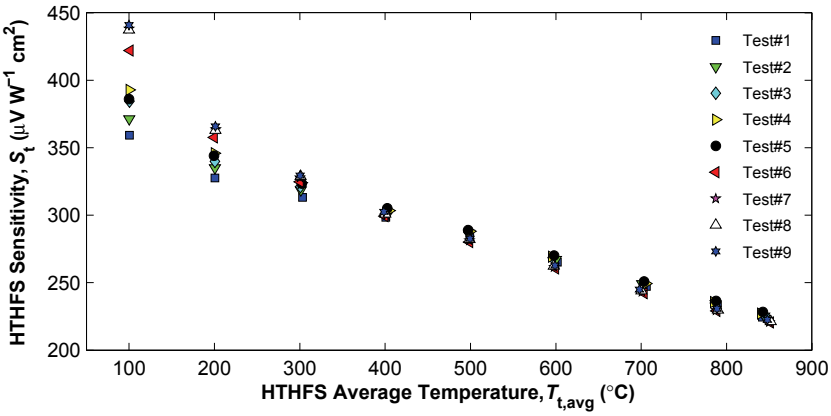

Figure 3.7: Calibrated sensitivity versus average temperature for all tests performed using the HTHFS. The results show good repeatability in the calibration particularly for $T_{\mathrm{t,avg}} \geq 300$ °C. Note: for Test#1-5: $L = 1.27$ cm, and for Test#6-9: $L = 2.54$ cm.

3.6.3 Reduced Pressure Tests

The heat flux model used in this analysis assumes that there is negligible convection exchange between the two heat flux sensors and the enclosure air. Some fluid motion is expected in the enclosure, however, it is thought to be confined near the enclosure sidewall. Buoyancy driven flow of the enclosure air is possible due to the temperature mismatch between the sidewall surface and adjacent air. However, based on experimental results in [36], weak buoyancy induced circulation is expected to be confined to the sidewall, and thus should have negligible effect at the sensor locations for this calibration system.

To investigate the assumption of negligible convection effects in the high temperature transfer calibration, experiments were performed with the system operated at reduced pressures. The entire calibration system was placed atop a baseplate with thermocouple and voltage feedthroughs. A bell jar encasing the entire calibration system was sealed to the baseplate with a rubber gasket. The chamber was pumped down to $p = 10^3$ Pa with a rotary vane mechanical pump, and maintained constant with a precision needle valve. The air pressure in the chamber was measured with a Pirani gage. Although an absolute pressure of $p = 10^3$ Pa is only in the low vacuum range, any natural convection should be eliminated with this order-of-magnitude change in pressure, while the effective thermal conductivity of the enclosure air should remain unchanged.

Two sets of experiments were performed with steady-state hot plate temperatures ranging from $100 - 600$ °C. The DWHFS was used in the first set of experiments, and the HTHFS was used in the second set of experiments. Each steady-state hot plate temperature was reached at atmospheric pressure, and then the system was pumped down and allowed to reach steady-state; this process was repeated for all desired thermal events. In the first set of experiments with the DWHFS, three sidewall configurations were tested with hot plate

temperatures ranging from $100 - 400$ °C. The average percentage change in the measured SB heat flux with pressure (from atmospheric pressure to $p = 10^3$ Pa) was 0.7% for the $L = 1.27$ cm configuration, 2.4% for the $L = 2.54$ cm configuration, and 5.0% for the $L = 5.08$ cm configuration. These results show that while natural convection is small, it increases with increasing plate separation distance. In the second set of experiments, the HTHFS was used in the $L = 1.27$ cm configuration, and tests were performed with hot plate temperatures from $100 - 600$ °C. The average change in the measured total SB heat flux with pressure was approximately 0.5%. The effects of natural convection are considered a source of uncertainty in the calibration, and are discussed in more detail in §3.7.

Abnormal response from both the DWHFS and HTHFS was observed at low pressures. The behavior of the two sensors at low pressure is not attributed to convection effects, as the measured change in output voltage is too great, and opposite for the two sensors. While the voltage output from the DWHFS increased at low pressure, the voltage output from the HTHFS decreased at low pressure. Tests were run at pressures as low as $p = 10^2$ Pa, and the effect on the two sensor's output was compounded. Upon further investigation, it was found that large radial temperature gradients in the hot plate existed when the system was operated at low pressure. These large measured temperature gradients are caused by an increase in bond line contact resistance at low pressures. Because the DWHFS thermopile is very thin and located on top of an inconel substrate, while the HTHFS is much thicker and is incorporated into an inconel housing, the effects of two-dimensional conduction through the hot plate could effect the two sensors differently. This result highlights one of the major complications associated with operating this system at low pressures.

3.7 Uncertainty Analysis

The uncertainty analysis is based on the practices outlined in [25]. Results from the HTHFS calibrations, which span the entire operating range of the calibration system, are used for this uncertainty analysis. The combined standard uncertainty in the calibrated working standard sensitivity, $u_c(S_{\mathrm{ws}})$, is calculated from

$$u_c(S_{\mathrm{ws}}) = \sqrt{\sum_{i=1}^{4} \left(\frac{\partial S_{\mathrm{ws}}}{\partial \chi_i} u(\chi_i) \right)^2} \tag{3.14}$$

where χ_i is each test variable on the right-hand side of Eq. 3.7, $u(\chi_i)$ is the associated uncertainty in each test variable, and $\partial S_{\mathrm{t}}/\partial \chi_i$ is the sensitivity coefficient for each test variable.

Type A evaluation of standard uncertainty, which is based on statistical methods, is used wherever possible. Type B evaluation is used in absence of statistical data; this relies on scientific judgment using all relevant information available. A root-sum-squares combination

is used when multiple sources contribute to the standard uncertainty in one quantity. Bias errors have been eliminated wherever possible by appropriate modeling. An overall coverage factor, k, for $u_c(S_{\mathrm{ws}})$ is taken to be the Student's t multiplier for 95% confidence and ν effective degrees of freedom. The number of effective degrees of freedom for the calibration, ν, is calculated using the Welch-Satterthwaite formula [25].

The standard uncertainty in V_{ws} and V_{sb} is a combination of sensor and measurement system uncertainties. Voltage bias error is measured at the start of each test, when the system is in thermal equilibrium (sensors have zero output), and removed from the data during post-processing. The typical gain error in the data acquisition system is provided by the manufacturer. Uncertainty in the SB heat flux sensor output is determined from linearity and repeatability information provided by the manufacturer. Uncertainty in the working standard heat flux sensor output repeatability is estimated to be ±0.5% of the reading.

The combined standard uncertainty in the calibration correction factor, $u_c(f)$, is calculated from the propagation of uncertainty in all of the quantities used in the heat flux model (Eqs. 3.8-3.12). Due to the complexity of the heat flux model, a sequential perturbation numerical technique, outlined in [26], is used to calculate $u_c(f)$ for each thermal event. The sequential perturbation scheme is also used to calculate the uncertainty in the modeled heat fluxes. Standard uncertainties in the quantities used to calculate f are listed in Table 3.1.

Table 3.1: Standard uncertainty values used in calculating $u_c(f)$.

Quantity	Symbol(s)	$u(x_i)$	Units
Hot surface temperatures	T_{ws}, T_{h}	$0.4 - 1.6\%$	°C
Sidewall surface temperatures	T_{w}	$0.5 - 2.4\%$	°C
Schmidt-Boelter surface temperature	T_{sb}	5.2	°C
Cold surface temperatures	T_{c}	1.5	°C
Lengths	L, D, r_{ws}, r_{sb}	0.013	cm
Hot plate surface emissivity	ϵ_{h}, $\epsilon_{\mathrm{t}} = \epsilon_{\mathrm{b}}$	0.05	–
Sidewall surface emissivity	ϵ_{w}	0.05	–
Cold plate surface emissivity	ϵ_{c}, $\epsilon_{\mathrm{sb}} = \epsilon_{\mathrm{cb}}$	0.02	–
Air thermal conductivity	κ_{air}	10%	W cm^{-1} °C^{-1}
Paint thermal conductivity	κ_{p}	0.39	W cm^{-1} °C^{-1}
Convective heat flux augmentation	$q''_{\mathrm{s,conv}}$	$0.05 \times q''_{\mathrm{s,cond}}(L = 1.27$ cm), $0.3 \times q''_{\mathrm{s,cond}}(L = 2.54$ cm)	W cm^{-2}

Error in the modeled surface temperatures is calculated as a root-sum-squares combination of possible error due to the data acquisition system, the accuracy of the thermocouple output,

and the assumed (worst-case) temperature variation along the surface between actual temperature measurements. For the hot surfaces, the uncertainty in the modeled temperatures is higher at higher temperatures. The range of uncertainty in the hot surface temperature for all thermal events is listed in Table 3.1. Thermal expansion in the physical dimensions of the system during testing is calculated using measured temperatures and material property data. Uncertainty in the system modeled dimensions is based on length measurement error.

The estimated error due to convection was based on experimental results from the reduced pressure tests. Here natural convection is considered to show up as bias error in the modeled conduction (like using a Nusselt number). Calibration error caused by natural convection can affect f by either introducing a small heat flux bias of equal magnitude between the two sensors, or by introducing a heat flux bias of unequal magnitude between the two sensors. Both of these scenarios are implemented in the sequential perturbation scheme, using the convective bias estimates listed in Table 3.1.

The combined standard uncertainty in the high temperature transfer calibration, $u_c(S_{\mathrm{ws}})$, is multiplied by the coverage factor, k, to get the expanded uncertainty, $U(S_{\mathrm{ws}})$. A coverage factor for each thermal event equal to the Student's t multiplier for ν effective degrees of freedom provides a 95% confidence interval about the measurement results. The calculated number of effective degrees of freedom in the calibration was high enough ($\nu > 60$ in all cases) that a coverage factor of $k = 2$ was used for all results (conservative choice). Figure 3.8 shows results and asscoiated expanded uncertainty for the two calibration system configurations tested; the results represent averages of all HTHFS tests classified according to L. The measured SB heat flux compares favorably with the modeled SB heat flux for both configurations, as shown in Fig. 3.8(a). HTHFS calibrated sensitivity results agree well with the theoretical sensitivity taken from [1], as shown in Fig. 3.8(b). The average expanded uncertainty in the high temperature transfer calibration is $\pm 6.0\%$ for the $L = 1.27$ cm configuration, and $\pm 7.7\%$ for the $L = 2.54$ cm configuration, for sensor temperatures from $300 - 850$ °C. The results presented here support the conclusion that the $L = 1.27$ cm configuration is the optimal choice for the calibration system. A summary of the calibration results and associated uncertainties is provided in Table 3.2 for the $L = 1.27$ cm system configuration.

3.8 Discussion

Transfer calibrations inherently rely on the accuracy of the calibration standard used. Uncertainty in this type of transfer calibration can be reduced by either reducing the uncertainty in the secondary standard's calibration or by choosing a reference sensor with higher linearity and repeatability. The SB sensor used in this study has a nominal output range of ± 10 mV, and the measurements made in this report use less than half of that range. A secondary standard with a sensitivity twice that of the sensor used here would be a more appropriate selection, and would aid in the reduction of uncertainty in this transfer calibration.

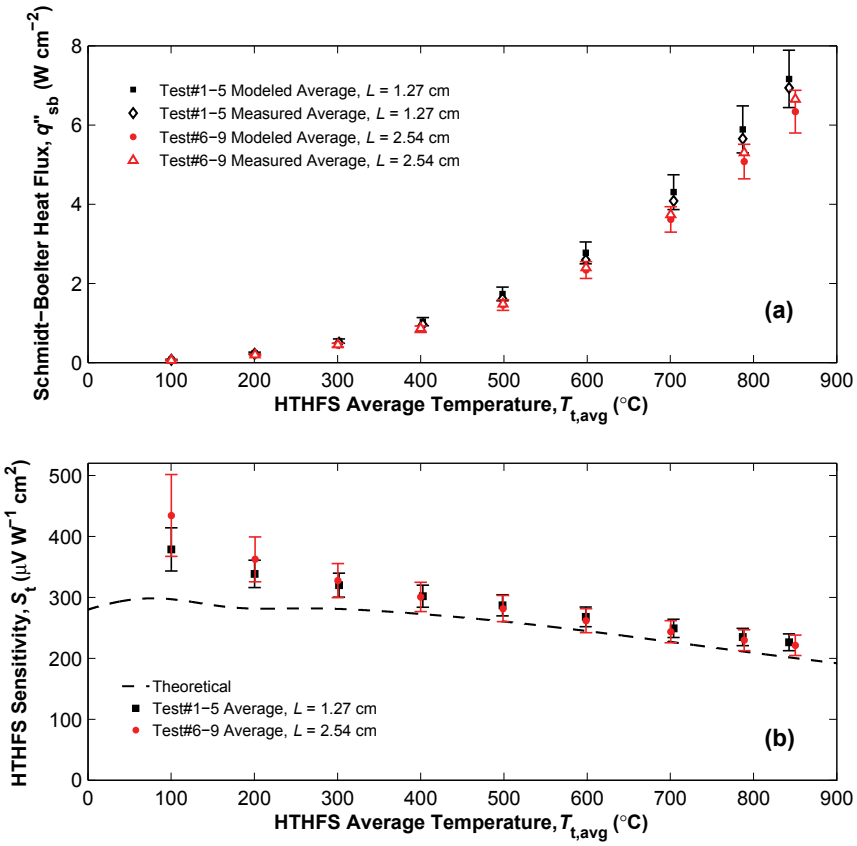

Figure 3.8: HTHFS averaged calibration results showing expanded uncertainty (95% confidence interval) for two different plate separation distances: (a) Schmidt-Boelter measured and modeled heat flux. (b) HTHFS calibrated sensitivity. Also shown in (b) is the HTHFS theoretical sensitivity versus temperature taken from [1].

Also, at additional cost, the SB sensor's calibration can be more directly traced to national power and temperature standards through special calibrations provided by the manufacturer (Medtherm Corp.). Alternatively, the sensor can be sent directly to a national lab, such as the National Institute of Standards and Technology, for room temperature calibration.

The analytical heat flux model developed in this study is used to predict any systematic discrepancy in the heat flux magnitude at each sensor location. With the system operated in the $L = 1.27$ cm configuration, the average calculated correction factor is $f = 1.014$ (for sensor temperatures ≥ 300 °C). This means the systematic discrepancy in the predicted heat flux magnitude at the two sensor locations is very small (1.4%), and the system is operating as it was designed to. The combined standard uncertainty in the correction factor (see Table 3.2) is actually larger than the correction is in the first place, however, it is necessary to apply this uncertainty in order the account for possible error in the heat flux model parameters.

Table 3.2: Calibration results and uncertainty as a function HTHFS mean temperature, $T_{\mathrm{t,avg}}$. Results averaged over the sample of five HTHFS calibrations with the system in the $L = 1.27$ cm configuration.

$T_{\mathrm{t,avg}}$ / (°C)	$u(V_{\mathrm{t}})$ / (μV)	$u(V_{\mathrm{sb}})$ / (μV)	$u(S_{\mathrm{sb}})$ / (μV W^{-1} cm^2)	$u_c(f)$	$U(S_{\mathrm{t}})$ / (μV W^{-1} cm^2)	S_{t} / (μV W^{-1} cm^2)
100	0.13	0.87	9.4	0.037	34	379
200	0.38	2.9	9.4	0.018	22	339
302	0.82	6.6	9.4	0.015	19	320
403	1.5	12	9.4	0.015	18	302
498	2.3	21	9.4	0.015	17	287
598	3.5	33	9.4	0.015	16	268
704	5.2	53	9.4	0.015	15	249
787	6.7	73	9.4	0.015	14	235
843	7.9	89	9.4	0.016	14	226

The two most important physical improvements to the calibration system were the redesign of the hot plate and the addition of sidewall thermocouples. The new hot plate design was intended to improve radial surface temperature uniformity. This goal was accomplished, and, aside from the large gradients measured during the low pressure tests, the maximum difference in hot plate surface temperature (measured at steady-state) was 7.4 °C at a mean hot plate surface temperature of 839 °C (< 1% of the measurement). The sidewall thermocouples allowed for a more accurate modeling of the sidewall control surface in the net-radiation analysis (see §3.5.4 and Fig. 3.5), and therefore no estimation of the radial heat loss through the sidewall was necessary. With careful choice of hot plate materials and working standard sensor mounting scheme, high temperature transfer calibrations can be performed on almost any type/configuration of heat flux sensor using the practices outlined here.

The normal spectral (≈ 0.9 μm) emissivity of the carbon black coating was measured at target surface temperatures in the range of $25 - 250$ °C in [2], with no measured variation with temperature. The hemispherical total emissivity of the coating was assumed equal to the normal spectral emissivity, with $\epsilon_{\mathrm{cb}} = 0.98$. This assumption was supported by in-cavity blackbody comparison calibrations performed with a water-cooled Gardon circular foil heat flux sensor. The emissivity of the high temperature flat black paint was determined ($\epsilon_{\mathrm{b}} = 0.80$) by a comparison calibration, described in §3.5.5. This emissivity was assumed constant for all surface temperatures. The close agreement between modeled and measured SB heat flux (see Fig. 3.8(a)) support this assumption. In the future, direct measurement of the total hemispherical emissivity of the paint versus surface temperature could aid in the reduction of uncertainty in the high temperature transfer calibration.

The reduced pressure tests were performed to determine the relative influence of natural convection on the calibration. For both the DWHFS and HTHFS tests, the difference in measured SB heat flux at two pressures was used to determine an estimate for the uncertainty

due to convection. It was found that the relative effect of convection increased with increasing plate separation distance. As shown in Fig. 3.6(c), there is a slight divergence in the HTHFS calibrated sensitivity at temperatures below 300 °C for the two different configurations. This is thought to be caused by bias error introduced by natural convection, which is larger for the $L = 2.54$ cm configuration. At low calibration heat fluxes ($q'' < 0.5$ W cm^{-2}) which correspond with hot plate temperatures of $T_h < 300$ °C, the effects of natural convection on the calibration are considerable, thus resulting in some scatter in calibration results (Fig. 3.7) and larger than desired calibration uncertainty (Fig. 3.8(b) and Table 3.2). Above 300 °C the calibrations performed in the two different configurations agree very well, suggesting that any unwanted natural convection effects are suppressed. This observation agrees well with the analysis in [37] which shows how high temperatures can be used to suppress buoyant convection in a gaseous enclosure.

3.9 Conclusions

Improvement of the high temperature transfer calibration technique has been demonstrated in this work. This research addresses the key issues and questions raised in the first study [1]. Initial characterization of the system revealed complications associated with the larger plate separation distances ($L = 5.08$ cm and $L = 7.62$ cm), suggesting the addition of sidewall thermocouples and improvement of the sidewall heat flux model. Implementation of the known temperatures sidewall model allows an accurate prediction of the systematic difference in heat flux magnitude between the two sensors during steady-state calibrations. A second set of experiments were performed using the $L = 1.27$ cm and $L = 2.54$ cm configurations with measured sidewall temperatures, and an uncertainty analysis was performed using the results. The uncertainty analysis revealed that the optimal configuration of the system uses a plate separation distance of $L = 1.27$ cm (enclosure aspect ratio of $L/D = 0.19$). On average, the predicted systematic discrepancy in the heat flux magnitude at the two sensor locations for this configuration is less than 1.5%, meaning that in practice the calibrations can be performed with no heat flux modeling. The uncertainty analysis shows that the expanded uncertainty in the transfer calibration is approximately ±6% for sensor temperatures ≥ 300 °C when the system is configured with $L = 1.27$ cm. This uncertainty is lower than that reported in [1] and the analysis presented in §3.7 is more rigorous.

3.10 Acknowledgments

Funding for this work was provided by NASA through NRA and GSRP grants.

Chapter 4

Adaptation of the In-Cavity Calibration Method for High Temperature Heat Flux Sensors

This chapter comprises sections from the International Journal of Heat and Mass Transfer Paper No. HMT_8230 accepted for publication on February 24, 2011. The full-length paper is reprinted here with permission.

4.1 Abstract

The need for in-situ heat flux measurements in hot structures, used in hypersonic vehicle thermal protection system development, combustion and propulsion research, and fire testing requires that heat flux sensors are characterized over their entire operating temperature range. The in-cavity heat flux sensor calibration technique has been adapted to accommodate elevated sensor temperatures, in an effort to develop a primary calibration scheme for high temperature heat flux sensors using an existing blackbody calibration system. The new scheme has been demonstrated through the calibration of a high temperature, thermopile-type heat flux sensor. The output temperature dependence of the High Temperature Heat Flux Sensor (HTHFS) has been successfully characterized over the range of $175 - 960$ °C with acceptable uncertainty limits. The calibrated HTHFS sensitivity agrees well with a theoretical sensitivity model, suggesting that the extended in-cavity calibration technique is a viable choice for primary calibration of heat flux sensors at elevated sensor temperatures.

4.2 Nomenclature

A	area (cm^2)
D	blackbody cavity diameter (cm)
F	radiation configuration factor
$\overline{h}$	convective heat transfer coefficient ($W\ cm^{-2}\ \ ^\circ C^{-1}$)
k	statistical coverage factor
l	length (cm)
L_c	characteristic length (cm)
N	number of thermocouple junction pairs in thermopile
q''	heat flux ($W\ cm^{-2}$)
r	radius (cm)
S	heat flux sensor sensitivity ($\mu V\ W^{-1}\ cm^2$)
S_e	relative Seebeck coefficient ($\mu V\ \ ^\circ C^{-1}$)
t	thickness (cm)
T	temperature (°C)
T_f	film temperature (°C)
T_∞	free stream argon gas temperature (°C)

u	standard uncertainty
u_c	combined standard uncertainty
u_r	uncertainty in the repeatability of the calibration
U	expanded uncertainty
V	thermoelectric voltage (μV)
x	distance (cm)
X	sum of squares function (μV^2 W^{-2} cm^4)

Greek Letters

χ	test variable
δ	Kronecker delta
ϵ	hemispherical total emissivity
κ	thermal conductivity (W cm^{-1} $^\circ C^{-1}$)
ν	number of effective degrees of freedom in the calibration
σ	Stefan-Boltzmann constant (W cm^{-2} K^{-4})

Subscripts

a	absorbed
avg	average
b	pertaining to the blackbody
bot	pertaining to the HTHFS thermopile bottom surface
cb	carbon black coating
conv	convection
i	index variable
inc	incident
j	index variable
o	oxidized
p	pertaining to the blackbody cavity partition
poly	polynomial
rad	radiation

t	pertaining to the HTHFS or total
top	pertaining to the HTHFS thermopile top surface
v	pertaining to the virtual black surface

4.3 Introduction

Thermal instrumentation plays an important role in aerospace, combustion, and fire research, where accurate hot-wall measurement of temperature and heat flux is desired. Material limitations often require that heat flux sensors, such as the Schmidt-Boelter and Gardon types, be actively cooled with pressurized water. The thermal disturbance to the surrounding environment caused by the presence of an actively cooled sensor can have major effect on the sensor's measurements. Significant modeling effort is required to determine appropriate heat flux corrections for cooled sensors in hot-wall testing scenarios, and these corrections can be very large [38].

Uncertainty in heat flux measurement can be reduced with the use of a passively cooled heat flux sensor which is designed to inherit the temperature of the parent structure (hot-wall). One such sensor is the High Temperature Heat Flux Sensor (HTHFS) [9], which is a thermopile-type temperature gradient sensor. Due to variability in material properties and manufacturing techniques used in heat flux sensor construction (all types), individual sensor calibration is necessary. The most common mode of heat transfer utilized in heat flux calibrations is radiation. Radiation facilities are capable of producing a wide range of consistent, known heat flux levels [10]. Heat flux calibrations are grouped in two categories: primary calibrations and secondary calibrations. Primary calibrations utilize a blackbody radiant source. The magnitude of heat flux incident on the sensor being calibrated is determined from measurements made by either a primary standard temperature detector or a primary standard radiometer. Secondary calibrations utilize a secondary-standard heat flux sensor to characterize the heat flux from a radiant source. Primary and secondary calibration methods are outlined in [27] and [28], respectively.

One of the three primary calibration methods in [27] utilizes a Variable-Temperature Blackbody (VTBB) as a radiant source for heat flux calibrations up to approximately 5 W cm^{-2}. This procedure, which is used by the National Institute of Standards and Technology [12], utilizes a reference standard radiometer, located 1.25 cm axially from the 2.54 cm aperture of the blackbody, to characterize the incident radiation. Calibration is transferred from the radiometer to the heat flux sensor of interest through a process of physical substitution. One issue with this approach is that the incident flux is provided from a narrow viewing angle, whereas in practice, heat flux sensors typically receive radiant heat flux from a large field of view. Variation between calibration conditions and those found in practice can lead to measurement errors due to the angular sensitivity of a particular heat flux sensor [14].

One study [39] suggested immersing the heat flux sensor to be calibrated into the VTBB cavity, where the sensor's viewing angle of the cavity is hemispherical. This in-cavity calibration method requires calculation of the incident radiation using the Stefan-Boltzmann law, which relates the blackbody temperature to heat flux, instead of using a reference standard radiometer to characterize the incident radiation, as in the narrow angle method [27, 12]. In an effort to extend heat flux calibrations above the 5 W cm^{-2} limit of the narrow angle method, Murthy et al. [32] used Monte-Carlo simulation to identify critical parameters affecting the steady-state in-cavity calibration of heat flux sensors in cylindrical blackbody cavities. In a follow-up study, Murthy et al. [13] experimentally demonstrated the feasibility of the in-cavity method for calibrating heat flux sensors at irradiance levels up to 50 W cm^{-2}. The results from the in-cavity calibration of two water-cooled Schmidt-Boelter heat flux sensors were in good agreement with results from narrow angle (outside of cavity) calibrations performed on the same two sensors [13]. Building upon their previous study [40], Abdelmessih and Horn [41] used finite element thermal modeling to analyze transient calibrations performed on a water-cooled Gardon circular foil heat flux sensor. The numerical model results (heat flux) were found to be in good agreement with experimental measurements made with the Gardon sensor [41]. Using the in-cavity calibration method, the optimum location for a 1.27 cm diameter heat flux sensor is approximately one cavity radius from the cavity base for the 2.54 cm diameter blackbody [13, 41].

The purpose of this study is to develop a primary calibration method for calibrating heat flux sensors at elevated sensor temperatures. To the authors' knowledge, no such method is currently in use. The need for high sensor temperature heat flux calibration is apparent, as many sensors are thought to have temperature dependency in their output [6]. For this reason, heat flux sensors should be calibrated over their intended operating temperature range to ensure accuracy in measurements. The problem with all of the aforementioned heat flux calibration procedures is that the calibration is for incident heat flux. Because the sensors typically used in the calibration procedures outlined in [27, 28] are water-cooled (maintained at room temperature), emission from the sensor to the surroundings is negligible; also, convection is assumed negligible in comparison to incident radiation. Therefore, the total heat flux to the water-cooled sensor is directly proportional to the incident radiation. This is not the case for sensors at elevated temperature, where sensor emission is comparable to the radiation incident on the sensor surface. The challenge is to adapt the established calibration methods to suit the needs of high temperature heat flux sensors; this requires determination of the total heat flux to a sensor being calibrated.

The current study is intended to extend the in-cavity method to calibrate heat flux sensors at elevated temperatures. To investigate this concept, an air-cooled version of the High Temperature Heat Flux Sensor (HTHFS) has been constructed with the same physical dimensions as the sensors used in [13] and [41]. During in-cavity calibrations of water-cooled sensors, the body of the sensors are maintained at a nearly constant temperature equal to that of the cooling water; this is due to the high mass flow rate and thermal capacitance of the cooling water. By reducing the heat removal capability of the cooling fluid (i.e., using

air instead of water), the resulting surface temperature of an air-cooled sensor during an in-cavity calibration will be much higher than that of a water-cooled sensor (under steady-state conditions), given the same blackbody cavity temperature. The proposed in-cavity high temperature calibration method is designed for steady-state measurements. For all experiments conducted in this study, the air-cooled HTHFS was located one cavity radius from the cavity base of a 2.54 cm diameter blackbody.

HTHFS output temperature dependence in the range of 100 °C to 900 °C has been successfully characterized using a secondary calibration technique, as reported in [1]. This method transfers calibration from a secondary-standard heat flux sensor (water-cooled) to the HTHFS (heated) with both sensors subject to equal magnitude, opposite direction heat flux. Results from [1] will serve as a comparison for the calibration results obtained in the current study.

4.4 Experimental Setup

The blackbody calibration furnace in the Flight Loads Lab (FLL) at NASA's Dryden Flight Research Center (DFRC) is used to calibrate optical pyrometers, optical thermometers, and heat flux sensors. The system is similar to that used by the National Institute of Standards and Technology (NIST) to perform heat flux sensor calibrations. In this study, the system is used to calibrate heat flux sensors using the in-cavity technique [13], as opposed to the narrow angle technique currently used by NIST [12]. The following sections outline the experimental setup and procedures used in this work.

4.4.1 Facility Description

The Variable-Temperature Blackbody (VTBB) system utilizes high alternating current (up to 2400 A), low voltage (< 25 V) electrical power to ohmically heat a graphite tube. A partition splits the graphite tube into two identical cylindrical cavities. The cavities have a diameter of $D = 2.54$ cm and a length of 14.2 cm, and the partition has a thickness of 0.5 cm. The graphite tube is held in place at both ends by graphite bushings within water-cooled copper end caps. The end caps are securely mounted to the system's heating electrodes. A labeled cutaway drawing of the heater assembly is shown in Fig. 4.1.

Electrical power is passed through the heater assembly via water-cooled copper electrodes connected to the system's power supply (not shown in Fig. 4.1). A proportional-integral-differential controller utilizes temperature feedback from an optical pyrometer to regulate power to the heater. The optical pyrometer measures the cavity partition temperature by sensing radiation from one end of the dual cavity blackbody. The optical pyrometer calibration is traceable to NIST temperature standards. Under steady-state operation, the control system maintains the cavity partition temperature, as indicated by the optical pyrometer,

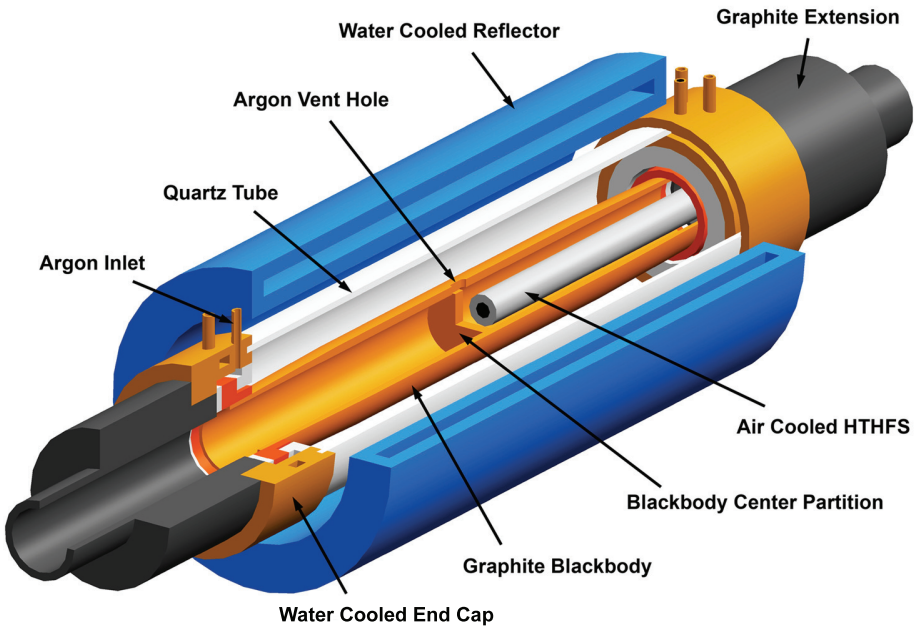

Figure 4.1: VTBB heater assembly cutaway drawing isometric view. The CAD model is shown with one quarter of the heater assembly cut away to reveal the in-cavity location of the air cooled HTHFS. The HTHFS is positioned in one end of the dual cavity blackbody coaxial to cavity at a distance of $L = 1.27$ cm from the blackbody partion wall. The optical pyrometer measures the partition temperature by sensing radiation from the open end of the dual cavity blackbody.

to within 0.1 °C of the set value. The center partition temperature indicated by the optical pyrometer will be referred to as the blackbody temperature in this paper.

To prevent oxidation of heated graphite components, air is purged from the system by pressurized argon gas. Argon enters the system through ports in both end caps, and exits through the graphite extensions at both ends of the blackbody. The general flow path of the argon gas is shown in Fig. 4.2. A quartz tube, held in place by the copper end caps, serves as a barrier to contain the argon gas. The quartz tube is surrounded by a water-cooled aluminum reflector. During testing (heating), laminar flow of argon exiting the graphite extensions prevents any air from entering the heater assembly. The flow rate of argon, set using a flow meter, is maintained at a constant value according to the manufacturer's specification [42]. System materials are labeled in Fig. 4.2. A more detailed description of VTBB system components and operation can be found in [40].

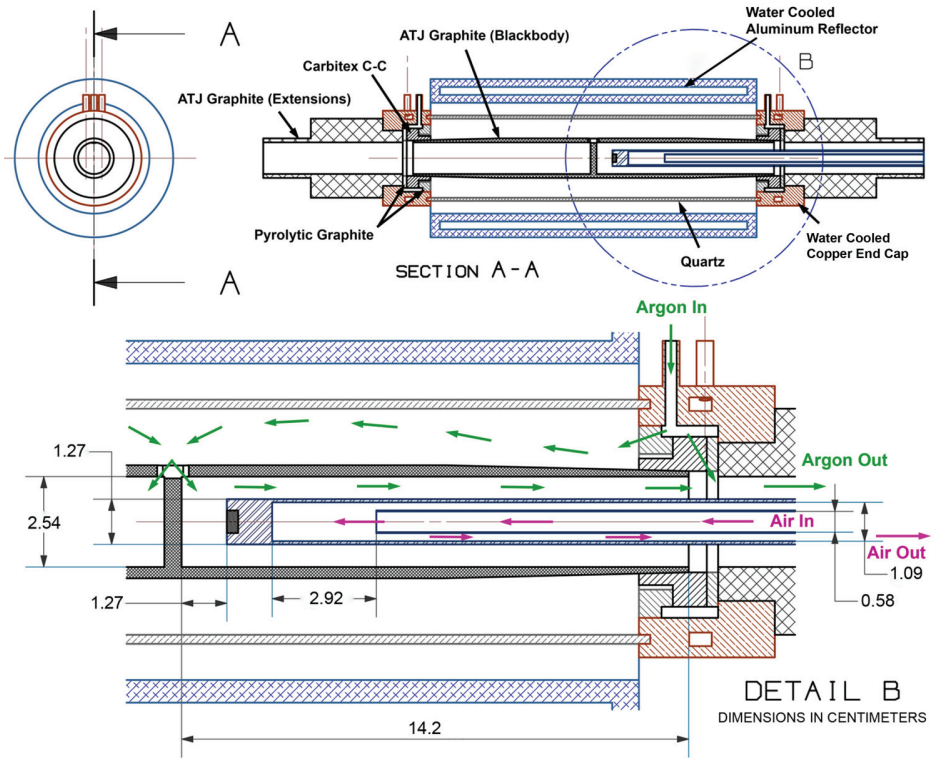

Figure 4.2: VTBB heater assembly section view showing system materials, gas flow paths, and location of the air-cooled HTHFS during testing.

4.4.2 High Temperature Heat Flux Sensor (HTHFS)

Fig. 4.1 and Fig. 4.2 both show the location of the air-cooled HTHFS used in this work as it is positioned within the cavity during testing. The in-cavity calibration procedure is discussed in more detail in §4.4.3. The cylindrical air-cooled HTHFS was developed specifically for this set of experiments.

Thermopile Design and Operation

The HTHFS is a thermopile differential temperature sensor that can operate at temperatures up to 1000 °C. The thermopile consists of bulk thermocouple alloys (K-type) welded together in a serpentine pattern to form a series connection of thermocouples. In this configuration, the sensor's thermal resistance is formed by the thermocouple alloys and thin ceramic plates, as shown in Fig. 4.3. The ceramic plates are used for electrical insulation between thermocouple junction pairs. A detailed description of the HTHFS thermopile design is given by Gifford et al. [9].

Sensor output voltage, V_t, is proportional to the temperature difference across the sensor's

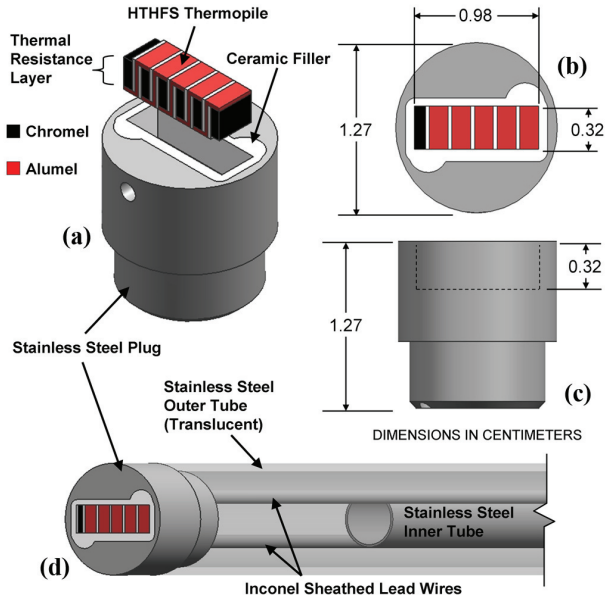

Figure 4.3: Air cooled HTHFS drawing showing labeled components and important dimensions. Clockwise from top left: (a) isometric exploded view of thermopile and stainless steel plug, (b) top view of sensor assembly showing sensing area, (c) side view of plug showing thermopile length (in direction of heat transfer) and plug length, and (d) air cooled HTHFS assembly view showing electrical and cooling tube routing.

thermal resistance

$$V_{\mathrm{t}} = NS_e \left(T_{\mathrm{t,top}} - T_{\mathrm{t,bot}}\right) \tag{4.1}$$

where N is the number of thermocouple junction pairs, and S_e is the relative Seebeck coefficient of the thermocouple alloys. Assuming one-dimensional, steady-state heat conduction, the thermopile voltage output (Eq. 4.1) is related to heat flux by Fourier's law:

$$q'' = -\kappa \frac{dT}{dx} = \kappa_{\mathrm{t}} \frac{T_{\mathrm{t,top}} - T_{\mathrm{t,bot}}}{l_{\mathrm{t}}} = \frac{\kappa_{\mathrm{t}} V_{\mathrm{t}}}{l_{\mathrm{t}} N S_e} \tag{4.2}$$

Here l_{t} and κ_{t} are, respectively, the length (in the direction of heat flow) and effective thermal conductivity of the sensor's thermal resistance layer.

Thermopile absolute temperature is measured by two surface thermocouples (K-type): one spot welded to the top of the sensor, and one spot welded to the bottom of the sensor. The negative (alumel) legs of the two surface thermocouples serve as the lead wires for the thermopile bulk output. The thermopile (0.98 cm $\times$ 0.32 cm $\times$ 0.32 cm) is secured in a stainless steel "plug" with a set screw and cast aluminum nitride. The thermopile used in this work has $N = 6$ thermocouple junction pairs. Details of the housing design are given in

the following section.

Housing Design

As shown in Fig. 4.3, the thermopile is secured in a 1.27 cm diameter stainless steel plug housing. The plug is welded to a 61-cm-long cooling body, which consists of two concentric stainless steel tubes. The outer tube has an outside diameter and inside diameter of 1.27 cm and 1.09 cm, respectively. The inner tube (outside diameter and inside diameter of 0.64 cm and 0.58 cm, respectively) is fastened to the inconel sheathed lead wires exiting the back side of the plug. The cooling body removes heat from the back of the plug using a confined circular jet of air. Pressurized air enters one end of the inner stainless steel tube, impinges vertically on the back side of the plug, and exits the cooling body through the space between the inner and outer tubes. The inner tube nozzle end is positioned a distance equal to five nozzle diameters (2.92 cm) from the back surface of the plug housing. The flow path of air is shown in Fig. 4.2.

Theoretical Sensitivity

The HTHFS sensitivity, S_t, is defined as

$$S_\mathrm{t} \equiv \frac{V_\mathrm{t}}{q''_\mathrm{t}} \tag{4.3}$$

where q''_t is the rate of heat transferred through the sensor by conduction divided by the sensor surface area, and V_t is the sensor output voltage. Combining Eqs. 4.2–4.3, the HTHFS sensitivity as a function of average thermopile temperature can be calculated (ignoring thermal expansion) from

$$S_\mathrm{t}(T) = \frac{l_\mathrm{t} N S_e(T)}{\kappa_\mathrm{t}(T)} \tag{4.4}$$

The relative Seebeck coefficient versus temperature for K-type thermocouples is taken from [21]. Assuming one-dimensional conduction and uniform temperature profiles perpendicular to the direction of heat transfer [16], the HTHFS effective thermal conductivity, κ_t, can be calculated as a function of average thermopile temperature according to

$$\kappa_\mathrm{t}(T) = \frac{\sum \kappa_i(T) A_i}{A_\mathrm{t}} \tag{4.5}$$

Here κ_i and A_i are, respectively, the thermal conductivity and surface area (perpendicular to direction of heat transfer, $\sum A_i = A_t$) of an individual thermopile material.

Thermal conductivity versus temperature data were taken from [17] for the two K-type thermocouple alloys. As described in [1], second-order polynomial models were fit to the thermocouple alloy data to predict their conductivities at higher temperature than reported in [17]. The third component in the HTHFS is the electrically insulating ceramic. The ceramic is made up of alumina and zirconia, with volume fractions of 85 % and 15 %, respectively. Ceramic composite thermal conductivity versus temperature was calculated using the Maxwell-Eucken method [18] with data taken from [19] and [20] for alumina and zirconia, respectively. The theroretical sensitivity of the HTHFS thermopile used in this work (calculated using Eq. 4.4) is plotted in Fig. 4.4.

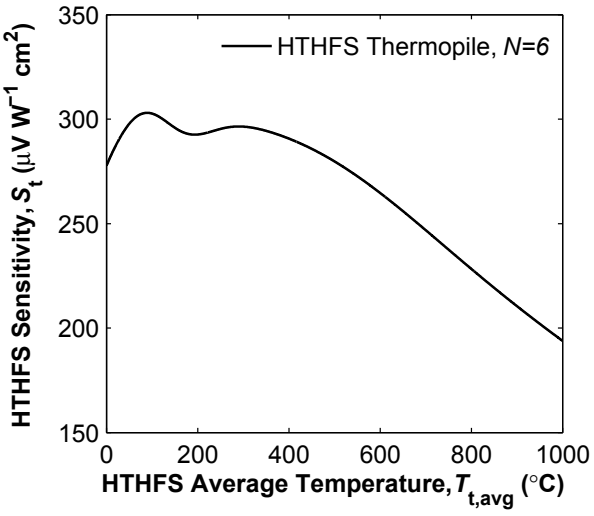

Figure 4.4: HTHFS theoretical sensitivity versus average temperature.

4.4.3 Calibration Procedure and Data Acquisition

Prior to heating, the VTBB system's closed loop water cooling system is turned on, allowing water to flow through the electrodes, aluminum reflector, and power transformer. Pressurized argon gas is fed into the system to purge out all air within the heated zone. After an initial purge, the argon flow rate is set to the manufacturer's specification [42], and is maintained constant for the duration of the test. The air-cooled HTHFS, which is mounted on a sliding optical rail system, is positioned within the cavity at the predetermined location (coaxial to the cavity, at a distance of 1.27 cm from the partition wall), as shown in Fig. 4.2. This position is maintained for the entire duration of the test. The optical rail system ensures that any repositioning of the HTHFS between tests is highly repeatable. Pressurized air is fed into the HTHFS cooling body, as described in §4.4.2, and exhausts to ambient surroundings, 48 cm away from the blackbody cavity end. Air line pressure is regulated to 2.0 atm for all tests presented in this work.

Blackbody temperature set points are programmed into the temperature controller, which sends a 0–5 V signal to the system's power controller, based on temperature feedback from the optical pyrometer. For these tests, blackbody temperature set points in the range of 500–1150 °C were used. At each set point, the system was allowed to reach steady state, where the time rate of change of temperature of both the blackbody and the HTHFS was less than 0.01 °C s^{-1} (averaged over 20 s). The optical pyrometer digital output was stored on the data acquisition computer via RS-232 serial port. All other measurement signals were read into National Instruments Compact–DAQ modules as analog differential inputs, and stored on the data acquisition computer using LabVIEW software. Because the calibration is concerned only with steady-state measurements, all signals were sampled at a rate of 3 Hz for the entire duration of each test. Thermocouple and HTHFS voltage signals were acquired using ±80 mV input range thermocouple modules with 24-bit analog-to-digital converter resolution. All thermocouples used in this study are K-type. Cold-junction temperature compensation for each thermocouple channel was provided by on-board thermistor measurements. A total of seven thermocouples were used: two in the HTHFS, one on the cooling air inlet tube outer surface, one in the cooling air exhaust stream, one in the cooling water, and two in ambient air.

4.5 Heat Flux Model of the Sensor in the Blackbody Cavity

The steady-state surface temperature of a sensor during in-cavity calibration is dictated by the balance between heat supplied by the blackbody source and heat removed by the cooling fluid. For in-cavity calibrations performed on water-cooled sensors, as in [13] and [41], the sensor is maintained at a constant low temperature (≈ 30 °C), and therefore emission from the sensor is neglected; also, at high blackbody temperatures convection is negligible in comparison to radiation. Calculation of the irradiance (incident radiant heat flux arriving from all hemispherical directions) is relatively straightforward using the Stefan-Boltzmann law, $q''_{\text{inc}} = \sigma T_b^4$, where σ is the Stefan-Boltzmann constant and T_b is the absolute temperature of the blackbody. It should be noted that modeling is required to determine the cavity's effective emissivity for the in-cavity calibration [32, 13]. Here, effective emissivity is the ratio of actual irradiance at the sensing location to the ideal irradiance (σT_b^4).

In the tests presented in this work, the air-cooled HTHFS reached steady-state temperatures ≈ 100–300 °C below the blackbody temperature. For this reason, the total heat flux to the HTHFS is much smaller in magnitude than the heat fluxes reported in [13] and [41]. Calculation of the HTHFS total heat flux, q''_t, requires calculation of emission and convection in addition to calculation of incident radiation. Heat flux modeling of the HTHFS in the blackbody cavity is discussed in the following sections.

4.5.1 Model Equations

For any thermal event, the HTHFS sensitivity can be determined by dividing the sensor output voltage by the applied total heat flux, as in Eq. 4.3. The heat flux model is used to calculate the total heat flux to the HTHFS from experimental temperature measurements. The HTHFS total heat flux, q''_{t}, can be calculated according to

$$q''_{\mathrm{t}} = q''_{\mathrm{t,conv}} + q''_{\mathrm{t,rad}} \tag{4.6}$$

where $q''_{\mathrm{t,conv}}$ and $q''_{\mathrm{t,rad}}$ are, respectively, the convective heat flux and the net radiative heat flux to the HTHFS surface. In this work the sign convention for heat flow is positive into the surface. The convective contribution is calculated from Newton's law of cooling

$$q''_{\mathrm{t,conv}} = \overline{h}\,(T_\infty - T_{\mathrm{t,top}}) \tag{4.7}$$

where $\overline{h}$, the average heat transfer coefficient over the HTHFS surface, is calculated using a correlation from [43] for laminar natural convection from a vertical, isothermal flat plate. In Eq. 4.7, the free stream temperature of the argon gas is assumed to be at the temperature of the blackbody (bounding assumption), that is, $T_\infty = T_{\mathrm{b}}$. Argon gas properties used to determine $\overline{h}$ are extrapolated from [44] and evaluated at the film temperature, $T_f = (T_{\mathrm{b}} + T_{\mathrm{t,top}})/2$. The characteristic length, L_c, for $\overline{h}$ is taken to be the diameter of the HTHFS cooling body, $L_c = 1.27$ cm.

The term $q''_{\mathrm{t,rad}}$ in Eq. 4.6 represents the net heat flux through the HTHFS surface by radiation heat transfer. In a similar manner as in [1], a net-radiation analysis for enclosures is used to determine $q''_{\mathrm{t,rad}}$. As shown in Fig. 4.5, the enclosure used in this analysis is formed by the blackbody cavity's partition and sidewall and the HTHFS front surface. The annular space (disk) between the HTHFS cooling body and blackbody cavity is modeled as a virtual black control surface, with $\epsilon_{\mathrm{v}} \approx 1$, similar to the approach used in [32]. Assuming diffuse-gray radiation exchange between enclosure surfaces with uniform radiosities, a general system of equations relating net radiative heat flux, $q''_{j,\mathrm{rad}}$ (positive into surface), and surface temperature, T_j, for the ith surface is [24]

$$\sum_{j=1}^{N} \left(F_{i-j} \frac{1-\epsilon_j}{\epsilon_j} - \frac{\delta_{ij}}{\epsilon_j} \right) q''_{j,\mathrm{rad}} = \sum_{j=1}^{N} \left(\delta_{ij} - F_{i-j} \right) \sigma T_j^4 \tag{4.8}$$

where, corresponding to a specific surface, $i = 1, 2, ..., N$, and ϵ_j is the hemispherical total emissivity of surface j. Also, $\delta_{ij} = 1$ when $i = j$ and is zero otherwise. The radiation view factor, F_{i-j}, is defined as the fraction of radiation leaving surface i that is intercepted by surface j. As outlined in [24], use of Eq. 4.8 requires that over each individual area, the temperature and surface properties are uniform, the surface properties are independent of wavelength and direction, all energy is emitted and reflected diffusely, and the incident and

reflected energy flux is uniform. Unlike in [13] and [41] where the sensor cooling bodies were highly polished, all surfaces of the HTHFS (cooling body included) are rough (compared to the wavelength of incident radiation) and oxidized and/or coated with a high emissivity matte coating, therefore the diffuse emission and reflection assumption is justified.

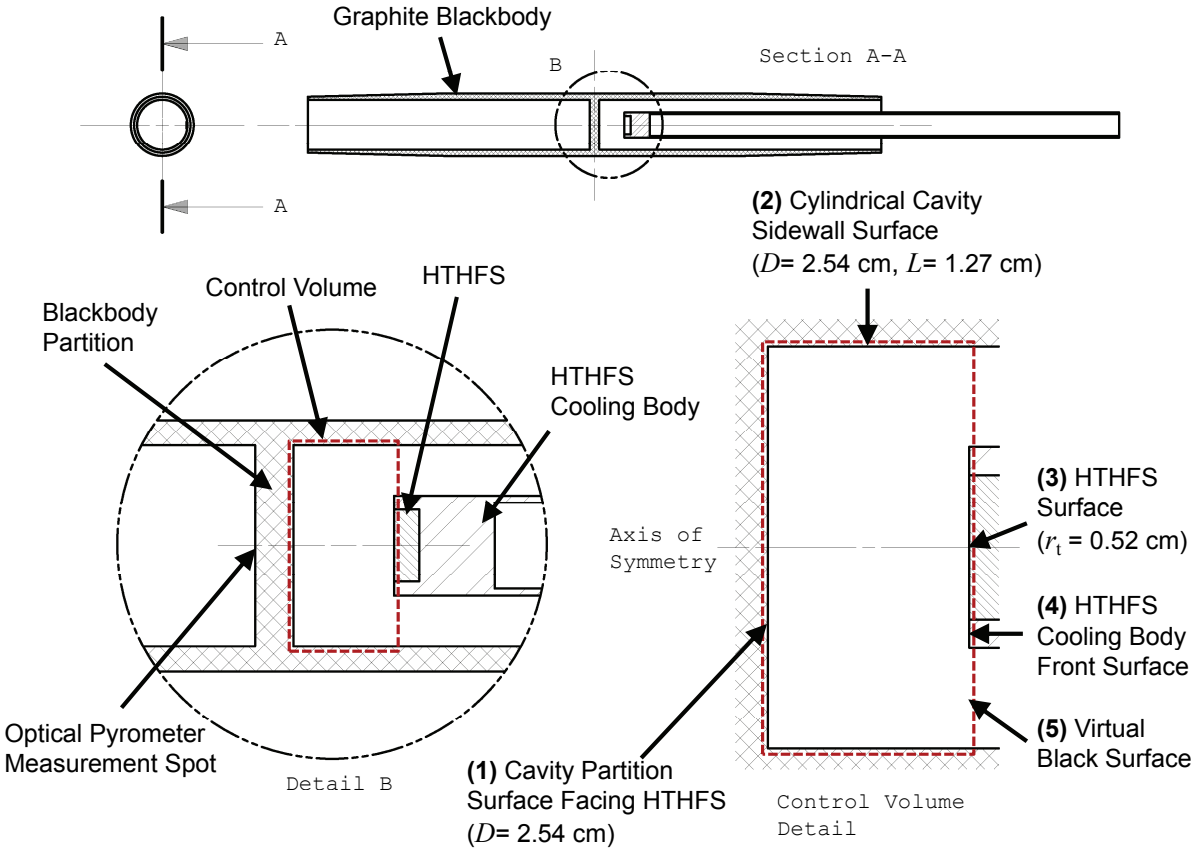

Figure 4.5: Section view detail of the HTHFS as positioned within the blackbody during testing. The control volume enclosure, shown schematically in two dimensions, is used in the net-radiation analysis. The enclosure is formed by the five control surfaces labeled on the bottom right.

4.5.2 Enclosure Discretization

The cylindrical enclosure shown schematically in Fig. 4.5 consists of five main control surfaces: (1) blackbody cavity partition wall, (2) blackbody cavity cylindrical sidewall, (3) HTHFS sensing area, (4) annulus immediately surrounding HTHFS sensing area, and (5) annulus between HTHFS cooling body and blackbody cavity sidewall. To improve the accuracy of the net-radiation analysis, large areas of the enclosure are divided into smaller

areas to more accurately support the assumptions used to derive Eq. 4.8. For this analysis, both the blackbody partition and sidewall are divided into five equal-area segments. The partition surface is divided into one central disc surrounded by four annular rings, and the sidewall is divided into five equal length sections. The remaining three enclosure surfaces are as specified in Fig. 4.5, with the HTHFS sensing area radius, r_t, equal to 0.52 cm. The same procedure of discretizing the blackbody cavity and using the net-radiation analysis (or leaving heat flux method, which is a variant of the net-radiation method) to determine heat flux to the sensor is also used for two other types of primary calibrations as outlined in [27]. The only difference between the current heat flux model and the models used in [27] is that the total heat flux (combination of convection and net radiation) is calculated instead of the incident heat flux.

4.5.3 Surface Temperatures and Properties

Solution of Eq. 4.8 in terms of heat flux requires knowledge of all enclosure surface temperatures and emissivities. The heat flux model (Eq. 4.6) used for this calibration study assumes the blackbody temperature is uniform over the control surfaces defined in Fig. 4.5. Nonuniformity in the blackbody surface temperature is known to exist [32, 40]. Over the control surfaces defined in Fig. 4.5, however, any nonuniformity is expected to be small relative to the blackbody absolute temperature. The blackbody cavity partition and sidewall are therefore modeled at a uniform temperature, which is measured with the optical pyrometer. The HTHFS sensing area and the ring surrounding this area (to the edge of the HTHFS cooling body) are modeled at a uniform temperature, $T_{t,top}$, as measured by the HTHFS top surface thermocouple. Blackbody and HTHFS surface temperature nonuniformity (axisymmetric only) is considered a source of uncertainty in the calibration, and is discussed in more detail in §4.7.

As in [40], the blackbody graphite walls were modeled with a surface emissivity of $\epsilon_b = 0.89$. For the first series of experiments, the HTHFS surface (sensing area and ring surrounding sensing area) was coated with a high emissivity carbon black coating. The emissivity of the carbon black coating, $\epsilon_{cb} = 0.98$, was measured (on a stainless steel target) using a pyrometer with a built-in emissivity measurement system. Multiple emissivity measurements were made at target surface temperatures in the range of $25 - 250$ °C. No variation in the measured carbon black coating emissivity with surface temperature was observed. The emissivity of the carbon black coating is assumed constant for the entire usable temperature range of the coating. Because the carbon coating burned off at high temperatures (> 600 °C), well below the maximum operating temperature of the HTHFS, a second series of tests was run with the HTHFS surface heavily oxidized. Determination of the oxidized HTHFS surface emissivity is discussed in §4.6.

The virtual black surface is an imaginary surface used to simplify the net-radiation analysis. The surface is modeled as a near perfect absorber and emitter, with $\epsilon_v \approx 1$. Because Eq. 4.8

requires $0 < \epsilon < 1$, a value of $\epsilon_v = 0.999$ was used. The virtual black surface is used to approximate the net radiation heat flux leaving the model enclosure (see Fig. 4.5). For simplicity, the temperature of the virtual black surface was modeled as an average of the appropriate bounding temperatures: the temperature of blackbody and the temperature of the HTHFS, that is, $T_v = (T_b + T_{t,top})/2$.

4.6 Experimental Results

Two series of three in-cavity high temperature calibration tests, each test consisting of multiple steady-state thermal events, were performed using a single HTHFS. As explained in §4.4.3, each test consists of a series of steady-state thermal events with the blackbody temperature increasing in increments of either 50 °C or 100 °C. The initial blackbody temperature set point for all tests was 500 °C (limited the by optical pyrometer's temperature measurement range). After an initial series of three calibrations (coated HTHFS), the HTHFS surface was heavily oxidized through a series of heating cycles in air. A second series of three calibrations was then performed with the HTHFS surface heavily oxidized. The results for the six calibrations are presented in the following sections.

4.6.1 Coated HTHFS Initial Testing

The first three tests each consist of seven steady-state thermal events with blackbody temperature set points from $500 - 800$ °C. All steady-state temperature and voltage results presented in this work represent the average of 20 s worth of data (60 samples). Fig. 4.6a shows the measured steady-state temperatures for the first test. These temperatures are used to calculate heat flux (Fig. 4.6b) according to Eqs. 4.6-4.8. Also shown in Fig. 4.6b is the incident heat flux calculated from the Stefan-Boltzmann law.

As shown in Fig. 4.6b, the HTHFS net absorbed radiation heat flux, $q''_{t,rad}$, is significantly different from the incident radiation, q''_{inc}. This is expected due to the high surface temperature of the HTHFS during the calibration. The modeled convective heat flux (see §4.5.1 for model description), $q''_{t,conv}$, is small, however, at low blackbody temperatures ($T_b < 700$ °C) it represents a significant portion of the total heat flux into the HTHFS, q''_t. The HTHFS voltage output for the first three tests is shown in Fig. 4.7a. The voltage output is divided by the calculated heat flux, according to Eq. 4.3, to get the HTHFS sensitivity for each steady-state thermal event. The HTHFS sensitivity versus average temperature for the three initial tests is shown in Fig. 4.7b. The primary cause for variation in V_t between successive tests is due to slight differences in HTHFS cooling air line pressure, which is set manually at the beginning of each test with a simple reducing valve. For a given steady-state blackbody temperature, variation in the HTHFS cooling air line pressure affects both the HTHFS temperature and total heat flux. This does not affect the sensitivity calibration, as can be seen in Fig. 4.7b,

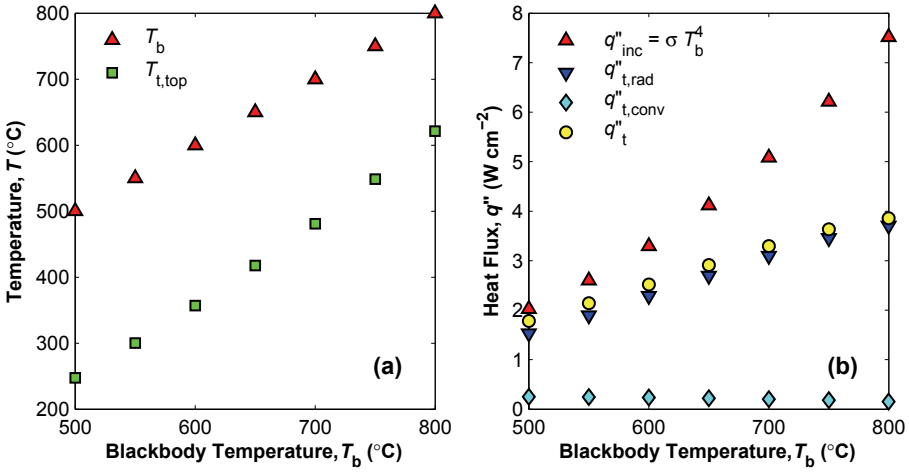

Figure 4.6: Test #1 results showing a) measured temperatures and b) calculated heat flux for the HTHFS with the carbon black coating.

because q''_t (calculated from measured temperatures) will vary in the same manner as V_t in response to any changes in line pressure.

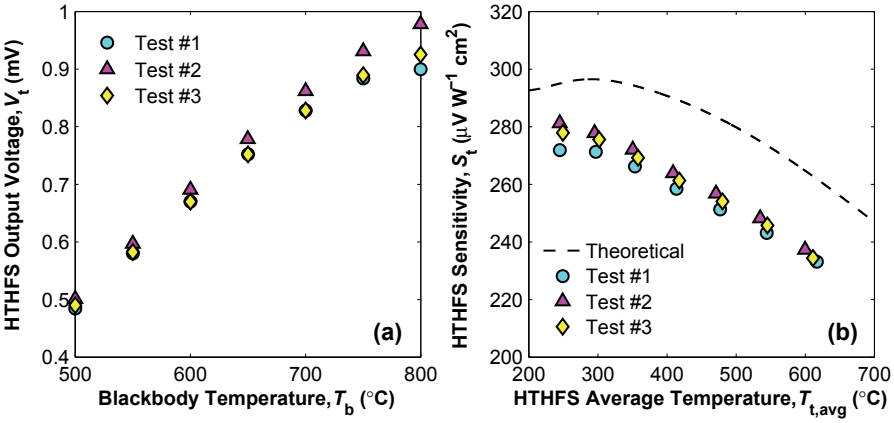

Figure 4.7: Test #1-3 results showing a) measured voltages and b) calculated HTHFS sensitivity for the HTHFS with the carbon black coating.

The experimental sensitivity results are tightly grouped, displaying the repeatability of the calibration; the calibration repeatability is utilized in the uncertainty analysis in §4.7. These results agree well with the theoretical prediction as shown in Fig. 4.7b, however, they cover only a fraction of the HTHFS measurement range bounded by the maximum temperature limit of the carbon black coating. For this reason, a second series of tests was run to determine the HTHFS sensitivity above 600 °C.

4.6.2 Oxidized HTHFS High Temperature Testing

After the initial three tests, the HTHFS coating was removed, leaving the metallic housing and thermopile surface exposed. A heavy oxidation layer was formed on the metallic surfaces by repetitive heating of the sensor in air. In [1] a heavily oxidized HTHFS surface was found to have surface emissivity of approximately 0.73 that was independent of temperature in the range of $200 - 900$ °C. Because the air-cooled HTHFS used in this study had surface area smaller than the target size of the emissivity measuring pyrometer, direct measurement of the oxidized surface emissivity was not possible. Instead, a parameter estimation routine was developed to determine the oxidized HTHFS surface emissivity, $\epsilon_{t,o}$, based on the coated HTHFS calibration results. A quadratic-polynomial was fit to the average calibration results from the first three tests (see Fig. 4.7b) as shown in Fig. 4.8. The sensitivity polynomial function, $S_{t,poly}(T_{t,avg})$, is used to determine the appropriate HTHFS sensitivity for temperatures in the range of $250 - 625$ °C; this temperature range is defined by the calibration results from the first three tests.

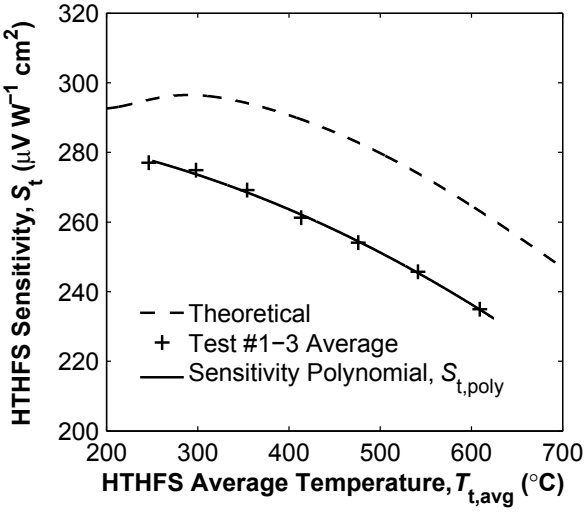

Figure 4.8: Test #1-3 averaged HTHFS sensitivity versus temperature and quadratic-polynomial fit.

The final three tests each consist of eleven steady-state thermal events with blackbody temperature set points from $500 - 1150$ °C. The HTHFS average temperature ranged from $170 - 960$ °C for these tests, covering the desired high temperature range of operation for the sensor. Five of the eleven thermal events in each test fell within the coated sensor calibration results ($250 \leq T_{t,avg} \leq 625$ °C). Because the HTHFS sensitivity is not expected to change between tests [9, 1], $\epsilon_{t,o}$ can be estimated using these results. Assuming that $\epsilon_{t,o}$ does not vary with temperature, the calibration temperature range can be extended.

For each of the oxidized HTHFS tests, a series of steps are performed to determine the

HTHFS sensitivity. First, $T_{\mathrm{t,avg}}$ and $q''_{\mathrm{t,conv}}$ are calculated for every steady-state thermal event. Data from thermal events in which $250 \leq T_{\mathrm{t,avg}} \leq 625$ °C are then used to estimate $\epsilon_{\mathrm{t,o}}$. The parameter estimation routine consists of calculations which are repeated in a loop with values of the oxidized HTHFS surface emissivity ranging from 0.001 to 0.999, as the loop parameter. The net-radiation system of equations (Eq. 4.8) are solved for each thermal event and each value of $\epsilon_{\mathrm{t,o}}$ (loop iteration), yielding $q''_{\mathrm{t,rad}}(i, \epsilon_{\mathrm{t,o}})$, where $i = 1, 2, ..., 5$ represents the thermal event number for $250 \leq T_{\mathrm{t,avg}}(i) \leq 625$ °C. The convective and radiative heat fluxes are added as in Eq. 4.6 to get $q''_{\mathrm{t}}(i, \epsilon_{\mathrm{t,o}})$. The HTHFS voltage is divided by the total heat flux to get $S_{\mathrm{t}}(i, \epsilon_{\mathrm{t,o}})$, according to Eq. 4.3. A sum of squares function, $X(\epsilon_{\mathrm{t,o}})$, is calculated as

$$X(\epsilon_{\mathrm{t,o}}) = \sum_{i=1}^{5} \left\{ S_{\mathrm{t,poly}}(T_{\mathrm{t,avg}}(i)) - S_{\mathrm{t}}(i, \epsilon_{\mathrm{t,o}}) \right\}^2 \tag{4.9}$$

where $S_{\mathrm{t,poly}}(T_{\mathrm{t,avg}}(i))$ is the predicted HTHFS sensitivity for each thermal event. The best estimate for $\epsilon_{\mathrm{t,o}}$ is determined by minimization of $X(\epsilon_{\mathrm{t,o}})$, which, as shown in Fig. 4.9, corresponds to the smallest value of $X(\epsilon_{\mathrm{t,o}})$ over the full range of possible emissivities, $0 < \epsilon_{\mathrm{t,o}} < 1$. Once $\epsilon_{\mathrm{t,o}}$ is determined for a test, the HTHFS sensitivity is recalculated using this estimated emissivity value for all steady-state thermal events of the test.

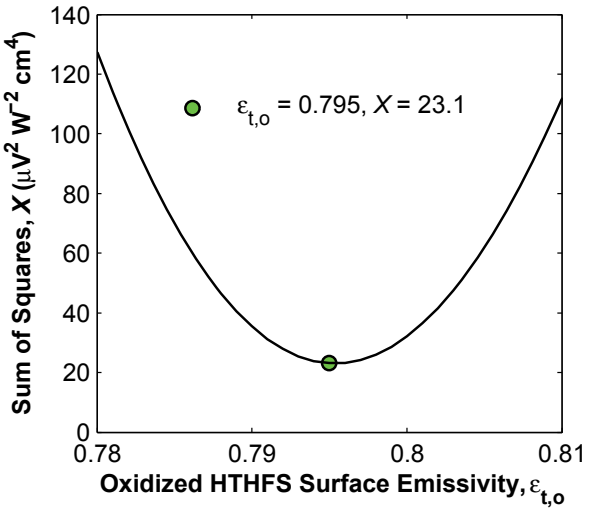

Figure 4.9: Test #4 oxidized HTHFS surface emissivity estimation: sum of squares minimization.

Figure 4.10 shows the in-cavity high temperature calibration results, including the sensitivity polynomial used in the parameter estimation scheme, theoretical HTHFS sensitivity (§4.4.2), and the calibration results for the three oxidized HTHFS tests. Also, listed in Figure 4.10 is the estimated value of the oxidized HTHFS surface emissivity for each of the corresponding tests. The mean estimated HTHFS emissivity and sample standard deviation for the three

oxidized tests was found to be 0.783 and 0.011, respectively. Average heat flux results for the three oxidized tests are listed in Table 4.1. The calibrated HTHFS sensitivity agrees well with the theoretical sensitivity model. The slightly lower magnitude of the experimental sensitivity as compared to the theoretical prediction suggests that the effective thermal conductivity of the thermopile is slightly higher than predicted. Good agreement between experiment and theory suggests the in-cavity high temperature calibration method is a viable choice for primary heat flux calibrations. Uncertainty in this calibration is discussed in the following section.

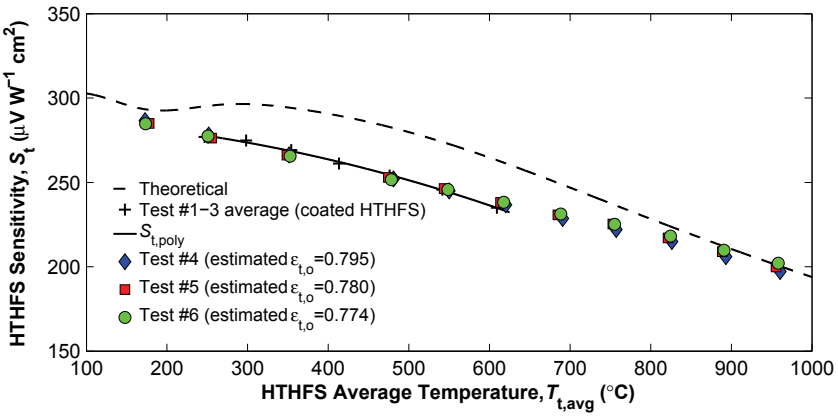

Figure 4.10: In-cavity high temperature heat flux sensor calibration results.

Table 4.1: Average heat flux for the three oxidized HTHFS tests (test #4-6).

T_b / (°C)	$T_{t,top}$ / (°C)	$q''_{t,conv}$ / (W cm^{-2})	$q''_{t,rad}$ / (W cm^{-2})	q''_t / (W cm^{-2})
500	177	0.34	1.36	1.71
600	256	0.36	2.17	2.53
700	356	0.35	3.19	3.54
800	485	0.31	4.30	4.61
850	555	0.28	4.84	5.13
900	625	0.26	5.37	5.62
950	697	0.23	5.85	6.08
1000	765	0.21	6.34	6.55
1050	833	0.19	6.74	6.92
1100	901	0.17	7.13	7.29
1150	968	0.15	7.44	7.59

4.7 Uncertainty Analysis

The uncertainty analysis for the in-cavity high temperature calibration follows procedures outlined in [25]. Each test variable, χ_i, used to determine the HTHFS sensitivity has an associated standard uncertainty, $u(\chi_i)$. The combined standard uncertainty in the resulting HTHFS sensitivity, $u_c(S_\mathrm{t})$, is determined according to [25] from

$$u_c(S_\mathrm{t}) = \sqrt{\sum_{i=1}^{2} \left(\frac{\partial S_\mathrm{t}}{\partial \chi_i} u(\chi_i) \right)^2 + (u_r)^2} \tag{4.10}$$

where $\partial S_\mathrm{t}/\partial \chi_i$ are the sensitivity coefficients for each quantity on the right-hand side of Eq. 4.3. The uncertainty in the repeatability of the sensitivity calibration, u_r, is taken to be the calculated standard deviation of the mean sensitivity determined from the sample of three tests (with oxidized HTHFS surface) reported in this work (Test #4-6 in Fig. 4.10).

Standard uncertainties are determined using either Type A or Type B evaluation methods. Type A evaluation of standard uncertainty is based on statistical methods, while Type B evaluation is based on scientific judgment using all relevant information available. In the present paper, standard uncertainties have been evaluated using Type A methods wherever possible. In general, $u(\chi_i)$ is either conservatively estimated or it is represented by a statistically estimated standard deviation. A root-sum-squares technique is used when multiple sources contribute to the standard uncertainty in one quantity, χ_i. Instead of using a coverage factor when determining $u(\chi_i)$, an overall coverage factor, k, for $u_c(S_\mathrm{t})$ is taken as the Student's t multiplier for 95 % confidence and ν effective degrees of freedom. The number of effective degrees of freedom for the sensitivity calibration, ν, is calculated using the Welch-Satterthwaite formula [25].

The standard uncertainty in V_t and V_sb is a combination of sensor and measurement system uncertainties. Bias error is measured at the start of each test, when the system is in thermal equilibrium (sensors have zero output), and removed from the data during post-processing. The measurement uncertainty associated with the data acquisition system was determined through calibration using a precision DC power supply. Uncertainty in the HTHFS output repeatability is estimated to be $\pm 0.5\%$ of the reading.

Heat flux, q''_t, is calculated using experimental measurements and system properties applied to Eqs. 4.6-4.8 as described in §4.5. The combined standard uncertainty in q''_t is calculated from the propagation of uncertainty in the quantities used to calculate the heat flux. Due to the complexity of Eqs. 4.6-4.8, a sequential perturbation numerical technique, outlined in [26], is used to calculate $u_c(q''_\mathrm{t})$. The standard uncertainty in the quantities used to calculate q''_t are listed in Table 4.2.

Errors in temperatures used to calculate q''_t can have a significant impact on the calibration uncertainty. Uncertainty in the HTHFS surface temperature was calculated as a combination

Table 4.2: Standard uncertainty values used in calculating $u_c(q''_t)$.

Quantity	Symbol(s)	$u(\chi_i)$	Units
HTHFS surface temperature	$T_{t,top}$	5.6	°C
Blackbody temperature (pyrometer measurement)	T_b	$0.0015 \times T_b$	°C
Temperature drop across partition thickness	$(\Delta T)_1$	$\frac{q''_p t_p}{2\kappa_p}$	°C
Axial temperature drop along sidewall	$(\Delta T)_2$	2	°C
Radial temperature drop along partition surface	$(\Delta T)_3$	3	°C
Virtual black surface temperature	T_v	$(T_b - T_{t,top})/4$	°C
Argon free stream temperature	T_∞	$0.1 \times T_b$	°C
Blackbody surface emissivity	ϵ_b	0.01	–
Carbon black coating emissivity	ϵ_{cb}	0.01	–
HTHFS oxidized surface surface emissivity	$\epsilon_{t,o}$	0.015	–
Convective heat transfer coefficient	$\overline{h}$	$0.2 \times \overline{h}$	W cm^{-2} °C^{-1}
Distance from sensor to blackbody partition	L	0.01	cm
Lengths	D, r_t	0.05	cm

of possible error due to the data acquisition system, the accuracy of the thermocouple output, and the assumed (worst-case) temperature variation along the surface of the HTHFS. Uncertainty in the blackbody temperature, which is the most significant source of uncertainty in this calibration, was estimated as a combination of possible errors arising from the pyrometer measurement and the assumed (worst-case) temperature distributions along the blackbody cavity surfaces.

Due to cavity thermal loading caused by the presence of the air-cooled HTHFS, the temperature of the partition surface facing the HTHFS is expected to be lower than the temperature measured by the pyrometer. The estimated temperature drop across the thickness of the partition was determined by modeling the partition as a plane wall with heat generation, as in [16]. Assuming one-dimensional, steady-state conduction through the partition wall with thickness t_p and thermal conductivity κ_p, the heat equation is solved considering one end of the wall perfectly insulated and the other end of the wall subject to a uniform (outgoing) heat flux, q''_p, which is determined for each thermal event of the calibration from Eq. 4.8. With these boundary conditions (designed to over-predict the temperature drop across the wall), the resulting temperature drop across the wall is $\Delta T = \frac{q''_p t_p}{2\kappa_p}$. Radial temperature variation along the surface of the partition (increasing temperature from cavity centerline to cavity wall), and axial temperature variation along the cavity sidewall (decreasing temperature from partition to location of virtual black surface), was estimated based on extrapolating results from [41]. A linear temperature variation across the partition surface and cavity sidewall was used in the sequential perturbation. Discretization of the cavity enclosure (see §4.5.2)

allows these temperature profiles to be used in the net-radiation analysis. The temperature of the virtual black surface had a minimal impact on the heat flux calculation, and therefore a large uncertainty was used; $T_{\mathrm{v}} \pm u(T_{\mathrm{v}})$ corresponds to a change in the modeled heat flux by less than 0.7%. All other uncertainty components listed in Table 4.2 were conservatively estimated to the authors' best knowledge.

The combined standard uncertainty in the HTHFS sensitivity calibration, $u_c(S_{\mathrm{t}})$, is multiplied by the coverage factor, k, to get the expanded uncertainty, $U(S_{\mathrm{t}})$. Coverage factors, taken as the Student's t multiplier for ν effective degrees of freedom, for each thermal event provide a 95 % confidence interval about the measurement results. A summary of the calibration results and associated uncertainties is provided in Table 4.3. Figure 4.11 shows averaged calibration results from the three oxidized HTHFS tests. The average experimental sensitivity is plotted with bars showing the expanded uncertainty in the calibration result, which is approximately ±8 % for sensor temperatures from 350 °C to 980 °C. The calibrated sensitivity is slightly lower than predicted with the model, suggesting that the actual thermopile has a higher thermal conductivity than the composite model.

Table 4.3: Calibration results and uncertainty as a function HTHFS mean temperature, $T_{\mathrm{t,avg}}$. Results averaged over the sample of three oxidized tests.

$T_{\mathrm{t,avg}}$ / (°C)	$u(V_{\mathrm{t}})$ / (μV)	$u_c(q''_{\mathrm{t}})$ / (W cm^{-2})	ν	k	$U(S_{\mathrm{t}})$ / (μV W^{-1} cm^2)	S_{t} / (μV W^{-1} cm^2)
175	2.6	0.092	14	2.14	33	285
253	3.7	0.11	17	2.11	25	277
351	5.0	0.12	18	2.10	20	267
478	6.2	0.14	16	2.12	17	252
547	6.7	0.16	15	2.13	16	246
617	7.1	0.17	14	2.14	16	238
688	7.4	0.19	15	2.13	15	230
755	7.8	0.21	16	2.12	15	224
824	8.0	0.23	17	2.11	15	216
891	8.1	0.25	19	2.09	15	208
958	8.1	0.28	20	2.09	16	200

4.8 Discussion

Currently there is no method in use for primary calibration of heat flux sensors at elevated sensor temperatures. The results from this study indicate that high sensor temperature primary calibrations are possible with the VTBB system. The steady-state temperature of a heat flux sensor being calibrated using the in-cavity method [13] can be dictated by the boundary conditions prescribed during testing. Specifically, limiting the convective cooling

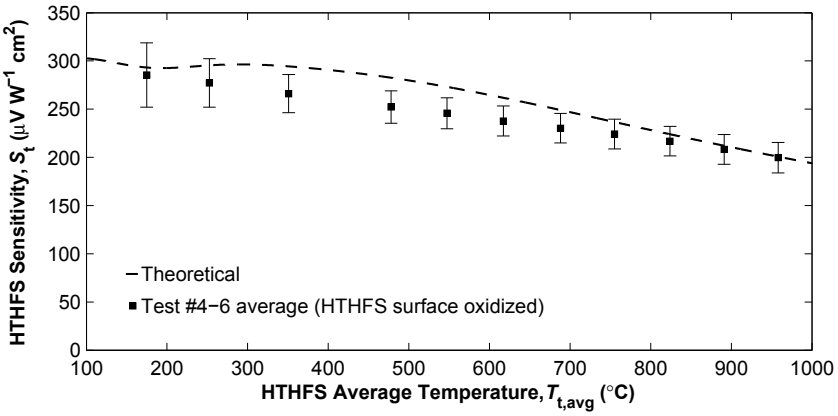

Figure 4.11: HTHFS calibrated sensitivity showing expanded uncertainty (95 %CI).

of the sensor (confined fluid-cooled sensor) and changing the blackbody temperature allows the sensitivity of the sensor to be calculated as a function of sensor temperature. This is critical for high temperature sensors, such as the HTHFS, where the thermal properties of the sensor's thermal resistance layer vary with temperature, which makes the sensor's output temperature dependent.

All sensitivity results presented in this study are based on net heat flow through the HTHFS (combination of absorbed radiation and convection). When sensor emission and convection is significant, as is the case here, sensitivity based on incident radiation is not appropriate. Normalized sensitivity results from this study (both for the coated and oxidized series of tests) are compared with those from a high temperature transfer calibration [1] in Fig. 4.12. Two separate HTHFSs of similar construction were used in these two calibrations. The experimental sensitivity from each calibration is normalized by the respective calibration point at $T_{\mathrm{t,avg}} \approx 300$ °C. The results from the two calibrations compare favorably, although the transfer results have a slightly more nonlinear trend with temperature. Further research into reducing uncertainty in the in-cavity high temperature calibration method may lead to standardization of this process.

Calibration of heat flux sensors at elevated temperatures is a complex process. Several factors which influence uncertainty in the calibration must be examined. The calculated expanded uncertainty in this calibration is $< \pm 8$ % for sensor temperatures from 350 °C to 980 °C. This calibration uncertainty is expected to be higher than the $U \leq \pm 3\%$ reported in [27] for several reasons. First, the value of the sensor's surface emissivity is required to calculate its sensitivity, and therefore the uncertainty in the sensor surface emissivity must be considered a source of uncertainty in the calibration. Also, because sensor emission is comparable to incident radiation in this calibration, the uncertainty in the measured sensor surface temperature (used to calculate emission) has a major impact on the calibration uncertainty. Standard uncertainty in the heat flux sensor's surface emissivity and temperature have little or no impact on the combined standard uncertainty of the primary calibrations for water-

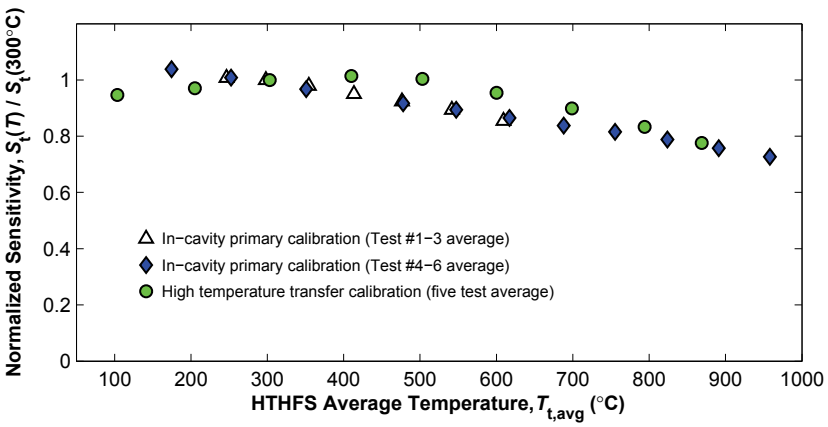

Figure 4.12: HTHFS experimental sensitivity comparison. The normalized results are for two similar HTHFS thermopiles, one calibrated using a transfer technique [1], and the other calibrated using the in-cavity technique.

cooled sensors [27]. Finally, the blackbody temperature distributions used in the uncertainty analysis for this calibration represent worst-case measurement scenarios; this is done to provide a conservative estimate for the calibration uncertainty. Thermal modeling of the in-cavity calibration, similar that done in [40], can reduce the calibration uncertainty by determining the thermal loading effect of the sensor on the blackbody. This type of modeling effort is worth pursuing, as the primary source of uncertainty in this calibration is in the blackbody temperature used in the heat flux model.

The heat flux model used in this work assumes no specular reflections within the blackbody cavity, therefore, this model is inappropriate for polished surfaces, such as those found on the cooling bodies of the sensors used in [13] and [41]. If specular surfaces are present, Monte-Carlo simulations, similar to those used in [32] extended to incorporate elevated sensor temperatures, may be appropriate to model radiation exchange within the cavity. The influence of mixed convection within the cavity, on both the sensor and the cavity wall temperature distributions, must be further investigated. Use of computational modeling, with either commercially available software or purpose-written codes, can prove to be very useful for this. Uncertainty in the calibration, particularly in the lower temperature range, can be reduced once the convective interactions are quantified with reasonable uncertainty.

Estimating the emissivity of the oxidized HTHFS surface was necessary in this study, due to the lack of well characterized coatings capable of withstanding temperatures in excess of 600 °C. The stability and/or temperature dependence of the oxidized HTHFS surface emissivity must be checked. The process of limiting the convective cooling of the sensor (confined fluid-cooled sensor) to be calibrated, could be used in the other two standardized primary calibration methods (vacuum blackbody cavity and spherical blackbody cavity, see [27]) to extend the calibration range to include elevated sensor temperatures. Cost-benefit analysis based on calibration uncertainty and cost of implementation may provide insight

as to which of the three primary calibration methods [27] is most appropriately suited to handle elevated sensor temperatures.

4.9 Conclusions

The in-cavity calibration method, as reported in [13], has been extended to include heat flux calibrations performed at elevated sensor temperatures. The process has been demonstrated by the calibration of an air-cooled HTHFS over the temperature range of $175 - 960$ °C. The temperature dependency in the HTHFS output is primarily caused by change in effective thermal conductivity with temperature of the sensor's thermal resistance layer. The experimental sensitivity (versus sensor average temperature) agrees very well with the theoretical sensitivity model, and suggests that the effective thermal conductivity of the sensor is slightly higher than used in the model. Standard uncertainties in the analytically modeled heat flux have been conservatively estimated to provide an initial assessment of possible calibration errors. The calibration expanded uncertainty is high in the low temperature range ($T_{\mathrm{t,avg}} < 350$ °C) due to the influence of convection uncertainty. The calibration expanded uncertainty is approximately $\pm 7\%$ for $T_{\mathrm{t,avg}} > 350$ °C, which is reasonable considering the inherent complications of heat flux calibration at high sensor temperatures. The results presented in this work suggest that the primary calibration of heat flux sensors at elevated temperatures is feasible with the existing VTBB system.

4.10 Acknowledgments

Funding for this work was provided by NASA through GSRP grants.

Chapter 5

On the Use of High Temperature Heat Flux Sensors in Thermal Research

The material in this chapter is intended for submission in the AIAA Journal of Thermophysics and Heat Transfer.

5.1 Abstract

The implementation of a novel thermopile heat flux sensor in several hot-wall measurment scenarios is presented here. The High Temperature Heat Flux Sensor (HTHFS) is capable of operation at temperatures greater than 1000 °C with simultaneous measurement of heat flux and surface temperatures. A unique data processing scheme is used which renders the sensor virtually insensitive to the material on which it is mounted. Hot surface measurements are demonstrated through controlled experiments performed using a radiant flat plate heater. Total heat flux measurements from the HTHFS at high temperature are compared to measurements made by a water-cooled Gardon reference sensor.

5.2 Nomenclature

A	area (cm^2)
C	specific heat $\left(J\ kg^{-1}\ K^{-1}\right)$
$\boldsymbol{g}$	gravitational vector
L	distance from heater plate to heat flux sensor (cm)
m	mass (kg)
N	number of thermocouple junction pairs in thermopile
q''	heat flux ($W\ cm^{-2}$)
S	heat flux sensor sensitivity ($\mu V\ W^{-1}\ cm^2$)
S_e	relative Seebeck coefficient ($\mu V\ \ ^\circ C^{-1}$)
t	time (s)
T	temperature (°C)
V	thermoelectric voltage (μV)
x	distance (cm)

Greek Letters

δ	thermal resistance layer thickness (cm)
ϵ	hemispherical total emissivity
κ	thermal conductivity ($W\ cm^{-1}\ \ ^\circ C^{-1}$)
σ	Stefan-Boltzmann constant ($W\ cm^{-2}\ K^{-4}$)

Subscripts

1	pertaining to the top surface
2	pertaining to the bottom surface
avg	average
conv	convection
diff	differential response
i	index variable
s	surface
slug	slug response
tot	total

5.3 Introduction

Hypersonic vehicles experience extreme thermal loads generated by the dissipation of the vehicle's kinetic and potential energy. The Thermal Protection System (TPS) employed in such vehicles is designed to protect the vehicle from thermal loading by regulating this energy dissipation. Controlled energy dissipation is essential. The instantaneous heat rate (i.e. peak heat flux) and total heat load must be maintained within acceptable limits defined by the vehicle's design, construction, and mission objective [45]. TPS validation depends on the accurate measure of the aforementioned thermal quantities, both the heat load imposed on the TPS and the heat transfer rate throughout the vehicle structure.

A critical hypersonic flight parameter considered in the design of a vehicle's TPS is the heat flux into the system. Both the peak heat flux and averaged total heat load encountered in hypersonic flight influence TPS material selection, shape, and size. Specifically, the heat absorbed by the system is important for monitoring structural system health. Robust sensors capable of making direct measurements to evaluate test structure performance both in-flight and on the ground are required [46]. This paper outlines the implementation of the High Temperature Heat Flux Sensor (HTHFS), which was designed to meet the aforementioned requirements.

5.4 Heat Flux Measurement

Heat flux measurement plays an important role in the qualification of a system's thermal control. Recent advances in sensor technology have resulted in the capability of heat flux

sensors to withstand temperatures in excess of 300 °C for long periods of time. Two examples are the High Temperature Heat Flux Sensor (HTHFS) [9] and the direct write heat flux sensor [30]. The ability to directly measure heat flux at high temperatures makes these sensors desirable for numerous potential applications in thermal research. The following sections outline use and implementation considerations for high temperature-capable heat flux sensors.

5.4.1 Sensor Measurement Principles

Heat flux sensor technology is typically based on the measurement of either a spatial temperature difference across a known thermal resistance (differential temperature sensor) or a change in temperature over time of a known thermal capacitance (slug calorimeter) to determine heat flux. Standard test methods for differential temperature sensors are outlined in [47, 7, 8], and standard test methods for slug calorimeters are outlined in [48]. Common types of differential temperature sensors are the thermopile, the circular foil or Gardon sensor, and the wire-wound or Schmidt-Boelter sensor. Slug calorimeters are composed of a cylindrical "slug" of metal with a thermocouple attached to the back surface. A detailed description of the different types of heat flux sensors is provided in [10].

A thermopile uses thermocouples connected in series across a thermal resistance layer to directly measure a spatial temperature difference. When heat flows through the sensor's thermal resistance layer, the thermopile's self-generating electromotive force, V, is directly proportional to the temperature difference across the sensor, that is

$$V = NS_e\Delta T \tag{5.1}$$

where N is the number of thermocouple junction pairs in the thermopile, and S_e is the relative Seebeck coefficient of the thermoelectric alloys. For the case of one-dimensional heat transfer through the sensor, the voltage output is directly proportional to the conduction heat flux by Fourier's law:

$$q''_{\text{diff}} = -\kappa\frac{dT}{dx} = \kappa\frac{\Delta T}{\delta} = \frac{\kappa V}{\delta N S_e} \tag{5.2}$$

where δ and κ are, respectively, the thickness and thermal conductivity of the thermopile's thermal resistance layer.

Instead of measuring a spatial temperature difference, a slug calorimeter measures the temperature change over time of a slug of material, typically a metal with a well known thermal capacitance, to infer heat flux. The bottom and sides of the slug calorimeter are typically well insulated to limit heat loss through the bottom of the slug. For the case of perfectly insulated bottom and sides, the heat flux measured by the slug calorimeter is determined from conservation of energy for a control volume surrounding the slug:

$$q''_{\text{slug}} = \rho C \delta \frac{dT_{\text{avg}}}{dt} \tag{5.3}$$

Here ρ, C, δ, and T_{avg} are the density, specific heat, thickness, and average temperature of the slug, respectively. The product $\rho C \delta$ represents the thermal mass of the slug per surface area.

5.4.2 Hot-Wall vs. Cold-Wall Heat Flux Measurement

Heat flux sensors are typically mounted on/in a test article to measure the heat flux to or from the article's surface. Typically the "bottom" side of the sensor is in good contact with the test article, while the "top" side of the sensor is exposed to the surrounding environment (incident radiation and convection). In this case, shown schematically in Fig. 5.1, the total heat transfer through the sensor by conduction is governed by an energy balance at the top surface:

$$q_{\text{tot}} = \alpha_{\text{s}} q_{\text{i}} - q_{\text{e}} - q_{\text{conv}} \tag{5.4}$$

where $\alpha_{\text{s}} q_{\text{i}}$ is the portion of the incident radiation absorbed by the opaque surface, with surface absorptivity α_{s}, q_{e} is the emission from the sensor, and q_{conv} is the convection exchange between the sensor and surrounding fluid. This surface energy balance demonstrates what the so-called "total" heat flux sensors respond to. Differential temperature sensors and slug calorimeters both use temperature measurements to infer the total heat flux, $q''_{\text{tot}} = q_{\text{tot}}/A_{\text{s}}$.

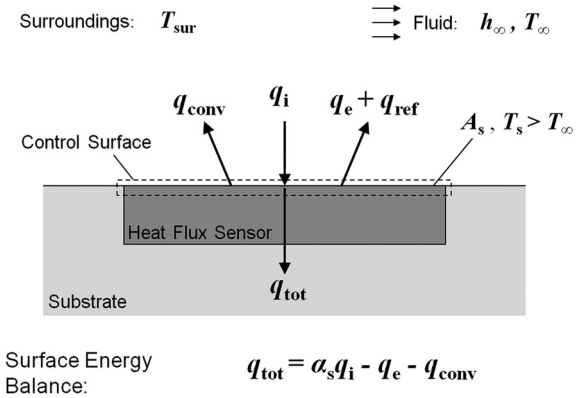

Figure 5.1: Heat flux sensor control surface schematic. The sensor is shown mounted flush with the surface of the substrate (test article). The total heat transfer through the sensor by conduction is a combination of the net radiation and convection to/from the sensor surface.

Cold-wall heat flux measurement refers to the measurement of heat flux with the sensor maintained at the temperature of the surrounding fluid (usually room temperature air).

This is achieved by actively cooling the heat flux sensor with pressurized water. Water-cooled sensors are often used to measure incident radiation. In the absence of forced convection, the total heat flux measured by water-cooled sensor (maintained at room temperature) is proportional to the radiation incident on the sensor surface. In this case, natural convection and emission are negligible in comparison to the incident radiation, and from Eq. 5.4, $q_{\text{tot}} = \alpha_{\text{s}} q_{\text{i}}$. Water-cooled sensors are usually calibrated against known levels of incident radiation.

Water-cooled sensors can also be used to measure mixed mode heat flux (convection and incident radiation), however, corrections are required if the sensor temperature is different from that of the structure in which it is mounted. These corrections can be very large, and therefore the use of water-cooled sensors in convective environments should be viewed with caution [38].

Hot-wall heat flux measurement refers to the measurement of heat flux with the sensor maintained at the temperature of the test article (test article temperature is greater than that of the surrounding environment). In this case the sensor is passively cooled, inheriting the temperature of the parent structure. When the temperature of the sensor/hot wall is sufficiently higher than the surrounding fluid, emission and convection exchange (natural convection in absence of forced convection) are no longer negligible as is often the case with a water-cooled heat flux sensor. Given the same boundary conditions, the total heat flux measured by a hot sensor would be less than that measured by a water-cooled sensor. In situ hot-wall heat flux measurements provide more information about an actual test structure's thermal response to a heat load than a corresponding cold-wall measurement can.

5.4.3 Hot-Wall Measurement Challenges and Advancements

The "true" hot-wall heat flux refers to the heat flux experienced by a test article without the presence of a heat flux sensor disturbing the natural heat flow paths through the article. Successful measurements of the true hot-wall heat flux can be made with heat flux sensors that are minimally intrusive to the measurement environment. Two critical attributes of hot-wall heat flux sensors are low thermal resistance and the ability to simultaneously measure heat flux and absolute temperature at temperatures greater than 300 °C. The HTHFS [9] has both of these attributes.

Differential temperature sensors and slug calorimeters both have limitations in the measurement of hot-wall heat flux. Differential temperature sensors measure the heat flowing through the sensor, and therefore should typically be mounted on a good heat sink. These sensors tend to have low output when installed in insulating materials. This is due to the inability of the insulating substrate to efficiently transfer heat. The principle of operation of the differential sensor is based on Fourier's law for steady-state heat conduction, and therefore the accuracy of the output suffers in some transient heating scenarios when the temperature profile through the sensor is not fully developed.

The bottom and sides of the slug calorimeter should be well insulated, as any heat escaping through these surfaces represents an error when calculating heat flux from Eq. 5.3. Noise in the temperature measurement is amplified when taking its temporal derivative. Also, because the output of the slug calorimeter is proportional to the temporal temperature derivative, the sensor cannot measure heat flux at steady-state.

Hubble and Diller [49] developed a novel method for heat flux measurement which combines the slug and differential response of special heat flux sensors. The Hybrid Heat Flux (HHF) method is a data processing routine which can be used on any sensor capable of making simultaneous measurement of both absolute temperature and differential temperature (spatial temperature gradient). For this type of sensor, the total heat flux through the sensor surface is simply a linear combination of the differential response and slug response of the sensor [49]:

$$q''_{\text{tot}} = q''_{\text{diff}} + \frac{1}{2} q''_{\text{slug}} \tag{5.5}$$

This method has been validated both numerically and experimentally in [49]. Use of the HHF method improves the sensor time response and also renders the sensor almost insensitive to the substrate on which it is mounted (thermal conductor or insulator). The HHF method is demonstrated in this study on measurements made by the HTHFS under three very different thermal scenarios.

5.5 Experimental Setup and Procedure

The Flight Loads Laboratory (FLL) at NASA's Dryden Flight Research Center is equipped with a radiation facility capable of calibrating heat flux sensors at heat flux levels in excess of 50 W cm^{-2}. The flat plate heater system [15] is typically used to perform heat flux transfer calibrations, in which a secondary standard heat flux sensor is used to characterize the incident heat flux produced by the heated graphite plate. The calibration of this secondary standard is transferred to a candidate sensor (working standard) by subjecting both sensors to the same incident heat flux. This transfer technique is relatively straightforward for water-cooled sensors, because they are maintained at room temperature during the tests. In calibrating water-cooled sensors using the flat plate transfer method, a procedure similar to that laid out in [28] is followed. In this study transfer calibrations are not performed. Instead, the flat plate heater system is simply used as radiant source to simulate high heat fluxes. The experiments performed here demonstrate the difference between hot-wall and cold-wall heat flux measurements.

5.5.1 Water-Cooled Gardon Sensor

The secondary standard sensor employed in this study is a water-cooled Gardon circular foil heat flux sensor. Because the Gardon sensor is water-cooled (maintained at room temperature during testing), emission and convection exchange with the surroundings is assumed negligible (in comparison with the incident radiation), and the output of the sensor is directly proportional to the incident radiation (see §5.4.2). Two Gardon sensors were used in this study, both of which were manufactured and calibrated by Medtherm Corporation. The design operating heat flux range for both Gardon sensors used in this study is 227 W cm^{-2} (both sensors have the same diameter and thickness circular foil).

5.5.2 High Temperature Heat Flux Sensor (HTHFS)

The HTHFS [9] is a thermopile sensor capable of measuring both absolute temperature and the differential temperature across the thermopile's thermal resistance layer. Most thermopiles use a uniform solid dielectric material as the thermal resistance layer, whereas the thermal resistance layer of the HTHFS is composed of three materials, as shown in Fig. 5.2(a). The thermal resistance layer is primarily made up of bulk K-type thermocouple alloys chromel and alumel. Thermopile junctions are formed by welding the bulk alloys in a serpentine series pattern. Thin ceramic plates are positioned in between neighboring junctions for electrical isolation. The recommended continuous use temperature limit of the sensor is 1000 °C.

Surface thermocouples (K-type) are welded on both sides of the thermopile as shown in Fig. 5.2. The voltage output from the thermopile is measured across the two positive legs (chromel) of the surface thermocouples. The thermopile is typically potted in an inconel housing with a high temperature castable aluminum nitride paste which cures after heating. Two configurations of the HTHFS are shown in Fig. 5.2(b-c) (both configurations are used in this study).

The HHF method is readily applied to HTHFS measurements. From Eq. 5.2-5.3 and Eq. 5.5, the total heat flux through the HTHFS surface as a function of time can be calculated from

$$q''_{\text{tot}}(t) = \frac{V(t)}{S} + \frac{1}{2}\rho C\delta \frac{d}{dt}\left(\frac{T_1 + T_2}{2}\right) \tag{5.6}$$

where S is the thermopile's calibrated sensitivity, and T_1 and T_2 are the top and bottom surface temperatures of the thermopile, respectively; $(T_1 + T_2)/2$ represents the average temperature of the thermopile, T_{avg}. In Eq. 5.6, S and C are functions of sensor temperature, and the sensor temperature varies with time according to the heating scenario. Any relative change in ρ and δ with temperature is assumed negligible in comparison with C.

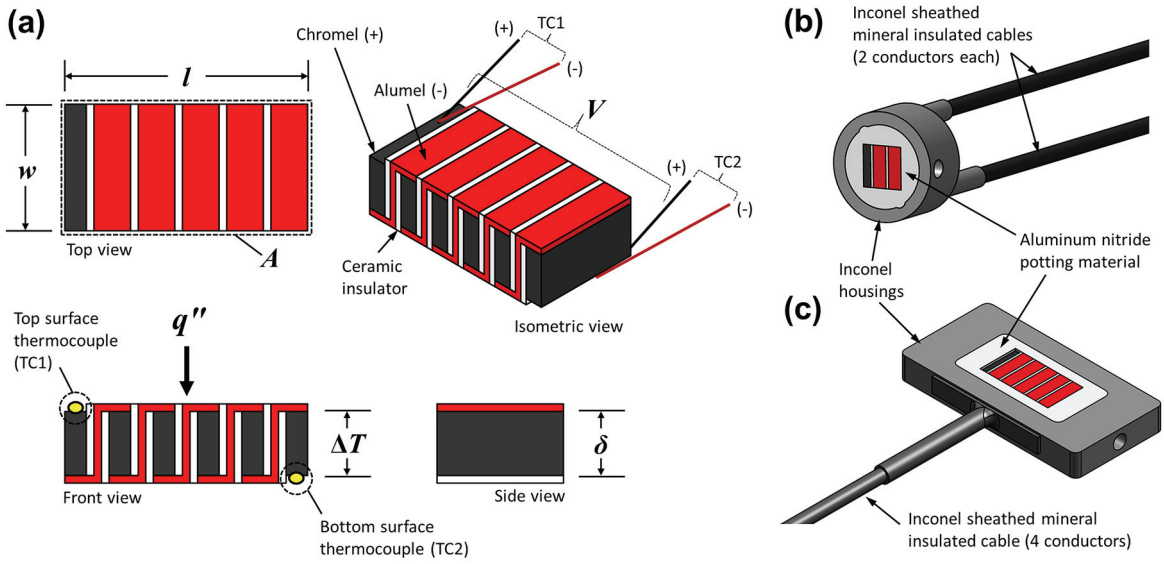

Figure 5.2: HTHFS schematic drawings: (a) $N = 5$ thermopile detail showing materials, important dimensions, and lead wire/surface thermocouple locations. Typical dimensions for the $N = 5$ thermopile shown are: $l = 1.0$ cm, $w = 0.5$ cm, and $\delta = 0.26$ cm. (b) Circular plug housing with $N = 2$ thermopile. (c) Rectangular flat housing with $N = 5$ thermopile.

Thermopile Sensitivity

At steady-state, the theoretical sensitivity (voltage response to applied heat flux) of the HTHFS as a function of average temperature is

$$S_{\text{theory}}\left(T_{\text{avg}}\right) = \frac{\delta N S_e\left(T_{\text{avg}}\right)}{\kappa\left(T_{\text{avg}}\right)} \tag{5.7}$$

The HTHFS theoretical sensitivity versus temperature was modeled in [2]. Small differences in material properties and manufacturing techniques require that heat flux sensors are individually calibrated at room temperature as outlined in [28]. Recent efforts [2, 1, 3] have focused on the calibration of the HTHFS at high sensor temperatures, with promising results. While individual room temperature calibration is necessary, individual high temperature calibration is much more time consuming and/or costly. Also, while room temperature heat flux calibrations are to some degree standardized [28, 12], high temperature heat flux calibrations are not.

For these reasons, a polynomial has been fit to available experimental HTHFS calibration data (sensitivity versus sensor temperature). Both room temperature and high temperature [2, 3] normalized calibration results from three different sensors are shown in Fig. 5.3. For each sensor, all data points are normalized by the sensor's calibrated room temperature sensitivity value. A polynomial has been fit to the experimental data, as shown in Fig. 5.3, so that the temperature dependent sensitivity of any HTHFS can be estimated based on one room temperature calibration.

Slug Calorimeter Properties

The thermal energy stored by the HTHFS during transient testing is a function of the thermopile's density, specific heat, volume, and temperature. Because the HTHFS thermopile is composed of three materials (see Fig. 5.2(a)), the composite specific heat is determined from a simple model and material property data. The composite density is simply the thermopile's total mass divided by its total volume. The composite specific heat (as a function of T_{avg}) is calculated as a mass-fraction weighted sum of the individual material specific heats, that is

$$C(T_{\text{avg}}) = \sum_{i=1}^{3} \frac{m_i}{m_{\text{tot}}} C_i(T_{\text{avg}}) \tag{5.8}$$

The mass of each material in the thermopile, m_i, is measured and the specific heat as function of temperature is determined from polynomial fits to specific heat data [4, 5] in the range of $27 - 1127$ °C for each thermopile material. The HTHFS composite specific heat versus temperature is shown in Fig. 5.4.

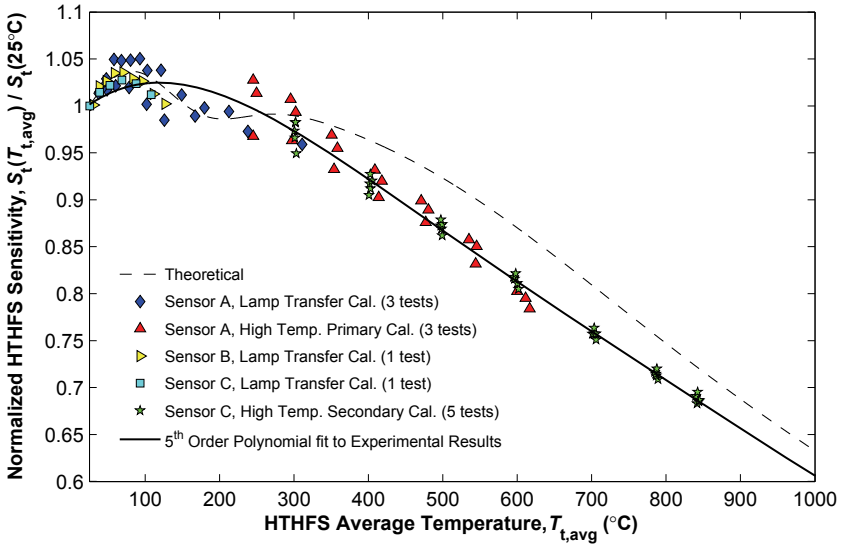

Figure 5.3: HTHFS normalized sensitivity versus average temperature. The experimental results span three types of calibrations performed on three different sensors. The high temperature results are taken from [2, 3]. Each experimental data point is normalized by the corresponding sensor's calibrated room temperature sensitivity. The theoretical sensitivity is based on a one-dimensional thermal model of the HTHFS thermopile [2].

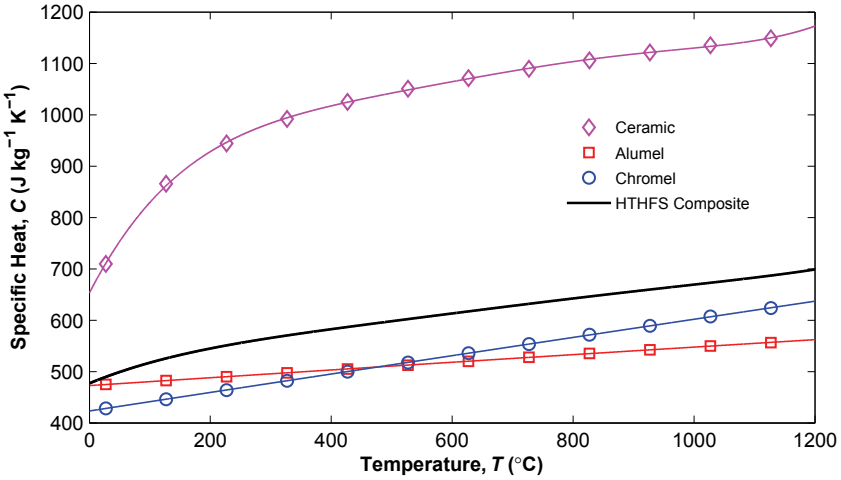

Figure 5.4: HTHFS Composite specific heat versus temperature. The points represent data taken from [4, 5] while the lines through the points are polynomial fits. Using these polynomials, the HTHFS composite specific heat is calculated from Eq. 5.8.

5.5.3 Experimental Setup

The flat plate heater system consists of a graphite plate heater element clamped between two copper electrodes. The graphite plate is subject to resistance heating as electrical power is passed through it. The plate provides radiant heat flux as it reaches temperatures up to 2800 °C. A secondary standard water-cooled Gardon sensor is placed on one side of the plate and a HTHFS is placed on the opposite side, as shown schematically in Fig. 5.5. The sensor surfaces are located at equal distances from the heater plate. During testing, the same radiative heat flux is incident upon the surface of both heat flux sensors.

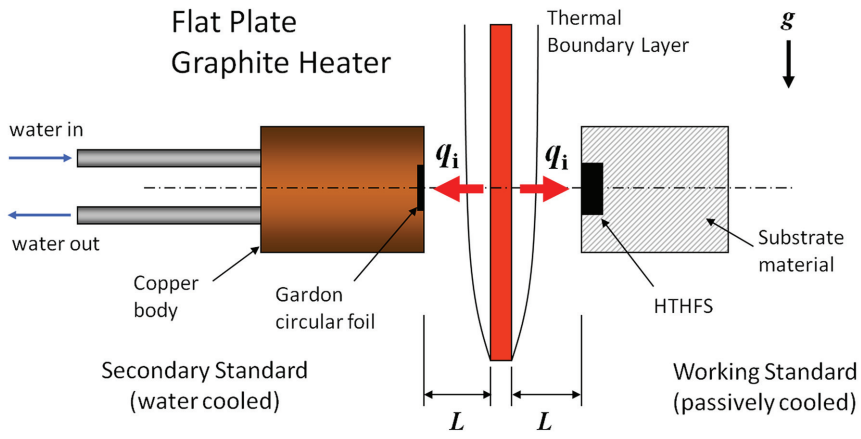

Figure 5.5: Flat plate heater system schematic. The radiation heat flux incident on the two sensor surfaces is equal.

Three different experimental cases were performed in this study, using three different HTHFS's. "Case 1" uses a $N = 3$ junction pair HTHFS which is potted in a circular plug housing, similar to the configuration shown in Fig. 5.2(b). The circular plug is press fit into one end of a long cooling body, as shown in Fig. 5.6(a), which consists of two concentric stainless steel tubes. Pressurized air is fed through the inner tube, impinges on the backside of the HTHFS plug housing, and exits the cooling body through the space between the inner and outer tubes. The cooling body has an outside diameter of 1.27 cm, and the design of the cooling body is similar to that reported in [2].

"Case 2" and "Case 3" both use $N = 5$ junction pair sensors which are potted in rectangular housings, as shown in Fig. 5.2(c). The rectangular housings have dimensions of 2.54 cm × 1.27 cm × 0.32 cm. In Case 2, the HTHFS is fastened to one end of a long rectangular steel column, which has the same perimeter as the rectangular HTHFS housing and an axial length of 30.5 cm. The outer surfaces of the steel column are insulated, as shown in Fig. 5.6(b), to promote one-dimensional conduction through the HTHFS and steel column. In Case 3, the HTHFS is flush-mounted in a fibrous alumina insulation board, as shown in Fig. 5.6(c).

The insulation board has a very low thermal conductivity (two orders of magnitude lower than the HTHFS) which typically causes problems for differential temperature sensors, as discussed in §5.4.3. As demonstrated in §5.6, the HHF method renders the HTHFS virtually insensitive to the material in which it is mounted.

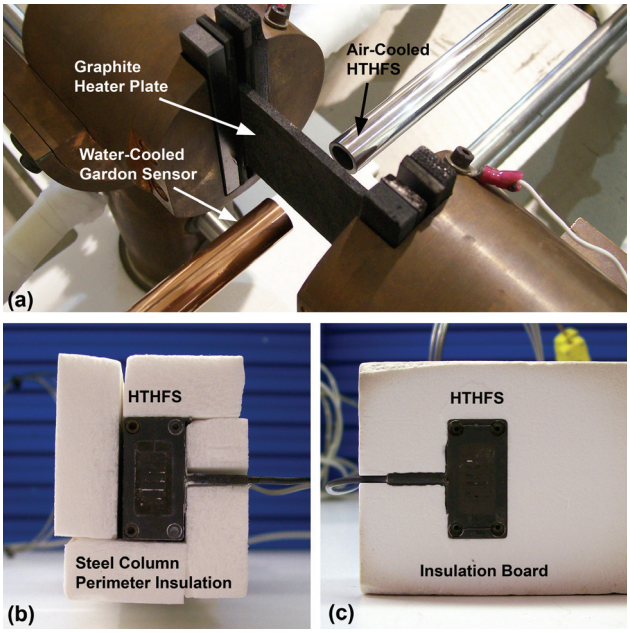

Figure 5.6: Three experimental cases for hot-wall heat flux measurement using the HTHFS: (a) Case 1: HTHFS mounted in an air-cooled stainless steel body. The overhead view of the calibration setup shows the flat graphite heater plate and the water-cooled Gardon sensor. (b) Case 2: HTHFS mounted on a long steel column (hidden) with an insulated perimeter to promote one-dimensional axial conduction. (c) Case 3: HTHFS flush mounted in a fibrous alumina insulation board.

5.5.4 Experimental Procedure

During testing, electrical power to the heater element is controlled manually to provide the desired levels of radiative heat flux incident on the two sensors. Heat flux and temperature signals were read into 24-bit National Instruments CompactDAQ modules as analog differential inputs. Cold-junction temperature compensation was provided by on board thermistor measurements. The ±80 mV range of the analog-to-digital converter provides significant resolution for the expected output from the heat flux sensors with a least significant bit of $0.16/2^{24} = 9.5$ nV. A sampling rate of 3 Hz was used for all tests. Post testing, the recorded data were analyzed using MATLAB software.

5.6 Experimental Results

The results from three separate experiments are presented here to demonstrate the difference between hot-wall and cold-wall heat flux measurements in different measurement scenarios. The HHF method is used to process the HTHFS voltage and temperature measurements. In all cases, the total heat flux through the HTHFS surface is calculated from Eq. 5.6. The HTHFS calibrated sensitivity and specific heat is determined (for every sample during the test) by using the polynomial lookup functions shown in Fig. 5.3 and Fig. 5.4, respectively. The temporal temperature gradient is calculated numerically using experimental data.

The heat flux incident on the standard sensor and the HTHFS in all tests is ideally equal. This allows the comparison of the heat flux measured by the water-cooled standard to that measured by each HTHFS in different installation configurations. Rearranging Eq. 5.4 (and dividing all terms by the surface area of the HTHFS), the total heat flux measured by the HTHFS can be used to predict the incident radiation. Assuming diffuse-gray radiation exchange, $\alpha_s = \epsilon_s$, and the emission heat flux from the HTHFS is calculated as $q''_e = \epsilon_s \sigma T_s^4$. The hemispherical total emissivity of the sensor surface, ϵ_s, is assumed constant in each test. Natural convection at the sensor surface is estimated using experimental temperatures applied to vertical isothermal flat plate correlations [43]. Although this heat flux model is very simple, it serves as a basis for comparison between water-cooled sensor measurements and the HTHFS hot-wall measurements.

5.6.1 Case 1: Actively Cooled HTHFS

The HTHFS shown in Fig. 5.6(a) is actively cooled using pressurized air, with a regulated line pressure of 2.0 atm. Active cooling of the HTHFS allows the sensor to reach steady-state operation for a given steady incident heat flux level. The temperature of the sensor at steady-state is dictated by the balance of heat supplied by the flat plate heater and heat removed by the cooling air. Measurement results from a single test are presented in Fig. 5.7. The test consists of six quasi steady-state thermal events, governed by the manual heater power settings used over the course of the test.

In Fig. 5.7(a) the HHF total heat flux measured by the HTHFS is a combination of the differential response and slug response of the sensor (see Eq. 5.6). It is apparent from Fig. 5.7(a) that the slug response of the HTHFS contributes little to the HHF total heat flux, as the active cooling body forces quasi steady-state conditions fairly quick at each incident heat flux interval. The slug term does, however, increase the time response of the HTHFS when the HHF method is applied [49]. The incident heat flux predicted from the HHF total heat flux measurement is within 5% of the incident heat flux measured by the water-cooled Gardon sensor.

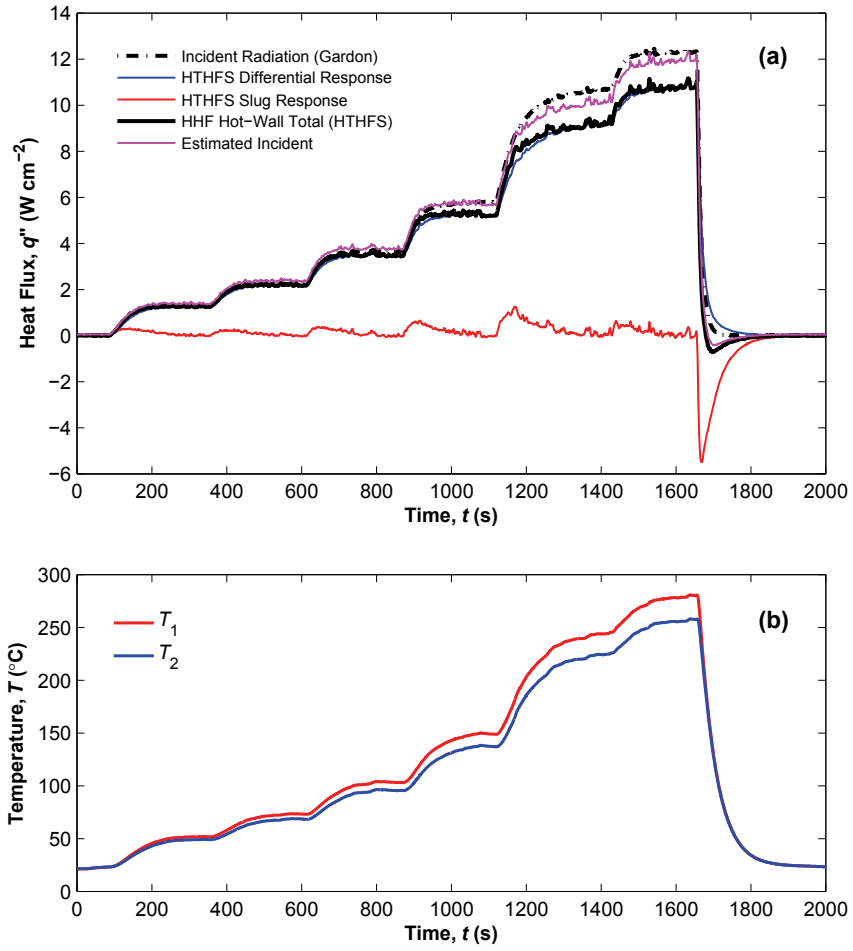

Figure 5.7: Case 1 heat flux and temperature data. The HTHFS is mounted in an air-cooled cylindrical body. (a) Heat flux versus time. (b) Sensor temperature versus time.

5.6.2 Case 2: Passively Cooled HTHFS on Efficient Heat Sink

The HTHFS shown in Fig. 5.6(b) is passively cooled by conduction through the sensor into the steel column substrate (heat sink) which has a high thermal mass. The installation configuration is representative of a sensor mounted in a large test article which is not actively cooled by forced convection. A high manual power setting was used to produce a very high incident heat flux ($\approx$ 60 W cm^{-2}) which causes a rapid sensor temperature ramp rate ($\approx$ 12 °C s^{-1}) as shown in Fig. 5.8(b). The slug response increases the time response of the HTHFS, as shown in Fig. 5.8(a). The incident heat flux predicted from the HTHFS measurements is within 5% of the incident heat flux measured by the water-cooled Gardon sensor. The decreasing incident heat flux over time in the middle portion of the test is due to graphite heater plate ablation at high temperature [15].

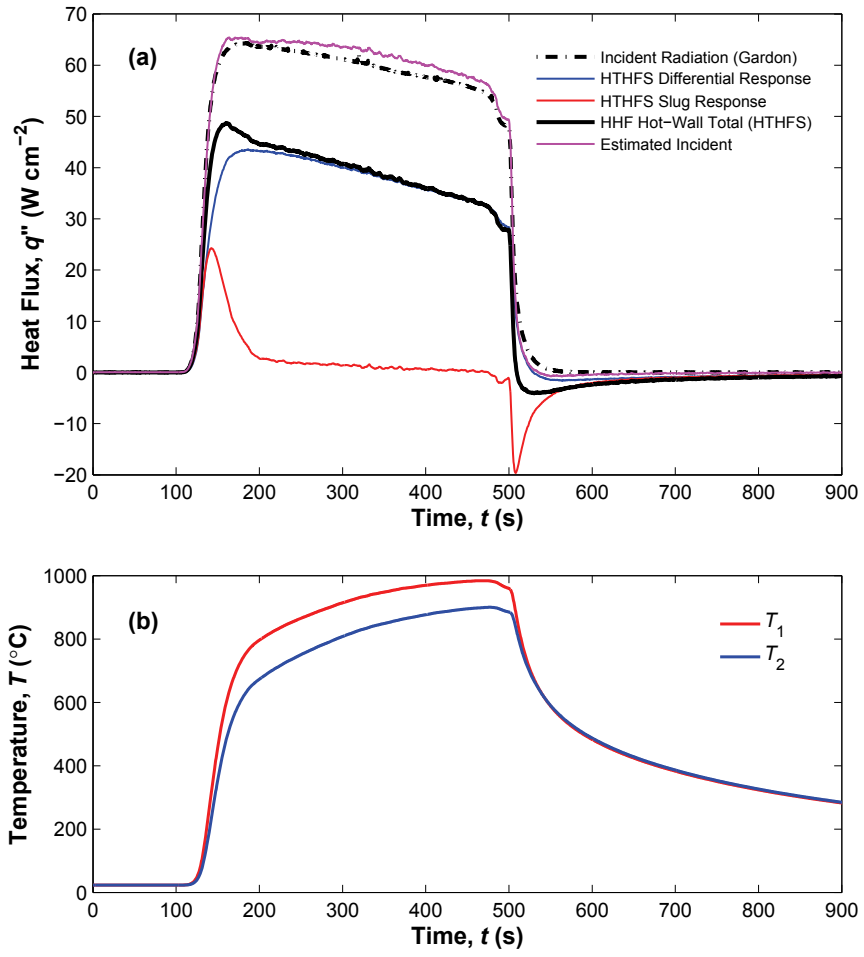

Figure 5.8: Case 2 heat flux and temperature data. The HTHFS is mounted on the end of a long steel column. (a) Heat flux versus time. (b) Sensor temperature versus time.

5.6.3 Case 3: Passively Cooled HTHFS on Thermal Insulator

The HTHFS shown in Fig. 5.6(c) is passively cooled by conduction through the sensor into the alumina insulation board. The low conductivity insulation board is representative of materials used in the TPS of hypersonic vehicles and in high temperature furnaces. A high manual power setting was used to produce a high incident heat flux (≈ 45 W cm^{-2}) which causes a rapid sensor temperature ramp rate ($\approx 16\,^{\circ}$C s^{-1}) as shown in Fig. 5.9(b). The sensor heats up to 1130 °C in slightly over one minute. As shown in Fig. 5.9(a), both the differential response and the slug response of the HTHFS are significant, and the HHF combination of the two components greatly improves the measurement result.

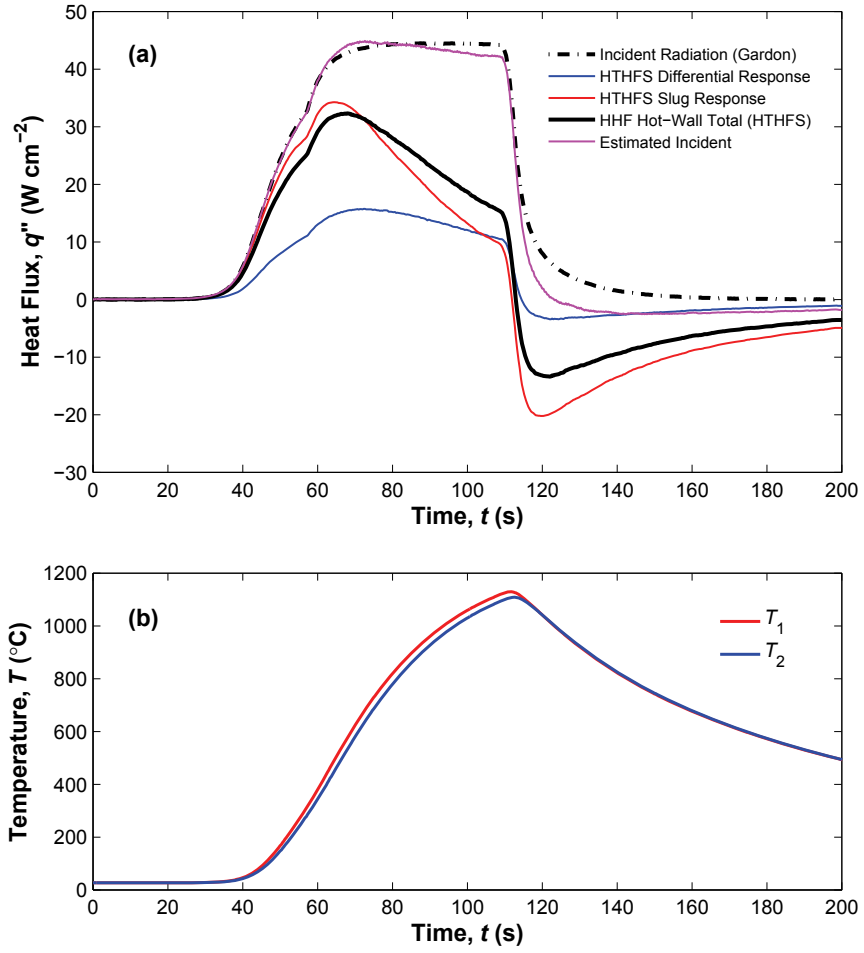

Figure 5.9: Case 3 heat flux and temperature data. The HTHFS mounted in a low thermal conductivity fibrous alumina insulation board. (a) Heat flux versus time. (b) Sensor temperature versus time.

The predicted incident heat flux agrees well with the Gardon measurement, especially consid-

ering the challenges of measuring heat flux in an insulating material. The incident heat flux predicted from the HTHFS measurements is within 8% of the incident heat flux measured by the water-cooled Gardon sensor during heating. The discrepancy between the predicted incident heat flux and the measured incident heat flux is greater on cool-down, and this is thought to be caused by radial heat transfer around the HTHFS sensing area.

5.7 Conclusions

This paper outlines the installation and use of the HTHFS in several different thermal scenarios. A flat plate heater system has been used to simulate high heat fluxes representative of those experienced by vehicles during hypersonic flight. The sensitivity and specific heat of the HTHFS are modeled as a function of temperature based on calibration data and material property data. The HHF data processing scheme [49] has been used to interpret measurements made by three different HTHFS under three very different thermal scenarios. When the HTHFS is mounted on an efficient heat sink, the calibrated thermopile output from the sensor provides a good measurement of the total heat flux through the sensor's surface. When the HTHFS is mounted on an inefficient heat sink (insulator), the calibrated thermopile output from the sensor does not provide a good measurement of the total heat flux, whereas the slug calorimeter response of the sensor provides a better measure of the total heat flux. In all cases, the HHF method provides a better measurement of the total heat flux through the HTHFS surface than the individual thermopile or slug responses do.

5.8 Acknowledgments

Funding for this work was provided by NASA through NRA and GSRP grants.

Chapter 6

Conclusions and Recommendations for Future Work

6.1 Research Conclusions

The first prototype transfer calibration system for high temperature heat flux sensors was successfully demonstrated in Chapter 2. Initial results provided useful information for further system improvement and optimization, which was presented in Chapter 3. This secondary calibration system is small, inexpensive, simple to operate, and the calibration method for high temperature heat flux sensors has an expanded uncertainty of $\pm 6\%$ for sensor temperatures in the range of $300 - 850$ °C. This calibration technique can be used on almost any type of spatial temperature gradient sensor, as demonstrated through calibrations performed on Virginia Tech's HTHFS and Mesoscribe's DWHFS. The methodology outlined in Chapters 2 and 3 can be followed to succesfully implement a high temperature calibration system with relatively low uncertainty and low cost.

In Chapter 4 the in-cavity method for primary calibration of heat flux sensors has been adapted for high temperature heat flux sensors. The "adaptation" simply involves the custom design of a cooling body (for the sensor to be calibrated) which uses air instead of water. The blackbody heater system used for this calibration is a typical model furnace which is used at several facilities in the United States for calibration of optical pyrometers. No customization of the furnace is required for the in-cavity calibration of heat flux sensors. For facilities equipped with a furnace similar to the one described in Chapter 4, implementation of the in-cavity calibration method for high temperature heat flux sensors is relatively straightforward.

Measurement of heat flux at high temperature requires careful implementation of sensors in test fixtures and appropriate interpretation of measurements made by the sensors during testing. The procedures outlined in Chapter 5 serve as a guideline for installation and use of the HTHFS in thermal research. The general sensitivity versus temperature trend for

the HTHFS was determined from calibrations performed in Chapters 2-4, and is in good agreement with the theoretical trend. The HHF method [49] is used to calculate the total heat flux through the sensor's surface during transient thermal testing. The HHF method accounts for the heat flow through the sensor and the heat storage in the sensor, and thus renders the HTHFS virtually insensitive to the material on which it is mounted.

6.2 Recommendations for Future Work

The work presented here provides the baseline experimental methods for calibration and implementation of heat flux sensors in extreme thermal environments. Future research in sensor design, calibration, and implementation will ensure that sensors like the HTHFS play a critical role in the evaluation of thermal systems. The two high temperature calibration methods presented in this work can be further improved to reduce the overall calibration uncertainty through the use of computational analysis software. The learning curve associated with FEA and CFD software can be steep, however, the benefits of rapid design evaluation is worth the cost. Convection is a major source of uncertainty in both the in-cavity primary calibration and the secondary transfer calibration. Some experimental methods have been presented here to assess or limit the effects of convection on the calibrations, however, no in-depth computational analysis has been performed.

The current HTHFS design is limited by the manufacturing process. It is essential that these sensors are miniaturized, without sacrificing durability. The serpentine sensor pattern is very simple, and can be tuned for almost any measurement scenario. Computational modeling can be used to improve the thermopile design (junction pattern, amount of one material versus another, sensor isolation layer or potting material) and the sensor housing design. The heat flux distortion caused by the presence of the sensor in different installation configurations must be addressed, both computationally and experimentally. The material, size, and shape of the thermopile isolation layer (potting material surrounding the thermopile) can be tuned to limit the effects of three-dimensional heat flux distortion in the sensor when installed in different types of measurement scenarios (i.e. thermal insulator, conductor, anisotropic materials, etc.). Sensor surface coatings that can withstand extreme thermal environments and have well defined/researched optical properties should also be investigated. The Zynolyte high temperature flat black paint appears to be a good candidate for sensor coating, however, in all of the analysis presented here, the emissivity was assumed constant (independent of wavelength and temperature). Painted samples (before and after high temperature curing) should be optically analyzed using any available techniques.

Bibliography

[1] C. A. Pullins, T. E. Diller, In situ high temperature heat flux sensor calibration, Int. J. Heat Mass Transfer 53 (2010) 3429–3438.

[2] C. A. Pullins, T. E. Diller, Adaptation of the in-cavity calibration method for high temperature heat flux sensors, Int. J. Heat Mass Transfer(in press).

[3] C. A. Pullins, T. E. Diller, Uncertainty reduction in the transfer calibration method for high temperature heat flux sensors, Int. J. Heat Mass Transfer(submitted for review).

[4] Y. S. Touloukian, Specific heat: metallic elements and alloys, Vol. 4 of Thermophysical properties of matter, IFI/Plenum, New York, 1970.

[5] Y. S. Touloukian, Specific heat: nonmetallic solids, Vol. 5 of Thermophysical properties of matter, IFI/Plenum, New York, 1970.

[6] T. E. Diller, Heat flux, in: J. G. Webster (Ed.), The Measurment, Instrumentation, and Sensors Handbook, CRC Press, Boca Raton, FL, 1999, Ch. 34, pp. 34.1–15.

[7] Standard test method for measuring heat flux using flush-mounted insert temperature-gradient gages, DOI: 10.1520/E2683-09, ASTM International, West Conshohocken, PA, 2009, www.astm.org (ASTM Standard E2683, 2009).

[8] Standard test method for measuring heat flux using surface-mounted one-dimensional flat gages, DOI: 10.1520/E2684-09, ASTM International, West Conshohocken, PA, 2009, www.astm.org (ASTM Standard E2684, 2009).

[9] A. R. Gifford, D. O. Hubble, C. A. Pullins, T. E. Diller, S. T. Huxtable, A durable heat flux sensor for extreme temperature and heat flux environments, AIAA J. Thermophysics and Heat Transfer 24 (1) (2010) 69–76.

[10] T. E. Diller, Advances in heat flux measurements, Advances in Heat Transfer 23 (1993) 279–368.

[11] W. M. Pitts, A. V. Murthy, J. L. de Ris, J. Filtz, K. Nygard, D. Smith, I. Wetterlund, Round robin study of total heat flux guage calibration at fire laboratories, Fire Safety Journal 41 (2006) 459–475.

[12] B. K. Tsai, C. E. Gibson, A. V. Murthy, E. A. Early, D. P. DeWitt, R. D. Saunders, NIST measurment services: Heat flux sensor calibration, NIST special publication 250–65, NIST (2004).

[13] A. V. Murthy, G. T. Fraser, D. P. DeWitt, Experimental in-cavity radiative calibration of high-heat-flux meters, AIAA J. Thermophysics and Heat Transfer 20 (2) (2006) 327–335.

[14] R. L. Alpert, L. Orloff, J. L. de Ris, Angular sensitivity of heat flux gages, in: L. A. Gritzo, N. J. Alvares (Eds.), Thermal Measurements: The Foundation of Fire Standards, ASTM STP 1427, 2002.

[15] S. Jiang, T. J. Horn, V. K. Dhir, Numerical analysis of a radiant heat flux calibration system, Proceedings of the ASME Heat Transfer Division 361 (5) (1998) 609–616.

[16] F. P. Incropera, D. P. DeWitt, Fundamentals of Heat and Mass Transfer, 5th Edition, John Wiley and Sons, Inc., Hoboken, NJ, 2002, pp. 814–815, 917.

[17] Y. S. Touloukian, Thermal conductivity: metallic elements and alloys, Vol. 1 of Thermophysical properties of matter, IFI/Plenum, New York, 1970.

[18] W. D. Kingery, H. K. Bowen, D. R. Uhlmann, Introduction to Ceramics, 2nd Edition, John Wiley, New York, 1976.

[19] R. G. Munro, Evaluated material properties for a sintered alpha-alumina, J. American Ceramic Society 80 (8) (1997) 1919–1928.

[20] N. P. Bansal, D. Zhu, Thermal conductivity of zirconia-alumina composites, Ceramics International 31 (2005) 911–916.

[21] M. C. Croarkin, W. F. Guthrie, G. W. Burns, M. Kaeser, G. F. Strouse, Temperature-electromotive force reference functions and tables for the letter-designated thermocouple types based on the ITS-90, NIST monograph 175, National Institute of Standards and Technology (1993).

[22] S. Schneider, J. Straub, Laminar natural convection in a cylindrical enclosure with different end temperatures, Int. J. Heat Mass Transfer 35 (2) (1992) 545–557.

[23] V. Kurian, M. N. Varma, A. Kannan, Numerical studies on laminar natural convection inside inclined cylinders of unity aspect ratio, Int. J. Heat Mass Transfer 52 (2009) 822–838.

[24] R. Siegel, J. R. Howell, Thermal Radiation Heat Transfer, 4th Edition, Taylor and Francis, New York, NY, 2002, pp. 208, 218–219.

[25] B. N. Taylor, C. E. Kuyatt, Guidelines for evaluating and expressing the uncertainty of NIST measurement results, NIST technical note 1297, NIST (1994).

[26] R. S. Figliola, D. E. Beasley, Theory and Design for Mechanical Measurements, 3rd Edition, John Wiley and Sons, Inc., Hoboken, NJ, 2000, pp. 161–163.

[27] Fire tests – Calibration and use of heat flux meters – Part 2: Primary calibration methods, First Edition, International Organization for Standardization, Geneva, Switzerland (ISO 14934-2:2006).

[28] Fire tests – Calibration and use of heat flux meters – Part 3: Secondary calibration method, First Edition, International Organization for Standardization, Geneva, Switzerland (ISO 14934-3:2006).

[29] Fire tests – Calibration and use of heat flux meters – Part 4: Guidance on the use of heat flux meters in fire tests, First Edition, International Organization for Standardization, Geneva, Switzerland (ISO/TS 14934-4:2007).

[30] MesoScribe Technologies Inc., URL http://www.mesoscribe.com/products/heat-flux-sensors/.

[31] C. T. Kidd, C. G. Nelson, How the Schmidt-Boelter gage really works, in: 41st Int. Instrumentation Symposium, Research Triangle Park, NC: ISA, 1995, pp. 347–368.

[32] A. V. Murthy, A. V. Prokhorov, D. P. DeWitt, High heat-flux sensor calibration: a Monte Carlo modeling, AIAA J. Thermophysics and Heat Transfer 18 (3) (2004) 333–341.

[33] O. Raghu, J. Philip, Thermal properties of paint coatings on different backings using a scanning photo acoustic technique, Measurement Science and Technology 17 (2006) 2945–2949.

[34] Y. S. Touloukian, D. P. DeWitt, Thermal radiative properties: metallic elements and alloys, Vol. 7 of Thermophysical properties of matter, IFI/Plenum, New York, 1970, p. 1216.

[35] A. F. Robertson, T. J. Ohlemiller, Low heat-flux measurements: some precautions, Fire Safety Journal 25 (1995) 109–124.

[36] H. C. de Groh, M. Kassemi, Effect of radiation on convection in a top-heated enclosure, AIAA J. Thermophysics and Heat Transfer 7 (4) (1993) 561–568.

[37] M. A. Kuczmarski, S. A. Gokoglu, Buoyancy suppression in gases at high temperatures, International Journal of Heat and Fluid Flow 28 (3) (2007) 496 – 511.

[38] M. Kandula, G. F. Haddad, R.-H. Chen, Three-dimensional thermal boundary layer corrections for circular heat flux gauges mounted in a flat plate with a surface temperature discontinuity, Int. J. Heat and Mass Transfer 50 (2007) 713–722.

[39] C. E. Brookley, W. E. Llewellyn, Determination of blackbody radiance at temperatures above 2300 °C, in: J. F. Schooley (Ed.), Temperature: its measurement and control in science and industry, Vol. 6, American Inst. of Physics, New York, 1992, pp. 1195–1199.

[40] T. J. Horn, A. N. Abdelmessih, Experimental and numerical characterization of a steady-state cylindrical blackbody cavity at 1100 degrees celsius, NASA/TM-2000-209022, NASA (2000).

[41] A. N. Abdelmessih, T. J. Horn, Experimental and computational characterization of high heat fluxes during transient blackbody calibrations, ASME J. Heat Transfer 132 (2) (2010) 24–36.

[42] Thermogage Inc., Frostburg, MD, Thermogage operation manual for model 48 kW calibration furnace (1991).

[43] S. W. Churchill, H. H. S. Chu, Correlating equations for laminar and turbulent free convection from a vertical plate, Int. J. Heat Mass Transfer 18 (1975) 1323.

[44] R. E. Bolz, G. L. Tuve, CRC Handbook of Tables for Applied Engineering Science, 2nd Edition, CRC Press, Boca Raton, FL, 1985, p. 56.

[45] M. D. Griffin, J. R. French, Space Vehicle Design, 2nd Edition, American Institute of Aeronautics and Astronautics, Inc., Washington D.C., 2004.

[46] Fundamental aeronautics hypersonics project reference document, Tech. rep., NASA Aeronautics Research Mission Directorate, United States, URL http://www.aeronautics.nasa.gov/nra_pdf/hyp_proposal_c1.pdf (2006).

[47] Standard test method for measuring heat flux using a copper-constantan circular foil, heat-flux transducer, DOI: 10.1520/E0511-07, ASTM International, West Conshohocken, PA, 2007, www.astm.org (ASTM Standard E511, 2007).

[48] Standard test method for measuring heat-transfer rate using a thermal capacitance (slug) calorimeter, DOI: 10.1520/E0457-08, ASTM International, West Conshohocken, PA, 2008, www.astm.org (ASTM Standard E457, 2008).

[49] D. O. Hubble, T. E. Diller, A hybrid method for measuring heat flux, ASME J. Heat Transfer 132 (3) (2010) 1–8.

Appendix A

HTHFS Construction

This appendix includes instructions for constructing a standard model HTHFS.

A.1 Thermopile Construction

The first step in thermopile construction is dicing long strips of each material. The strips are put together in a jig and spot welded. Individual thermopiles are diced to length (from the long thermopile) using the low speed dicing saw. The number and size for each piece of material in a typical thermopile strip is:

1. Chromel (6): 1.33 in $\times$ 0.101 in $\times$ 0.034 in
2. Alumel (5): 1.33 in $\times$ 0.188 in $\times$ 0.012 in
3. Zirconia-Toughened Alumina ZTA (10): 1.33 in $\times$ 0.095 in $\times$ 0.010 in

The length dimension (same for each material) is not critical, however, the bulk sheet of chromel is $\approx$ 1.33 in wide, and therefore this is a convenient dimension for the thermopile strip. Thermopile materials, the welding jig, and a thermopile strip are shown in Fig. A.1.

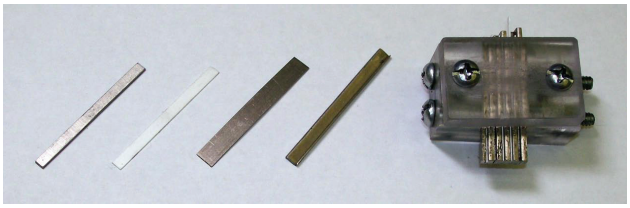

Figure A.1: From right to left: chromel, zirconia-toughened alumina (ZTA), unbent alumel, bent alumel, and jig for welding thermopile strip together.

Once all of the individual thermopile pieces are diced, bend the alumel pieces using a custom clamp assembly. The clamp assembly consists of two clamp plates, two guide plates, two dies, and one plate for hammering the dies through the guides. Fasten an unbent piece of alumel between the two clamp plates, as shown in Fig. A.2. Fasten the outer guide plates to the clamp plates, and hammer the dies through the guides in opposite directions, as shown in Fig. A.3. Align the thermopile materials using the acrylic jig, as shown in Fig. A.4, and weld the assembly together. The spot welder settings for this step are "short pulse" and $50 - 75$ W $\cdot$ s (high range). Use the machined/filed copper electrodes (the electrodes tips are thin enough to weld each junction without arcing to a neighboring junction), and set the weld pressure somewhere between 5 and 8 by turning the knob on top of the spot welder head. Manipulate the thermopile strip in the jig to spot weld along the entire length of each element. The thermopile strip should hold together tight enough so that the ceramic strips stay in place.

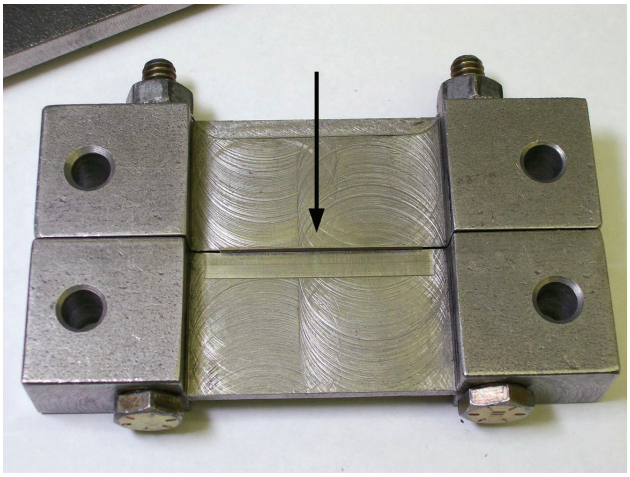

Figure A.2: Alumel bending clamps side view (outer guide plates are not installed). The arrow shows the direction for the die to bend the alumel piece.

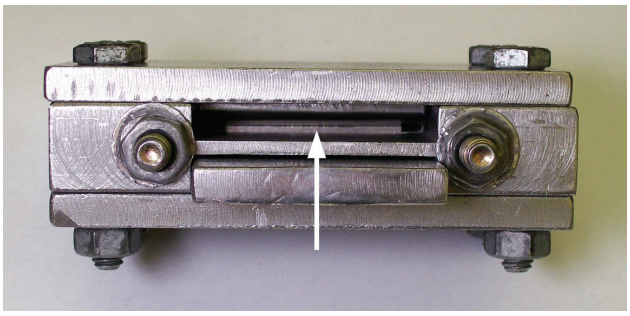

Figure A.3: Alumel bending clamp assembly top view (both dies in place). The arrow shows the unbent piece of alumel.

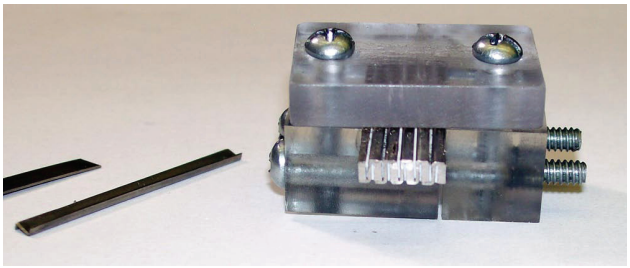

Figure A.4: Left: Bent strip of alumel. Right: Long thermopile (5 bent alumel strips, 6 chromel strips, 10 ZTA strips) assembled in jig for spot welding.

After welding, dice the individual thermopiles to the desired length (using the metal dicing blade) from the long strip. A typical thermopile has dimensions of $0.38\,\text{in} \times 0.20\,\text{in} \times 0.125\,\text{in}$. Each individual thermopile should be deburred, sanded flat/smooth by hand, and cleaned with acetone or alcohol. A finished thermopile is pictured in Figs. A.5-A.6.

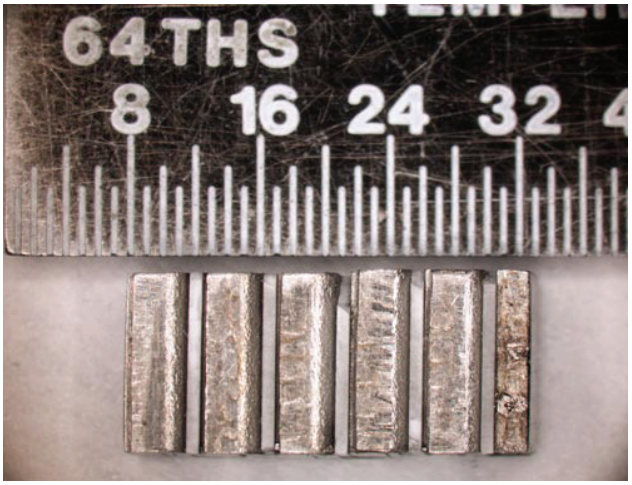

Figure A.5: Top view of diced thermopile.

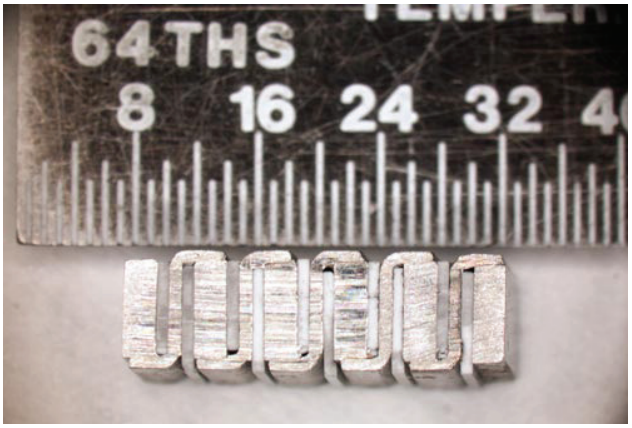

Figure A.6: Side view of diced thermopile.

A.2 Strain Relief Tube Preparation

An inconel tube is used to provide strain relief for the lead wire cable. The tube is splayed at one end, and slid over the lead wire cable. After the leads are welded to the thermopile, the strain relief tube is welded first to the cable sheath, and then to the inconel sensor housing. Use the dicing saw and a steel jig to cut the strain relief tube. Fasten the steel jig to the dicing saw movable arm, and secure a section of inconel tube in the jig using the set screw. The jig is used to both cut the tube to length and to cut the slot down the center of the tube (the jig is drilled and tapped in two locations for these two different cuts). First cut the strain relief tube to a length of 0.75 in, and then cut a 0.375 in slot lengthwise in the tube, as shown in Figs. A.7-A.8. After cutting, deburr all edges by hand with sandpaper.

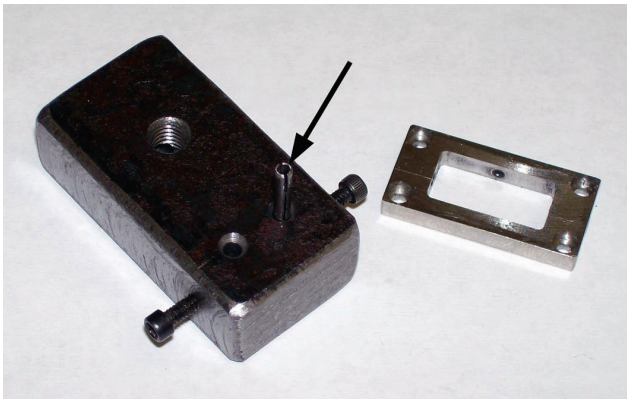

Figure A.7: Left: Jig for dicing inconel strain relief tubes. Right: HTHFS inconel housing (1.0 in $\times$ 0.5 in $\times$ 0.125 in).

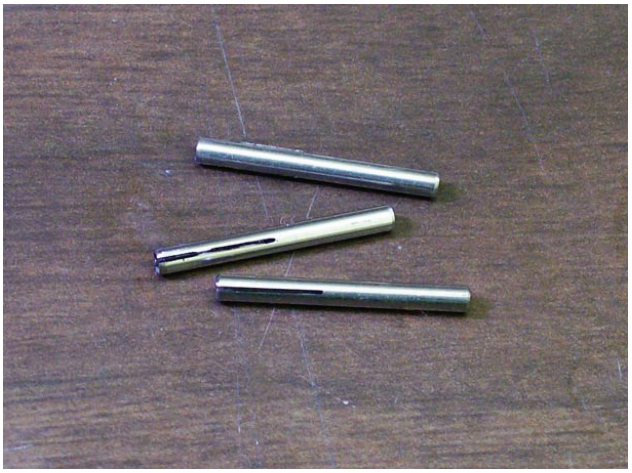

Figure A.8: Inconel strain relief tubes diced to length (0.75 in) with 0.375 in axial slot.

Bend the "arms" on the split end of the tube to $\approx 45°$ using needle nose pliers, as shown in Fig. A.9. Flatten and bend the arms to 90° using the table-top vise, as shown in Fig. A.10.

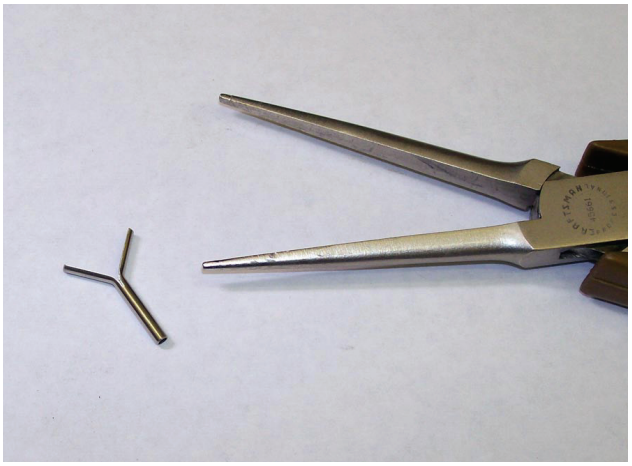

Figure A.9: Strain relief tube showing arms bent to $\approx 45°$ with needle nose pliers.

The bend point for each arm must be in the same axial location so that the strain relief tube arms sit flat on the sensor housing, as shown in Fig. A.11. Run a 1/16 in drill through the strain relief tube to remove any burrs. This step ensures that the tube will slide over the lead wire cable easily.

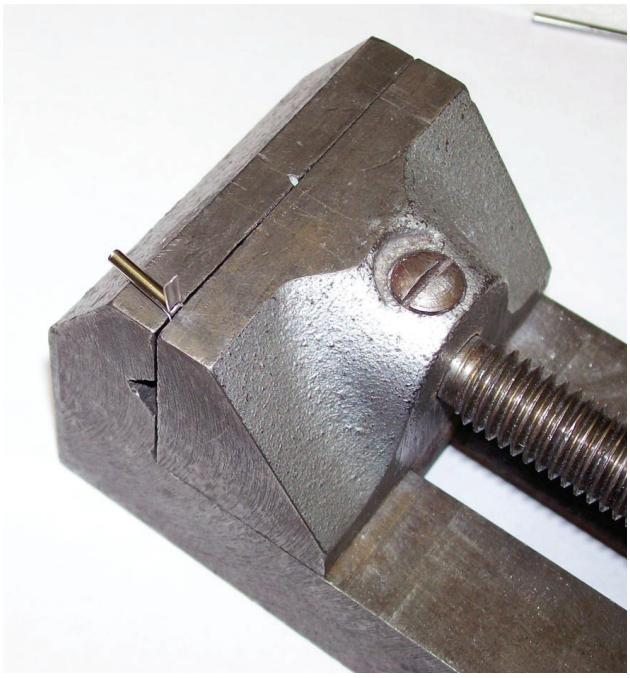

Figure A.10: Strain relief tube showing arms bent to 90° with vise.

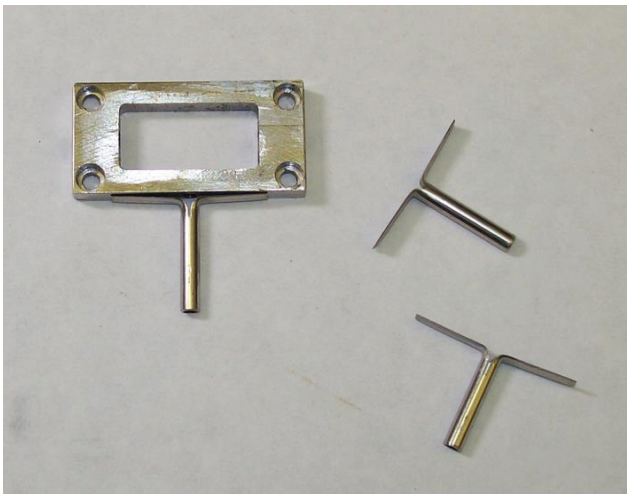

Figure A.11: Finished strain relief tubes and inconel housing.

A.3 Lead Wire Preparation: Thermopile End

The dual thermocouple cable is stripped using the thermocouple wire stripper mounted in a hand drill. Secured the cable in a vise, with ≈ 1 in of the cable hanging out of the end of the vise. Locate the tool over the end of the sheath and apply slight pressure on the tool while turning it clockwise. After the cut has started, the tool will self-feed until it runs against the edge of the vise. Slip the tool off over the exposed wires. The four exposed conductors should be ≈ 0.75 in long. If the very ends of the conductors are kinked, clip them off with snips or heavy duty scissors. The conductors should be very straight, and should not be twisted together. If the conductors are twisted severely, clip them off and start over (this process takes practice and patience). Clean each conductor with alcohol wipes to remove the mineral insulation.

Slip the strain relief tube (unsplayed end first) over the lead wire cable sheath until the bent arms are level with the end of the sheath (where the exposed conductors start), as shown in Fig. A.12. Dice a short (≈ 0.050 in long) four-bore ceramic tube on the dicing saw using the ceramic blade. The four-bore ceramic tube ensures that the conductors do not electrically short to the cable's inconel sheath. Slide the short four-bore ceramic tube over the conductors, taking care not to cross the wires. Break four single-bore ceramic tubes using tweezers. The single-bore ceramic tubes should be ≈ 0.125 in long, and free of sharp edges (this step takes some practice). The single-bore ceramic tubes prevent the four conductors from electrically shorting to each other or to the inconel sensor housing. Slide a single-bore ceramic tube over each conductor. Once this step is complete, the lead wire assembly should look like the one shown in Fig. A.12. With a multimeter, check to make sure the conductors are not shorted to the inconel cable sheath.

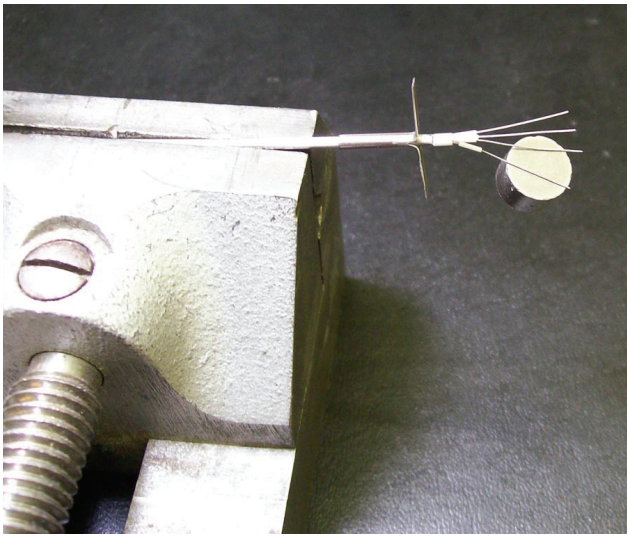

Figure A.12: Inconel sheathed dual thermocouple cable stripped to expose conductors. The strain relief tube, four-bore ceramic tube, and four single-bore ceramic tubes are all installed. A magnet (as shown) is used to differentiate between the alumel conductors (magnetic) and the chromel conductors (non-magnetic).

A.4 Thermopile Installation

Using a magnet, as shown in Fig. A.12, determine which two conductors are alumel (magnetic). The two alumels should be next to each other (if they are caddy corner it is likely the wires are twisted near the cable sheath - if this is the case, start over). Mark the tip of the two alumel wires with a sharpie. Feed the wires through the hole in the bottom of the inconel sensor housing. Bend and rout the wires so that a chromel-alumel pair goes to each side of the housing (do not crisscross wires), as shown in Fig. A.13.

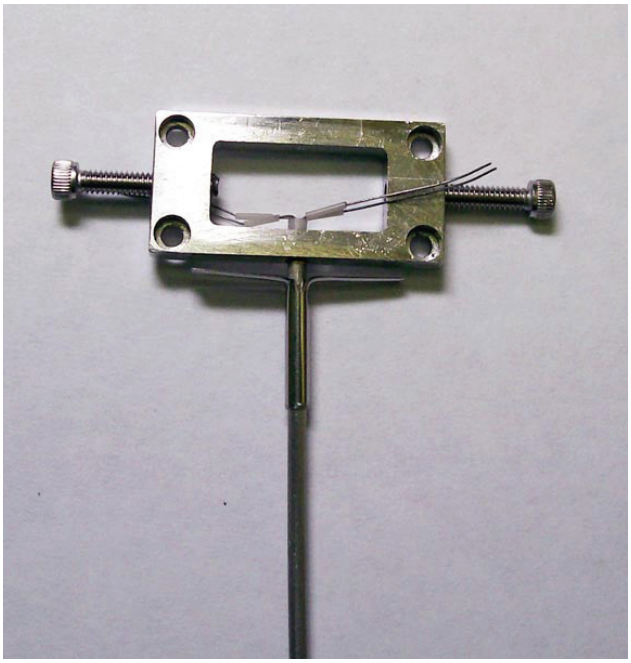

Figure A.13: The lead wire assembly is fed through the hole in the the inconel housing (top face shown). By convention, the "top" thermocouple pair is on the right when viewing the sensor housing top face.

Center a thermopile in the housing and secure it in place using set screws (preferred) or machine screws. Place small ZTA ceramic plates in between the screws and the thermopile for electrical insulation, as shown in Fig. A.14.

In preparation for welding each lead wire to the thermopile, use tape to position each lead wire individually. Weld each wire separately (do not twist the wires together). The spot welder settings for this step are "short pulse" and $15 - 20$ W $\cdot$ s (low range). Use the machined/filed copper electrodes (clean often with file/sandpaper), and set the weld pressure somewhere between 0 and 2 by turning the knob on top of the spot welder head. The chromel piece on which the leads are welded to is wide enough for the two lead wires to fit side by side, as shown in Fig. A.15. Weld at three or four spots along each lead wire, careful not to weld too close to the end of the thermopile. When one thermocouple pair is welded to

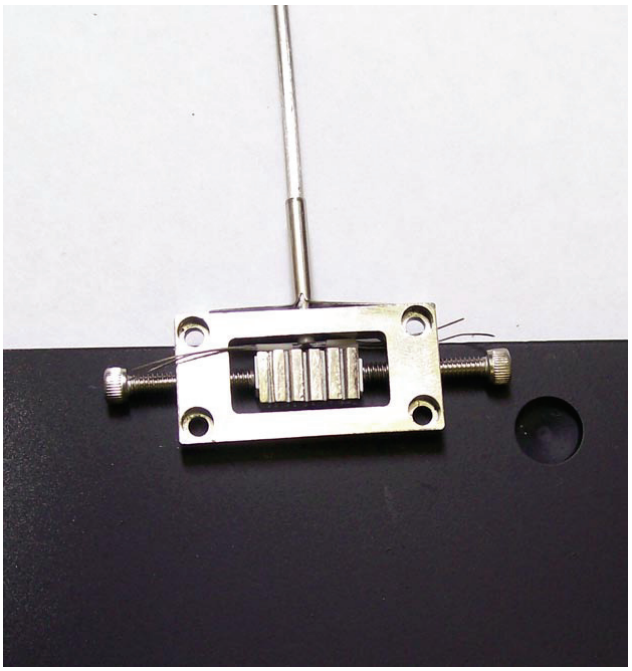

Figure A.14: Machine screws (shown) or set screws (preferred) are used to secure the thermopile in the housing; small strips of ZTA are used to electrically insulate the thermopile from the housing. One thermocouple pair is routed to the top side of the thermopile, and the other thermocouple pair is routed to the bottom side of the thermopile.

the thermopile, clip the excess wire with cutters or small scissors. Flip the sensor over and repeat the process for the second thermocouple pair. After welding, check to make sure the thermopile is not electrically shorted to the housing.

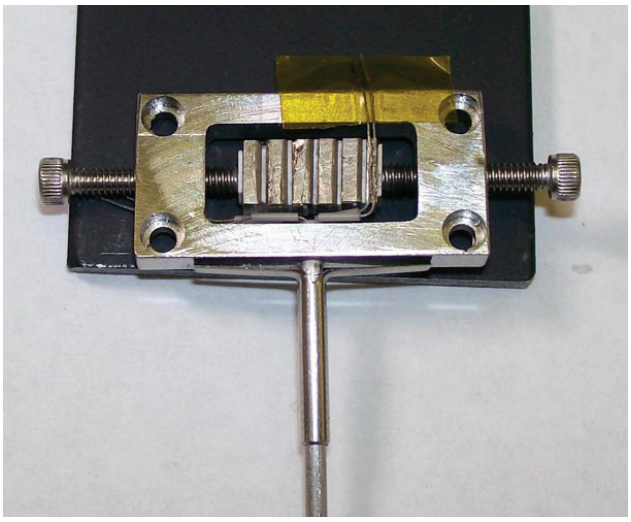

Figure A.15: Tape is used to hold the thermocouple lead wires in place for welding. The excess lengths of lead wire are clipped off after welding.

After the lead wires are welded to the thermopile, the inconel strain relief tube is welded to the sheath and then to the housing. Position the strain relief tube as desired, without twisting the lead wire cable or housing. The spot welder settings for this step are "short pulse" and $25 - 35$ W $\cdot$ s (low range). Use the rounded end copper electrodes, and set the weld pressure somewhere between 5 and 8 by turning the knob on top of the spot welder head. Weld the strain relief tube to the cable sheath at seven or eight spots along the tube. Reposition the electrodes, and weld the strain relief tube arms to the housing at several spots along each arm, as shown in Fig. A.16. Twist the housing relative to the lead cable to make sure the welds are strong. Make sure the thermopile is centered well. It is critical to make sure that the thermopile is flat and not protruding out of the housing (especially the lead wires).

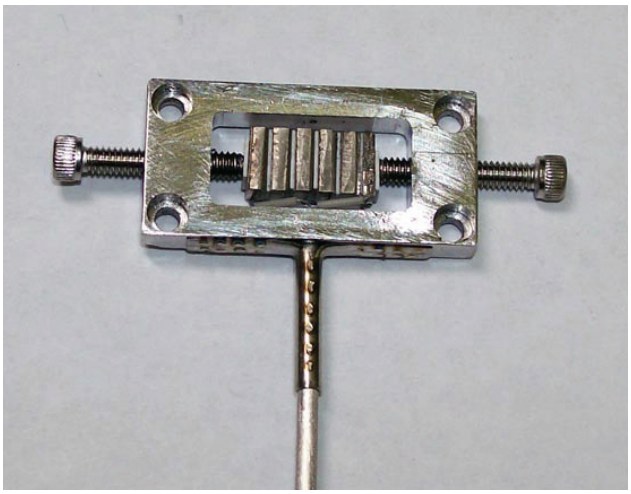

Figure A.16: Sensor assembly after lead wire and strain relief tube spot welding.

A.5 Sensor Potting

The void spaces between the thermopile and housing are filled with a castable ceramic potting material. Aremco Ceramacast 675-N powder is mixed with water to produce a mortar-like paste. After air drying and curing, the paste hardens. Use a dropper to add one drop of water at a time to a small pile of ceramic powder while continuously mixing. The ratio of water to powder is specified by weight by the manufacturer, but the easiest way to get the right ratio is by adding small amounts of water to the powder until the mixture holds together like mortar. The mixture should be thick and should not flow freely. Fill the void areas of the sensor/housing with the ceramic paste. Continuously work the mixture over the top of the thermopile and into the void areas from both sides to eliminate any air pockets. Pile up excess paste over the sensing area; the excess is sanded away after curing. If set screws were used in the housing instead of machine screws, fill the void area behind the set screw with the paste. This process takes about five to ten minutes until the paste sets up enough and does not flow. There must be enough ceramic paste to ensure the sensor assembly is a uniform thickness (thickness of the housing) after sanding; voids form local air pockets when the sensor is installed on a flat surface (not desired).

Allow the paste to air dry for at least 8 hours. Place the sensor in an oven to cure the ceramic paste. Cure at 200 °F (slightly below water boiling point) for three to four hours followed by two to three hours at 250 °F (above water boiling point). Allow the sensor to cool down slowly in the oven, after the oven is turned off. After cool down, sand away the excess ceramic paste until the potted area is flush with the sensor housing. Sand in stages: start with 220 or 320 grit sandpaper, and switch to 600 grit sandpaper to finish. Lay the sandpaper on a flat surface and move the sensor over the sandpaper to remove material. Keep the sensor as flat as possibly during sanding. Some of the thermopile may become visible during sanding (see Fig. A.17), but the lead wires should never become visible. If machine screws were used to secure the thermopile, grind them off using a Dremel cutoff wheel (make sure to cut in a direction such that the rotation of the cutoff wheel serves to tighten the screw) and file/sand them flush with the housing.

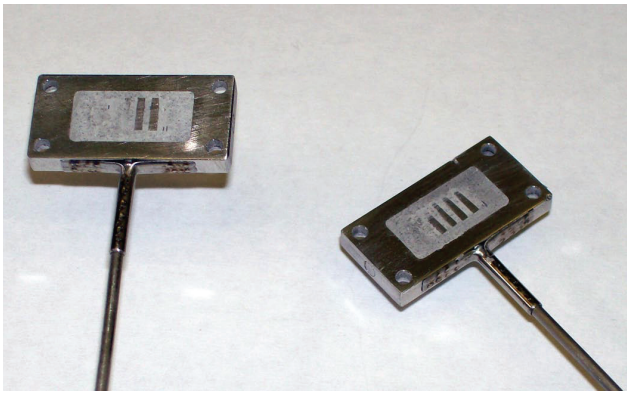

Figure A.17: Two sensors shown after the potting material (Aremco Ceramacast 675-N) was cured and sanded flush.

A.6 Lead Wire Preparation: Connector End

Strip the connector end of the lead wire cable, as described in §A.3. Mark the end of the two alumels, as described in §A.4. Check the resistance across the leads to make sure the sensor works correctly: chromel-chromel should have the highest resistance, alumel-alumel should have the lowest resistance, and both chromel-alumel resistances should be somewhere in between. No conductor should be shorted to the inconel cable sheath.

Cut four Kapton tubes to a length of 7/16 in. Mix a small amount of Loctite Hysol D609 5-minute epoxy, and apply it to the conductors near the sheath. Slide a Kapton tube over each conductor, and wipe away excess epoxy. Let the epoxy set up and dry for ten minutes. Slide the connector mounting bracket locking nut and brass collet over the cable, and kink each thermocouple pair outward, as shown in Fig. A.18. Slide the connector mounting bracket over cable sheath, and rout a thermocouple pair to each side of the bracket (the kinks in the wires should help in this step). Tighten the locking nut to the connector mounting bracket so that the bracket is fastened tightly to the cable sheath. Push the two brass nuts out of one thermocouple mini-plug connector, and remove the screws from two connector faceplates. Install the two mini-plug connectors (screw the lead wires to the terminals, make sure there are no electrical shorts), and fasten them together to the mounting bracket using the long screws provided with the mounting bracket. Make sure the wires are not crisscrossed. If installed correctly, only one mini-plug connector white label will be visible, and the like metals will be on the same side (not caddy corner), as shown in Fig. A.19.

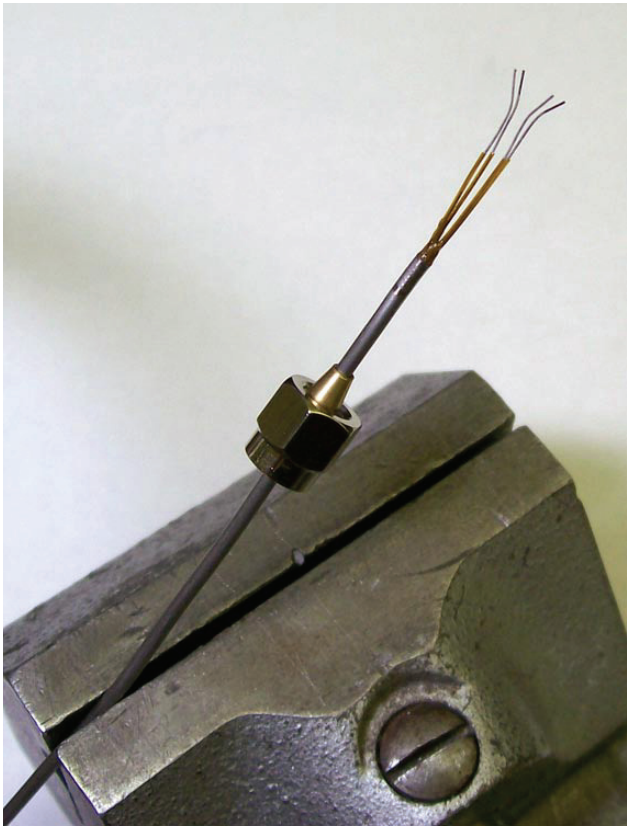

Figure A.18: Connector end of lead wire cable. The individual conductors are sheathed with Kapton tubes, and the collet and locking nut for the connector mounting bracket is installed.

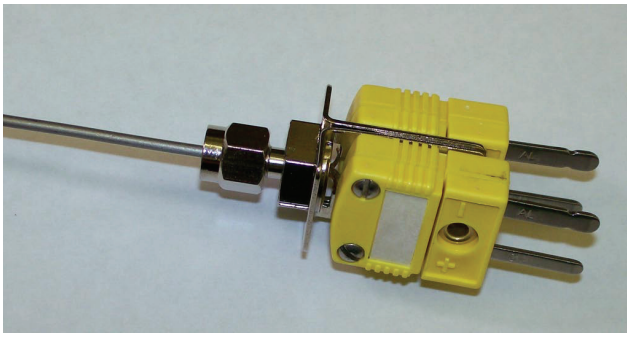

Figure A.19: Connector end of lead wire cable. The mini-plug thermocouple connectors and connector mounting bracket are installed.

A.7 Painting

Coat the sensing area with three thin layers of Zynolyte high temperature flat black paint. During painting, hold the sensor at least 10 in away from the spray nozzle. Allow five to ten minutes between each coating application. Allow the paint to dry for at least one day before handling or testing. A finished sensor is shown in Fig. A.20.

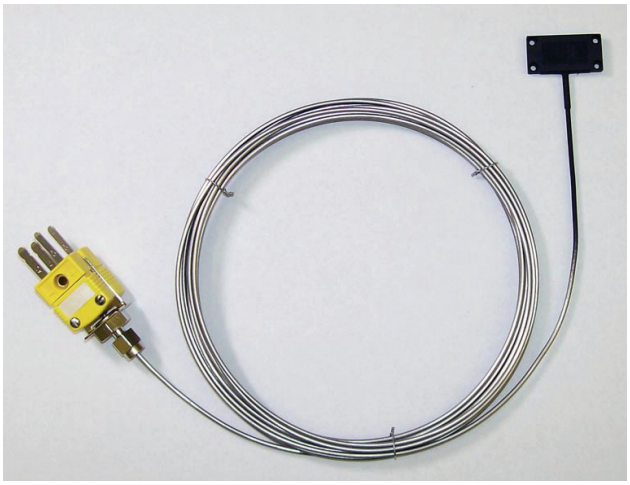

Figure A.20: Finished HTHFS; the sensing area is coated with Zynolyte high temperature flat black paint.

Appendix B

High Temperature Transfer Calibration Procedure

This appendix outlines the high temperature transfer calibration experimental setup and procedure.

B.1 Hot Plate Preparation

The hot plate base is made from stainless steel, and houses an inconel-sheathed electrical resistance heater. Six blind holes are drilled and tapped in the hot plate base for the faceplate to be mechanically fastened to the base. The faceplate is sanded and cleaned in preparation for welding (surface thermocouples and mounting straps) and painting. Sand the faceplate thoroughly with 220 grit sandpaper (the surface should be slightly rough to allow paint to adhere properly). Clean the faceplate and heat flux sensor with a lint-free wipe and acetone. A cleaned sensor (custom HTHFS) and faceplate (originally designed for Mesoscribe DWHFS) are shown in Fig. B.1.

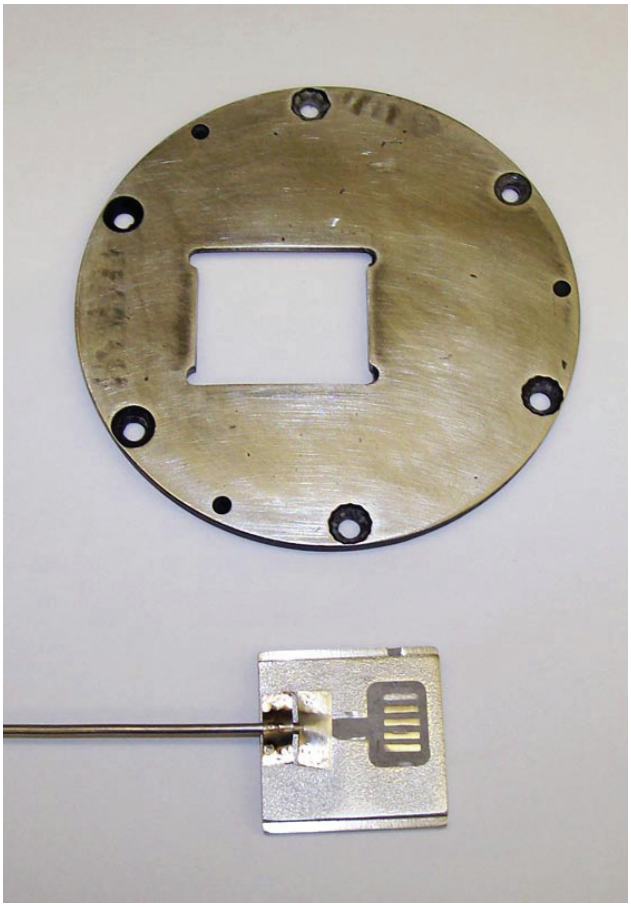

Figure B.1: Custom HTHFS designed to fit in the Mesoscribe hot plate mounting bracket.

Position the sensor in the faceplate so that the sensing area is centered. Weld surface thermocouples (N-type or K-type; match to the type the sensor uses) at three radial locations from the center of the sensor (3/8, 1/2, and 1 in), as shown in Fig. B.2. The spot welder settings for this step are "short pulse" and $10 - 15$ W $\cdot$ s (low range). Use the rounded end copper electrodes, and set the weld pressure somewhere between 2 and 4 by turning the knob

on top of the spot welder head. For a given thermocouple, weld each wire $\approx 1/8$ in apart (see Fig. B.2); the faceplate serves as the thermocouple intermediate metal. This method gives a better measurement of the true surface temperature. Sheath the thermocouple wires with ceramic tubes (metal wires should only touch the plate at the junction location), and run the wires along the surface of the faceplate. Fasten the thermocouple wires and the sensor lead wires down with stainless steel strips (0.003 in shim stock, cut to size with snips or heavy duty scissors) welded in a few locations (same welder settings), as shown in Fig. B.3.

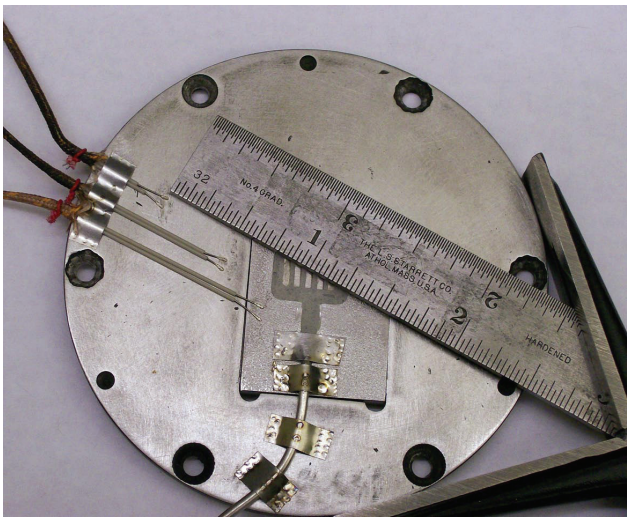

Figure B.2: HTHFS installed in the hot plate mounting bracket showing the location of the surface thermocouples.

Before the faceplate is mounted to the hot plate base, clean the blind holes in the hot plate base by running a $4-40$ tap through the threads. Coat the threads of the $4-40$ screws with copper anti-seize. Place the screws in the faceplate, in preparation for mounting the plate to the base. Apply a thin layer of Aremco Ceramabond 865 to the hot plate base surface. Make sure there is a mound of paste at the center of the plate where the sensor will be mounted (this ensures there is no air pocket under the sensor). This process must be quick as the Ceramabond sets up very quickly. Press the faceplate/sensor assembly against the hot plate base, ensuring the faceplate screws align with the holes in the base. Tighten the screws in a star pattern to spread the wet Ceramabond evenly; some paste will flow through the holes near the sensor and near the screws. Wipe any excess paste away with a paper towel. Allow the adhesive to dry for ≈ 4 hours before curing. Cure at 200 °F (93 °C) for 2 hours minimum.

After the ceramic adhesive is cured, paint the surface of the faceplate assembly with three coats of Zynolyte, using the same technique described in §A.7. The painted surface, prior to high temperature curing, should look like that shown in Fig. B.4.

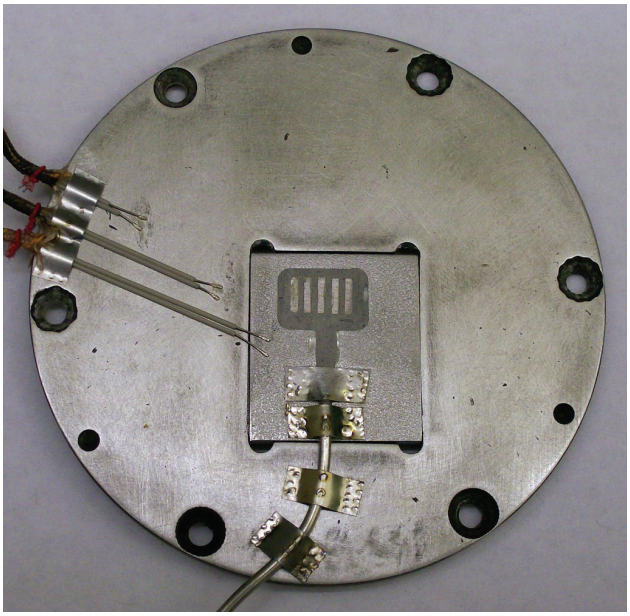

Figure B.3: HTHFS hot plate surface prepared for painting.

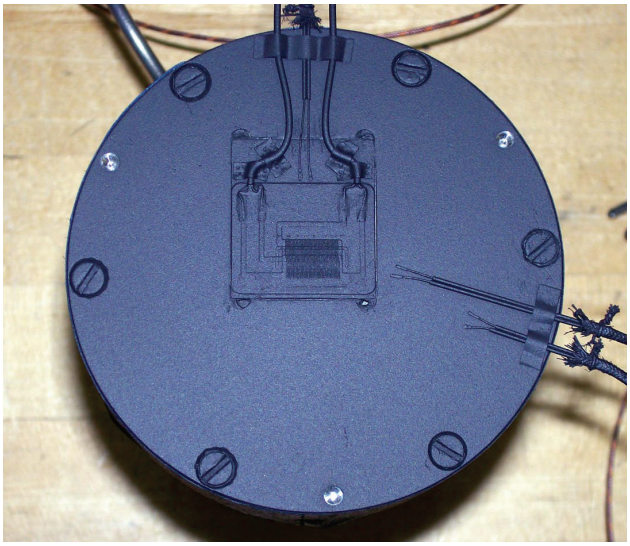

Figure B.4: Hot plate surface (with Mesoscribe DWHFS) after painting, prior to high temperature curing.

Allow the paint to dry overnight before high temperature curing. Surround all surfaces of the hot plate with thick insulation. The hot plate resistance heater is used for heat input. Monitor the temperature of the hot plate using the sensor and surface thermocouples. Connect the thermocouples to the data acquisition system, and use LabVIEW to display the measurements. Plug the heater into the variable transformer, which is used to regulate the voltage to the heater. Slowly ramp the hot plate up to 600 °C over the course of ≈ 2 hours. Hold at this temperature for $2 - 3$ hours, then very slowly ramp the temperature up to 700 °C. Hold at this temperature for 1 hour, then turn the heater off. Leave the insulation covering all hot plate surfaces so that the system cools down very slowly. The cured paint is slightly gray in appearance ($\epsilon = 0.8$), as shown in Fig. B.5.

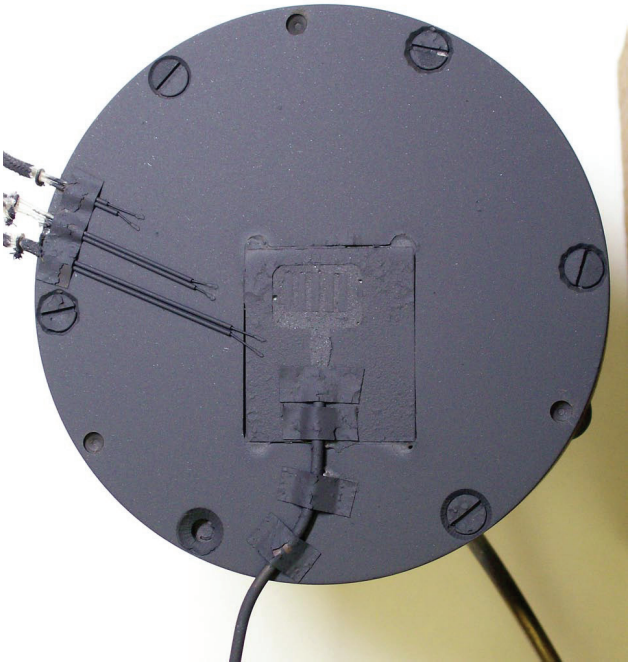

Figure B.5: Painted hot plate surface (with HTHFS) after high temperature curing.

B.2 Cold Plate Preparation

The cold plate houses the reference standard Schmidt-Boelter (SB) heat flux sensor. Before the sensor is mounted in the cold plate, spot weld two K-type thermocouples (nylon sheathed) to the cold plate surface, in the locations shown in Fig. B.6 (5/8, and 1 in from the center). Fasten the SB sensor in the cold plate with three screws; use spacers on the back side to make sure the sensor surface is flush with the surface of the cold plate. First, coat the surface of the cold plate with two layers of Zynolyte (allow to dry overnight), and then coat the surface with one layer of GE Aerocoat carbon soot (reference coating, $\epsilon = 0.98$).

Figure B.6: Cold plate with Schmidt-Boelter reference sensor installed. The surface is coated first with two layers of Zynolyte (as shown), and then with one layer of GE Aerocoat carbon soot (not shown).

B.3 Sidewall Tube Preparation

Instrument the $L = 0.5$ in (1.27 cm) machined stainless steel sidewall tube with five thermocouples, welded at different axial locations along the tube's inner surface, as shown in Fig. B.7. Clean the sidewall inner surface, but do not paint it. Allow the sidewall to oxidize during testing. The data processing code (see §C.1) accounts for the emissivity of the oxidized stainless sidewall.

B.4 Calibration Setup

The cold plate is sits on top of a piece of insulation which is placed on an aluminum table. This setup provides relief for the cold plate water lines. A slot is machined in both the

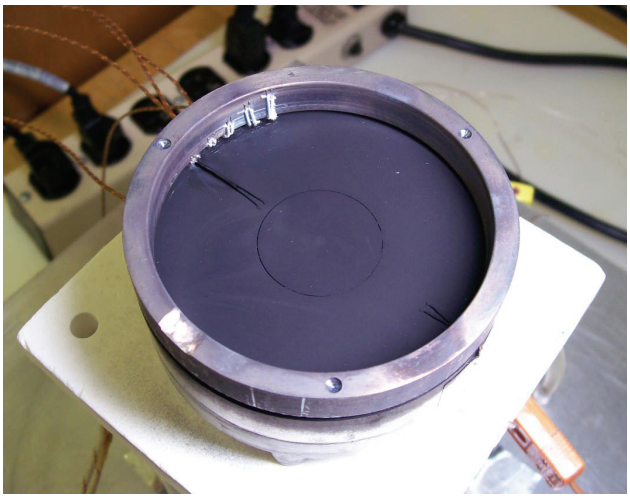

Figure B.7: $L = 0.5$ in (1.27 cm) stainless steel sidewall tube positioned on the cold plate with stainless steel bearings. The positioning bearings sit in blind holes drilled into the cold plate, hot plate, and sidewall tube surfaces. Five N-type thermocouples are welded at different axial locations along the sidewall tube's inner surface. The cold plate is shown with the GE Aerocoat carbon soot surface coating.

insulation and the aluminum table for the water lines and signal wires. Position the sidewall on top of the cold plate surface using three stainless steel spheres ($r = 0.125$ in) which sit in the blind holes drilled in the sidewall and the cold plate surface. When positioned correctly, there should be a small gap (0.063 in) between the cold plate and the sidewall. The gap provides space for the surface thermocouples to be routed outside of the calibration volume, and also limits axial conduction from the hot plate to the cold plate through the sidewall. Insulate the external curved surface of the cold plate and sidewall with 1.0 in thick flexible alumina mat before positioning the hot plate on top of the sidewall. Once the insulation is in place, use three stainless steel spheres to position the hot plate on top of the sidewall (make sure the system fits together well with little or no wobble). Insulate the remaining external surfaces of the hot plate with flexible alumina mat. Use fine, glass sheathed thermocouple wire to tie down the alumina insulation, as shown in Fig. B.8.

B.5 Calibration Procedure

The calibration system components are shown in Fig. B.9. Connect all signal wires to the NI Compact–DAQ modules, which are mounted in the module chassis. The filepath to the appropriate LabVIEW Virtual Instrument (VI) on the data acquisition laptop is: `My Documents\LabVIEW\High_Temp_Calibration\System_rev03`. Make sure each VI channel matches the corresponding physical channel. Turn the data acquisition system on, and allow it to warm up for at least fifteen minutes. When the calibration system is at thermal

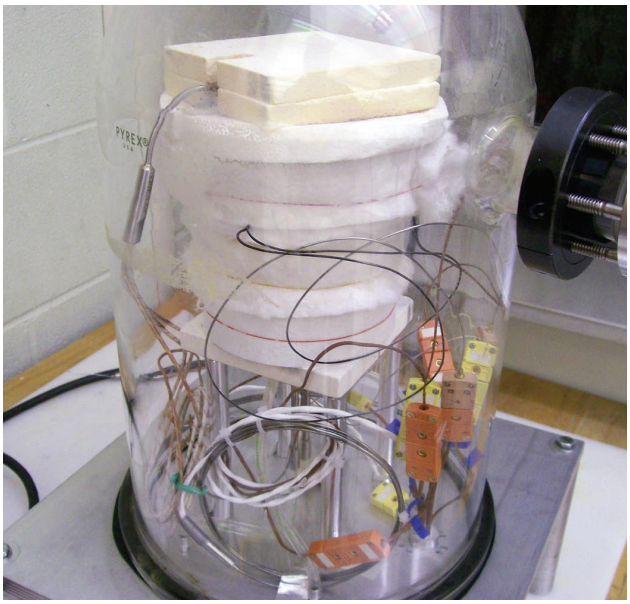

Figure B.8: Fibrous insulation is installed on all external surfaces of the calibration system during testing. The bell jar shown is only used for reduced pressure tests.

equilibrium with the surroundings (before the water pump or heater are turned on) run the LabVIEW VI and check to make sure a text file of raw data is being written in the location specified in the VI. Collect steady-state data at thermal equilibrium for at least two minutes: heat flux sensor bias voltage is measured, averaged, and subtracted from the test data during data processing.

Make sure the water lines are hooked up correctly (one inlet and one outlet for both the cold plate and the SB sensor). Plug the water pump into the wall socket. Burp any air out of the cold plate and SB sensor by rocking the entire system back and forth several times (push down on the top of the hot plate insulation to make sure the hot plate, cold plate, and sidewall stay in position relative to each other). After the system is burped, turn the variable transformer on (make sure the knob is set to zero at first) and ramp the heater voltage to the desired setting; see Table B.1 for reference. Measure the voltage supplied to the heater with a true-RMS multimeter. The maximum temperature of the hot plate surface is governed by the heater temperature limit of 1000 °C; make sure not to exceed this limit.

The thermal events can be run in any order with no hysteresis, provided the system is allowed to reach steady-state. The general criteria for steady-state is that the hot plate temperature does not change more than ≈ 0.2 °C over a time period of five consecutive minutes. For each thermal event, maintain the SB sensor body temperature at ≈ 26 °C by adding small amounts of ice to the water bath. Avoid condensation forming on the cold plate surface and SB sensor by keeping the surface temperatures above the dew point (add ice in small amounts at a time). When the calibration is complete, allow the system to cool down with

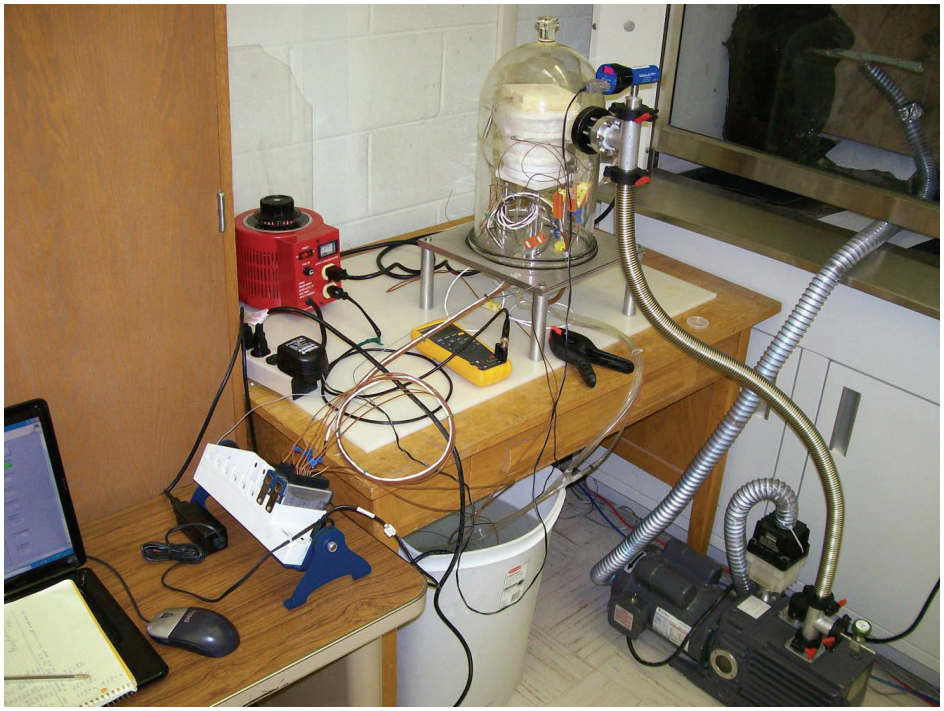

Figure B.9: High temperature transfer calibration system components (clockwise from bottom left): computer, data acquisition system, variable transformer, multimeter, calibration test section, vacuum pump, and water reservoir. The bell jar and vacuum pump are only used for reduced pressure tests.

Table B.1: Approximate heater voltage settings for desired steady-state hot plate temperatures.

$T_{\text{hot plate}}$ / (°C)	V_{heater} / (VAC RMS)
100	14
200	23
300	33
400	44
500	55
600	67
700	83
800	96
850	107

the water running to maintain the SB sensor and cold plate below 100 °C. The LabVIEW VI can be stopped during cool down. Turn the water pump off once the system is cool. Process the raw data using the code provided in §C.1.

Appendix C

MATLAB Code

This appendix includes the MATLAB code used to process the experimental data presented in this document.

C.1 Secondary Transfer Calibration

This section outlines the MATLAB code used to process the data presented in Chapters 2-3. The general sequence to processing experimental data with this code is:

1. Run the m-file "Individual_Calibrations.m": In this file all of the important information for each test is stored and the raw data are averaged over defined steady-state time envelopes. The steady-state averaged data are then used to determine the heat flux distribution on all enclosure control surfaces.

2. Write data to MATLAB matrix file: Set "writedata" variable equal to 1 to write all of the processed data to a matrix file for further analysis and comparison with other test results. Make sure all of the user defined inputs are correct (i.e. plate separation distance, surface emissivity, etc.).

3. Repeat the previous two steps for all relevant tests.

4. Run the m-file "Calibration_Results.m": This file is used to compare all test results at once.

C.1.1 Stand-Alone Files

Individual_Calibrations.m:

```
%% Clay Pullins
%%Radiation Calibrations: Schmidt-Boelter high temperature transfer calibrations
close all; clear all; clc;

%calibrbation constants
sigma=5.67*10^-8; %Stefan-Boltzmann constant [W m^-2 K^-4]
conversion=.0001; %convert from W/m^2 to W/cm^2
sb_sensitivity=625.2; %Medtherm calibration %VT lamp calibration SB test#3: 611.7 [microV/(W/cm^2)]
eh=0.8; ec=0.98; %plate surface emissivity
D=2.607*.0254; %cavity diamter [m]
L=0.5*0.0254; %cavity length (m)
% Lsw=0.373*0.0254; %cavity length (m)

%% load data file
testnum=7;
writedata=0; %write the processed data to a matrix file? 1-yes (overwrites if file already exists)

filepath='C:\Documents and Settings\cpullins\My Documents\MATLAB\High_Temp_System\System_rev03\HTHFS\Data\';
testnumber=num2str(testnum); suffix='.lvm';
fulloutputname=strcat(filepath,'test',testnumber,suffix);
fid=fopen(fulloutputname);
for j=1:23
    erase=fgetl(fid);
```

```
end
if testnum<=3
    a=fscanf(fid, '%f',[15, inf]); A=a'; [nan,ncol]=size(A); fclose(fid);
    time=A(:,1); tc1=A(:,2); tc2=A(:,3); sb_tc=A(:,4); hp1=A(:,5); hp2=A(:,6); hp3=A(:,7);...
        heater=A(:,8);
    cp1=A(:,9); cp2=A(:,10); water=A(:,11); air=A(:,12); hthfs_v1=A(:,13); hthfs_v2=A...
        (:,14); sb_hf=A(:,15);
elseif testnum>=16
    a=fscanf(fid, '%f',[14, inf]); A=a'; [nan,ncol]=size(A); fclose(fid);
    time=A(:,1); tc1=A(:,2); tc2=A(:,3); hp1=A(:,4); hp2=A(:,5); hp3=A(:,6);
    cp1=A(:,7); water=A(:,8); air=A(:,9); hthfs_v1=A(:,10); hthfs_v2=A(:,11); sb_hf=A...
        (:,12);
    sw1=A(:,13); sw5=A(:,14);
    %estimated:
    sb_tc=0.7.*water+0.3.*cp1; heater=hp1; cp2=cp1;
else
    a=fscanf(fid, '%f',[20, inf]); A=a'; [nan,ncol]=size(A); fclose(fid);
    time=A(:,1); tc1=A(:,2); tc2=A(:,3); sb_tc=A(:,4); hp1=A(:,5); hp2=A(:,6); hp3=A(:,7);...
        heater=A(:,8);
    cp1=A(:,9); cp2=A(:,10); water=A(:,11); air=A(:,12); hthfs_v1=A(:,13); hthfs_v2=A...
        (:,14); sb_hf=A(:,15);
    sw1=A(:,16); sw2=A(:,17); sw3=A(:,18); sw4=A(:,19); sw5=A(:,20);
end


%remove sensor voltage bias
offset1=mean(hthfs_v1(1:60)); hthfs_v1=hthfs_v1-offset1;
offset2=mean(hthfs_v2(1:60)); hthfs_v2=hthfs_v2-offset2;
offset3=mean(sb_hf(1:60)); sb_hf=sb_hf-offset3;

sens2=hthfs_v2./sb_hf.*sb_sensitivity;

%individual test steady state points
if testnum==1
    ss=[10000 15400];
    v=[13.4 98];
elseif testnum==2
    ss=[23200 25050 26400 28200 30150 31750 34450 37500 41950];
    v=[101.8 91.6 76.8 63.68 51.68 40.68 30.45 21.9 13];
elseif testnum==3
    ss=[2700 3600 4930 5950 7040 8480 10230 12700 17450];
    v=[101 91.6 76.8 62.8 51.7 40.44 30.26 21.96 13];
elseif testnum==4
    ss=[3050 6250 8650];
    v=[14.36 24.58 34.49];
elseif testnum==5
    ss=[2700 5330 8230 10800 13240 16700];
    v=[14.4 24.37 34.17 44.16 55.03 67.9];
elseif testnum==6
    ss=[3170 6450 8340 10750 14200 19150];
    v=[67.9 54.94 43.36 33.48 23.64 13.84];
elseif testnum==7
    ss=[4270 6400 8650 10220 13200 15030 17500 20800 27500];
    v=[106.5 96.9 82.3 67.6 55 43.91 33.44 23.75 14.12];
elseif testnum==8
    ss=[3400 4780 6500 8800 11150 13250 16550 20150 25130];
    v=[106.6 96.3 82.6 67 54.72 43.9 33.4 23.62 14.02];
elseif testnum==9
    ss=[4600 5740 6950 8850 10930 13700 16330 19500 24600];
    v=[106.5 96 82.4 67 55.12 43.99 33.34 23.42 13.82];
elseif testnum==10
    ss=[3650 8400 9900 11780 14450 16650 19700 23050 29300];
    v=[105.4 95.4 82.6 66.5 54.84 44.12 33 23.48 13.86];
elseif testnum==11
```

```
    ss=[4100 6000 8200 11050 14150 17900 22050 26900 33200];
    v=[105.2 94.2 80.1 65.82 53.65 42.7 32.45 22.96 13.45];
elseif testnum==12
    ss=[3350 4900 6950 9370 12550 15850 19900 25500 32300];
    v=[105 94.1 79.6 65.6 53.5 42.7 32.43 23.07 13.4];
elseif testnum==13
    ss=[3080 4500 6350 9700 13000 16700 20400 24700 31100];
    v=[105.9 94.2 79.6 65.7 53.84 42.57 32.46 22.95 13.3];
elseif testnum==14
    ss=[4470 6150 8250 11750 15300 19550 23850 29100 35200];
    v=[104.4 94.4 79.4 65.8 53.7 42.48 32.56 22.97 13.46];
elseif testnum==15
    ss=[3150 3970 5020 6950 9730 11650 14200 18550 25950];
    v=[106.4 96.1 82.4 67.4 54.85 44.46 33.67 23.64 13.89];
elseif testnum==16
    ss=[2600 9400 17150 3540 11020 18920 4670 12820 21000]; %sorted by pressure
    v=[14.4 33.3 55.65 14.02 33.16 55.34 13.2 32.16 54.5];
elseif testnum==17
    ss=[4430 12770 22140 7000 14200 24600 9650 16650 27350]; %sorted by pressure
    v=[67.6 43.67 23.78 67.4 43.53 23.46 67.8 42.83 22.64];
end

%% steady state calculations
num_samples=100; %average data over 100 seconds (sampling rate = 1 Hz)
for i=1:length(ss)
    V1(i)=mean(hthfs_v1(ss(i)-num_samples:ss(i)));
    V2(i)=mean(hthfs_v2(ss(i)-num_samples:ss(i)));
    TC1(i)=mean(tc1(ss(i)-num_samples:ss(i)));
    TC2(i)=mean(tc2(ss(i)-num_samples:ss(i)));
    SB_HF(i)=mean(sb_hf(ss(i)-num_samples:ss(i)));
    SB_TC(i)=mean(sb_tc(ss(i)-num_samples:ss(i)));
    CP1(i)=mean(cp1(ss(i)-num_samples:ss(i)));
    CP2(i)=mean(cp2(ss(i)-num_samples:ss(i)));
    HP1(i)=mean(hp1(ss(i)-num_samples:ss(i)));
    HP2(i)=mean(hp2(ss(i)-num_samples:ss(i)));
    HP3(i)=mean(hp3(ss(i)-num_samples:ss(i)));
    water_T(i)=mean(water(ss(i)-num_samples:ss(i)));
    heater_T(i)=mean(heater(ss(i)-num_samples:ss(i)));
    if testnum>=4 && testnum<=15
        SW1(i)=mean(sw1(ss(i)-num_samples:ss(i)));
        SW2(i)=mean(sw2(ss(i)-num_samples:ss(i)));
        SW3(i)=mean(sw3(ss(i)-num_samples:ss(i)));
        SW4(i)=mean(sw4(ss(i)-num_samples:ss(i)));
        SW5(i)=mean(sw5(ss(i)-num_samples:ss(i)));
    elseif testnum>=16
        SW1(i)=mean(sw1(ss(i)-num_samples:ss(i)));
        SW5(i)=mean(sw5(ss(i)-num_samples:ss(i)));
    end
end

%% data processing
Tavg=(TC1+TC2)./2;
Sens1=V1./SB_HF.*sb_sensitivity;
Sens2=V2./SB_HF.*sb_sensitivity;
sb_heatflux=SB_HF.*(10^6)./sb_sensitivity; %[W/cm^2]


%conduction / convection estimation - properties evaluated at Tfilm
Tfilm=(0.5.*TC1+0.5.*SB_TC)+273.15;

[nan,nan,nan,nan,nan,nan,nan,Ka]=Air_Properties(Tfilm);

%change in cavity dimensions due to thermal expansion
CTE_HX=16.3*10^-6; %thermal expansion coefficient for inconel HX from 20-900 C (Matweb) [C↩
```

```
    ^-1]
CTE_SS=18.7*10^-6; %thermal expansion coefficient for 304 stainless steel from 0-650 C (↩
    Matweb) [C^-1]

% D1=7/64*.0254; %room temp. diameter of holes drilled in plates [m]
% D2=1/8*.0254; %room temp. diameter of stainless steel bearings [m]
%
% D3=D1.*(1+CTE_HX.*(HP3-25)); %at temp diameter of inconel holes [m]
% D4=D2.*(1+CTE_SS.*((HP3+SW1)./2-25)); %at temp diameter of stainless ball bearings ↩
    nearest hot plate [m]
% D5=D1.*(1+CTE_SS.*(SW1-25)); %at temp diameter of stainless sidewall holes nearest hot ↩
    plate [m]
%
% D6=D1.*(1+CTE_SS.*(SW5-25)); %at temp diameter of stainless sidewall holes nearest cold ↩
    plate [m]
% D7=D2.*(1+CTE_SS.*((SW5+CP2)./2-25)); %at temp diameter of stainless ball bearings ↩
    nearest cold plate [m]
% D8=D1; %at temp diameter of aluminum holes - assume no expansion since they are ↩
    maintained at roughly room temp [m]
%
% l1=.5.*((D4.^2-D3.^2).^.5+(D4.^2-D5.^2).^.5); %at temp gap between hot plate and ↩
    sidewall [m]
% l2=Lsw.*(1+CTE_SS.*(SW3-25)); %at temp length of stainless sidewall [m]
% l3=.5.*((D7.^2-D6.^2).^.5+(D7.^2-D8.^2).^.5); %at temp gap between hot plate and ↩
    sidewall [m]
% Lc=l1+l2+l3; %at temp plate separation, complex model [m]

if testnum>=4 && testnum<=15
    Lc=L.*(1+CTE_SS.*(SW3-25)); %at temp plate separation, simple model [m]
    Dc=D.*(1+CTE_SS.*(SW3-25)); %at temp cavity diameter [m]
elseif testnum>=16
    Lc=L.*(1+CTE_SS.*((SW1+SW5)./2-25)); %at temp plate separation, simple model [m]
    Dc=D.*(1+CTE_SS.*((SW1+SW5)./2-25)); %at temp cavity diameter [m]
else
    Lc=L.*(1+CTE_SS.*((HP3+CP2)./2-25)); %at temp plate separation, simple model [m]
    Dc=D.*(1+CTE_SS.*((HP3+CP2)./2-25)); %at temp cavity diameter [m]
end


%% radiosity balance - N surface enclosure:
%cavity size
rc=Dc/2;
rs=(1/32)*.0254; %SB sensing area radius [m]

%temperature drop across paint layer
dT=sb_heatflux.*(0.0025*2.54/(0.00875));

%simple model
[q_tot]=Adiabatic_Sidewall_Simple_Model(Tavg,SB_TC,eh,ec,D,L);

%build temperature matrix T
T(1,:)=TC1-dT; %hot sensing area temperature
T(2,:)=(TC1+HP1)./2-dT; %hot sensor body temperature
T(3,:)=HP2-dT;
T(4,:)=HP3-dT;
T(5,:)=SB_TC+dT; %Schmidt-Boelter sensing area
T(6,:)=SB_TC+dT; %Schmidt-Boelter body area
T(7,:)=CP1+dT;
T(8,:)=CP2+dT;
T=T+273.15; %convert from C to K

%1-D conduction
qcond=conversion.*Ka.*(T(1,:)-T(5,:))./Lc;

```

```
%call in discretization function
[H,C,W,N,l,r]=Cavity_Discretization(rs,Lc,rc,T);

%call view factor model
[F]=Cylindrical_Cavity_View_Factors(Lc,Dc,rc,H,C,W,N,r);

%emissivities
% [e]=Plate_Surface_Emissivities(T,N,H,C,ec);
e=ones(N,length(ss)).*0.5; %initializes emissivities at typical sidewall value
%individual models alter sidewall emissivity according to the calculated / prescribed sidewall temperature
e(1:H,:)=eh; %hot surface emissivity
e(H+1:H+C,:)=ec; %cold surface emissivity

%adiabatic model
[Q1]=Adiabatic_Sidewall_Radiosity_Model(e,F,T);
Jsw1=Q1(H+C+1:N,:); %ideal radiosities
Tsw1=(Jsw1./sigma).^.25; %ideal sidewall temperatures
% qh1=Q1(1:H,:).*conversion; qc1=Q1(H+1:H+C,:).*conversion; %surface heat flux [W/cm^2]
qh1=Q1(1,:).*conversion; qc1=-1.*Q1(H+1,:).*conversion; %surface heat flux magnitude [W/cm^2] - adabatic sidewall
qth1=qh1+qcond; %[W/cm^2]
qtc1=qc1+qcond; %[W/cm^2]
CF1=qtc1./qth1;

%heat loss model
[Q2,Touter,Tinner,e2]=Sidewall_Heat_Loss_Radiosity_Model(e,F,H,C,W,T,Dc,Lc,testnum);
Jsw2=Q2(H+C+1:N,:); %radiosities
Tsw2=(Jsw2./sigma).^.25; %sidewall temperatures
% qh2=Q2(1:H,:).*conversion; qc2=Q2(H+1:H+C,:).*conversion; %surface heat flux [W/cm^2]
qh2=Q2(1,:).*conversion; qc2=-1.*Q2(H+1,:).*conversion; %surface heat flux magnitude [W/cm^2] - adabatic sidewall
qth2=qh2+qcond; %[W/cm^2]
qtc2=qc2+qcond; %[W/cm^2]
CF2=qtc2./qth1;

%known temperatures model
%prescribed or measured sidewall temperatures
if testnum<4
    delta=(HP3-CP2)./W;
    T2(1,:)=(HP3+273.15)-.5.*delta;
    for i=2:W
        T2(i,:)=T2(i-1,:)-delta;
    end
    T3=[T;T2]; e3=e;
elseif testnum>=16
    Twall=[HP3;SW1;SW5;CP2]+273.15;
    [T2,e3]=Sidewall_Temperature_Emissivity(Lc,H,C,W,Twall,e,testnum);
    T3=[T;T2];
else
    Twall=[HP3;SW1;SW2;SW3;SW4;SW5;CP2]+273.15;
    [T2,e3]=Sidewall_Temperature_Emissivity(Lc,H,C,W,Twall,e,testnum);
    T3=[T;T2];
end

[Q3]=Known_Temperatures_Radiosity_Model(e3,F,T3);
Jsw3=sigma.*T2.^4-((1-e3(H+C+1:N,:))./e3(H+C+1:N,:)).*Q3(H+C+1:N,:);


if testnum>=4
    %hot and cold sensor modeled total heat flux
    qh=Q3(1,:).*conversion; qc=-1.*Q3(H+1,:).*conversion; %surface heat flux magnitude [W/cm^2]
else
```

```
    qh=Q2(1,:).*conversion; qc=-1.*Q2(H+1,:).*conversion; %surface heat flux magnitude [W/cm^2]
end

qth=qh+qcond; %[W/cm^2]
qtc=qc+qcond; %[W/cm^2]


%measurement vs model heat flux
dis_tot=(sb_heatflux-qtc)./sb_heatflux.*100;
%correction factor and corrected sensitivity
CF=qtc./qth;
Senscor1=Sens1.*CF;
Senscor2=Sens2.*CF;

%% uncertainty analysis
%Clay Pullins  3/1/11
% measurands
V_t=V1'.*(10^6);
V_sb=SB_HF'.*(10^6);
S_sb=sb_sensitivity;

% sensitivity coefficients
s(:,1)=S_sb.*CF'./V_sb; %dS_t/dV_t [cm^2/W]
s(:,2)=-V_t.*S_sb.*CF'./(V_sb.^2); %dS_t/dV_sb [cm^2/W]
s(:,3)=V_t.*CF'./V_sb; %dS_t/dS_sb [dimensionless]
s(:,4)=V_t.*S_sb./V_sb; %dS_t/dCF [microV/W/cm^2]

%uncertainty in CF, calibration repeatability, and qtc at each steady-state point
u1=[0.0156309730;
    0.0153773757;
    0.0151407098;
    0.0148235264;
    0.0147240884;
    0.0148449508;
    0.0150391588;
    0.0184809355;
    0.0366637909]; %uc(CF) for 1/2 inch sidewall

u2=[0.0267819428;
    0.0261202127;
    0.0256324996;
    0.0256552299;
    0.0266494285;
    0.0289409405;
    0.0328254834;
    0.0421533883;
    0.0733867718]; %uc(CF) for 1 inch sidewall

urep1=[0.686207102903050;
    0.577880170014868;
    0.596561442101621;
    0.889287620516768;
    0.843604335392096;
    1.155374729390007;
    1.966826425704631;
    3.313270636733503;
    5.985797634628856]; %ur(St) for 1/2 inch sidewall

urep2=[0.457390865681756;
    0.327823934053710;
    0.570316575593129;
    0.498723901475783;
    0.554613818457040;
```

```
    0.712612832084306;
    1.028884981504528;
    1.726482519441694;
    4.263417002736373]; %ur(St) for 1 inch sidewall

uqc1=[0.3624314511;
    0.2972140262;
    0.2197543197;
    0.1377085719;
    0.0871224686;
    0.0520257623;
    0.0268920700;
    0.0124064459;
    0.0056300051]; %uc(qtc) for 1/2 inch sidewall

uqc2=[0.2708518991;
    0.2185457970;
    0.1604739351;
    0.1060839630;
    0.0676764203;
    0.0410422531;
    0.0230303093;
    0.0115723473;
    0.0052839930]; %uc(qtc) for 1 inch sidewall

% standard uncertainty
uvt=0.001.*V_t; %[microV] DAQ gain error
uvsb=0.001.*V_sb; %[microV] DAQ gain error
ussb=9.378; %[microV/W/cm^2]

% individual test conditions
if testnum==1
    ucf=[u1(9);u1(1)];
    ur=[urep1(9);urep1(1)];
elseif testnum==4
    ucf=[u1(9);u1(8);u1(7)];
    ur=[urep1(9);urep1(8);urep1(7)];
elseif testnum==5
    ucf=[u1(9);u1(8);u1(7);u1(6);u1(5);u1(4)];
    ur=[urep1(9);urep1(8);urep1(7);urep1(6);urep1(5);urep1(4)];
elseif testnum==6
    ucf=u1(4:9);
    ur=urep1(4:9);
elseif testnum==7 || testnum==8 || testnum==9 || testnum==10  || testnum==15
    ucf=u1;
    ur=urep1;
elseif testnum==16
    ucf=[u1(9);u1(7);u1(5);u1(9);u1(7);u1(5);u1(9);u1(7);u1(5)];
    ur=[urep1(9);urep1(7);urep1(5);urep1(9);urep1(7);urep1(5);urep1(9);urep1(7);urep1(5)];
elseif testnum==17
    ucf=[u1(8);u1(6);u1(4);u1(8);u1(6);u1(4);u1(8);u1(6);u1(4)];
    ur=[urep1(8);urep1(6);urep1(4);urep1(8);urep1(6);urep1(4);urep1(8);urep1(6);urep1(4)];
else
    ucf=u2;
    ur=urep2;
end

%precision errors: voltage measurement (linearity and repeatability - root sum squares ↩
    combination)
upvsb=((0.02.*V_sb).^2+(0.005.*V_sb).^2).^0.5;
utvsb=(upvsb.^2+(uvsb).^2).^0.5;
utvt=((0.005.*V_t).^2+(uvt).^2).^0.5;

% combined standard uncertainty in each measurand
```

```
sq(:,1)=(s(:,1).*utvt).^2;
sq(:,2)=(s(:,2).*utvsb).^2;
sq(:,3)=(s(:,3).*ussb).^2;
sq(:,4)=(s(:,4).*ucf).^2;
% sq(:,5)=ur.^2;

[nrow,nan]=size(sq);

for z=1:nrow
    uc(z,1)=sqrt(sum(sq(z,:))); % combined standard uncertainty in the calibration
end

if testnum>=7 && testnum<=15
    % effective degrees of freedom
    nu=ones(nrow,4);
    nu(:,1)=50; %V_t
    nu(:,2)=50; %V_sb
    nu(:,3)=50; %S_sb
    nu(:,4)=[21;
        21;
        21;
        21;
        21;
        22;
        26;
        45;
        33]; %f
%     nu(:,5)=3; %u_r

    for i=1:nrow
        nu_eff(i,1)=uc(i).^4./sum(sq(i,:).^2./nu(i,:));
    end
end

%% sidewall radiosity and temperature plots
x=1/(2*W):1/W:1-1/(2*W);
X=(1/16)*.0254/L:(L-1/8*.0254)/(4*L):1-(1/16)*.0254/L;
% for i=1:length(ss)
%     figure; hold on; box on; title(['Thermal Event #' num2str(i)],'FontSize',10,'FontName','arial');
%     plot(x,Jsw1(:,i).*conversion, 'k>-','linewidth',1,'MarkerEdgeColor','k','MarkerFaceColor','g','MarkerSize',5);
%     plot(x,Jsw2(:,i).*conversion, 'ko-','linewidth',1,'MarkerEdgeColor','k','MarkerFaceColor','m','MarkerSize',5);
%     plot(x,Jsw3(:,i).*conversion, 'kd-','linewidth',1,'MarkerEdgeColor','k','MarkerFaceColor','c','MarkerSize',5);
%     xlabel('Nondimensional Distance, {\itx/L}','FontSize',10,'FontName','arial','FontWeight','bold')
%     ylabel('Sidewall Radiosity, {\itJ}_w (W cm^{-2})','FontSize',10,'FontName','arial','FontWeight','bold')
%     hh=legend('Reradiating Surface Model','Estimated Radial Heat Loss Model','Known Temperatures Model',1); legend('boxoff');
%     set(hh,'FontSize',8,'FontName','arial')
%     figure; hold on; box on; title(['Thermal Event #' num2str(i)],'FontSize',10,'FontName','arial');
%     plot(x,Tsw1(:,i)-273.15, 'k>-','linewidth',1,'MarkerEdgeColor','k','MarkerFaceColor','g','MarkerSize',5);
%     plot(x,Tsw2(:,i)-273.15, 'ko-','linewidth',1,'MarkerEdgeColor','k','MarkerFaceColor','m','MarkerSize',5);
%     plot(x,T2(:,i)-273.15, 'kd-','linewidth',1,'MarkerEdgeColor','k','MarkerFaceColor','c','MarkerSize',5);
%     plot(0,HP3(i),'k^','linewidth',1,'MarkerEdgeColor','k','MarkerFaceColor','r','MarkerSize',6);
%     plot(X,[SW1(i)  SW2(i) SW3(i) SW4(i) SW5(i)],'ks','linewidth',1,'MarkerEdgeColor','k
```

```
    ','MarkerFaceColor','y','MarkerSize',6);
%     plot(1,CP2(i),'kv','linewidth',1,'MarkerEdgeColor','k','MarkerFaceColor','b','↩
    MarkerSize',6);
%     xlabel('Nondimensional Distance, {\itx/L}','FontSize',10,'FontName','arial','↩
    FontWeight','bold')
%     ylabel('Sidewall Temperature, {\itT}_w (\circC)','FontSize',10,'FontName','arial','↩
    FontWeight','bold')
%     hh=legend('Reradiating Surface Model','Estimated Radial Heat Loss Model','Known ↩
    Temperatures Model',...
%         'Measured Hot Plate Temperature','Measured Sidewall Temperatures','Measured Cold↩
     Plate Temperature',1); legend('boxoff');
%     set(hh,'FontSize',8,'FontName','arial')
% end

%% write data matrix file

Data=zeros(length(ss),18);
Data(:,1)=sb_heatflux; %measured absorbed heat flux (W/cm^2)
Data(:,2)=V1; %sensor output voltage Cr-Cr (V)
Data(:,3)=V2; %sensor output voltage Al-Al (V)
Data(:,4)=TC1; %sensor top thermocouple (deg C)
Data(:,5)=TC2; %sensor bottom thermocouple (deg C)
Data(:,6)=Tavg; %sensor average temperature (deg C)
Data(:,7)=qcond; %conduction through cavity magnitude (W/cm^2)
Data(:,8)=qth; %modeled hot plate heat flux magnitude (W/cm^2)
Data(:,9)=qtc; %modeled cold plate heat flux magnitude (W/cm^2)
Data(:,10)=Senscor1; %HFS sensitivity (Cr-Cr) to absorbed heat flux corrected (microV W^-1↩
    cm^2)
Data(:,11)=Senscor2; %HFS sensitivity (Al-Al) to absorbed heat flux corrected (microV W^-1↩
    cm^2)
Data(:,12)=e3(1,:); %hot surface emissivity
Data(:,13)=e3(H+C,:); %cold surface emissivity
Data(:,14)=v; %Variac voltage (VAC RMS)
Data(:,15)=dis_tot; %heat flux measurement vs model discrepancy (sb total vs model total)
Data(:,16)=-1.*qc1(1,:)+qcond; %adiabatic sidewall model cold plate heat flux magnitude (W↩
    /cm^2)
Data(:,17)=CF; %correction factor
Data(:,18)=uc; %combined standard uncertainty in the sensitivity calibration (microV W^-1 ↩
    cm^2)

if writedata==1
    savename=strcat('test',testnumber,'.mat');
    save(savename,'Data');
else
end

if testnum<=15
    sequence=length(ss);
else
    sequence=[3 3 3];
end

%% transient plots
A(:,ncol+1)=hthfs_v1./sb_hf; %voltage ratio

%sensor voltage vs time
Transient_Figure(testnum,A,[10 11 12],[1 1 6.5 4],'best')

%sensor voltage ratio vs time
Transient_Figure(testnum,A,[11],[1 1 6.5 4],'northwest')

%temperature vs time
Transient_Figure(testnum,A,[2 3 4 5 6],[1 1 6.5 4],'best')
```

```
%% sensitivity vs temperature
Single_Test_Steady_State_Figure(Data,1,sequence,testnum,6,10,[1 1 8 5],'bestoutside')


%% voltage vs temperature
Single_Test_Steady_State_Figure(Data,1,sequence,testnum,6,2,[1 1 8 5],'bestoutside')


%% cold plate heat flux vs hot plate temperature
Single_Test_Steady_State_Figure(Data,1,sequence,testnum,6,[1 8 9],[1 1 8 5],'bestoutside')


%% heat flux discrepancy vs hot plate temperature
Single_Test_Steady_State_Figure(Data,1,sequence,testnum,6,15,[1 1 8 5],'bestoutside')


%% high temp. paper #2 figure: sidewall temperature and radiosity

for i=5
    figure1=figure('Units','Inches','Position',[2 0.5 6.5 6]); hold on;
    %temperature
    sp1=subplot(2,1,1); hold on; box on; ylim([0 550]);
    set(sp1,'Units','Inches','Position',[.8 3.4 5.2 2.2]);
    plot(x,Tsw1(:,i)-273.15, 'kx-','linewidth',.5,'MarkerSize',5);
    plot(x,Tsw2(:,i)-273.15, 'k*-','linewidth',.5,'MarkerSize',5);
    plot(x,T2(:,i)-273.15, 'ko-','linewidth',.5,'MarkerEdgeColor','k','MarkerFaceColor','w','MarkerSize',5);
    plot(0,HP3(i),'k^','linewidth',1,'MarkerEdgeColor','k','MarkerFaceColor','k','MarkerSize',7);
    plot(X,[SW1(i)  SW2(i) SW3(i) SW4(i) SW5(i)],'kd','linewidth',1,'MarkerEdgeColor','k','MarkerFaceColor','k','MarkerSize',7);
    plot(1,CP2(i),'kv','linewidth',1,'MarkerEdgeColor','k','MarkerFaceColor','k','MarkerSize',7);
    xlabel('Nondimensional Distance Along Sidewall, {\itx/L}','FontSize',10,'FontName','arial','FontWeight','bold')
    ylabel('Sidewall Temperature, {\itT}_w (\circC)','FontSize',10,'FontName','arial','FontWeight','bold')
    h1=legend('Reradiating Surface Model','Estimated Radial Heat Loss Model','Known Temperatures Model',...
        'Measured Hot Plate Temperature','Measured Sidewall Temperatures','Measured Cold Plate Temperature',1); legend('boxoff');
    set(h1,'FontSize',8,'FontName','Arial','Units','Inches','Position',[.9 3.5 2 1])
    annotation(figure1,'textbox',[0.84 0.8 0.05 0.1],'String',{'(a)'},...
        'FontWeight','bold','FontSize',12,'FontName','Arial','LineStyle','none');
    %radiosity
    sp2=subplot(2,1,2); hold on; box on; %xlim([0 900]); ylim([0 8]);
    set(sp2,'Units','Inches','Position',[.8 .6 5.2 2.2]);
    plot(x,Jsw1(:,i).*conversion, 'kx-','linewidth',.5,'MarkerSize',5);
    plot(x,Jsw2(:,i).*conversion, 'k*-','linewidth',.5,'MarkerSize',5);
    plot(x,Jsw3(:,i).*conversion, 'ko-','linewidth',.5,'MarkerEdgeColor','k','MarkerFaceColor','w','MarkerSize',5);
    xlabel('Nondimensional Distance Along Sidewall, {\itx/L}','FontSize',10,'FontName','arial','FontWeight','bold')
    ylabel('Sidewall Radiosity, {\itJ}_w (W cm^{-2})','FontSize',10,'FontName','arial','FontWeight','bold')
    h2=legend(['Reradiating Surface Model:   {\fontsize{9}\fontname{times}{\bf{\itf}}} = ' num2str(CF1(i),'%10.3f')],...
        ['Estimated Radial Heat Loss Model:   {\fontsize{9}\fontname{times}{\bf{\itf}}} = ' num2str(CF2(i),'%10.3f')],...
        ['Known Temperatures Model:   {\fontsize{9}\fontname{times}{\bf{\itf}}} = ' num2str(CF(i),'%10.3f')],1); legend('boxoff');
    set(h2,'FontSize',8,'FontName','Arial','Units','Inches','Position',[1 .75 2 .5])
    annotation(figure1,'textbox',[.84 0.335 0.05 0.1],'String',{'(b)'},...
```

```
        'FontWeight','bold','FontSize',12,'FontName','Arial','LineStyle','none');
end
```

Calibration_Results.m:

```
%% Clay Pullins
%%Radiation Calibrations: High temperature calibration system HTHFS rev03
close all; clear all; clc;

filepath='C:\Documents and Settings\cpullins\My Documents\MATLAB\High_Temp_System\System_rev03\HTHFS\';
prefix='test';
suffix='.mat';

%data column headers:
hf=1; %(1) measured absorbed heat flux (W/cm^2)
V1=2; %(2) sensor output voltage Cr-Cr (V)
V2=3; %(3) sensor output voltage Al-Al (V)
TC1=4; %(4) sensor top thermocouple (deg C)
TC2=5; %(5) sensor bottom thermocouple (deg C)
Tavg=6; %(6) %sensor average temperature (deg C)
cond=7; %(7) conduction magnitude (W/cm^2)
qh=8; %(8) modeled hot plate heat flux magnitude (W/cm^2)
qc=9; %(9) modeled cold plate heat flux magnitude (W/cm^2)
S1=10; %(10) HTHFS sensitivity to absorbed heat flux Cr-Cr (microV W^-1 cm^2)
S2=11; %(11) HTHFS sensitivity to absorbed heat flux Al-Al (microV W^-1 cm^2)
eh=12; %(12) hot surface emissivity
ec=13; %(13) cold surface emissivity
Variac=14; %(14) Variac voltage (VAC RMS)
dis=15; %(15) heat flux measurement vs model discrepancy (sb total vs model total, %)
qa=16; %(16) adiabatic sidewall model cold plate heat flux magnitude (W/cm^2)
CF=17; %(17) correction factor
uc=18; %(18) combined standard uncertainty in the sensitivity calibration (microV W^-1 cm^2)


last_test=17;
start=1;
for j=1:last_test
    testnumber=num2str(j); fulloutputname=strcat(filepath,prefix,testnumber,suffix);
    a=importdata(fulloutputname); [rows columns]=size(a); L(j)=rows; %L(1)=6;
    A(start:start+rows-1,:)=a; start=start+rows;
    eval(['test' num2str(j) '_hf' '=a(:,1);']);
    eval(['test' num2str(j) '_V1' '=a(:,2);']);
    eval(['test' num2str(j) '_V2' '=a(:,3);']);
    eval(['test' num2str(j) '_TC1' '=a(:,4);']);
    eval(['test' num2str(j) '_TC2' '=a(:,5);']);
    eval(['test' num2str(j) '_Tavg' '=a(:,6);']);
    eval(['test' num2str(j) '_cond' '=a(:,7);']);
    eval(['test' num2str(j) '_qh' '=a(:,8);']);
    eval(['test' num2str(j) '_qc' '=a(:,9);']);
    eval(['test' num2str(j) '_S1' '=a(:,10);']);
    eval(['test' num2str(j) '_S2' '=a(:,11);']);
    eval(['test' num2str(j) '_eh' '=a(:,12);']);
    eval(['test' num2str(j) '_ec' '=a(:,13);']);
    eval(['test' num2str(j) '_Variac' '=a(:,14);']);
    eval(['test' num2str(j) '_dis' '=a(:,15);']);
    eval(['test' num2str(j) '_qa' '=a(:,16);']);
    eval(['test' num2str(j) '_CF' '=a(:,17);']);
    eval(['test' num2str(j) '_uc' '=a(:,18);']);
    clear a
```

```
end

%temperature
Tavg1=(test7_Tavg+test8_Tavg+test9_Tavg+test10_Tavg+test15_Tavg)./5;
Tavg2=(test11_Tavg+test12_Tavg+test13_Tavg+test14_Tavg)./4;

%sensitivity
S1avg1=(test7_S1+test8_S1+test9_S1+test10_S1+test15_S1)./5;
S1avg2=(test11_S1+test12_S1+test13_S1+test14_S1)./4;

%sb heat flux
qsbavg1=(test7_hf+test8_hf+test9_hf+test10_hf+test15_hf)./5;
qsbavg2=(test11_hf+test12_hf+test13_hf+test14_hf)./4;

%modeled cold plate heat flux
qcavg1=(test7_qc+test8_qc+test9_qc+test10_qc+test15_qc)./5;
qcavg2=(test11_qc+test12_qc+test13_qc+test14_qc)./4;

%correction factor
CFavg1=(test7_CF+test8_CF+test9_CF+test10_CF+test15_CF)./5;
CFavg2=(test11_CF+test12_CF+test13_CF+test14_CF)./4;

%uncertainty
k=2; %coverage factor
Uavg1=k.*(test7_uc+test8_uc+test9_uc+test10_uc+test15_uc)./5;
Uavg2=k.*(test11_uc+test12_uc+test13_uc+test14_uc)./4;

uqc1=k.*[0.3624314511;
    0.2972140262;
    0.2197543197;
    0.1377085719;
    0.0871224686;
    0.0520257623;
    0.0268920700;
    0.0124064459;
    0.0056300051]; %uc(qtc) for 1/2 inch sidewall

uqc2=k.*[0.2708518991;
    0.2185457970;
    0.1604739351;
    0.1060839630;
    0.0676764203;
    0.0410422531;
    0.0230303093;
    0.0115723473;
    0.0052839930]; %uc(qtc) for 1 inch sidewall

%repeatability
devsq1_S1=[(test7_S1-S1avg1).^2 (test8_S1-S1avg1).^2 (test9_S1-S1avg1).^2 (test10_S1-↩
    S1avg1).^2 (test15_S1-S1avg1).^2];
S_std_dev_mean1=(1/(5*(5-1)).*sum(devsq1_S1,2)).^0.5;

devsq2_S1=[(test11_S1-S1avg2).^2 (test12_S1-S1avg2).^2 (test13_S1-S1avg2).^2 (test14_S1-↩
    S1avg2).^2];
S_std_dev_mean2=(1/(4*(4-1)).*sum(devsq2_S1,2)).^0.5;


%% lamp bank calibration results 3/29/11; e-zynolyte,cured=0.82
SL1=[331.9832 336.7552 339.2138 341.1385 339.8473 335.9610];
TL=[25.3251 38.6763 52.5409 68.6934 87.8367 108.0330];


%% call in theoretical sensitivity model
% N=5; %number of HTHFS thermopile junctions
```

```
% W=0.127*.0254; %HTHFS width (m)
% L=0.125*.0254; %HTHFS thickness (m)
[T,rho,C,K,St1_1,St1_2,Se,t]=HTHFS_Theory(5,0.127*.0254,0.125*.0254); clc;
[nan,nan,nan,nan,St2_1,St2_2,nan,nan]=HTHFS_Theory(6,0.127*.0254,0.125*.0254); clc;


%% HF3 sensitivity vs temperature
% Multiple_Test_Steady_State_Figure(A,L,[7:10 15:17],Tavg,S2,[0 900],[0 600],[1 1 8.5 5],'bestoutside')


%% HF3 voltage vs temperature
% Multiple_Test_Steady_State_Figure(A,L,1:last_test,Tavg,Vs1,[75 900],[0 .002],[1 1 8.5 5],'bestoutside')


%% sb measured heat flux vs hot plate temperature (L=0.5 in)
% Multiple_Test_Steady_State_Figure(A,L,[7:10 15:17],Tavg,hf,[75 900],[0 8],[1 1 8.5 5],'bestoutside')


%% heat flux discrepancy vs hot plate temperature (L=0.5 in)
% Multiple_Test_Steady_State_Figure(A,L,7:last_test,Tavg,dis,[75 900],[-10 10],[1 1 8.5 5],'bestoutside')


%% high temp. paper #2 figure: heat flux, correction factor, and sensitivity vs temperature

%heat flux
figure1=figure('Units','Inches','Position',[2 1 6.5 6]); hold on;
sp1=subplot(2,2,1); hold on; box on; xlim([0 900]); ylim([0 8]);
set(sp1,'Units','Inches','Position',[.8 3.4 2.2 2.3]);
plot(test7_Tavg,test7_hf, 'ko', 'linewidth', .5,'MarkerEdgeColor','k','MarkerFaceColor','b','MarkerSize',5);
% plot(test7_Tavg,test7_qc, 'kx', 'linewidth', 1,'MarkerSize',5);
plot(test11_Tavg,test11_hf, 'kd', 'linewidth', .5,'MarkerEdgeColor','k','MarkerFaceColor','r','MarkerSize',5);
% plot(test11_Tavg,test11_qc, 'k+', 'linewidth',1,'MarkerSize',5);
xlabel('HTHFS Average Temperature, {\itT}_{t,avg} (\circC)','FontSize',10,'FontName','Arial','FontWeight','bold')
ylabel('Measured SB Heat Flux, {\itq}"_{sb} (W cm^{-2})','FontSize',10,'FontName','Arial','FontWeight','bold')
h1=legend('{\itL} = 1.27 cm', '{\itL} = 2.54 cm',2); legend('boxoff');
set(h1,'FontSize',8,'FontName','arial','Position',[.8 5.15 1 .5])
annotation(figure1,'textbox',[0.135 0.55 0.05 0.1],'String',{'(a)'},...
    'FontWeight','bold','FontSize',12,'FontName','Arial','LineStyle','none');

%correction factor
sp2=subplot(2,2,2); hold on; box on; xlim([0 900]); ylim([.94 1.06]);
set(sp2,'Units','Inches','Position',[3.8 3.4 2.2 2.3]);
plot(test7_Tavg,test7_CF, 'ko', 'linewidth', .5,'MarkerEdgeColor','k','MarkerFaceColor','b','MarkerSize',5);
plot(test11_Tavg,test11_CF, 'kd', 'linewidth', .5,'MarkerEdgeColor','k','MarkerFaceColor','r','MarkerSize',5);
xlabel('HTHFS Average Temperature, {\itT}_{t,avg} (\circC)','FontSize',10,'FontName','Arial','FontWeight','bold')
ylabel('Calibration Correction Factor, {\itf}','FontSize',10,'FontName','Arial','FontWeight','bold')
h2=legend('{\itL} = 1.27 cm','{\itL} = 2.54 cm',2); legend('boxoff');
set(h2,'FontSize',8,'FontName','arial','Position',[4.85 5.15 1 .5])
annotation(figure1,'textbox',[0.6 0.55 0.05 0.1],'String',{'(b)'},...
    'FontWeight','bold','FontSize',12,'FontName','Arial','LineStyle','none');
```

```
%sensitivity
sp3=subplot(2,2,3); hold on; box on; xlim([0 900]); ylim([200 450]);
set(sp3,'Units','Inches','Position',[.8 .5 5.2 2.2]);
plot(test7_Tavg,test7_S1, 'ko', 'linewidth', 1,'MarkerEdgeColor','k','MarkerFaceColor','b','MarkerSize',6);
plot(test11_Tavg,test11_S1, 'kd', 'linewidth', 1,'MarkerEdgeColor','k','MarkerFaceColor','r','MarkerSize',6);
xlabel('HTHFS Average Temperature, {\itT}_{t,avg} (\circC)','FontSize',10,'FontName','Arial','FontWeight','bold')
ylabel('HTHFS Sensitivity, {\itS}_t (\muV W^{-1} cm^{2})','FontSize',10,'FontName','Arial','FontWeight','bold')
h3=legend('{\itL} = 1.27 cm','{\itL} = 2.54 cm',2);  legend('boxoff');
set(h3,'FontSize',8,'FontName','arial','Position',[4.8 2.1 1 .5])
annotation(figure1,'textbox',[.135 0.055 0.05 0.1],'String',{'(c)'},...
    'FontWeight','bold','FontSize',12,'FontName','Arial','LineStyle','none');


%% high temp. paper #2 figure: sensitivity vs temperature for all tests

%sensitivity
figure('Units','Inches','Position',[2 2 6.5 3]); hold on; box on;
xlim([50 900]); ylim([200 450]);
plot(test7_Tavg,test7_S1, 'ks', 'linewidth', .5,'MarkerEdgeColor','k','MarkerFaceColor','b','MarkerSize',5);
plot(test8_Tavg,test8_S1, 'kv', 'linewidth', .5,'MarkerEdgeColor','k','MarkerFaceColor','g','MarkerSize',5);
plot(test9_Tavg,test9_S1, 'kd', 'linewidth', .5,'MarkerEdgeColor','k','MarkerFaceColor','c','MarkerSize',5);
plot(test10_Tavg,test10_S1, 'k>', 'linewidth', .5,'MarkerEdgeColor','k','MarkerFaceColor','y','MarkerSize',5);
plot(test15_Tavg,test15_S1, 'ko', 'linewidth', .5,'MarkerEdgeColor','k','MarkerFaceColor','k','MarkerSize',5);
plot(test11_Tavg,test11_S1, 'k<', 'linewidth', .5,'MarkerEdgeColor','k','MarkerFaceColor','r','MarkerSize',5);
plot(test12_Tavg,test12_S1, 'kp', 'linewidth', .5,'MarkerEdgeColor','k','MarkerFaceColor','m','MarkerSize',5);
plot(test13_Tavg,test13_S1, 'k^', 'linewidth', .5,'MarkerEdgeColor','k','MarkerFaceColor','w','MarkerSize',5);
plot(test14_Tavg,test14_S1, 'kh', 'linewidth', .5,'MarkerEdgeColor','k','MarkerFaceColor','b','MarkerSize',5);
xlabel('HTHFS Average Temperature, {\itT}_{t,avg} (\circC)','FontSize',10,'FontName','Arial','FontWeight','bold')
ylabel('HTHFS Sensitivity, {\itS}_t (\muV W^{-1} cm^{2})','FontSize',10,'FontName','Arial','FontWeight','bold')
h1=legend('Test#1','Test#2','Test#3','Test#4','Test#5','Test#6','Test#7','Test#8','Test#9',2);  legend('boxoff');
set(h1,'FontSize',8,'FontName','arial','Units','Inches','Position',[5 1 .7 1.7])


%% high temp. paper #2 figure: low pressure tests

% Q(1:3,1)=test16_Tavg(1:3);
% test16_qdiff=test16_hf(1:3)-test16_hf(4:6)-(test16_qc(1:3)-test16_qc(4:6));
% Q(1:3,2)=test16_qdiff./test16_hf(1:3).*100;
% Q(1:3,3)=test16_qdiff./test16_cond(1:3).*100;
% test16_V1diff=test16_V1(1:3)-test16_V1(4:6);
% Q(1:3,4)=test16_V1diff./test16_V1(1:3).*100;
% test16_qh1diff=test16_V1diff.*(10^6)./test16_S1(1:3)-(test16_qh(1:3)-test16_qh(4:6));
% Q(1:3,5)=test16_qh1diff./test16_cond(1:3).*100;
% test16_V2diff=test16_V2(1:3)-test16_V2(4:6);
% Q(1:3,6)=test16_V2diff./test16_V2(1:3).*100;
% test16_qh2diff=test16_V2diff.*(10^6)./test16_S2(1:3)-(test16_qh(1:3)-test16_qh(4:6));
% Q(1:3,7)=test16_qh2diff./test16_cond(1:3).*100;
%% test16_S1diff=test16_S1(1:3)-test16_S1(4:6);
```

```
%% Q(1:3,7)=test16_S1diff./test16_S1(1:3).*100;
%% test16_S2diff=test16_S2(1:3)-test16_S2(4:6);
%% Q(1:3,8)=test16_S2diff./test16_S2(1:3).*100;
%% test16_CFdiff=test16_CF(1:3)-test16_CF(4:6);
%% Q(1:3,9)=test16_CFdiff./test16_CF(1:3).*100;
%
%
%
% Q(4:6,1)=test17_Tavg(1:3);
% test17_qdiff=test17_hf(1:3)-test17_hf(4:6)-(test17_qc(1:3)-test17_qc(4:6));
% Q(4:6,2)=test17_qdiff./test17_hf(1:3).*100;
% Q(4:6,3)=test17_qdiff./test17_cond(1:3).*100;
% test17_V1diff=test17_V1(1:3)-test17_V1(4:6);
% Q(4:6,4)=test17_V1diff./test17_V1(1:3).*100;
% test17_qh1diff=test17_V1diff.*(10^6)./test17_S1(1:3)-(test17_qh(1:3)-test17_qh(4:6));
% Q(4:6,5)=test17_qh1diff./test17_cond(1:3).*100;
% test17_V2diff=test17_V2(1:3)-test17_V2(4:6);
% Q(4:6,6)=test17_V2diff./test17_V2(1:3).*100;
% test17_qh2diff=test17_V2diff.*(10^6)./test17_S2(1:3)-(test17_qh(1:3)-test17_qh(4:6));
% Q(4:6,7)=test17_qh2diff./test17_cond(1:3).*100;
%% test17_S1diff=test17_S1(1:3)-test17_S1(4:6);
%% Q(4:6,7)=test17_S1diff./test17_S1(1:3).*100;
%% test17_S2diff=test17_S2(1:3)-test17_S2(4:6);
%% Q(4:6,8)=test17_S2diff./test17_S2(1:3).*100;
%% test17_CFdiff=test17_CF(1:3)-test17_CF(4:6);
%% Q(4:6,9)=test17_CFdiff./test17_CF(1:3).*100;
%
%
% Qs=sortrows(Q,1);
%
%%heat flux
% figure('Units','Inches','Position',[2 2 6.5 4]); hold on; box on;
% xlim([75 625]); ylim([0 3]);
% plot(test16_Tavg(1:3),test16_hf(1:3), 'kd', 'linewidth', 1,'MarkerEdgeColor','k','↩
    MarkerFaceColor','y','MarkerSize',6);
% plot(test16_Tavg(4:6),test16_hf(4:6), 'kd', 'linewidth', 1,'MarkerEdgeColor','k','↩
    MarkerFaceColor','m','MarkerSize',6);
% plot(test16_Tavg(7:9),test16_hf(7:9), 'kd', 'linewidth', 1,'MarkerEdgeColor','k','↩
    MarkerFaceColor','r','MarkerSize',6);
% plot(test17_Tavg(1:3),test17_hf(1:3), 'kd', 'linewidth', 1,'MarkerEdgeColor','k','↩
    MarkerFaceColor','g','MarkerSize',6);
% plot(test17_Tavg(4:6),test17_hf(4:6), 'kd', 'linewidth', 1,'MarkerEdgeColor','k','↩
    MarkerFaceColor','c','MarkerSize',6);
% plot(test17_Tavg(7:9),test17_hf(7:9), 'kd', 'linewidth', 1,'MarkerEdgeColor','k','↩
    MarkerFaceColor','b','MarkerSize',6);
% plot(test7_Tavg,test7_hf, 'kx');
% plot(test8_Tavg,test8_hf, 'k+');
% plot(test9_Tavg,test9_hf, 'k*');
% plot(test10_Tavg,test10_hf, 'kp');
% plot(test15_Tavg,test15_hf, 'kh');
% xlabel('HTHFS Average Temperature, {\itT}_{t,avg} (\circC)','FontSize',10,'FontName','↩
    Arial','FontWeight','bold')
% ylabel('Schmidt-Boelter Measured Heat Flux, {\itq}"_{sb,meas} (W cm^{-2})','FontSize↩
    ',10,'FontName','Arial','FontWeight','bold')
% h1=legend('Test#10 ({\itp}=101 kPa)','Test#10 ({\itp}=10 kPa)','Test#10 ({\itp}=1.0 kPa)↩
    ',...
%     'Test#11 ({\itp}=101 kPa)','Test#11 ({\itp}=10 kPa)','Test#11 ({\itp}=1.0 kPa)',2); ↩
    legend('boxoff');
% set(h1,'FontSize',8,'FontName','arial','Units','Inches','Position',[.8 2 1.5 1.5]);


%% high temp. paper #2 figure: heat flux and sensitivity versus temperature with error ↩
    bars
```

```
%heat flux
figure1=figure('Units','Inches','Position',[2 1 6.5 6]); hold on;
sp1=subplot(2,1,1); hold on; box on; xlim([0 900]); ylim([0 8]);
set(sp1,'Units','Inches','Position',[.8 3.4 5.2 2.2]);
errorbar(Tavg1,qcavg1,uqc1, 'ks','linewidth',.8,'MarkerEdgeColor','k','MarkerFaceColor','k','MarkerSize',3);
plot(Tavg1,qsbavg1, 'kd', 'linewidth', 1,'MarkerEdgeColor','k','MarkerFaceColor','w','MarkerSize',4);
errorbar(Tavg2,qcavg2,uqc2, 'ro','linewidth',.8,'MarkerEdgeColor','r','MarkerFaceColor','r','MarkerSize',3);
plot(Tavg2,qsbavg2, 'r^', 'linewidth', 1,'MarkerEdgeColor','r','MarkerFaceColor','w','MarkerSize',4);
xlabel('HTHFS Average Temperature, {\itT}_{t,avg} (\circC)','FontSize',10,'FontName','Arial','FontWeight','bold')
ylabel('Schmidt-Boelter Heat Flux, {\itq}"_{sb} (W cm^{-2})','FontSize',10,'FontName','Arial','FontWeight','bold')
h1=legend('Test#1-5 Modeled Average, {\it L} = 1.27 cm','Test#1-5 Measured Average, {\it L} = 1.27 cm',...
    'Test#6-9 Modeled Average, {\it L} = 2.54 cm','Test#6-9 Measured Average, {\it L} = 2.54 cm',3); legend('boxoff');
set(h1,'FontSize',8,'FontName','Arial','Units','Inches','Position',[.9 4.7 2 .7])
annotation(figure1,'textbox',[0.835 0.55 0.05 0.1],'String',{'(a)'},...
    'FontWeight','bold','FontSize',12,'FontName','Arial','LineStyle','none');

%sensitivity
sp2=subplot(2,1,2); hold on; box on; xlim([0 900]); ylim([0 500]);
set(sp2,'Units','Inches','Position',[.8 .5 5.2 2.2]);
xlim([0 900]); ylim([0 520]);
plot(T,St1_1, 'k-','linewidth',1);
errorbar(Tavg1,S1avg1,Uavg1, 'ks','linewidth',.8,'MarkerEdgeColor','k','MarkerFaceColor','k','MarkerSize',4);
errorbar(Tavg2,S1avg2,Uavg2, 'ro','linewidth',.8,'MarkerEdgeColor','r','MarkerFaceColor','r','MarkerSize',3);
% plot(TL,SL1,'bo');
xlabel('HTHFS Average Temperature, {\itT}_{t,avg} (\circC)','FontSize',10,'FontName','Arial','FontWeight','bold')
ylabel('HTHFS Sensitivity, {\itS}_t (\muV W^{-1} cm^2)','FontSize',10,'FontName','Arial','FontWeight','bold')
h2=legend('Theoretical','Test#1-5 Average, {\it L} = 1.27 cm','Test#6-9 Average, {\it L} = 2.54 cm',3); legend('boxoff');
set(h2,'FontSize',8,'FontName','arial','Position',[1 .75 1 .5])
annotation(figure1,'textbox',[.835 0.055 0.05 0.1],'String',{'(b)'},...
    'FontWeight','bold','FontSize',12,'FontName','Arial','LineStyle','none');
```

C.1.2 Function M-Files

Air_Properties.m:

```
function [ALPHA,BETA,MU,NU,RHO,Pr,Cp,K]=Air_Properties(Tfilm)
%Air at atmospheric pressure
%Tfilm is absolute temperature in Kelvin

%Source: Incropera and DeWitt 4th edition
% T_mat=300:50:900; %abs. temp. (K)
% A_mat=[22.5 29.9 38.3 47.2 56.7 66.7 76.9 87.3 98 109 120 131 143].*10^-6; %alpha vs. abs. temp. (m^2/s)
% N_mat=[15.89 20.92 26.41 32.39 38.79 45.57 52.69 60.21 68.1 76.37 84.93 93.8 102.9].*10^-6; %nu vs. abs. temp. (m^2/s)
```

```
% K_mat=[26.3 30 33.8 37.3 40.7 43.9 46.9 49.7 52.4 54.9 57.3 59.6 62].*10^-3; %k vs. abs. temp. (W/(m*K))
%
% pa=polyfit(T_mat,A_mat,2);
% pn=polyfit(T_mat,N_mat,2);
% pk=polyfit(T_mat,K_mat,2);

pa=[6.4116e-011 1.2569e-007 -2.1777e-005]; %these coefficients are from the above commented code
pn=[7.4422e-011 5.6380e-008 -7.9190e-006];
pk=[-3.0969e-008 9.6306e-005 2.0320e-004];


ALPHA=pa(1).*Tfilm.^2+pa(2).*Tfilm+pa(3); %[m^2/s]
NU=pn(1).*Tfilm.^2+pn(2).*Tfilm+pn(3); %[m^2/s]
K=pk(1).*Tfilm.^2+pk(2).*Tfilm+pk(3); %[W/(m K)]
Cp=1008; %[J/(kg K)]
RHO=K./(ALPHA.*Cp); %[kg/m^3]
MU=RHO.*NU; %[N*s/m^2]
BETA=1./Tfilm; %[1/K]
Pr=NU./ALPHA; %Prandtl number

% T=200:1:2000;
% Aair=pa(1).*T.^2+pa(2).*T+pa(3);
% Nair=pn(1).*T.^2+pn(2).*T+pn(3);
% Kair=pk(1).*T.^2+pk(2).*T+pk(3);
%
% figure; hold on; box on;
% plot(T_mat,A_mat, 'bo', 'linewidth', 1);
% plot(T,Aair, 'b-', 'linewidth', 1);
% xlabel('Temperature, T (K)','FontSize',10,'FontName','Helvetica','FontWeight','bold')
% ylabel('Air Prandtl Number','FontSize',10,'FontName','Helvetica','FontWeight','bold')
%
% figure; hold on; box on;
% plot(T_mat,K_mat, 'ro', 'linewidth', 1);
% plot(T,Kair, 'r-', 'linewidth', 1);
% xlabel('Temperature, T (K)','FontSize',10,'FontName','Helvetica','FontWeight','bold')
% ylabel('Air Thermal Conductivity, \kappa (W m^{-1} K^{-1})','FontSize',10,'FontName','Helvetica','FontWeight','bold')
%
% figure; hold on; box on;
% plot(T_mat,N_mat, 'ko', 'linewidth', 1);
% plot(T,Nair, 'k-', 'linewidth', 1);
% xlabel('Temperature, T (K)','FontSize',10,'FontName','Helvetica','FontWeight','bold')
% ylabel('Air Kinematic Viscosity, \nu (m^{2} s^{-1})','FontSize',10,'FontName','Helvetica','FontWeight','bold')
```

Cavity_Discretization.m:

```
function [H,C,W,N,l,r]=Cavity_Discretization(rs,Lc,rc,T)
%code for setting up the geoemtry of the calibration enclosure
%cavity discretization
H=4; %number of areas for which the hot plate is to be discretized
C=4; %number of areas for which the cold plate is to be discretized
W=50; %number of areas for which the adiabatic sidewall is to be discretized
N=H+C+W; %number of surfaces inside the cavity

l=ones(W,length(Lc));
r=ones(H+C,length(Lc));

for i=1:length(Lc)
```

```
    l(:,i)=Lc(i)./W; %all segments same area
end

%change in cavity dimensions due to thermal expansion
CTE_HX=16.3*10^-6; %thermal expansion coefficient for inconel HX from 20-900 C (Matweb) [C↩
    ^-1]

%user specified discretized cavity dimensions (only for disk and ring radii)
r(1,:)=((9/64)*.0254).*(1+CTE_HX.*(T(1,:)-25));
r(2,:)=(0.35*.0254).*(1+CTE_HX.*(T(1,:)-25));
r(3,:)=(0.75*.0254).*(1+CTE_HX.*(T(1,:)-25));
r(4,:)=rc; %[m]

r(5,:)=rs; %sensing area radius [m]
r(6,:)=.5*.0254;
r(7,:)=0.75*.0254;
r(8,:)=rc; %[m]

%%automatically calculated discretized cavity dimensions (uniform (dr)radii)
% r(1)=rc/H;
% for i=2:H
%     r(i)=r(i-1)+rc/H;
% end
% r(H+1)=rc/C;
% for i=H+2:H+C
%     r(i)=r(i-1)+rc/C;
% end

%%automatically calculated discretized cavity dimensions (equal area segments)
% Ap=pi*rc^2; Adhp=Ap/H;
% for i=1:H+C
%     if i==1
%         r(i)=(Adhp/pi)^.5; %central disk - hot plate
%     elseif i<=H
%         r(i)=(Adhp/pi+r(i-1)^2)^.5;
%     elseif i==H+1
%         r(i)=rs;
%     elseif i==H+2
%         r(i)=rb;
%     elseif i==H+C
%         r(i)=rc;
%     else
%         Adcp=pi*(rc^2-rb^2)/(C-2);
%         r(i)=(Adcp/pi+r(i-1)^2)^.5;
%     end
% end
```

Cylindrical_Cavity_View_Factors.m:

```
function [F]=Cylindrical_Cavity_View_Factors(L,D,rc,H,C,W,N,r)
%view factors for right, cylindrical enclosure with N discrete surfaces
[nan,ncol]=size(r); %# of steady-state thermal events

%cavity areas
for z=1:ncol
    for i=1:N
        if i<=H+C
            if i==1 || i==H+1
                A(i,z)=pi*r(i,z)^2; %central disk - hot plate
            else
                A(i,z)=pi*(r(i,z)^2-r(i-1,z)^2);
```

```
            end
        else
            A(i,z)=pi*D(z)*L(z)/W;
        end
    end
end

%view factor calculation
F=zeros(N,N,ncol); %zero out view factor matrix, size NxN
%numbering system: surface 1:H - hot plate; surface H+1:H+1+C - cold plate; surface H+C+1:N - sidewall

%anonymous functions for view factor calculation:
%see URL:[http://www.engr.uky.edu/rtl/Catalog/] for each geometric configuration (same names as listed here)
C41 = @(r1,r2) (.5*(1+(1+r2^2)/r1^2-((1+(1+r2^2)/r1^2)^2-4*(r2/r1)^2)^.5)); %r1=r(1)/L
C47 = @(h,r2,r3) (.5*(r3^2-r2^2-((1+r3^2+h^2)^2-4*r3^2)^.5+((1+r2^2+h^2)^2-4*r2^2)^.5)); %H=L/r(1), r2=rsmall/r(1), r3=rbig/r(1)
C52 = @(h,r2,r3,r4) (1/(2*(r2^2-1))*(((r2^2+r3^2+h^2)^2-(2*r2*r3)^2)^.5-((r2^2+r4^2+h^2)^2-(2*r2*r4)^2)^.5+...
    ((1+r4^2+h^2)^2-(2*r4)^2)^.5-((1+r3^2+h^2)^2-(2*r3)^2)^.5)); %h=L/r(i-1), r2=r(i)/r(i-1), r3=r(j-1)/r(i-1), r4=r(j)/r(i-1)
C78 = @(x) ((1+x)-(1+x^2)^.5); %x=L/W/D
C82 = @(r,n,rc,L) ((W*r^2)/(4*rc*L)*(-1*(2*n+1)*(L/(W*r))^2-(((n*L/(W*r))^2+(rc/r)^2+1)^2-4*(rc/r)^2)^.5+...
    ((((n+1)*L/(W*r))^2+(rc/r)^2+1)^2-4*(rc/r)^2)^.5)); %r=r(1,H+1), n=j-i-(H+W)
C85 = @(c1,c2,r1,r2) (-1/(4*(c2-c1))*((c2^4+2*c2^2*(1+r1^2)+(1-r1^2)^2)^.5-(c2^4+2*c2^2*(1+r2^2)+(1-r2^2)^2)^.5+...
    (c1^4+2*c1^2*(1+r2^2)+(1-r2^2)^2)^.5-(c1^4+2*c1^2*(1+r1^2)+(1-r1^2)^2)^.5)); %c1=(n)*L/(W*rc), c2=(n+1)*L/(W*rc), r1=r(i-1)/rc, r2=r(i)/rc
C87 = @(l,n) (1/(4*l)*(2*l^2+2*l*(n+1)*(4+(l*(n+1))^2)^.5-l*n*(4+(l*n)^2)^.5-(l*(n+2))*(4+(l*(n+2))^2)^.5));

%1. calculate diagonal - only contribution from inner cylinder seeing itself
for z=1:ncol
    for i=H+C+1:N
        F(i,i,z)=C78(L(z)/W/D(z));
    end
    %2. calculate upper triangle
    for i=1:N-1 %rows
        for j=2:N %columns
            if j>i %upper triangular portion
                if i==1 && j==H+1 %hot center disk to opposing center disk
                    F(i,j,z)=C41(r(i,z)/L(z),r(j,z)/L(z));

                elseif i==1 && j>H+1 && j<=H+C %hot center disk to opposing rings
                    F(i,j,z)=C47(L(z)/r(i,z),r(j-1,z)/r(i,z),r(j,z)/r(i,z));

                elseif i==1 && j>H+C %hot center disk to sidewall rings
                    F(i,j,z)=C82(r(i,z),j-H-C-1,rc(z),L(z))*A(j,z)/A(i,z);

                elseif i<=H && j==H+1 %hot rings to opposing center disk
                    F(i,j,z)=C47(L(z)/r(j,z),r(i-1,z)/r(j,z),r(i,z)/r(j,z))*A(j,z)/A(i,z);

                elseif i<=H && j>=H+2 && j<=H+C %hot rings to opposing cold rings
                    F(i,j,z)=C52(L(z)/r(i-1,z),r(i,z)/r(i-1,z),r(j-1,z)/r(i-1,z),r(j,z)/r(i-1,z));

                elseif i<=H && j>H+C %hot rings to sidewall rings
                    F(i,j,z)=C85((j-H-C-1)*L(z)/(W*rc(z)),(j-H-C)*L(z)/(W*rc(z)),r(i-1,z)/rc(z),r(i,z)/rc(z))*A(j,z)/A(i,z);

                elseif i==H+1 && j>H+C %cold center disk to sidewall rings
                    F(i,j,z)=C82(r(i,z),H+C+W-j,rc(z),L(z))*A(j,z)/A(i,z);
```

```
                elseif i<=H+C && j>H+C %cold rings to sidewall rings
                    F(i,j,z)=C85((H+C+W-j)*L(z)/(W*rc(z)),(H+C+W+1-j)*L(z)/(W*rc(z)),r(i-1,z)/rc(z),r(i,z)/rc(z))*A(j,z)/A(i,z);

                elseif i>=H+C+1  %condition for inner cylinder viewing inner cylinder
                    F(i,j,z)=C87(L(z)/W/rc(z),j-i-1);
                else
                end
            else
            end
        end
    end

    %3. calculate lower triangle using reciprocity
    for i=2:N %rows
        for j=1:N-1 %columns
            if i>j %lower triangular portion
                F(i,j,z)=F(j,i,z)*A(j,z)/A(i,z);
            else
            end
        end
    end
end
```

Adiabatic_Sidewall_Radiosity_Model.m:

```
function [Q]=Adiabatic_Sidewall_Radiosity_Model(e,F,T)
%heat flux model for reradiating sidewall (zero net radiation heat transfer through sidewall)
[N,nan,nan]=size(F);
[m, ncol]=size(T);
sigma=5.67*10^-8; %Stefan-Boltzmann [W/m^2/K^4]
d=zeros(N,N);
K=zeros(N,N);
P=zeros(N,1);

%fill matrix and load vector
for z=1:ncol
    for i=1:N %all rows (ith surface)
        for j=1:N %all columns
            if i==j
                d(i,j)=1; %Kronecker delta
            end
            if j<=m
                K(i,j)=(d(i,j)/e(j,z)-F(i,j,z)*(1-e(j,z))/e(j,z)); %left of partitioned matrix
                p(i,j)=(d(i,j)-F(i,j,z))*sigma*T(j,z)^4;
            elseif j>m
                K(i,j)=(-d(i,j)+F(i,j,z));
            end
        end
        P(i,z)=sum(p(i,:));
    end
    %solve radiosity matrix
    Q(:,z)=K\P(:,z); %solves for q'' in {W/m^2)
end
```

Sidewall_Heat_Loss_Radiosity_Model.m:

```
function [qpp,Touter,Tinner,e]=Sidewall_Heat_Loss_Radiosity_Model(e,F,H,C,W,T,D,L,testnum)
%model for estimating sidewall radial heat loss
rc=D/2;
[N,nan,nan]=size(F);
sigma=5.67*10^-8; %Stefan-Boltzmann [W/m^2/K^4]
[nan, ncol]=size(T);
d=zeros(N,N);
K=zeros(N,N);
P=zeros(N,1);

%W is number of known DOF (heat fluxes)
m=N-W; %number of unknown heat fluxes

%sidewall heat loss
Tinf=295;  %[K]
rwo=1.5*.0254; %sidewall outer radius [m]
rs=2.5*.0254; %insulation outer radius [m]
eins=0.3; %insulation emissivity
maxiterations=10;
for z=1:ncol
    n=1;
    while n<=maxiterations
        for i=1:N %all rows (ith surface)
            for j=1:N %all columns
                if i==j
                    d(i,j)=1; %Kronecker delta
                else
                end
                if j<=m
                    K(i,j)=(d(i,j)/e(j,z)-F(i,j,z)*(1-e(j,z))/e(j,z)); %left of ↩
                        partitioned matrix
                    p(i,j)=(d(i,j)-F(i,j,z))*sigma*T(j,z)^4;
                elseif j>m
                    K(i,j)=(-d(i,j)+F(i,j,z));
                    if n>=2
                        p(i,j)=(-d(i,j)/e(j,z)+F(i,j,z)*(1-e(j,z))/e(j,z))*(-1/Rtotpp(z,n↩
                            -1)*(Twi(z,n-1)-Tinf)); %allowing for small heat loss
                    end
                else
                end
            end
            P(i,z)=sum(p(i,:));
        end
        %solve radiosity matrix and nate to match sidewall losses
        q(:,z,n)=K\P(:,z); %solves for q'' in {W/m^2)

        Jw(:,z,n)=q(m+1:N,z,n); %[W/m^2]
        Tw(:,z,n)=real((Jw(:,z,n)./sigma).^(.25));

        Twi(z,n)=mean(Tw(:,z,n));

        if n==1
            Ts(z,n)=0.2*Twi(z,n)+0.8*Tinf;
        elseif n==2
            if Qdiff(z,n-1)>0
                Ts(z,n)=Ts(z,n-1)+5;
            else
                Ts(z,n)=Ts(z,n-1)-5;
            end
        else
            %newton's method for root finding:
            Ts(z,n)=real(Ts(z,n-1)-(Qdiff(z,n-1)*(Ts(z,n-1)-Ts(z,n-2)))/(Qdiff(z,n-1)-↩
                Qdiff(z,n-2)));
```

```
        end

        %conduction through sidewall
        [ksw(z,n),kins(z,n),kins2(z,n),e(H+C+1:N,z)]=Sidewall_Properties(Twi(z,n),Ts(z,n));

        if testnum==100
            Rcw(z,n)=1/(2*pi*L(z))*(log(rwo/rc(z))/kins2(z,n)+log(rs/rwo)/kins(z,n));
        else
            Rcw(z,n)=1/(2*pi*L(z))*(log(rwo/rc(z))/ksw(z,n)+log(rs/rwo)/kins(z,n));
        end
        Qcw(z,n)=(Twi(z,n)-Ts(z,n))/Rcw(z,n);

        %convection and radiation outer boundary condition
        [nan,nan,nan,nan,nan,nan,nan,nan,nan,nan,nan,hconv(z,n)]=Air_Natural_Convection(Ts(z,n),Tinf,L(z));
        hrad(z,n)=eins*sigma*(Ts(z,n)+Tinf)*(Ts(z,n)^2+Tinf^2);
        Rsinf(z,n)=1/(2*pi*L(z)*rs*(hconv(z,n)+hrad(z,n)));
        Qsinf(z,n)=(Ts(z,n)-Tinf)/Rsinf(z,n);

        Rtot(z,n)=Rsinf(z,n)+Rcw(z,n);
        Rtotpp(z,n)=Rtot(z,n)*pi*D(z)*L(z);
        Qdiff(z,n)=Qcw(z,n)-Qsinf(z,n);
        n=n+1;
    end
end
Touter=Ts(:,end);
Tinner=Twi(:,end);
qpp=q(:,:,end);
```

Sidewall_Properties.m:

```
function [kss,kins,kins2,ess]=Sidewall_Properties(Twi,Ts)
%all absolute temperatures in Kelvin

T1=Twi;
T2=(Ts+Twi)/2;
T3=0.8*Twi+0.2*Ts;

%304 stainless steel: Incropera and DeWitt 4th edition
T_ss=200:200:1200; %abs. temp. (K)
K_ss=[12.6 16.6 19.8 22.6 25.4 28]; %k vs. abs. temp. (W/(m*K))
pkss=polyfit(T_ss,K_ss,2);

%Zircar alumina mat: see http://www.zircarceramics.com/
T_ins=273+[315 540 760 980]; %abs. temp. (K)
K_ins=[.07 .09 .13 .17]; %k vs. abs. temp. (W/(m*K))
pkins=polyfit(T_ins,K_ins,1);

%Zircar ZAL-45 rigid board
T_ins2=273+[250 525 800 1075]; %abs. temp. (K)
K_ins2=[.16 .2 .23 .29]; %k vs. abs. temp. (W/(m*K))
pkins2=polyfit(T_ins2,K_ins2,1);

%18-8 oxidized stainless steel emissivity: pg. 1216 curve 42 Touloukian
%thermal radiative properties metallic elements and alloys v.7
T_s=[431 499 550 649 752 805]; %abs. temp. (K)
e_s=[0.372 0.413 0.444 0.505 0.567 0.602]; %total hemispherical emissivity
pks=polyfit(T_s,e_s,1);

kss=pkss(1).*T1.^2+pkss(2).*T1+pkss(3);
```

```
kins=pkins(1).*T2+pkins(2);
kins2=pkins2(1).*T3+pkins2(2);
ess=pks(1).*T1+pks(2);

% T=200:1:2000;
% Kss=pkss(1).*T.^2+pkss(2).*T+pkss(3);
% Kins=pkins(1).*T+pkins(2);
% Kins2=pkins2(1).*T+pkins2(2);
%
% figure; hold on; box on;
% plot(T_ss,K_ss, 'ro', 'linewidth', 1);
% plot(T,Kss, 'r-', 'linewidth', 1);
% xlabel('Temperature, T (K)','FontSize',10,'FontName','Helvetica','FontWeight','bold')
% ylabel('SS 304 Thermal Conductivity, \kappa (W m^{-1} K^{-1})','FontSize',10,'FontName'
    ,'Helvetica','FontWeight','bold')
%
% figure; hold on; box on;
% plot(T_ins,K_ins, 'bo', 'linewidth', 1);
% plot(T,Kins, 'b-', 'linewidth', 1);
% xlabel('Temperature, T (K)','FontSize',10,'FontName','Helvetica','FontWeight','bold')
% ylabel('Fibrous Insulation Thermal Conductivity, \kappa (W m^{-1}K^{-1})','FontSize'
    ,10,'FontName','Helvetica','FontWeight','bold')
%
% figure; hold on; box on;
% plot(T_ins2,K_ins2, 'go', 'linewidth', 1);
% plot(T,Kins2, 'g-', 'linewidth', 1);
% xlabel('Temperature, T (K)','FontSize',10,'FontName','Helvetica','FontWeight','bold')
% ylabel('Rigid Insulation Thermal Conductivity, \kappa (W m^{-1}K^{-1})','FontSize',10,'
    FontName','Helvetica','FontWeight','bold')
```

Sidewall_Temperature_Emissivity.m:

```
function [Tmat,emat]=Sidewall_Temperature_Emissivity(L,H,C,W,T,e,testnum)
%all absolute temperatures in Kelvin
[nrow,ncol]=size(T);

Tmat=zeros(W,ncol);
emat=e;

%18-8 oxidized stainless steel emissivity: pg. 1216 curve 42 Touloukian
%thermal radiative properties metallic elements and alloys v.7
T_s=[431 499 550 649 752 805]; %abs. temp. (K)
e_s=[0.372 0.413 0.444 0.505 0.567 0.602]; %total hemispherical emissivity
pes=polyfit(T_s,e_s,1);

%determine the number of sections assigned to the air gap space
l=L(1)/W; %discrete sidewall section length (m)
lgap=1/16*0.0254; %air gap space between plate surface and sidewall [m]
if l>lgap
    ngap=1;
else
    ngap=floor(lgap/l); %round down
end
W2=W-2*ngap;

%air gap temperature drops
delta_hot=T(1,:)-T(2,:); dt_h=delta_hot/ngap;
delta_cold=T(nrow-1,:)-T(nrow,:); dt_c=delta_cold/ngap;

%polynomial for sidewall temperature
T2=T(2:nrow-1,:);
```

```
[nro,nan]=size(T2);
X=0:(L(1)-2*lgap)/(nro-1):L(1)-2*lgap;
for j=1:ncol
    if testnum>=16
        p(j,:)=polyfit(X',T2(:,j),1);
    else
        p(j,:)=polyfit(X',T2(:,j),3);
    end
end

x=0;
dx=(L(1)-2*lgap)/(W2-1);
Tmat(1,:)=T(1,:)-0.5.*dt_h;
emat(H+C+1,:)=0.999;
for i=2:W
    if i<=ngap
        emat(H+C+i,:)=0.999;
        Tmat(i,:)=Tmat(i-1,:)-dt_h;
    elseif i<=ngap+W2
        for j=1:ncol
            if testnum>=16
                Tmat(i,j)=p(j,1).*x+p(j,2);
            else
                Tmat(i,j)=p(j,1).*x.^3+p(j,2).*x.^2+p(j,3).*x+p(j,4);
            end
            if testnum>=15
                emat(H+C+i,j)=0.86;
            else
                emat(H+C+i,j)=pes(1).*Tmat(i,j)+pes(2);
            end
        end
        x=x+dx;
    else
        emat(H+C+i,:)=0.999;
        if i==ngap+W2+1
            Tmat(i,:)=Tmat(i-1,:)-0.5*dt_c;
        else
            Tmat(i,:)=Tmat(i-1,:)-dt_c;
        end
    end
end

% xx=0:(L-2*lgap)/((nro-1)*100):L-2*lgap;
% Tt=p(1,1).*xx.^3+p(1,2).*xx.^2+p(1,3).*xx+p(1,4);
%
% figure; hold on; box on;
% plot(X,T2(:,1), 'ro', 'linewidth', 1);
% plot(xx,Tt, 'r-', 'linewidth', 1);
% xlabel('Distance, x (m)','FontSize',10,'FontName','Helvetica','FontWeight','bold')
% ylabel('Sidewall Temperature, T (K)','FontSize',10,'FontName','Helvetica','FontWeight','↩
    bold')
```

Known_Temperatures_Radiosity_Model.m:

```
function [Q]=Known_Temperatures_Radiosity_Model(e,F,T)
%model for known temperatures throughout the calibration enclosure
[N, ncol]=size(T);
sigma=5.67*10^-8; %Stefan-Boltzmann [W/m^2/K^4]
d=zeros(N,N);
K=zeros(N,N);
P=zeros(N,1);
```

```
8
%fill matrix and load vector
for z=1:ncol
    for i=1:N %all rows (ith surface)
        for j=1:N %all columns
13          if i==j
                d(i,j)=1; %Kronecker delta
            end
            K(i,j)=(d(i,j)/e(j,z)-F(i,j,z)*(1-e(j,z))/e(j,z));
            p(i,j)=(d(i,j)-F(i,j,z))*sigma*T(j,z)^4;
18      end
        P(i,z)=sum(p(i,:));
    end
    %solve radiosity matrix
    Q(:,z)=K\P(:,z); %solves for q'' in {W/m^2)
23 end
```

HTHFS_Theory.m:

```
function [Tt, rho, C_t, Kbar_1, St_1, St_1_2, SAB, t]=HTHFS_Theory(N,W,L)
2 %HTHFS theoretical operation

%HTHFS specifications:
%N = number of thermopile junctions
%W = thermopile width (diced to this dimension) [m]
7 %L = thermopile length in direction of heat transfer [m]
% N=5; %number of HTHFS thermopile junctions
% W=0.2*.0254; %HTHFS width (m)
% L=0.125*.0254; %HTHFS thickness (m)


12
%% experimental conductivity and heat capacity data
%thermal conductivity
TT=273:.1:1500; %temperature (K)
Tt=TT-273;
17 Tk1=[273 373 473 573 673 773 873 1073 1273]; %[K]
K1=[29 25 22 17 13.5 12 10 8.5 7.2]; %ZTA thermal conductivity (W/m/K) Source: Rohde
Tk2=[363.4 389.2 405.1 441.3 473.2 573.2 673.2 773.2]; %[K]
K2=[29.3 29.7 30.1 30.7 31.8 35 38.1 41.2]; %Alumel thermal conductivity (W/m/K) Source: ↩
    Touloukian 1970
Tk3=[373.2 473.2 573.2 673.2 773.2 794.7]; %[K]
22 K3=[19 20.9 22.8 24.7 26.6 27.1]; %Chromel thermal conductivity (W/m/K) Source: Touloukian↩
     1970

p1=polyfit(Tk1,K1,2);
p2=polyfit(Tk2,K2,2);
p3=polyfit(Tk3,K3,2);
27
%ZTA thermal conductivity calculation
vd=.15; %volume fraction of dispersed phase (zirconia)
kd=2.3; %thermal conductivity of dispersed phase (10 mole percent yttria-stabilized ↩
    zirconia); reference: Bansal 2005
kc=5.85+(15360.*exp(-.002.*(TT-273)))./(TT+243); %thermal conductivity of continuous phase↩
     (alumina) at temp; reference: Munro 1997
32 K1poly=kc.*(1+2*vd.*(1-kc./kd)./(2.*kc./kd+1))./(1-vd.*(1-kc./kd)./(kc./kd+1)); %Maxwell-↩
    Eucken Model; reference: Kingery 1976
% K1poly=p1(1).*TT.^2+p1(2).*TT+p1(3);
% K1poly=p1(1).*TT.^3+p1(2).*TT.^2+p1(3).*TT+p1(4);
% K2poly=p2(1).*TT+p2(2);
K2poly=p2(1).*TT.^2+p2(2).*TT+p2(3);
37 % K3poly=p3(1).*TT+p3(2);
```

```
K3poly=p3(1).*TT.^2+p3(2).*TT+p3(3);

%specific heat capacity
Tc=[300 400 500 600 700 800 900 1000 1100 1200 1300 1400]; %[K] applies to heat capacity ↩
    data below
C1_1=4184.*[.1857 .2291 .2508 .264 .2731 .2801 .2858 .2907 .2952 .2993 .3031 .3068]; %↩
    Alumina specific heat [J/(kg K)] Source: Touloukian 1970
C1_2=4184.*[.1091 .1238 .1314 .1362 .1397 .1425 .1448 .1469 .1489 .1507 .1524 .1541]; %↩
    Zirconia specific heat [J/(kg K)] Source: Touloukian 1970
C2=4184.*[.1135 .1153 .1171 .1189 .1207 .1225 .1243 .1261 .1279 .1296 .1314 .133]; %Alumel↩
     specific heat [J/(kg K)] Source: Touloukian 1970
C3=4184.*[.1024 .1066 .1109 .1152 .1195 .1237 .1280 .1323 .1366 .1408 .1451 .1490]; %↩
    Chromel specific heat [J/(kg K)] Source: Touloukian 1970

p4=polyfit(Tc,C2,2);
p5=polyfit(Tc,C3,2);

C2poly=p4(1).*TT.^2+p4(2).*TT+p4(3);
C3poly=p5(1).*TT.^2+p5(2).*TT+p5(3);

%Seebeck vs. Temperature ITS-90
co=[-0.176004136860E-01;
    0.389212049750E-01;
    0.185587700320E-04;
    -0.994575928740E-07;
    0.318409457190E-09;
    -0.560728448890E-12;
    0.560750590590E-15;
    -0.320207200030E-18;
    0.971511471520E-22;
    -0.121047212750E-25];

ao=[0.118597600000E+00; -0.118343200000E-03;  0.126968600000E+03];


E=ao(1).*exp(ao(2).*(Tt-ao(3)).^2)+co(1)+co(2).*Tt+co(3).*Tt.^2+co(4).*Tt.^3+co(5).*Tt.^4+↩
    co(6).*Tt.^5+...
    co(7).*Tt.^6+co(8).*Tt.^7+co(9).*Tt.^8+co(10).*Tt.^9;

SAB=diff(E);
SAB(end+1)=SAB(end);
SAB=SAB.*10^4; %RSC for K-type TC's [microV/C]
% SAB=E./Tt.*1000;

%% sensitivity and specific heat calculation
%derivation can be found in logbook #2 pages 13-16, 33
t1=.01*.0254; %ZTA [m]
t2=.012*.0254; %Alumel [m]
t3=.034*.0254; %Chromel [m]
l1=L-t2; %ZTA [m]
l3=L-2*t2; %Chromel [m]
N1=2*N; N2=N; N3=N+1;
t=N1*t1+N2*t2+N3*t3; %thermopile length in direction of stack
A=t*W; %thermopile surface area
V=L*W*(N1*t1+N2*t2+N3*t3); %thermopile total volume [m^3]
V1=W*(N1*l1*t1); %ZTA / ceramic volume [m^3]
V3=W*(N3*l3*t3); %chromel volume [m^3]
V2=V-(V1+V3);  %alumel volume [m^3]
rho1_1=3960; m1_1=rho1_1*0.85*V1; %Alumina density [kg/m^3] and mass [kg]
rho1_2=6000; m1_2=rho1_2*0.15*V1; %Zirconia density [kg/m^3] and mass [kg]
m1=m1_1+m1_2; mf1_1=m1_1/m1; mf1_2=m1_2/m1;
C1=mf1_1.*C1_1+mf1_2.*C1_2;
p6=polyfit(Tc,C1,5);
C1poly=p6(1).*TT.^5+p6(2).*TT.^4+p6(3).*TT.^3+p6(4).*TT.^2+p6(5).*TT+p6(6);
```

```
rho2=8610; m2=rho2*V2; %Alumel density [kg/m^3] and mass [kg]
rho3=8730; m3=rho3*V3; %Chromel density [kg/m^3] and mass [kg]
m=m1+m2+m3; %thermopile total mass [kg]
rho=m/V; %thermopile composite density [kg/m^3]
mf1=m1/m; mf2=m2/m; mf3=m3/m; %mass fractions
C_t=mf1.*C1poly+mf2.*C2poly+mf3.*C3poly; %HTHFS composite specific heat capacity


%Method1: Assumes cross-sections normal to the direction of heat flow are isothermal
%Sensor Surface
Ltop=t2;
As1=W*(2*t1+t2+t3*(1+1/N));
At1=W*t1; At2=As1-At1;
RttA=(Ltop*As1).*(K1poly.*At1+K2poly.*At2).^-1;
%Sensor Core
Lcore=l3;
Ac1=2*t1*W; Ac2=t2*W; Ac3=As1-(Ac1+Ac2);
RtcA=(Lcore*As1).*(K1poly.*Ac1+K2poly.*Ac2+K3poly*Ac3).^-1;
R1totA=RtcA+2.*RttA;
St_1=N.*SAB.*R1totA.*(100^2); %lower bound
Kbar_1=(Lcore+2*Ltop)./R1totA;

%Method1_2: does not include top and bottom layer for sensitivity - this is
%the most correct way to model the sensor
St_1_2=N.*SAB.*RtcA.*(100^2);

%Method2: Assumes surfaces parallel to the direction of heat flow are
%adiabatic - very similar to Method1
As2=As1/2;
As21=.5*t2*W;
As22=t1*W;
As23=As2-(As21+As22);
R1=(l1+t2)/As21./K2poly;
R2=(1/As22).*(t2./K2poly+l1./K1poly);
R3=(1/As23).*((2*t2)./K2poly+l3./K3poly);
R2totA=As2./(1./R1+1./R2+1./R3);
St_2=N.*SAB.*R2totA.*(100^2); %upper bound


%% plots
% %heat capacity
% figure; hold on; box on;
% % plot(Tc-273,C1_1, 'mo','linewidth',1);
% % plot(Tc-273,C1_2, 'co','linewidth',1);
% plot(Tc-273,C1, 'md','linewidth',1);
% plot(Tc-273,C2, 'rs','linewidth',1);
% plot(Tc-273,C3, 'bo','linewidth',1);
% plot(Tt,C_t, 'k--','linewidth',1);
% plot(Tt,C1poly, 'm-','linewidth',1);
% plot(Tt,C2poly, 'r-','linewidth',1);
% plot(Tt,C3poly, 'b-','linewidth',1);
% xlabel('Temperature, {\itT} (\circC)','FontSize',10,'FontName','arial','FontWeight','↩
    bold')
% ylabel('Specific Heat Capacity, {\itC} (J kg^{-1} K^{-1})','FontSize',10,'FontName','↩
    arial','FontWeight','bold')
% h=legend('ZTA Composite','Alumel','Chromel','HTHFS Composite',2); legend('boxoff');
% set(h,'FontSize',8,'FontName','arial')
%
% %thermal conductivity
% figure; hold on; box on;
% plot(Tt,Kbar_1, 'k','linewidth',1); xlim([0 900]);
% xlabel('Temperature, {\itT} (\circC)','FontSize',12,'FontName','Arial','FontWeight','↩
    bold')
```

```
% ylabel('HTHFS Thermal Conductivity, {\it\kappa}_t (W m^{-1} K^{-1})','FontSize',12,'FontName','Arial','FontWeight','bold')

%%sensitivity
% figure; hold on; box on;
% xlim([0 900]); ylim([0 400]);
% plot(Tt,St_1, 'k--','linewidth',1);
% plot(Tt,St_2, 'r--','linewidth',1);
% xlabel('HTHFS Average Temperature, {\itT}_t (\circC)','FontSize',10,'FontName','arial','FontWeight','bold')
% ylabel('HTHFS Sensitivity, {\itS}_t (\muV W^{-1} cm^2)','FontSize',10,'FontName','arial','FontWeight','bold')
% h=legend('Method 1','Method 2'); legend('boxoff');
% set(h,'FontSize',8,'FontName','arial')

%% fig2 (Elsevier format)
%%element thermal conductivity
% figure('Units','Inches','Position',[4 4 6.5 3.5]); hold on;
% sp1=subplot(1,2,1); hold on; box on; xlim([0 900]);
% set(sp1,'Units','Inches','Position',[.5 .5 2.5 2.75]);
% plot(Tt,K1poly./100, 'k','linewidth',1);
% plot(Tk2-273,K2./100, 'mo','linewidth',1,'markersize',5);
% plot(Tk3-273,K3./100, 'r^','linewidth',1,'markersize',5);
% plot(Tt,Kbar_1./100, 'k--','linewidth',1);
%% plot(Tt,Kbar_1_2./100, 'b--','linewidth',1);
% plot(Tt,K2poly./100, 'm','linewidth',1);
% plot(Tt,K3poly./100, 'r','linewidth',1);
% title('(a)','FontSize',10,'FontName','Arial')
% xlabel('Temperature, {\itT} (\circC)','FontSize',10,'FontName','Arial','FontWeight','bold')
% ylabel('Thermal Conductivity, {\it\kappa} (W cm^{-1} K^{-1})','FontSize',10,'FontName','Arial','FontWeight','bold')
% h=legend('ZTA composite','Alumel','Chromel','HTHFS composite',2); legend('boxoff');
% set(h,'FontSize',8,'FontName','Helvetica','Position',[.61 2.6 1.1 .55])
%
%%sensitivity
% sp2=subplot(1,2,2); hold on; box on; xlim([0 900]); ylim([0 350]);
% set(sp2,'Units','Inches','Position',[3.75 .5 2.5 2.75]);
% plot(Tt,St_1, 'k--', 'linewidth', 1);
%% plot(Tt,St_1_2, 'b--', 'linewidth', 1);
% title('(b)','FontSize',10,'FontName','Arial')
% xlabel('HTHFS Average Temp., {\itT}_{t,avg} (\circC)','FontSize',10,'FontName','Arial','FontWeight','bold')
% ylabel('HTHFS Sensitivity, {\itS}_t (\muV W^{-1} cm^2)','FontSize',10,'FontName','Arial','FontWeight','bold')
%% h=legend('Theoretical','Experimental',1); legend('boxoff');
%% set(h,'FontSize',8,'FontName','Helvetica','Position',[3.875 .625 1.1 .45])
clc
```

C.2 Primary In-Cavity Calibration

This section outlines the MATLAB code used to process the data presented in Chapter 4. The general sequence to processing experimental data with this code is:

1. Run the m-file "Plug01_Parameter_Estimation.m": In this file all of the important information for each test is stored and the raw data are averaged over defined steady-state time envelopes. For the tests where the sensor is coated, no parameter estimation is performed. For the tests where the sensor is oxidized, the parameter estimation scheme uses the coated sensor results to estimate the appropriate emissivity for the oxidized sensor surface.
2. Write data to MATLAB text file: Set "writedata" variable equal to 1 to write all of the processed data to a matrix file for further analysis and comparison with other test results. Make sure all of the user defined inputs are correct.
3. Repeat the previous two steps for all relevant tests.
4. Run the m-file "Plug01_VTBB_Results.m": This file is used to compare all test results at once.

C.2.1 Stand-Alone Files

Plug01_Parameter_Estimation.m:

```
%% Clay Pullins
%NASA DFRC 2010 Data Processing
close all; clear all; clc;

%calibration constants
plunge_gardon_sensitivity=0.000043205; %V/W/cm^2 (absorbed) MEDTHERM calibration 2/8/10

e_eff=1; %effective bb cavity emissivity for 1/2 in. Gardon sensor in 1 in BB; Lpg = 0.5 in; (see Murthy 2006) = 0.984

conversion=.0001; %convert from W/m^2 to W/cm^2
sb_constant=5.67*10^-8; %Stefan-Boltzmann constant (W/(m^2*K^4))

%valid test numbers: plug02: 1 ;plug01: 1,2
config=2; % =1: plug02, =2: plug01
testnum=4;  testnumber=num2str(testnum);
writedata=0; %write the processed data to a text file? 1-yes (overwrites if file already exists)
if config==1
    prefix='ac_plug02_plunge';
else
    prefix='ac_plug01_plunge';
end

%% load data file
```

```
filepath='C:\Documents and Settings\cpullins\My Documents\MATLAB\DFRC\BB_Tests\Raw_Data\';
suffix='.lvm';
fulloutputname=strcat(filepath,prefix,testnumber,suffix);
fid=fopen(fulloutputname);
for i=1:23
    erase=fgetl(fid);
end
a=fscanf(fid, '%f',[18, inf]);
A=a';
fclose(fid);

%steady state envelope:
if config==1
    if testnum==1
        ss(1,:)=[1210 1230]; ss(2,:)=[1560 1580]; ss(3,:)=[1920 1940]; ss(4,:)=[2250 2270]; ss(5,:)=[2610 2630];
        ss(6,:)=[2940 2980]; ss(7,:)=[3310 3330]; ss(8,:)=[3620 3640]; ss(9,:)=[3960 3980];
        ss=ss.*3;
        N=2; %number of HTHFS thermocouple junction pairs
        delta=0.125*.0254; %HTHFS thickness
        lg=0.127*.0254; %HTHFS diced length
    else
    end
elseif config==2
    N=5; %number of HTHFS thermocouple junction pairs
    delta=0.125*.0254; %HTHFS thickness
    lg=0.127*.0254; %HTHFS diced length
    if testnum==1
        ss(1,:)=[970 990]; ss(2,:)=[1310 1330]; ss(3,:)=[1680 1700]; ss(4,:)=[2040 2060]; ss(5,:)=[2380 2400];
        ss(6,:)=[2740 2770]; ss(7,:)=[3100 3120]; ss(8,:)=[3500 3530]; ss(9,:)=[3840 3860]; ss(10,:)=[4200 4220];
        ss=ss.*3;
    elseif testnum==2
        ss(1,:)=[1500 1520]; ss(2,:)=[1980 2000]; ss(3,:)=[2380 2400]; ss(4,:)=[2960 2980]; ss(5,:)=[3650 3670];
        ss(6,:)=[4040 4060]; ss(7,:)=[4440 4460]; ss(8,:)=[4770 4790]; ss(9,:)=[5080 5100]; %ss(10,:)=[5480 5500];
        ss=ss.*3;
    elseif testnum==3
        ss(1,:)=[850 870]; ss(2,:)=[1410 1430]; ss(3,:)=[1810 1830]; ss(4,:)=[2210 2230]; ss(5,:)=[2640 2660];
        ss(6,:)=[3050 3070]; ss(7,:)=[3420 3440]; ss(8,:)=[3760 3780]; ss(9,:)=[4160 4180]; ss(10,:)=[4460 4480]; ss(11,:)=[4780 4800];
        ss=ss.*3;
    elseif testnum==4
        ss(1,:)=[800 820]; ss(2,:)=[1160 1180]; ss(3,:)=[1520 1540]; ss(4,:)=[1900 1920]; ss(5,:)=[2280 2300];
        ss(6,:)=[2610 2630]; ss(7,:)=[2960 2980]; ss(8,:)=[3270 3290]; ss(9,:)=[3560 3580]; ss(10,:)=[3790 3810]; ss(11,:)=[4040 4060];
        ss=ss.*3;
    elseif testnum==5
        ss(1,:)=[670 690]; ss(2,:)=[960 980]; ss(3,:)=[1280 1300]; ss(4,:)=[1650 1670]; ss(5,:)=[1950 1970];
        ss(6,:)=[2260 2280]; ss(7,:)=[2560 2580]; ss(8,:)=[2910 2930]; ss(9,:)=[3360 3380]; ss(10,:)=[3740 3760]; ss(11,:)=[4130 4150];
        ss=ss.*3;
    elseif testnum==6
        ss(1,:)=[600 620]; ss(2,:)=[960 980]; ss(3,:)=[1300 1320]; ss(4,:)=[1630 1650]; ss(5,:)=[1950 1970];
        ss(6,:)=[2220 2240]; ss(7,:)=[2500 2520]; ss(8,:)=[2780 2800]; ss(9,:)=[3060 3080]; ss(10,:)=[3280 3300]; ss(11,:)=[3530 3550];
        ss=ss.*3;
```

```
    elseif testnum==7
        ss(1,:)=[840 860]; ss(2,:)=[1260 1280]; ss(3,:)=[1680 1700]; ss(4,:)=[2100 2120]; ss(5,:)=[2460 2480];
        ss(6,:)=[2820 2840]; ss(7,:)=[3155 3175]; %ss(8,:)=[3450 3470]; ss(9,:)=[3810 3830]; %ss(10,:)=[4270 4290];
%         ss(11,:)=[4630 4650]; ss(12,:)=[4930 4950];
        ss=ss.*3;
    elseif testnum==8
        ss(1,:)=[810 830]; ss(2,:)=[1230 1250]; ss(3,:)=[1630 1650]; ss(4,:)=[2030 2050]; ss(5,:)=[2350 2370];
        ss(6,:)=[2800 2820]; ss(7,:)=[3130 3150]; ss(8,:)=[3390 3410]; ss(9,:)=[3730 3750];
        ss=ss.*3;
    elseif testnum==9
        ss(1,:)=[900 920]; ss(2,:)=[1290 1310]; ss(3,:)=[1700 1720]; ss(4,:)=[2050 2070]; ss(5,:)=[2430 2450];
        ss(6,:)=[2800 2820]; ss(7,:)=[3120 3140]; %ss(8,:)=[3580 3600]; ss(9,:)=[3870 3890]; ss(10,:)=[4180 4200];
        ss=ss.*3;
    elseif testnum==10
        ss(1,:)=[745 765]; ss(2,:)=[1120 1140]; ss(3,:)=[1510 1530]; ss(4,:)=[1890 1910]; ss(5,:)=[2260 2280];
        ss(6,:)=[2660 2680]; ss(7,:)=[2980 3000]; %ss(8,:)=[3620 3640]; ss(9,:)=[3910 3930]; ss(10,:)=[4190 4210]; ss(11,:)=[4500 4520];
        ss=ss.*3;
    else
    end
else
end

%% recorded data
%electrical and flow data
time=A(:,1); current=240.*A(:,13); voltage=5.*A(:,12); fm1=A(:,14); fm2=A(:,15); control=A(:,18);

%temperature and heat flux data
hf_standard_v=A(:,2); hf_secondary_v=A(:,3); %two heat flux sensors
bbt=A(:,16); %blackbody temperature (from optical pyrometer) %relevant for tests 1-5
ktc1=A(:,4); ktc2=A(:,5); ktc3=A(:,6); ktc4=A(:,7); %thermocouples
ktc5=A(:,8); ktc6=A(:,9); ktc7=A(:,10); ktc8=A(:,11); %thermocouples

%test variable assignments
T_gardon=ktc5;
T_air=ktc8;
power=current.*voltage;


%% data processing
std_offset=mean(hf_standard_v(1:180));
hf_standard=hf_standard_v-std_offset;
sec_offset=mean(hf_secondary_v(1:180));
hf_secondary=hf_secondary_v-sec_offset;

bbs=smooth(bbt,10);
bb_emissive_power=(sb_constant*conversion).*((bbs+273.15).^4);
bb_flux_plug=(e_eff*sb_constant*conversion).*((bbs+273.15).^4-(ktc1+273.15).^4);


%% call in theoretical model
[Tt,rho,Cc,K,Sens1_1,Sens2_1,Se,t]=HTHFS_Theory(N,lg,delta);
[Tt,rho,Cc,K,Sens1_2,Sens2_2,Se,t]=HTHFS_Theory(N+1,lg,delta);

% steady state calculations
iter=length(ss);
```

```
for i=1:iter
    bb_ep(i)=mean(bb_emissive_power(ss(i,1):ss(i,2)));
    bb_T(i)=mean(bbs(ss(i,1):ss(i,2)));
    TC1(i)=mean(ktc1(ss(i,1):ss(i,2)));
    TC2(i)=mean(ktc2(ss(i,1):ss(i,2)));
    bb_flux(i)=mean(bb_flux_plug(ss(i,1):ss(i,2)));
    hthfs_v1(i)=mean(hf_standard(ss(i,1):ss(i,2)));
    hthfs_v2(i)=mean(hf_secondary(ss(i,1):ss(i,2)));
    T_air_out(i)=mean(ktc4(ss(i,1):ss(i,2)));
    T_room(i)=mean(ktc7(ss(i,1):ss(i,2)));
end

%conduction / convection estimation - properties evaluated at Tfilm
Tavg=(TC1+TC2)./2;
Tfilm=(0.5.*bb_T+0.5.*TC1)+273.15;
%argon property polynomial coefficients
pr=[-1.2731e-015 7.8362e-012 -1.8816e-008 2.2435e-005 -1.3914e-002 4.2178e+000];
pk=[6.3974e-012 -2.7450e-008 6.2510e-005 1.2142e-003];
pm=[8.3828e-015 -3.2922e-011 7.5690e-008 3.0419e-006];

RHOa=pr(1).*Tfilm.^5+pr(2).*Tfilm.^4+pr(3).*Tfilm.^3+pr(4).*Tfilm.^2+pr(5).*Tfilm+pr(6); %[kg/m^3]
Ka=pk(1).*Tfilm.^3+pk(2).*Tfilm.^2+pk(3).*Tfilm+pk(4); %[W/(m K)]
MUa=pm(1).*Tfilm.^3+pm(2).*Tfilm.^2+pm(3).*Tfilm+pm(4); %[kg/(m s)]
Cpa=518.8; %[J/(kg K)]

Aa=Ka./(RHOa.*Cpa); %[m^2/s]
NUa=MUa./RHOa; %[m^2/s]
Ba=1./Tfilm; %[1/K]
Pra=NUa./Aa; %Prandtl number

%conduction
qcond=conversion.*Ka.*(bb_T-TC1)./(0.5*.0254);

%natural convection
g=9.81; %gravitational constant [m/s^2]
Lc=0.5*.0254; %characteristic length for natural convection, HTHFS diameter
Ra=g.*Ba.*(bb_T-TC1).*Lc^3./(NUa.*Aa); %Rayleigh number
Nu=0.68+0.67.*Ra.^0.25./(1+(0.492./Pra).^(9/16)).^(4/9); %laminar natural convection empirical correlation, see Incropera eq. 9.27
ha=Ka.*Nu./Lc; %heat transfer coefficient [W/(m^2 K)]
qconv=conversion.*ha.*(bb_T-TC1);

%% radiosity balance - N surface enclosure:
%cavity size
D=1*.0254; %cavity diamter [m]
rc=D/2;
L=0.5*.0254; %length from face of sensor to VTBB center partition [m]
rs=0.205*.0254; %HTHFS sensing area radius [m]
rb=0.25*.0254; %HTHFS body area radius [m]


%call in discretization function
[H,C,W,N,l,r,T]=HTHFS_Plunge_Discretization(rs,rb,L,rc,bb_T,TC1);

%call view factor model
[F]=Cylindrical_Cavity_View_Factors(L,D,rc,H,C,W,N,l,r);

% %narrow angle results 5/13/10
% Tta=[34.1968 50.9742 66.2634 81.2920 101.2925]; %narrow angle test: bbtransfer3 - emission corrected
% St=[242.9121 249.9298 251.6973 253.0488 251.2798];

%% emissivity parameter estimation
```

```
Ti=[246.5383 298.2067 354.2100 413.4783 476.1517 541.5500 609.3067]; %average results from tests 7,9,10
Si=[276.9964 274.8700 269.1653 261.2117 254.0467 245.6758 234.9532];
% ppi=[3.0659e-007 -5.1773e-004 1.4834e-001 2.6773e+002];  %3rd degree
% ppi=[-1.2420e-004 -1.2178e-002 2.8840e+002]; %2nd degree
ppi=polyfit(Ti,Si,2);
TT=250:.1:625; %appropriate range is 250-625 degC
SS=ppi(1).*TT.^2+ppi(2).*TT+ppi(3);

count=0;
loc=1;
for i=1:iter
    if Tavg(i) > 250 && Tavg(i) < 625
        count=count+1;
        Tpar(count)=Tavg(i);
    elseif Tavg(i) < 650
        loc=loc+1;
    else
    end
end
n=round(Tpar.*10)-2500;
Tmodel=TT(n+1);
Smodel=SS(n+1);

iter2=1;
for et=0.6:.001:0.99
    e(iter2)=et;
    %Radiosity Matrix
    [QQ]=Plug01_Radiosity_Matrix(et,F,H,C,T,config,testnum);
    qq(iter2,:)=QQ(H+1,:).*(conversion);
    S(iter2,:)=hthfs_v2(loc:loc+count-1)./(qq(iter2,loc:loc+count-1)+qconv(loc:loc+count-1)).*(10^6);
    for k=1:count
        lsq(iter2,k)=(Smodel(k)-S(iter2,k))^2; %least squares method
    end
    sumsq(iter2)=sum(lsq(iter2,:));
    iter2=iter2+1;
end
[value,location]=min(sumsq); %'location' is the column number for the best estimate of HTHFS emissivity
HTHFS_emissivity=e(location);
% HTHFS_emissivity=0.795; %test#4

[Q]=Plug01_Radiosity_Matrix(HTHFS_emissivity,F,H,C,T,config,testnum);
q1=Q(H+1,:).*(conversion); %[W/cm^2]
qv=Q(H+C,:).*(conversion); %[W/cm^2]
qbb1=Q(1,:); %[W/m^2]
dT=qbb1.*(.2*.0254)./(2*50);
% q2=Q(H+2,:).*(conversion);
% q3=Q(H+3,:).*(conversion);
St=hthfs_v2./(q1+qconv).*10^6;

qt=q1+qconv;


%% uncertainty analysis
%Clay Pullins  2/26/10
% measurands
format long
V_t=hthfs_v2'.*(10^6); %[microV]
q_t=qt' %[W/cm^2]

% sensitivity coefficients
s(:,1)=1./q_t; %dS_t/dV_t [cm^2/W]
```

```
s(:,2)=-V_t./(q_t.^2); %dS_t/dq_t" [microV*cm^4/W^2]

% standard uncertainty
uvt=0.0018.*V_t; %[microV] DAQ gain error

%sequential perturbation
utqt=[0.0925230829;
    0.1074862229;
    0.1240149148;
    0.1431295453;
    0.1553517126;
    0.1696818904;
    0.1863017397;
    0.2059446294;
    0.2271081766;
    0.2517237268;
    0.2790688494];

%calibration process uncertainty
squr=[0.6053;
    0.5765;
    0.2474;
    0.3979;
    0.4332;
    0.5207;
    0.8074;
    1.0669;
    0.9632;
    1.1467;
    1.4408].^2; %[microV W^-1 cm^2]^2

%precision errors: voltage measurement
utvt=((0.005.*V_t).^2+(uvt).^2).^0.5;

% combined standard uncertainty
sq(:,1)=(s(:,1).*utvt).^2;
sq(:,2)=(s(:,2).*utqt(1:iter)).^2;
sq(:,3)=squr(1:iter);


for z=1:length(sq)
    uc(z,1)=sqrt(sum(sq(z,:))); % standard propogation of uncertainty
end

% effective degrees of freedom
nu=zeros(iter,3); %degrees of freedom for V_t, q_t", and u_r
nu(:,1)=utvt.^4./((0.005.*V_t).^2./2+(uvt).^2./20); %=nu_eff(V_t)
nnu=[13.21742722;
15.94701711;
16.70757615;
14.57366534;
13.69512407;
13.41163757;
13.76155925;
14.3338323;
15.62064225;
16.89936821;
18.25880362]; %=nu_eff(q"_t), see uncertainty spreadsheet
nu(:,2)=nnu(1:iter);
nu(:,3)=2; %based on three calibrations: nu=n-1 =3-1 =2

nu_eff=uc.^4./(sq(:,1).^2./nu(:,1)+sq(:,2).^2./nu(:,2)+sq(:,3).^2./nu(:,3));
```

```
%% write data to text file

Data(:,1)=bb_T; %BB partition temperature
Data(:,2)=TC1;
Data(:,3)=TC2;
Data(:,4)=T_room;
Data(:,5)=T_air_out;
Data(:,6)=bb_ep;
Data(:,7)=bb_flux;
Data(:,8)=q1;
Data(:,9)=qconv;
Data(:,10)=hthfs_v1.*10^6;
Data(:,11)=hthfs_v2.*10^6;
Data(:,12)=uc;
Data(:,13)=nu_eff;
[nrows,ncolumns]=size(Data);

if writedata==1
    %write data file
    filepath='C:\Documents and Settings\cpullins\My Documents\MATLAB\DFRC\BB_Tests\Plug01_Calibrations\Processed_Data\';
    fulloutputname=strcat(filepath,prefix,testnumber,suffix);
    fid=fopen(fulloutputname,'wt');
    for zz=1:nrows
        fwrite(fid, sprintf('%6.2f\t %6.2f\t %6.2f\t %6.2f\t %6.2f\t %6.6f\t %6.6f\t %6.6f\t %6.6f\t %6.2f\t %6.2f\t %6.5f\t %6.2f\t\n', Data(zz,:)));
    end
    fclose(fid);
else
end

%% plots
%heat flux
figure; hold on; box on; xlim([500 1200]);
plot(bb_T,bb_ep, 'k^-', 'linewidth', 1);
plot(bb_T,bb_flux, 'ro-', 'linewidth', 1);
plot(bb_T,q1, 'bs-', 'linewidth', 1);
% plot(Tcfd,qcfd_rad, 'md-', 'linewidth', 1);
% plot(bb_T,qcond, 'b+-', 'linewidth', 1);
% plot(Tcfd,qcfd_cond, 'md-', 'linewidth', 1);
xlabel('VTBB Temperature, T_b (\circC)','FontSize',10,'FontName','Helvetica','FontWeight','bold')
ylabel('Heat Flux, q" (W/cm^2)','FontSize',10,'FontName','Helvetica','FontWeight','bold')
h=legend('Blackbody Emissive Power','Blackbody Exchange, \epsilon_{eff}=1','Radiosity Model',2); legend('boxoff');
set(h,'FontSize',10,'FontName','Helvetica');

%paper plot
%oxidized HTHFS emissivity parameter estimation (Elsevier format)
%sum of squares function
figure1=figure('Units','Inches','Position',[4 3.5 3.5 3]); hold on; box on;
xlim([0.78 0.81]); ylim([0 140]);
plot(e(location),sumsq(location), 'ko','linewidth',1,'MarkerEdgeColor','k','MarkerFaceColor','g','MarkerSize',6);
plot(e,sumsq, 'k','linewidth',1);
xlabel('Oxidized HTHFS Surface Emissivity, {\it\epsilon}_{t,o}','FontSize',10,'FontName','Helvetica','FontWeight','bold')
ylabel('Sum of Squares, {\itX} (\muV^2 W^{-2} cm^{4})','FontSize',10,'FontName','Helvetica','FontWeight','bold')
h=legend(['{\it\epsilon}_{t,o} = ' num2str(e(location),'%10.3f') ', {\itX} = ' num2str(sumsq(location),'%10.1f')],1); legend('boxoff');
set(h,'FontSize',10,'FontName','arial','Position',[.25 .6 .5 .3])
```

Plug01_VTBB_Results.m:

```
%% Clay Pullins
%%Radiation Calibrations: 1" VTBB Plunge Calibrations
close all; clear all; clc;


%% experimental results
prefix='ac_plug01_plunge';
filepath='C:\Documents and Settings\cpullins\My Documents\MATLAB\DFRC\BB_Tests\Plug01_Calibrations\Processed_Data\';
suffix='.lvm';

%air cooled plug01 plunged into 1" VTBB uninsulated
%[(1)BB Partition Temp. (c), (2)TC1 (C), (3)TC2 (C), (4)Room Temp. (C), (5)Air Exit Temp. (C), (6)BB Emissive Power (W/cm^2),
%(7)BB Exchange (W/cm^2), (8)Radiosity Model (W/cm^2), (9)Convection (W/cm^2), (10)HTHFS V1 (microV), (11)HTHFS V2 (microV),
%(12)uncertainty, (13)effective degrees of freedom]
ntest=13;
for i=1:ntest
    testnum=i;
    testnumber=num2str(testnum); fulloutputname=strcat(filepath,prefix,testnumber,suffix);
    fid=fopen(fulloutputname); a=fscanf(fid, '%f',[13, inf]); [nrow,ncol]=size(transpose(a));

    eval(['test' num2str(i) '=transpose(a);']);
    eval(['Tb' num2str(i) '=a(1,:);']);
    eval(['TC1_' num2str(i) '=a(2,:);']);
    eval(['TC2_' num2str(i) '=a(3,:);']);
    eval(['Troom' num2str(i) '=a(4,:);']);
    eval(['Tairexit' num2str(i) '=a(5,:);']);
    eval(['Ep' num2str(i) '=a(6,:);']);
    eval(['Ex' num2str(i) '=a(7,:);']);
    eval(['rad' num2str(i) '=a(8,:);']);
    eval(['conv' num2str(i) '=a(9,:);']);
    eval(['v' num2str(i) '=a(10,:);']);
    eval(['V' num2str(i) '=a(11,:);']);
    eval(['uc' num2str(i) '=a(12,:);']);
    eval(['nu_eff' num2str(i) '=a(13,:);']);

    eval(['T' num2str(i) '=(a(2,:)+a(3,:))./2;']);
    eval(['model' num2str(i) '=a(8,:)+a(9,:);']);
    eval(['S' num2str(i) '=a(11,:)./(a(8,:)+a(9,:));']);
    fclose(fid);
end


%% Data processing

Ti=(T7+T9+T10)./3;
Si=(S7+S9+S10)./3; norm_Si=Si./274.87; %normalized by sensitivity at 300 deg C
ui=(uc7+uc9+uc10)./3;

ppi=polyfit(Ti,Si,2);
TT=250:.1:625; %appropriate range is 250-625 degC
SS=ppi(1).*TT.^2+ppi(2).*TT+ppi(3);

%repeatability of calibration
n=3;
testavg_S=(S4+S5+S6)./3;
norm_S=testavg_S./274.87; %normalized by sensitivity at 300 deg C
```

```
devsq_S=[(S4-testavg_S).^2;(S5-testavg_S).^2;(S6-testavg_S).^2];
S_std_dev_mean=(1/(n*(n-1)).*sum(devsq_S)).^0.5;

%uncertainty
nuo=(nu_eff4+nu_eff5+nu_eff6)./3;
nui=(nu_eff7+nu_eff9+nu_eff10)./3;
ko=[2.14 2.11 2.1 2.12 2.13 2.14 2.13 2.12 2.11 2.09 2.09]; %taken from students t distribution for nuo
ki=[2.14 2.12 2.11 2.13 2.14 2.14 2.14]; %taken from students t distribution for nuo
testavg_u=(uc4+uc5+uc6)./3;
avgU=ko.*testavg_u;
avgUi=ki.*ui;
testavg_T=(T4+T5+T6)./3;
testavg_Ttop=(TC1_4+TC1_5+TC1_6)./3;
testavg_conv=(conv4+conv5+conv6)./3;
testavg_rad=(rad4+rad5+rad6)./3;
testavg_qmodel=(model4+model5+model6)./3;

%results from high temperature transfer calibration (N=5 junction pair thermopile)
transfer_T=[103.6400 205.0000 303.0900 409.8800 503.0300 600.1000 698.9200 794.0400 868.8700];
transfer_S=[238.9094 244.8833 252.2448 255.7831 253.3012 240.8938 226.7325 210.2465 195.9108];
transfer_norm_S=transfer_S./252.2448; %normalized by sensitivity at 300 deg C
transfer_U=[29.9912 21.7657 20.1944 18.5014 17.0155 14.9002 13.5807 12.3302 11.4411];
transfer_norm_U=transfer_U./252.2448; %normalized by sensitivity at 300 deg C

% %CFD results 4/29/10
% qcfd_rad=[0.064539 0.10453 0.14632 0.19601 0.25208 0.2929 0.33104 0.36203]./(4.9578*10^-2);
% qcfd_cond=[0.144 0.165 0.175 0.176 0.172 0.158 0.143 0.134];
% Tcfd=[500 600 700 800 900 1000 1100 1200];


%% call in theoretical model
N=6; %number of HTHFS thermopile junctions
W=0.127*.0254; %HTHFS width (m)
L=0.125*.0254; %HTHFS thickness (m)
[T,rho,C,K,S_old,S_t,Se,t]=HTHFS_Theory(N,W,L); clc;


%% plot1
% temperature and heat flux fig (Elsevier format) Test#7 (sensor coated with GE Aerocoat)
%temperature
figure1=figure('Units','Inches','Position',[4 3.5 6.5 3.5]); hold on;
sp1=subplot(1,2,1); hold on; box on; %xlim([0 900]);
set(sp1,'Units','Inches','Position',[.6 .5 2.5 2.75]);
plot(Tb7,Tb7, 'k^','linewidth',1,'MarkerEdgeColor','k','MarkerFaceColor','r','MarkerSize',6);
plot(Tb7,TC1_7, 'ks','linewidth',1,'MarkerEdgeColor','k','MarkerFaceColor','g','MarkerSize',6);
xlabel('Blackbody Temperature, {\itT}_b (\circC)','FontSize',10,'FontName','Arial','FontWeight','bold')
ylabel('Temperature, {\itT} (\circC)','FontSize',10,'FontName','Arial','FontWeight','bold')
h=legend('{\itT}_b','{\itT}_{t,top}',2); legend('boxoff');
set(h,'FontSize',10,'FontName','arial','Position',[.6 2.7 .8 .5])
annotation(figure1,'textbox',[0.4 0.17 0.05 0.1],'String',{'(a)'},...
    'FontWeight','bold','FontSize',12,'FontName','Arial','LineStyle','none');

%heat flux
sp2=subplot(1,2,2); hold on; box on; %xlim([0 900]); ylim([0 350]);
set(sp2,'Units','Inches','Position',[3.75 .5 2.5 2.75]);
```

```
plot(Tb7,Ep7, 'k^', 'linewidth', 1,'MarkerEdgeColor','k','MarkerFaceColor','r','MarkerSize',6);
plot(Tb7,rad7, 'kv','linewidth',1,'MarkerEdgeColor','k','MarkerFaceColor','b','MarkerSize',6);
plot(Tb7,conv7, 'kd','linewidth',1,'MarkerEdgeColor','k','MarkerFaceColor','c','MarkerSize',6);
plot(Tb7,model7, 'ko', 'linewidth', 1,'MarkerEdgeColor','k','MarkerFaceColor','y','MarkerSize',6);
xlabel('Blackbody Temperature, {\itT}_b (\circC)','FontSize',10,'FontName','Arial','FontWeight','bold')
ylabel('Heat Flux, {\itq}" (W cm^{-2})','FontSize',10,'FontName','Arial','FontWeight','bold')
h=legend('{\itq}"_{inc} = \sigma {\itT}_b^4','{\itq}"_{t,rad}','{\itq}"_{t,conv}','{\itq}"_{t}',2);  legend('boxoff');
set(h,'FontSize',10,'FontName','arial','Position',[3.7 2.3 1.4 .9])
annotation(figure1,'textbox',[0.885 0.17 0.05 0.1],'String',{'(b)'},...
    'FontWeight','bold','FontSize',12,'FontName','Arial','LineStyle','none');


%% plot2
%coated configuration voltage and sensitivity (Elsevier format)
%voltage
figure2=figure('Units','Inches','Position',[4 3.5 6.5 3]); hold on;
sp1=subplot(1,2,1); hold on; box on; %xlim([0 900]);
set(sp1,'Units','Inches','Position',[.6 .5 2.4 2.4]);
plot(Tb7,V7./1000, 'ko','linewidth',1,'MarkerEdgeColor','k','MarkerFaceColor','c','MarkerSize',6);
plot(Tb9,V9./1000, 'k^','linewidth',1,'MarkerEdgeColor','k','MarkerFaceColor','m','MarkerSize',6);
plot(Tb10,V10./1000, 'kd','linewidth',1,'MarkerEdgeColor','k','MarkerFaceColor','y','MarkerSize',6);
xlabel('Blackbody Temperature, {\itT}_b (\circC)','FontSize',10,'FontName','Arial','FontWeight','bold')
ylabel('HTHFS Output Voltage, {\itV}_t (mV)','FontSize',10,'FontName','Arial','FontWeight','bold')
h=legend('Test #1','Test #2','Test #3',2); legend('boxoff');
set(h,'FontSize',10,'FontName','arial','Position',[.6 2.2 .8 .6])
annotation(figure2,'textbox',[0.4 0.17 0.05 0.1],'String',{'(a)'},...
    'FontWeight','bold','FontSize',12,'FontName','Arial','LineStyle','none');

%sensitivity
sp2=subplot(1,2,2); hold on; box on; xlim([200 700]); ylim([200 320]);
set(sp2,'Units','Inches','Position',[3.75 .5 2.4 2.4]);
plot(T,S_t, 'k—', 'linewidth', 1);
plot(T7,S7, 'ko','linewidth',1,'MarkerEdgeColor','k','MarkerFaceColor','c','MarkerSize',6);
plot(T9,S9, 'k^','linewidth',1,'MarkerEdgeColor','k','MarkerFaceColor','m','MarkerSize',6);
plot(T10,S10, 'kd','linewidth',1,'MarkerEdgeColor','k','MarkerFaceColor','y','MarkerSize',6);
xlabel('HTHFS Average Temperature, {\itT}_{t,avg} (\circC)','FontSize',10,'FontName','Arial','FontWeight','bold')
ylabel('HTHFS Sensitivity, {\itS}_t (\muV W^{-1} cm^{2})','FontSize',10,'FontName','Arial','FontWeight','bold')
h=legend('Theoretical','Test #1','Test #2','Test #3',2);  legend('boxoff');
set(h,'FontSize',10,'FontName','arial','Position',[3.8 0.6 .8 .75])
annotation(figure2,'textbox',[0.885 0.17 0.05 0.1],'String',{'(b)'},...
    'FontWeight','bold','FontSize',12,'FontName','Arial','LineStyle','none');


%% plot3
% sensitivity (Elsevier format)
figure3=figure('Units','Inches','Position',[4 3.5 3.5 3]); hold on; box on;
xlim([200 700]); ylim([200 320]);
```

```
plot(T,S_t, 'k—', 'linewidth', 1);
plot(Ti,Si, 'k+', 'linewidth', 1);
plot(TT,SS, 'k-', 'linewidth', 1);
xlabel('HTHFS Average Temperature, {\itT}_{t,avg} (\circC)','FontSize',10,'FontName','arial','FontWeight','bold')
ylabel('HTHFS Sensitivity, {\itS}_t (\muV W^{-1} cm^2)','FontSize',10,'FontName','arial','FontWeight','bold')
h=legend('Theoretical','Test #1-3 Average','Sensitivity Polynomial, {\itS}_{t,poly}',3); legend('boxoff');
set(h,'FontSize',10,'FontName','Arial','Units','Inches','Position',[.75 .6 1.4 .6]);

% sensitivity (Elsevier format)
figure4=figure('Units','Inches','Position',[4 3.5 3.5 3]); hold on; box on;
xlim([0 1000]); ylim([150 350]);
plot(T,S_t, 'k-', 'linewidth', 1);
% plot(Ti,Si, 'k+', 'linewidth', 1);
% plot(TT,SS, 'k-', 'linewidth', 1);
xlabel('HTHFS Average Temperature, {\itT}_{t,avg} (\circC)','FontSize',10,'FontName','arial','FontWeight','bold')
ylabel('HTHFS Sensitivity, {\itS}_t (\muV W^{-1} cm^2)','FontSize',10,'FontName','arial','FontWeight','bold')
h=legend('HTHFS Thermopile, \it{N}=6',3); legend('boxoff');
set(h,'FontSize',10,'FontName','Arial','Units','Inches','Position',[1.2 2.3 1.4 .6]);


%% plot4
% sensitivity (Elsevier format)
figure('Units','Inches','Position',[4 3.5 6.5 3]); hold on; box on;
xlim([100 1000]); ylim([150 350]);
plot(T,S_t, 'k—', 'linewidth', 1);
plot(Ti,Si, 'k+', 'linewidth', 1);
plot(TT,SS, 'k-', 'linewidth', 1);
plot(T4,S4, 'kd','linewidth',0.5,'MarkerEdgeColor','k','MarkerFaceColor','b','MarkerSize',6);
plot(T5,S5, 'ks','linewidth',0.5,'MarkerEdgeColor','k','MarkerFaceColor','r','MarkerSize',6);
plot(T6,S6, 'ko','linewidth',0.5,'MarkerEdgeColor','k','MarkerFaceColor','g','MarkerSize',6);
xlabel('HTHFS Average Temperature, {\itT}_{t,avg} (\circC)','FontSize',10,'FontName','arial','FontWeight','bold')
ylabel('HTHFS Sensitivity, {\itS}_t (\muV W^{-1} cm^2)','FontSize',10,'FontName','arial','FontWeight','bold')
h=legend('Theoretical','Test #1-3 average (coated HTHFS)','{\itS}_{t,poly}',...
    'Test #4 (estimated {\it\epsilon}_{t,o}=0.795)','Test #5 (estimated {\it\epsilon}_{t,o}=0.780)',...
    'Test #6 (estimated {\it\epsilon}_{t,o}=0.774)',3); legend('boxoff');
set(h,'FontSize',9,'FontName','Arial','Units','Inches','Position',[1 .55 1 1.1]);


%% plot5
figure('Units','Inches','Position',[4 3.5 6.5 3]); hold on; box on;
% figure; hold on; box on;
xlim([100 1000]); ylim([0 350]);
plot(T,S_t, 'k—','linewidth',1);
% errorbar(Ti,Si,avgUi, 'ro','linewidth',.5,'MarkerEdgeColor','r','MarkerFaceColor','r','MarkerSize',4);
errorbar(testavg_T,testavg_S,avgU, 'ks','linewidth',.5,'MarkerEdgeColor','k','MarkerFaceColor','k','MarkerSize',4);
% plot(transfer_T,transfer_S, 'ro','linewidth',1);
xlabel('HTHFS Average Temperature, {\itT}_{t,avg} (\circC)','FontSize',10,'FontName','Arial','FontWeight','bold')
ylabel('HTHFS Sensitivity, {\itS}_t (\muV W^{-1} cm^2)','FontSize',10,'FontName','Arial','FontWeight','bold')
h=legend('Theoretical','Test #4-6 average (HTHFS surface oxidized)',3); legend('boxoff');
```

```
% set(h,'FontSize',10,'FontName','Arial');
set(h,'FontSize',10,'FontName','Arial','Units','Inches','Position',[1.1 .6 .75 .5]);

%%% ORNL plot
% figure('Units','Inches','Position',[4 3.5 3.5 3]); hold on; box on;
%% figure; hold on; box on;
% xlim([100 1000]); ylim([0 350]);
% plot(T,S_t, 'k--','linewidth',1);
%% errorbar(Ti,Si,avgUi, 'ro','linewidth',.5,'MarkerEdgeColor','r','MarkerFaceColor','r','MarkerSize',4);
% plot(testavg_T,testavg_S, 'kd','MarkerEdgeColor','k','MarkerFaceColor','k','MarkerSize',5);
%% plot(transfer_T,transfer_S, 'ro','linewidth',1);
% xlabel('HTHFS Average Temperature, {\itT}_{t,avg} (\circC)','FontSize',10,'FontName','Arial','FontWeight','bold')
% ylabel('HTHFS Sensitivity, {\itS}_t (\muV W^{-1} cm^2)','FontSize',10,'FontName','Arial','FontWeight','bold')
% h=legend('Theoretical','Experimental',3); legend('boxoff');
%% set(h,'FontSize',10,'FontName','Arial');
% set(h,'FontSize',10,'FontName','Arial','Units','Inches','Position',[.8 .6 .75 .5]);


%% plot6
figure('Units','Inches','Position',[4 3.5 6.5 3]); hold on; box on;
% figure; hold on; box on;
xlim([50 1000]); ylim([0 1.2]);
% plot(T,S_t, 'k--','linewidth',1);
plot(Ti,norm_Si, 'k^','linewidth',1); %,'MarkerEdgeColor','k','MarkerFaceColor','b','MarkerSize',6);
plot(testavg_T,norm_S, 'kd','linewidth',1,'MarkerEdgeColor','k','MarkerFaceColor','b','MarkerSize',6);
% errorbar(testavg_T,norm_S,avgU./274.87, 'ks','linewidth',.5,'MarkerEdgeColor','k','MarkerFaceColor','k','MarkerSize',4);
plot(transfer_T,transfer_norm_S, 'ko','linewidth',1,'MarkerEdgeColor','k','MarkerFaceColor','g','MarkerSize',6);
% errorbar(transfer_T,transfer_norm_S,transfer_norm_U, 'ro','linewidth',.5,'MarkerEdgeColor','r','MarkerFaceColor','r','MarkerSize',4);
xlabel('HTHFS Average Temperature, {\itT}_{t,avg} (\circC)','FontSize',10,'FontName','Arial','FontWeight','bold')
ylabel('Normalized Sensitivity, {\itS}_t({\itT}) / {\itS}_t(300\circC)','FontSize',10,'FontName','Arial','FontWeight','bold')
h=legend('In-cavity primary calibration (Test #1-3 average)','In-cavity primary calibration (Test #4-6 average)'...
    ,'High temperature transfer calibration (five test average)',3); legend('boxoff');
% set(h,'FontSize',10,'FontName','Arial');
set(h,'FontSize',8,'FontName','Arial','Units','Inches','Position',[1.2 .8 1.5 .6]);


%% plot7
%% temperature and heat flux fig (Elsevier format)
%%temperature
% figure1=figure('Units','Inches','Position',[4 3.5 6.5 3.5]); hold on;
% sp1=subplot(1,2,1); hold on; box on; xlim([500 1200]);
% set(sp1,'Units','Inches','Position',[.6 .5 2.5 2.75]);
% plot(Tb4,Tb4, 'k^','linewidth',1,'MarkerEdgeColor','k','MarkerFaceColor','r','MarkerSize',6);
% plot(Tb4,TC1_4, 'ks','linewidth',1,'MarkerEdgeColor','k','MarkerFaceColor','g','MarkerSize',6);
% xlabel('Blackbody Temperature, {\itT}_b (\circC)','FontSize',10,'FontName','Arial','FontWeight','bold')
% ylabel('Temperature, {\itT} (\circC)','FontSize',10,'FontName','Arial','FontWeight','bold')
% h=legend('{\itT}_b','{\itT}_{t,top}',2); legend('boxoff');
% set(h,'FontSize',10,'FontName','arial','Position',[.6 2.7 .8 .5])
```

```
% %% annotation(figure1,'textbox',[0.4 0.17 0.05 0.1],'String',{'(a)'},...
% %%     'FontWeight','bold','FontSize',12,'FontName','Arial','LineStyle','none');
%
% %heat flux
% sp2=subplot(1,2,2); hold on; box on; xlim([500 1200]); %ylim([0 350]);
% set(sp2,'Units','Inches','Position',[3.75 .5 2.5 2.75]);
% plot(Tb4,Ep4, 'k^', 'linewidth', 1,'MarkerEdgeColor','k','MarkerFaceColor','r','MarkerSize',6);
% plot(Tb4,rad4, 'kv','linewidth',1,'MarkerEdgeColor','k','MarkerFaceColor','b','MarkerSize',6);
% plot(Tb4,conv4, 'kd','linewidth',1,'MarkerEdgeColor','k','MarkerFaceColor','c','MarkerSize',6);
% plot(Tb4,model4, 'ko', 'linewidth', 1,'MarkerEdgeColor','k','MarkerFaceColor','y','MarkerSize',6);
% xlabel('Blackbody Temperature, {\itT}_b (\circC)','FontSize',10,'FontName','Arial','FontWeight','bold')
% ylabel('Heat Flux, {\itq}" (W cm^{-2})','FontSize',10,'FontName','Arial','FontWeight','bold')
% h=legend('{\itq}"_{inc} = \sigma {\itT}_b^4','{\itq}"_{t,rad}','{\itq}"_{t,conv}','{\itq}"_{t}',2);  legend('boxoff');
% set(h,'FontSize',10,'FontName','arial','Position',[3.7 2.3 1.4 .9])
% %% annotation(figure1,'textbox',[0.885 0.17 0.05 0.1],'String',{'(b)'},...
% %%     'FontWeight','bold','FontSize',12,'FontName','Arial','LineStyle','none');
```

C.2.2 Function M-Files

HTHFS_Plunge_Discretization.m:

```
function [H,C,W,N,l,r,T]=HTHFS_Plunge_Discretization(rs,rb,L,rc,Thot,Tcold)
% %cavity discretization
H=5; %number of areas for which the VTBB center partition is to be discretized
C=3; %number of areas for which the sensor is to be discretized + surroundings
W=5; %number of areas for which the VTBB sidewall is to be discretized
N=H+C+W; %number of surfaces inside the cavity

l(1:W)=L/W; %all segments same area

% %user specified discretized cavity dimensions (only for disk and ring radii)
% r(1)=0.1*.0254; r(2)=0.2*.0254; r(3)=0.3*.0254; r(4)=0.4*.0254; r(5)=rc; %[m]
%
% r(6)=rs; %sensing area radius [m]
% r(7)=0.16*.0254; r(8)=0.172*.0254;
% r(9)=rb;
% r(10)=rc; %[m]

% %automatically calculated discretized cavity dimensions (uniform (dr)radii)
% r(1)=rc/H;
% for i=2:H
%     r(i)=r(i-1)+rc/H;
% end
% r(H+1)=rc/C;
% for i=H+2:H+C
%     r(i)=r(i-1)+rc/C;
% end

%automatically calculated discretized cavity dimensions (equal area segments)
Ap=pi*rc^2; Adhp=Ap/H;
for i=1:H+C
```

```
    if i==1
        r(i)=(Adhp/pi)^.5; %central disk - hot plate
    elseif i<=H
        r(i)=(Adhp/pi+r(i-1)^2)^.5;
    elseif i==H+1
        r(i)=rs;
    elseif i==H+2
        r(i)=rb;
    elseif i==H+C
        r(i)=rc;
    else
        Adcp=pi*(rc^2-rb^2)/(C-2);
        r(i)=(Adcp/pi+r(i-1)^2)^.5;
    end
end

%temperatures
for i=1:N
    if i<=H
        T(i,:)=Thot+273.15; %center partition
    elseif i>H && i<=H+2
        T(i,:)=Tcold+273.15; %cold sensor
    elseif i>H+2 && i<=H+C
        T(i,:)=(Tcold+Thot)./2+273.15; %imaginary area - perfect absorber (emissivity * ↩
            view factor weighted - 1 surface)
    else
        T(i,:)=Thot+273.15; %sidewall
    end
end
```

Plug01_Radiosity_Matrix.m:

```
function [Q]=Plug01_Radiosity_Matrix(et,F,H,C,T,config,testnum)
N=length(F);
sigma=5.67*10^-8; %Stefan-Boltzmann [W/m^2/K^4]
[nrows ncol]=size(T);
d=zeros(N,N);
K=zeros(N,N);
P=zeros(N,1);

%emissivities
e(1:H)=0.89; %ATJ graphite center partition
e(H+1)=et; %sensor area
e(H+2)=et; %surrounding metal surface
e(H+3:H+C)=0.999; %imaginary area - ideal absorber
e(H+C+1:N)=0.89; %ATJ graphite sidewall

%fill matrix and load vector
for z=1:ncol
    if testnum==2
        if z<=4
            e(H+1:H+2)=0.98;
        else
            e(H+1:H+2)=0.72;
        end
    elseif testnum==7 || testnum==9 || testnum==10
        e(H+1:H+2)=0.98;
    else
    end
    for i=1:N %all rows (ith surface)
        for j=1:N %all columns
```

```
            if i==j
                d(i,j)=1; %Kronecker delta
            else
            end
            K(i,j)=(-d(i,j)/e(j)+F(i,j)*(1-e(j))/e(j));
            p(i,j)=(d(i,j)-F(i,j))*sigma*T(j,z)^4;
        end
        P(i,z)=sum(p(i,:));
    end
    %solve radiosity matrix
    Q(:,z)=K\P(:,z); %solves for q'' in {W/m^2)
end
```

C.3 HTHFS Applications

This section outlines the MATLAB code used to process the data presented in Chapter 5.

C.3.1 Stand-Alone Files

HTHFS_Sensitivity.m:

```
%% Clay Pullins
%%Sensitivity vs temperature results for several calibrations
%%Chromel-Chromel sensitivities only (very good agreement); Alumel-Alumel seems to vary more
close all; clear all; clc;


%% call in theoretical sensitivity model
% N=5; %number of HTHFS thermopile junctions
% W=0.127*.0254; %HTHFS width (m)
% L=0.125*.0254; %HTHFS thickness (m)
[Tt,rho,C,K,St_old,St,Se,t]=HTHFS_Theory(5,0.2*.0254,0.125*.0254); clc;
Stnorm=St./St(251);


%% HTHFS plug01 normalized sensitivity vs average temperature

%lamp calibration results 11/3/10
S1room1=166.0245./Stnorm(389); %room temp sensitivity
T1L1=[38.8664; 47.8592; 57.9674; 68.0565; 80.2669; 92.8275; 121.4113; 149.0088; 179.7645; 212.5808];
S1L1=[166.0245; 168.2753; 171.6401; 171.4240; 171.5380; 171.7699; 169.7563; 165.4470; 163.2217; 162.5668]./S1room1;

T1L2=[48.6189; 103.0103; 166.9606; 237.8840; 310.7881];
S1L2=[166.3450; 169.7249; 161.8001; 159.1116; 156.8308]./S1room1;

%lamp bank calibration results 3/29/11
S1room=168.0814./Stnorm(373); %room temp sensitivity
T1L3=[37.3152; 43.8368; 60.3743; 78.4230; 101.7952; 125.9235];
S1L3=[168.0814; 169.1860; 169.3895; 169.0845; 166.1192; 163.3199]./S1room;

T1L=cat(1,T1L1,T1L2,T1L3);
S1L=cat(1,S1L1,S1L2,S1L3);

%high temperature in-cavity primary calibrations
%only results for coated sensor used
T1H7=[245.0200; 297.2200; 353.7150; 413.7750; 476.9700; 544.2050; 616.7350]; %test7
S1H7=[160.4754; 159.7043; 154.6352; 149.6655; 145.2671; 137.9398; 129.9836]./S1room;

T1H9=[244.9650; 295.3250; 350.6250; 408.7500; 470.9500; 534.9750; 599.9450]; %test9
S1H9=[170.4164; 167.0057; 160.6900; 154.5132; 149.0805; 142.1977; 133.0954]./S1room;

T1H10=[249.6300; 302.0750; 358.2900; 417.9100; 480.5350; 545.4700; 611.2400]; %test10
S1H10=[168.0865; 164.7043; 158.3495; 152.5315; 147.4792; 141.0268; 131.8683]./S1room;

T1H=cat(1,T1H7,T1H9,T1H10);
S1H=cat(1,S1H7,S1H9,S1H10);
```

```
%% HTHFS plug03 normalized sensitivity vs average temperature
%flat plate transfer calibration
S2room=93.7369./Stnorm(389); %room temp sensitivity
T2P1=[32.7293; 38.9532; 50.4524; 67.3947; 93.9775; 132.7811; 216.4299; 181.1191; ...
    118.0417];
S2P1=[92.0623; 93.7369; 93.8007; 96.9204; 95.9388; 93.0162; 89.7809; 90.8300; 95.8401]./...
    S2room;

T2P2=[50.4936; 71.0353; 99.3616; 143.3366; 234.1373; 268.8912];
S2P2=[97.7409; 99.1424; 96.1298; 92.2225; 89.3848; 90.8565]./S2room;

T2P=cat(1,T2P1,T2P2);
S2P=cat(1,S2P1,S2P2);


%% HTHFS rev03 normalized sensitivity vs average temperature
%lamp bank calibration results 3/29/11; e_zynolyte,cured=0.8
S3room=331.9832; %room temp sensitivity
T3L1=[25.3251; 38.6763; 52.5409; 68.6934; 87.8367; 108.0330];
S3L1=[331.9832; 336.7552; 339.2138; 341.1385; 339.8473; 335.9610]./S3room;

%high temperature transfer calibrations, updated 3/29/11 with proper e_zynolyte,cured=0.8
%results where Tavg<300 degC omitted - high uncertainty
T3H7=[841.9205; 789.2365; 706.0315; 601.9065; 499.2923; 400.8112; 303.0901]; %test7
S3H7=[226.7143; 235.2863; 249.2899; 267.2024; 286.1714; 300.4194; 315.1776]./S3room;

T3H8=[844.1537; 787.0111; 701.1817; 600.1242; 498.2792; 402.7843; 301.1107]; %test8
S3H8=[227.4694; 236.5979; 251.3283; 269.2710; 288.5105; 302.7314; 320.6336]./S3room;

T3H9=[844.8633; 786.3800; 703.3098; 596.3234; 497.4641; 401.7289; 300.7574]; %test9
S3H9=[227.9419; 237.1617; 251.4630; 270.7399; 289.6385; 304.4607; 323.1651]./S3room;

T3H10=[839.8619; 784.8286; 705.5826; 595.0317; 499.3473; 404.6689; 301.7581]; %test10
S3H10=[229.3802; 237.8578; 251.4601; 271.4584; 290.0995; 305.4891; 326.0834]./S3room;

T3H15=[842.3669; 787.6659; 703.4368; 597.9913; 497.2501; 402.5438; 302.2855]; %test15
S3H15=[230.8067; 239.0244; 253.4566; 272.7543; 291.7322; 307.8558; 326.2055]./S3room;

T3H=cat(1,T3H7,T3H8,T3H9,T3H10,T3H15);
S3H=cat(1,S3H7,S3H8,S3H9,S3H10,S3H15);


%% HTHFS plug02 normalized sensitivity vs average temperature
%single lamp transfer calibration
S4room=127.5215; %room temp sensitivity
T4L1=[24.4130;  30.3702;  38.4819;  47.7431;  58.6951;  70.1903;  83.4472;  96.5757; ...
    110.8884; 126.8879];
S4L1=[127.5215; 127.6485; 130.1773; 130.9139; 131.9829; 132.0837; 131.2469; 130.8685; ...
    129.1457; 127.8113]./S4room;


%% all results

T=cat(1,T1L1,T1L2,T1L3,T1H7,T1H9,T1H10,T3L1,T3H7,T3H8,T3H9,T3H10,T3H15,T4L1);
S=cat(1,S1L1,S1L2,S1L3,S1H7,S1H9,S1H10,S3L1,S3H7,S3H8,S3H9,S3H10,S3H15,S4L1);

%force polynomial through points from the theoretical model to extend calibration range
T=cat(1,T,25.*ones(100,1),1200.*ones(2,1));
S=cat(1,S,Stnorm(251).*ones(100,1),Stnorm(12001).*ones(2,1));

% T=cat(1,T,zeros(10,1),25.*ones(100,1),1000.*ones(10,1),1100.*ones(10,1),1200.*ones(10,1)...
    );
% S=cat(1,S,Stnorm(1).*ones(10,1),Stnorm(251).*ones(100,1),0.6109.*ones(10,1),0.5668.*ones...
```

```
    (10,1),Stnorm(12001).*ones(10,1));


p=polyfit(T,S,5); clc;
Tx=25:1:1200;
Spoly=polyval(p,Tx);



%% applications paper figure: normalized sensitivity versus temperature

%all test results labeled
figure1=figure('Units','Inches','Position',[2 2 6.5 4]);
hold on; box on; xlim([25 1000]); ylim([0.6 1.1]);
plot(Tt,Stnorm, 'k--', 'linewidth', .5);
plot(T1L,S1L, 'kd', 'linewidth', 0.5,'MarkerEdgeColor','k','MarkerFaceColor','b','MarkerSize',5);
plot(T1H,S1H, 'k^', 'linewidth', 0.5,'MarkerEdgeColor','k','MarkerFaceColor','r','MarkerSize',5);
% plot(T2P,S2P, 'kv', 'linewidth', 0.5,'MarkerEdgeColor','k','MarkerFaceColor','y','MarkerSize',5);
plot(T4L1,S4L1, 'k>', 'linewidth', 0.5,'MarkerEdgeColor','k','MarkerFaceColor','y','MarkerSize',5);
plot(T3L1,S3L1, 'ks', 'linewidth', 0.5,'MarkerEdgeColor','k','MarkerFaceColor','c','MarkerSize',5);
plot(T3H,S3H, 'kp', 'linewidth', 0.5,'MarkerEdgeColor','k','MarkerFaceColor','g','MarkerSize',5);
plot(Tx,Spoly, 'k-', 'linewidth', 1);
xlabel('HTHFS Average Temperature, {\itT}_{t,avg} (\circC)','FontSize',10,'FontName','Arial','FontWeight','bold')
ylabel('Normalized HTHFS Sensitivity, {\itS}_t({\itT}_{t,avg}) / {\itS}_t(25\circC)','FontSize',10,'FontName','Arial','FontWeight','bold')
h1=legend('Theoretical','Sensor A, Lamp Transfer Cal. (3 tests)',...
    'Sensor A, High Temp. Primary Cal. (3 tests)',...
    'Sensor B, Lamp Transfer Cal. (1 test)',...
    'Sensor C, Lamp Transfer Cal. (1 test)','Sensor C, High Temp. Secondary Cal. (5 tests)',...
    '5^{th} Order Polynomial fit to Experimental Results',3); legend('boxoff');
set(h1,'FontSize',8,'FontName','Arial','Units','Inches','Position',[1 .6 2 1.4])

%polynomial plot
figure; hold on; box on; xlim([25 900]); ylim([.6 1.1]); grid on
plot(Tx,Spoly, 'k-', 'linewidth', 2);
xlabel('HTHFS Average Temperature, {\itT}_{t,avg} (\circC)','FontSize',10,'FontName','Arial','FontWeight','bold')
ylabel('Normalized HTHFS Sensitivity, {\itS}_t({\itT}_{t,avg})/{\itS}_t(25\circC)','FontSize',10,'FontName','Arial','FontWeight','bold')
% h2=legend('Theoretical','Experimental (all tests)','Polynomial fit to Experimental',3); legend('boxoff');
% set(h2,'FontSize',8,'FontName','arial','Position',[1 .75 1 .5])


%%%all tests with polynomial
% figure('Units','Inches','Position',[2 2 6.5 4]);
% hold on; box on; xlim([25 1200]); ylim([.5 1.2]);
% plot(Tt,Stnorm, 'k--', 'linewidth', 1);
% plot(T,S,'kx');
% plot(Tx,Spoly, 'k-', 'linewidth', 1);
% xlabel('HTHFS Average Temperature, {\itT}_{t,avg} (\circC)','FontSize',10,'FontName','Arial','FontWeight','bold')
% ylabel('Normalized HTHFS Sensitivity, {\itS}_t({\itT}_{t,avg})/{\itS}_t(25\circC)','FontSize',10,'FontName','Arial','FontWeight','bold')
% h2=legend('Theoretical','Experimental (all tests)','Polynomial fit to Experimental',3); legend('boxoff');
```

```
% set(h2,'FontSize',8,'FontName','arial','Position',[1 .75 1 .5])

%%English units
% figure2=figure('Units','Inches','Position',[2 2 6.5 4]);
% hold on; box on; xlim([77 1800]); ylim([0.6 1.1]);
% plot(Tt.*1.8+32.2,Stnorm, 'k--', 'linewidth', .75);
% plot(T1L.*1.8+32.2,S1L, 'kd', 'linewidth', 0.5,'MarkerEdgeColor','k','MarkerFaceColor','b','MarkerSize',5);
% plot(T1H.*1.8+32.2,S1H, 'k^', 'linewidth', 0.5,'MarkerEdgeColor','k','MarkerFaceColor','r','MarkerSize',5);
% plot(T2P.*1.8+32.2,S2P, 'kv', 'linewidth', 0.5,'MarkerEdgeColor','k','MarkerFaceColor','y','MarkerSize',5);
% plot(T4L1.*1.8+32.2,S4L1, 'k>', 'linewidth', 0.5,'MarkerEdgeColor','k','MarkerFaceColor','m','MarkerSize',5);
% plot(T3L1.*1.8+32.2,S3L1, 'ks', 'linewidth', 0.5,'MarkerEdgeColor','k','MarkerFaceColor','c','MarkerSize',5);
% plot(T3H.*1.8+32.2,S3H, 'kp', 'linewidth', 0.5,'MarkerEdgeColor','k','MarkerFaceColor','g','MarkerSize',5);
%% plot(Tx.*1.8+32.2,Spoly, 'k-', 'linewidth', .75);
% xlabel('HTHFS Average Temperature, {\itT}_{avg} (\circF)','FontSize',10,'FontName','Arial','FontWeight','bold')
% ylabel('Normalized HTHFS Sensitivity, {\itS}({\itT}_{avg}) / {\itS}(75\circF)','FontSize',10,'FontName','Arial','FontWeight','bold')
% h1=legend('Theoretical','Sensor A, Lamp Transfer Cal. (3 tests)',...
%     'Sensor A, In-Cavity Primary Cal. (3 tests)','Sensor B, Flat Plate Transfer Cal. (2 tests)',...
%     'Sensor C, Lamp Transfer Cal. (1 test)',...
%     'Sensor D, Lamp Transfer Cal. (1 test)','Sensor D, High Temp. Transfer Cal. (5 tests)',...
%     '5^{th} Order Polynomial fit to Experimental Results',3); legend('boxoff');
% set(h1,'FontSize',8,'FontName','Arial','Units','Inches','Position',[1 .6 1.8 1.4])
```

HTHFS_Gardon_Transfer_Calibrations.m:

```
%% Clay Pullins
%NASA DFRC Data Processing
close all; clear all; clc;

%constants
ag=.92; %gardon gage absorptivity
L_conv=1.5*.0254; %convection vertical length (m)
conversion=.0001; %convert from W/m^2 to W/cm^2
sb_constant=5.67*10^-8; %Stefan-Boltzmann constant (W/(m^2*K^4))
g=9.81; %acceleration due to gravity (m/s^2)


%% variable air properties:
T_mat=300:50:900; %abs. temp. (K)
A_mat=[22.5 29.9 38.3 47.2 56.7 66.7 76.9 87.3 98 109 120 131 143].*10^-6; %alpha vs. abs. temp. (m^2/s)
N_mat=[15.89 20.92 26.41 32.39 38.79 45.57 52.69 60.21 68.1 76.37 84.93 93.8 102.9].*10^-6; %nu vs. abs. temp. (m^2/s)
K_mat=[26.3 30 33.8 37.3 40.7 43.9 46.9 49.7 52.4 54.9 57.3 59.6 62].*10^-3; %k vs. abs. temp. (W/(m*K))
a_poly=polyfit(T_mat,A_mat,2);
n_poly=polyfit(T_mat,N_mat,2);
k_poly=polyfit(T_mat,K_mat,2);


%% load data file
%valid files:
```

```
%Gage2 vs Gardon64: 3,8,14,30(black)
%VT03 vs Gardon64: 5,7,15,29(black)
%VT04 vs Gardon64: 6,16
%Plug01 vs Gardon32: 9,10,17,18,20,26,28(black)
%Plug01 vs Gardon64: 19
prefix='transfer';
testnum=16;
testnumber=num2str(testnum);

filepath='C:\Documents and Settings\cpullins\My Documents\MATLAB\DFRC\Flat_Plate_Tests\Raw_Data\';
suffix='.lvm';
fulloutputname=strcat(filepath,prefix,testnumber,suffix);
fid=fopen(fulloutputname);
for i=1:23
    erase=fgetl(fid);
end
a=fscanf(fid, '%f',[18, inf]);
A=a';
if testnum==7 || testnum==8
    A=A(1:3500,:);
elseif testnum==15
    A=A(1:2600,:);
elseif testnum==16
    A=A(1:4000,:);
end
[nrows,ncolumns]=size(A);
start=1;
stop=nrows;

%electrical and flow data
time=A(:,1); current=240.*A(:,13); voltage=5.*A(:,12); fm1=A(:,14); fm2=A(:,15); control=A(:,18);
%temperature and heat flux data
hf_standard_v=A(:,2); hf_secondary_v=A(:,3); %two heat flux sensors
% plate=A(:,17); %heater plate temperature (from optical pyrometer) %relevant for tests 1-5
ktc1=A(:,4); ktc2=A(:,5); ktc3=A(:,6); ktc4=A(:,7); %thermocouples
ktc5=A(:,8); ktc6=A(:,9); ktc7=A(:,10); ktc8=A(:,11); %thermocouples


%% call in test info function
[ss,std_sens,hthfs_sens,Lpg,e_t,lg,wg]=Test_Info_TG(testnum,hf_standard_v,hf_secondary_v);


%% call in theoretical model
N=5; %number of HTHFS thermopile junctions
delta=0.125*.0254; %HTHFS thickness (m)
[TT,rho,C,K,S,Se,tt]=HTHFS_Theory(N,lg,delta);
pc=polyfit(TT,C,5);

%viewfactor calculation
Ag=.08*.0254^2; %[m^2]
rg=(Ag/pi)^.5; %[m]
Ap=2.1*1.671*.0254^2; %[m^2]
rp=(Ap/pi)^.5; %[m]
Rg=rg/Lpg; Rp=rp/Lpg; S1=1+((1+Rp^2)/Rg^2);
Fgp=.5*(S1-(S1^2-4*(rp/rg)^2)^.5);


%% data processing
T_gardon=ktc5;
T_air=ktc8;
power=current.*voltage;
```

```
std_offset=mean(hf_standard_v(1:180));
sec_offset=mean(hf_secondary_v(1:180));
hf_standard=hf_standard_v-std_offset;
hf_secondary=hf_secondary_v-sec_offset; %gets rid of dc offset for hf sensors
incident_flux=hf_standard./(std_sens*ag);
sensor_ratio=hf_standard./hf_secondary;

tc2_offset=mean(ktc1(1:180))-mean(ktc2(1:180)); ktc2=ktc2+tc2_offset; %gets rid of dc offset for tc sensors
ktc1s=smooth(ktc1,10); %moving average filter, 10 data points
ktc2s=smooth(ktc2,10); %moving average filter, 10 data points

%hthfs natural convection parameters:
film=(ktc8+ktc1)./2+273.15; %film temperature (K)
beta=1./film; %ideal gas thermal expansion coeficient (1/K)
alpha=a_poly(1).*film.^2+a_poly(2).*film+a_poly(3); %thermal diffusivity (m^2/s)
nu=n_poly(1).*film.^2+n_poly(2).*film+n_poly(3); %momentum diffusivity (m^2/s)
k=k_poly(1).*film.^2+k_poly(2).*film+k_poly(3); %thermal conductivity (W/(m*K))
prandtl=nu./alpha; %Prandtl number (dimensionles)
Ra_L=(g.*beta.*(ktc1-ktc8).*(L_conv^3))./(nu.*alpha); %Rayleigh number at HTHFS length, L (dimensionless)
Nu_L=(0.825+(.387.*Ra_L.^(1/6))./(1+(.492./prandtl).^(9/16)).^(8/27)).^2; %Avg. Nusselt number for HTHFS face with length, L (Incropera 9.26)
% Nu_L=0.68+(.67.*Ra_L.^.25)./(1+(.492./prandtl).^(9/16)).^(4/9); %Avg. Nusselt number for HTHFS face with length, L (Incropera 9.27)
h_L=k./L_conv.*Nu_L; %Avg. heat transfer coefficient for HTHFS face with length, L (W/(m^2*K))
%hthfs heat transfer calculations:
emission=e_t*sb_constant*conversion.*((ktc1+273.15).^4); %(W/(cm^2))
reflection=(1-e_t).*incident_flux; %(W/(cm^2))
convection=conversion.*h_L.*(ktc1-ktc8); %(W/(cm^2))
loss=emission+reflection+convection; %(W/(cm^2))
avg_temp=(ktc1s+ktc2s)./2; %uses two surface thermocouples
% avg_temp=(ktc1+ktc2)./2; %uses two surface thermocouples
temp_diff=ktc1s-ktc2s;
% avg_temp2=ktc2s(num/2+1:length(ktc1)+num/2)+hf_secondary./(2*N*Sab); %uses TC2 and thermopile differential temperature


%% call in hybrid heat flux model
rate=3; %sampling rate (Hz)
[thermopile_cal_flux,slug_flux,net_flux,hthfs_S,c_hthfs,dT_dt,ds_dT,dc_dT]=...
    HHF(time,rate,hthfs_sens,avg_temp,hf_secondary,rho,pc,delta,conversion,0.5);

est_abs=incident_flux-loss;
est_incident=(net_flux+emission+convection)./e_t;

percent_diff=abs(incident_flux-est_incident)./incident_flux.*100;


% quasi-steady state averages
% iter=length(ss)/2;
% si=1;
% for i=1:iter
%     hf_incident(i)=mean(incident_flux(ss(si):ss(si+1)));
%     hf_incident_est(i)=mean(est_incident(ss(si):ss(si+1)));
%     percent_inc_diff(i)=abs(hf_incident(i)-hf_incident_est(i))/hf_incident(i);
%     si=si+2;
% end
%
% Incident_Flux_Percent_Diff=100.*percent_inc_diff
% Average_Percent_Diff=mean(Incident_Flux_Percent_Diff)
```

```
%% uncertainty analysis
%Clay Pullins  4/9/11
% measurands
v=hf_secondary.*10^6; %[microV]
s=hthfs_S.*10^6; %[microV/(W/cm^2)]
r=rho/(100^3); %[kg/cm^3]
d=delta*100; %[cm]
c=c_hthfs; %[J/(kg K)]
T=avg_temp; %[deg C]
t=time; %[s]

% sensitivity coefficients
sc(:,1)=1./s; %dq"/dv [W/(cm^2 microV)]
sc(:,2)=-1.*v./s.^2; %dq"/ds [W^2/(cm^4 microV)]
sc(:,3)=(1/2*d).*c.*dT_dt; %dq"/dr [W cm / kg]
sc(:,4)=(1/2*r).*c.*dT_dt; %dq"/dd [W/cm^3]
sc(:,5)=(1/2*r*d).*dT_dt; %dq"/dc [kg K/(cm^2 s)]
sc(:,6)=-1.*v./s.^2.*ds_dT+(1/2*r*d).*dT_dt.*dc_dT; %dq"/dT [W/(cm^2 K)]
sc(:,7)=1./s.*gradient(v).*rate+(1/2*r*d).*c.*gradient(dT_dt).*rate; %dq"/dt [W/(cm^2 s)]

% standard uncertainties
%voltage
uv1=0.001.*v; %[microV] DAQ gain error
uv2=0.005.*v; %[microV] estimated repeatability
u(:,1)=(uv1.^2+uv2.^2).^0.5;
%sensitivity
u(:,2)=0.03.*s; %[microV/(W/cm^2)]
%density
u(:,3)=0.025*r; %[kg/cm^3]
%thickness
u(:,4)=0.003*2.54; %[cm]
%specific heat
u(:,5)=0.1.*c; %[J/(kg K)]
%temperature
uT1=1; %[deg C] DAQ error (typical)
uT3=0.02.*avg_temp; %[deg C] surface temperature measurement error
for i=1:length(time)
    if avg_temp(i)<275
        uT2(i)=1.1; %[deg C] TC error
    else
        uT2(i)=0.004.*avg_temp(i); %[deg C] TC error
    end
    u(:,6)=(uT1.^2+uT2(i).^2+uT3(i).^2).^0.5; %[deg C]
end
%time
u(:,7)=50*10^-6; %[s]


[nrow,ncol]=size(sc);

for i=1:ncol
    % combined standard uncertainty in each measurand
    sq(:,i)=(sc(:,i).*u(:,i)).^2;
end

for i=1:nrow
    % combined standard uncertainty in the heat flux
    uc(i,1)=sqrt(sum(sq(i,:)));
end


%% plots
yzero(1:length(time))=0; %y scale zero - for heat flux plots
% %sensor voltage
```

```
% figure; hold on; box on;
% plot(hf_standard, 'k', 'linewidth', 1);
% plot(hf_secondary, 'r', 'linewidth', 1);
% xlabel('Time, t (s)','FontSize',10,'FontName','arial','FontWeight','bold')
% ylabel('Sensor Output, V (V)','FontSize',10,'FontName','arial','FontWeight','bold')
% h=legend('Standard','Secondary',1); legend('boxoff');
% set(h,'FontSize',8,'FontName','arial');
%
%%sensor output ratio
% figure; hold on; box on; ylim([0 3]);
% plot(sensor_ratio, 'k', 'linewidth', 1);
% xlabel('Time, t (s)','FontSize',10,'FontName','arial','FontWeight','bold')
% ylabel('Sensor Output, V (V)','FontSize',10,'FontName','arial','FontWeight','bold')

%%heat flux
% figure; hold on; box on;
% plot(time,incident_flux, 'k-.', 'linewidth', 2);
% plot(time,thermopile_cal_flux, 'b--', 'linewidth', 1);
% plot(time,slug_flux, 'r--', 'linewidth', 1);
%% plot(time,thermopile_cal_flux+0.5.*abs(slug_flux)', 'c--', 'linewidth', 1);
%% plot(time,est_abs, 'g', 'linewidth', 2);
% plot(time,net_flux, 'k-', 'linewidth', 2); %xlim([850 1200]);
%% plot(time,net_flux+2.*uc, 'k--', 'linewidth', 1); %xlim([850 1200]);
%% plot(time,net_flux-2.*uc, 'k--', 'linewidth', 1); %xlim([850 1200]);
%% plot(time,est_incident, 'm', 'linewidth', 1);
% plot(time,thermopile_cal_flux-.5.*slug_flux, 'g-', 'linewidth', 1);
% plot(time,yzero, 'k:', 'linewidth', 1);
% xlabel('Time, t (s)','FontSize',12,'FontName','arial','FontWeight','bold')
% ylabel('Heat Flux, q" (W/cm^2)','FontSize',12,'FontName','arial','FontWeight','bold')
% h=legend('Incident (Gardon)','Calibrated Differential Response','Slug Response','HHF ↩
    Total','HHF Out',1); legend('boxoff');
% set(h,'FontSize',10,'FontName','arial');
%
%%heat flux
% figure; hold on; box on;
% plot(time,incident_flux, 'r-', 'linewidth', 2);
%% plot(time,thermopile_cal_flux, 'b--', 'linewidth', 1);
%% plot(time,slug_flux, 'r--', 'linewidth', 1);
%% plot(time,thermopile_cal_flux+0.5.*abs(slug_flux)', 'c--', 'linewidth', 1);
%% plot(time,est_abs, 'g', 'linewidth', 2);
% plot(time,net_flux, 'k-', 'linewidth', 2); %xlim([850 1200]);
%% plot(time,net_flux+2.*uc, 'k--', 'linewidth', 1); %xlim([850 1200]);
%% plot(time,net_flux-2.*uc, 'k--', 'linewidth', 1); %xlim([850 1200]);
% plot(time,est_incident, 'm', 'linewidth', 1);
% plot(time,yzero, 'k:', 'linewidth', 1);
% xlabel('Time, t (s)','FontSize',12,'FontName','arial','FontWeight','bold')
% ylabel('Heat Flux, q" (W/cm^2)','FontSize',12,'FontName','arial','FontWeight','bold')
% h=legend('Incident (Gardon)','HHF Total','Est. Incident',1); legend('boxoff');
% set(h,'FontSize',10,'FontName','arial');
%
%%heat flux losses
%% figure; hold on; box on;
%% plot(time,emission, 'r', 'linewidth', 1);
%% plot(time,reflection, 'g', 'linewidth', 1);
%% plot(time,convection, 'b', 'linewidth', 1);
%% xlabel('Time, t (s)','FontSize',10,'FontName','arial','FontWeight','bold')
%% ylabel('HTHFS Heat Flux Loss, q" (W/cm^2)','FontSize',10,'FontName','arial','↩
    FontWeight','bold')
%% h=legend('Emission','Reflection','Convection',2); legend('boxoff');
%% set(h,'FontSize',8,'FontName','arial');
%
%%temperatures
% figure; hold on; box on;
% plot(time,ktc1s(1:length(time)), 'r', 'linewidth', 1);
```

```
% plot(time,ktc2s(1:length(time)), 'b', 'linewidth', 1); %xlim([850 1250]);
% xlabel('Time, t (s)','FontSize',10,'FontName','arial','FontWeight','bold')
% ylabel('Temperature, T (\circC)','FontSize',10,'FontName','arial','FontWeight','bold')
% h=legend('TC1','TC2',1); legend('boxoff');
% set(h,'FontSize',8,'FontName','arial');

% %expanded uncertainty
% figure; hold on; box on; ylim([0 20])
% plot(time,abs(2.*uc./net_flux.*100), 'k', 'linewidth', 1);
% xlabel('Time, t (s)','FontSize',10,'FontName','arial','FontWeight','bold')
% ylabel('Heat Flux Expanded Uncertainty, U(q") (W cm^{-2})','FontSize',10,'FontName','arial','FontWeight','bold')
%
% %standard uncertainties
% figure; hold on; box on;
% plot(time,sq(:,1), 'b');
% plot(time,sq(:,2),'c');
% plot(time,sq(:,3),'g');
% plot(time,sq(:,4),'k');
% plot(time,sq(:,5),'r');
% plot(time,sq(:,6),'m');
% plot(time,sq(:,7),'y');
% xlabel('Time, t (s)','FontSize',10,'FontName','arial','FontWeight','bold')
% ylabel('Uncertainty Components, Sc(x_i)*u(x_i) (W cm^{-2})','FontSize',10,'FontName','arial','FontWeight','bold')
% h=legend('V','S','\rho','\delta','C','T','t',1); legend('boxoff');
% set(h,'FontSize',8,'FontName','arial');


%% paper figures

if testnum==7
    %heat flux
    figure1=figure('Units','Inches','Position',[2 0.5 6.5 7]); hold on;
    sp1=subplot(2,1,1); hold on; box on;
    xlim([0 900]); %ylim([0 8]);
    set(sp1,'Units','Inches','Position',[.8 3.4 5.2 3.2]);
    plot(time,incident_flux, 'k-.', 'linewidth', 2);
    plot(time,thermopile_cal_flux, 'b-', 'linewidth', 1);
    plot(time,slug_flux, 'r-', 'linewidth', 1);
    plot(time,net_flux, 'k-', 'linewidth', 2); %xlim([850 1200]);
    plot(time,est_incident, 'm-', 'linewidth', 1);
%     plot(time,thermopile_cal_flux-.5.*slug_flux, 'g--', 'linewidth', 1);
%     plot(time,yzero, 'k--', 'linewidth', 0.5);
    xlabel('Time, {\itt} (s)','FontSize',12,'FontName','Arial','FontWeight','bold')
    ylabel('Heat Flux, {\itq}" (W cm^{-2})','FontSize',12,'FontName','Arial','FontWeight','bold')
    h1=legend('Incident Radiation (Gardon)','HTHFS Differential Response','HTHFS Slug Response',...
        'HHF Hot-Wall Total (HTHFS)','Estimated Incident',3); legend('boxoff');
    set(h1,'FontSize',8,'FontName','Arial','Units','Inches','Position',[3.8 5.6 2 .8])
    annotation(figure1,'textbox',[0.15 0.82 0.05 0.1],'String',{'(a)'},...
        'FontWeight','bold','FontSize',12,'FontName','Arial','LineStyle','none');
    %temperature
    sp2=subplot(2,1,2); hold on; box on;
    set(sp2,'Units','Inches','Position',[.8 .5 5.2 2.2]);
    xlim([0 900]); %ylim([0 520]);
    plot(time,ktc1s(1:length(time)), 'r', 'linewidth', 1.5);
    plot(time,ktc2s(1:length(time)), 'b', 'linewidth', 1.5);
    xlabel('Time, {\itt} (s)','FontSize',12,'FontName','arial','FontWeight','bold')
    ylabel('Temperature, {\itT} (\circC)','FontSize',12,'FontName','arial','FontWeight','bold')
    h2=legend('{\itT}_1','{\itT}_2',3); legend('boxoff');
    set(h2,'FontSize',10,'FontName','arial','Position',[5.1 2 .5 .5])
```

```
    annotation(figure1,'textbox',[.15 0.26 0.05 0.1],'String',{'(b)'},...
        'FontWeight','bold','FontSize',12,'FontName','Arial','LineStyle','none');
end


if testnum==16
    %heat flux
    figure1=figure('Units','Inches','Position',[2 0.5 6.5 7]); hold on;
    sp1=subplot(2,1,1); hold on; box on;
    xlim([0 200]); %ylim([0 8]);
    set(sp1,'Units','Inches','Position',[.8 3.4 5.2 3.2]);
    plot(time-150,incident_flux, 'k-.', 'linewidth', 2);
    plot(time-150,thermopile_cal_flux, 'b-', 'linewidth', 1);
    plot(time-150,slug_flux, 'r-', 'linewidth', 1);
    plot(time-150,net_flux, 'k-', 'linewidth', 2); %xlim([850 1200]);
    plot(time-150,est_incident, 'm', 'linewidth', 1);
%     plot(time-150,thermopile_cal_flux-.5.*slug_flux, 'g--', 'linewidth', 1);
%     plot(time-150,yzero, 'k--', 'linewidth', 0.5);
    xlabel('Time, {\itt} (s)','FontSize',12,'FontName','Arial','FontWeight','bold')
    ylabel('Heat Flux, {\itq}" (W cm^{-2})','FontSize',12,'FontName','Arial','FontWeight','bold')
    h1=legend('Incident Radiation (Gardon)','HTHFS Differential Response','HTHFS Slug Response',...
        'HHF Hot-Wall Total (HTHFS)','Estimated Incident',3); legend('boxoff');
    set(h1,'FontSize',8,'FontName','Arial','Units','Inches','Position',[3.9 5.6 1.6 .8])
    annotation(figure1,'textbox',[0.15 0.82 0.05 0.1],'String',{'(a)'},...
        'FontWeight','bold','FontSize',12,'FontName','Arial','LineStyle','none');
    %temperature
    sp2=subplot(2,1,2); hold on; box on;
    set(sp2,'Units','Inches','Position',[.8 .5 5.2 2.2]);
    xlim([0 200]); %ylim([0 520]);
    plot(time-150,ktc1s(1:length(time)), 'r', 'linewidth', 1.5);
    plot(time-150,ktc2s(1:length(time)), 'b', 'linewidth', 1.5);
    xlabel('Time, {\itt} (s)','FontSize',12,'FontName','arial','FontWeight','bold')
    ylabel('Temperature, {\itT} (\circC)','FontSize',12,'FontName','arial','FontWeight','bold')
    h2=legend('{\itT}_1','{\itT}_2',3); legend('boxoff');
    set(h2,'FontSize',10,'FontName','arial','Position',[5.1 2 .5 .5])
    annotation(figure1,'textbox',[.15 0.26 0.05 0.1],'String',{'(b)'},...
        'FontWeight','bold','FontSize',12,'FontName','Arial','LineStyle','none');
end

% if testnum==7
%     %heat flux
%     figure1=figure('Units','Inches','Position',[2 0.5 6.5 7]); hold on;
%     sp1=subplot(2,1,1); hold on; box on;
%     xlim([0 800]); %ylim([0 8]);
%     set(sp1,'Units','Inches','Position',[.8 3.4 5.2 3.2]);
%     plot(time,incident_flux.*.88, 'k--', 'linewidth', 1.5);
%     plot(time,thermopile_cal_flux.*.88, 'b--', 'linewidth', 1);
%     plot(time,slug_flux.*.88, 'r--', 'linewidth', 1);
%     plot(time,net_flux.*.88, 'k-', 'linewidth', 1.5); %xlim([850 1200]);
%     plot(time,est_incident.*.88, 'm', 'linewidth', 1);
%     plot(time,yzero, 'k--', 'linewidth', 0.5);
%     xlabel('Time, {\itt} (s)','FontSize',10,'FontName','Arial','FontWeight','bold')
%     ylabel('Heat Flux, {\itq}" (BTU ft^{-2} s^{-1})','FontSize',10,'FontName','Arial','FontWeight','bold')
%     h1=legend('Measured Incident (Gardon)','Differential Response','Slug Response','HHF Total','Estimated Incident',3); legend('boxoff');
%     set(h1,'FontSize',8,'FontName','Arial','Units','Inches','Position',[4.1 5.6 1.5 .8])
% %     annotation(figure1,'textbox',[0.15 0.82 0.05 0.1],'String',{'(a)'},...
% %         'FontWeight','bold','FontSize',12,'FontName','Arial','LineStyle','none');
%     %temperature
%     sp2=subplot(2,1,2); hold on; box on;
```

```
%     set(sp2,'Units','Inches','Position',[.8 .5 5.2 2.2]);
%     xlim([0 800]);
%     plot(time,ktc1s(1:length(time)).*1.8+32.2, 'r', 'linewidth', 1.5);
%     plot(time,ktc2s(1:length(time)).*1.8+32.2, 'b', 'linewidth', 1.5);
%     xlabel('Time, {\itt} (s)','FontSize',10,'FontName','arial','FontWeight','bold')
%     ylabel('Temperature, {\itT} (\circF)','FontSize',10,'FontName','arial','FontWeight↩
    ','bold')
%     h2=legend('{\itT}_1','{\itT}_2',3); legend('boxoff');
%     set(h2,'FontSize',10,'FontName','arial','Position',[5.1 2 .5 .5])
% %     annotation(figure1,'textbox',[.15 0.26 0.05 0.1],'String',{'(b)'},...
% %         'FontWeight','bold','FontSize',12,'FontName','Arial','LineStyle','none');
% end
%
%
% if testnum==16
%     %heat flux
%     figure1=figure('Units','Inches','Position',[2 0.5 6.5 7]); hold on;
%     sp1=subplot(2,1,1); hold on; box on;
%     xlim([0 200]); ylim([-20 45]);
%     set(sp1,'Units','Inches','Position',[.8 3.4 5.2 3.2]);
%     plot(time-150,incident_flux.*.88, 'k--', 'linewidth', 1.5);
%     plot(time-150,thermopile_cal_flux.*.88, 'b--', 'linewidth', 1);
%     plot(time-150,slug_flux.*.88, 'r--', 'linewidth', 1);
%     plot(time-150,net_flux.*.88, 'k-', 'linewidth', 1.5); %xlim([850 1200]);
%     plot(time-150,est_incident.*.88, 'm', 'linewidth', 1);
%     plot(time-150,yzero, 'k--', 'linewidth', 0.5);
%     xlabel('Time, {\itt} (s)','FontSize',10,'FontName','Arial','FontWeight','bold')
%     ylabel('Heat Flux, {\itq}" (BTU ft^{-2} s^{-1})','FontSize',10,'FontName','Arial','↩
    FontWeight','bold')
%     h1=legend('Measured Incident (Gardon)','Differential Response','Slug Response','HHF ↩
    Total','Estimated Incident',3); legend('boxoff');
%     set(h1,'FontSize',8,'FontName','Arial','Units','Inches','Position',[3.9 5.6 2 .8])
% %     annotation(figure1,'textbox',[0.15 0.82 0.05 0.1],'String',{'(a)'},...
% %         'FontWeight','bold','FontSize',12,'FontName','Arial','LineStyle','none');
%     %temperature
%     sp2=subplot(2,1,2); hold on; box on;
%     set(sp2,'Units','Inches','Position',[.8 .5 5.2 2.2]);
%     xlim([0 200]); ylim([0 2200]);
%     plot(time-150,ktc1s(1:length(time)).*1.8+32.2, 'r', 'linewidth', 1.5);
%     plot(time-150,ktc2s(1:length(time)).*1.8+32.2, 'b', 'linewidth', 1.5);
%     xlabel('Time, {\itt} (s)','FontSize',10,'FontName','arial','FontWeight','bold')
%     ylabel('Temperature, {\itT} (\circF)','FontSize',10,'FontName','arial','FontWeight↩
    ','bold')
%     h2=legend('{\itT}_1','{\itT}_2',3); legend('boxoff');
%     set(h2,'FontSize',10,'FontName','arial','Position',[5.1 2 .5 .5])
% %     annotation(figure1,'textbox',[.15 0.26 0.05 0.1],'String',{'(b)'},...
% %         'FontWeight','bold','FontSize',12,'FontName','Arial','LineStyle','none');
% end
clc
```

Plunge_Sensor_Transfer_Calibrations.m:

```
%% Clay Pullins
%NASA DFRC Data Processing
close all; clear all; clc;

conversion=.0001; %convert from W/m^2 to W/cm^2
sb_constant=5.67*10^-12; %Stefan-Boltzmann constant (W/(cm^2*K^4))
plunge_gardon_sensitivity=0.000043205; %V/W/cm^2 (absorbed) MEDTHERM calibration 2/8/10
```

```
%% test configuration
config=2; % config=1: HTHFS is water cooled plug02; config=2: HTHFS is air cooled plug03
testnum=2;  testnumber=num2str(testnum);
writedata=0; %write the processed data to a text file? 1-yes (overwrites if file already exists)

N=3; %number of junction pairs
delta=0.125*.0254; %HTHFS thickness
lg=0.15*.0254; %HTHFS diced length
eg=0.98; %sensor surface emissivity - all sensors coated with GE Aerocoat

%call in theoretical model
[TT,rho,C,K,S,Se,tt]=HTHFS_Theory(N,lg,delta);
pc=polyfit(TT,C,5);

if config==1
    prefix='gardon_plug02_transfer';
    if testnum==1 %uncontrolled heater ramp-up
        %steady state event start times (s):
        ss=3.*[307]; %multiply by sampling rate
    elseif testnum==2
        ss=3.*[360 620 920 1180 1280 1400 1690 1840 2000 2220 2480];
    elseif testnum==3
        ss=3.*[480 720 980 1230 1520 1720];
    else
    end
elseif config==2
    prefix='gardon_plug03_transfer';
    if testnum==1
        %steady state event start times (s):
        ss=3.*[360 520 750 950 1180 1430 1680 1910 2160 2370 2590]; %multiply by sampling rate
    elseif testnum==2
        ss=3.*[530 780 1040 1290 1600 1830];
    else
    end
else
end


%% load data file
filepath='C:\Documents and Settings\cpullins\My Documents\MATLAB\DFRC\Flat_Plate_Tests\Raw_Data\';
suffix='.lvm';
fulloutputname=strcat(filepath,prefix,testnumber,suffix);
fid=fopen(fulloutputname);
for i=1:23
    erase=fgetl(fid);
end
a=fscanf(fid, '%f',[18, inf]);
A=a';
if config==2 && testnum==2
    A=A(1:7000,:);
end
[nrows,ncolumns]=size(A);
start=1;
stop=nrows;
fclose(fid);


%% recorded data
%electrical and flow data
time=A(:,1); current=240.*A(:,13); voltage=5.*A(:,12); fm1=A(:,14); fm2=A(:,15); control=A(:,18);
```

```
if config==1
    if testnum==1
        hf2_v=A(:,17);
    else
        hf2_v=A(:,16);
    end
elseif config==2
    hf2_v=A(:,16);
else
end

%temperature and heat flux data
hf1_v1=A(:,2); hf1_v2=A(:,3); %heat flux sensors
bbt=A(:,16); %blackbody temperature (from optical pyrometer) %relevant for tests 1-5
ktc1=A(:,4); ktc2=A(:,5); ktc3=A(:,6); ktc4=A(:,7); %thermocouples
ktc5=A(:,8); ktc6=A(:,9); ktc7=A(:,10); ktc8=A(:,11); %thermocouples

power=current.*voltage;

hf1_offset1=mean(hf1_v1(1:60)); hf1_v1=hf1_v1-hf1_offset1;
hf1_offset2=mean(hf1_v2(1:60)); hf1_v2=hf1_v2-hf1_offset2;
hf2_offset=mean(hf2_v(1:60)); hf2_v=hf2_v-hf2_offset; %removes bias voltage offset from heat flux sensors

bb_emissive_power=(sb_constant).*((bbt+273.15).^4); %[W/cm^2]


%% transient calculations

T_gardon=ktc5;
T_air=ktc8;
power=current.*voltage;

incident_flux=hf2_v./(plunge_gardon_sensitivity*eg);


ktc1=smooth(ktc1,10); %moving average filter, 10 data points
ktc2=smooth(ktc2,10); %moving average filter, 10 data points

% convection estimation - properties evaluated at Tfilm
%air property polynomial coefficients
pa=[6.4116e-011 1.2569e-007 -2.1777e-005];
pn=[7.4422e-011 5.6380e-008 -7.9190e-006];
pk=[-3.0969e-008 9.6306e-005 2.0320e-004];

%hthfs natural convection parameters:
Tfilm=(ktc6+ktc1)./2+273.15; %film temperature (K)
Aa=pa(1).*Tfilm.^2+pa(2).*Tfilm+pa(3); %[m^2/s]
NUa=pn(1).*Tfilm.^2+pn(2).*Tfilm+pn(3); %[m^2/s]
Ka=pk(1).*Tfilm.^2+pk(2).*Tfilm+pk(3); %[W/(m K)]
Cpa=1008; %[J/(kg K)]
Ba=1./Tfilm; %[1/K]
Pra=NUa./Aa; %Prandtl number
g=9.81; %gravitational constant [m/s^2]
Lc=0.5*.0254; %characteristic length for natural convection, HTHFS diameter
Ra=g.*Ba.*(ktc1-ktc6).*Lc^3./(NUa.*Aa); %Rayleigh number
Nu=0.68+0.67.*Ra.^0.25./(1+(0.492./Pra).^(9/16)).^(4/9); %laminar natural convection empirical correlation, see Incropera eq. 9.27
ha=Ka.*Nu./Lc; %heat transfer coefficient [W/(m^2 K)]
hthfs_qconv=conversion.*ha.*(ktc1-ktc6); %natural convection


%hthfs heat transfer calculations:
```

```
emission=eg*sb_constant.*((ktc1+273.15).^4); %(W/(cm^2))
reflection=(1-eg).*incident_flux; %(W/(cm^2))
convection=conversion.*ha.*(ktc1-ktc6); %(W/(cm^2))
loss=emission+reflection+convection; %(W/(cm^2))
avg_temp=(ktc1+ktc2)./2; %uses two surface thermocouples


%% call in hybrid heat flux model
if config==1
    hthfs_sens=.000222;
    hthfs_hfv=hf1_v2;
else
    hthfs_sens=.000183;
    hthfs_hfv=hf1_v2;
end
rate=3; %sampling rate (Hz)
[thermopile_cal_flux,slug_flux,net_flux,hthfs_S,c_hthfs,dT_dt,ds_dT,dc_dT]=...
    HHF(time,rate,hthfs_sens,avg_temp,hthfs_hfv,rho,pc,delta,conversion,0.5);

est_abs=incident_flux-loss;
est_incident=(net_flux+emission+convection)./eg;

percent_diff=abs(incident_flux-est_incident)./incident_flux.*100;


%% steady state calculations
% iter=length(ss);
%
% for i=1:iter
%     Tair(i)=mean(ktc6(ss(i):ss(i)+60));
%
%     hthfs_TC1(i)=mean(ktc1(ss(i):ss(i)+60));
%     hthfs_TC2(i)=mean(ktc2(ss(i):ss(i)+60));
%     hthfs_v1(i)=mean(hf1_v1(ss(i):ss(i)+60));
%     hthfs_v2(i)=mean(hf1_v2(ss(i):ss(i)+60));
%
%     gardon_TC(i)=mean(ktc3(ss(i):ss(i)+60));
%     gardon_v(i)=mean(hf2_v(ss(i):ss(i)+60));
% end
%
%
% %data processing
% hthfs_Tavg=(hthfs_TC1+hthfs_TC2)./2;
%
% %Gardon measured absorbed heat flux
% gardon_abs_hf=gardon_v./plunge_gardon_sensitivity;
%
% % convection estimation - properties evaluated at Tfilm
% %air property polynomial coefficients
% pa=[6.4116e-011 1.2569e-007 -2.1777e-005];
% pn=[7.4422e-011 5.6380e-008 -7.9190e-006];
% pk=[-3.0969e-008 9.6306e-005 2.0320e-004];
%
% %natural convection hthfs
% Tfilm=(0.5.*Tair+0.5.*hthfs_TC1)+273.15;
% Aa=pa(1).*Tfilm.^2+pa(2).*Tfilm+pa(3); %[m^2/s]
% NUa=pn(1).*Tfilm.^2+pn(2).*Tfilm+pn(3); %[m^2/s]
% Ka=pk(1).*Tfilm.^2+pk(2).*Tfilm+pk(3); %[W/(m K)]
% Cpa=1008; %[J/(kg K)]
% Ba=1./Tfilm; %[1/K]
% Pra=NUa./Aa; %Prandtl number
% g=9.81; %gravitational constant [m/s^2]
% Lc=0.5*.0254; %characteristic length for natural convection, HTHFS diameter
% Ra=g.*Ba.*(hthfs_TC1-Tair).*Lc^3./(NUa.*Aa); %Rayleigh number
```

```
% Nu=0.68+0.67.*Ra.^0.25./(1+(0.492./Pra).^(9/16)).^(4/9); %laminar natural convection ↩
    empirical correlation, see Incropera eq. 9.27
% ha=Ka.*Nu./Lc; %heat transfer coefficient [W/(m^2 K)]
% hthfs_qconv=conversion.*ha.*(hthfs_TC1-Tair); %natural convection
%
%
% %natural convection Gardon
% Tfilm=(0.5.*Tair+0.5.*gardon_TC)+273.15;
% Aa=pa(1).*Tfilm.^2+pa(2).*Tfilm+pa(3); %[m^2/s]
% NUa=pn(1).*Tfilm.^2+pn(2).*Tfilm+pn(3); %[m^2/s]
% Ka=pk(1).*Tfilm.^2+pk(2).*Tfilm+pk(3); %[W/(m K)]
% Cpa=1008; %[J/(kg K)]
% Ba=1./Tfilm; %[1/K]
% Pra=NUa./Aa; %Prandtl number
% g=9.81; %gravitational constant [m/s^2]
% Lc=0.5*.0254; %characteristic length for natural convection, HTHFS diameter
% Ra=g.*Ba.*(gardon_TC-Tair).*Lc^3./(NUa.*Aa); %Rayleigh number
% Nu=0.68+0.67.*Ra.^0.25./(1+(0.492./Pra).^(9/16)).^(4/9); %laminar natural convection ↩
    empirical correlation, see Incropera eq. 9.27
% ha=Ka.*Nu./Lc; %heat transfer coefficient [W/(m^2 K)]
% gardon_qconv=conversion.*ha.*(gardon_TC-Tair); %natural convection
%
% incident_hf=gardon_abs_hf./eg+sb_constant.*(gardon_TC+273.15).^4+gardon_qconv./eg;
%
% %HTHFS absorbed heat flux and sensitivity
% hthfs_abs_hf=eg.*(incident_hf-sb_constant.*(hthfs_TC1+273.15).^4)-hthfs_qconv;
%
% hthfs_St1=hthfs_v1./hthfs_abs_hf.*(10^6);
% hthfs_St2=hthfs_v2./hthfs_abs_hf.*(10^6);
%
% %call in HTHFS theoretical model
% [Tt,rho,C,K,Sens1_1,Sens2_1,Se,t]=HTHFS_Theory(N,lg,delta);
% [Tt,rho,C,K,Sens1_2,Sens2_2,Se,t]=HTHFS_Theory(N+1,lg,delta);

%% uncertainty analysis
%Clay Pullins  4/9/11
% measurands
v=hthfs_hfv.*10^6; %[microV]
s=hthfs_S.*10^6; %[microV/(W/cm^2)]
r=rho/(100^3); %[kg/cm^3]
d=delta*100; %[cm]
c=c_hthfs; %[J/(kg K)]
T=avg_temp; %[deg C]
t=time; %[s]

% sensitivity coefficients
sc(:,1)=1./s; %dq"/dv [W/(cm^2 microV)]
sc(:,2)=-1.*v./s.^2; %dq"/ds [W^2/(cm^4 microV)]
sc(:,3)=(1/2*d).*c.*dT_dt; %dq"/dr [W cm / kg]
sc(:,4)=(1/2*r).*c.*dT_dt; %dq"/dd [W/cm^3]
sc(:,5)=(1/2*r*d).*dT_dt; %dq"/dc [kg K/(cm^2 s)]
sc(:,6)=-1.*v./s.^2.*ds_dT+(1/2*r*d).*dT_dt.*dc_dT; %dq"/dT [W/(cm^2 K)]
sc(:,7)=1./s.*gradient(v).*rate+(1/2*r*d).*c.*gradient(dT_dt).*rate; %dq"/dt [W/(cm^2 s)]

% standard uncertainties
%voltage
uv1=0.001.*v; %[microV] DAQ gain error
uv2=0.005.*v; %[microV] estimated repeatability
u(:,1)=(uv1.^2+uv2.^2).^0.5;
%sensitivity
u(:,2)=0.03.*s; %[microV/(W/cm^2)]
%density
u(:,3)=0.025*r; %[kg/cm^3]
%thickness
```

```
u(:,4)=0.003*2.54; %[cm]
%specific heat
u(:,5)=0.05.*c; %[J/(kg K)]
%temperature
uT1=1; %[deg C] DAQ error (typical)
uT3=0.02.*avg_temp; %[deg C] surface temperature measurement error
for i=1:length(time)
    if avg_temp(i)<275
        uT2(i)=1.1; %[deg C] TC error
    else
        uT2(i)=0.004.*avg_temp(i); %[deg C] TC error
    end
    u(:,6)=(uT1.^2+uT2(i).^2+uT3(i).^2).^0.5; %[deg C]
end
%time
u(:,7)=50*10^-6; %[s]


[nrow,ncol]=size(sc);

for i=1:ncol
    % combined standard uncertainty in each measurand
    sq(:,i)=(sc(:,i).*u(:,i)).^2;
end

for i=1:nrow
    % combined standard uncertainty in the heat flux
    uc(i,1)=sqrt(sum(sq(i,:)));
end



%% plots

% %sensor voltage
% figure; hold on; box on;
% plot(time,hf1_v2, 'k', 'linewidth', 1);
% plot(time,hf2_v, 'r', 'linewidth', 1);
% xlabel('Time, t (s)','FontSize',10,'FontName','Helvetica','FontWeight','bold')
% ylabel('Sensor Output, V (V)','FontSize',10,'FontName','Helvetica','FontWeight','bold')
% h=legend('HF1','HF2',1); legend('boxoff');
% set(h,'FontSize',8,'FontName','Helvetica');
%
% %sensor temperature
% figure; hold on; box on;
% plot(time,ktc1, 'm', 'linewidth', 1);
% plot(time,ktc2, 'r', 'linewidth', 1);
% xlabel('Time, t (s)','FontSize',10,'FontName','Helvetica','FontWeight','bold')
% ylabel('Sensor Temperature, T (\circC)','FontSize',10,'FontName','Helvetica','FontWeight↩
    ','bold')
% h=legend('HF1 TC1','HF1 TC2',1); legend('boxoff');
% set(h,'FontSize',8,'FontName','Helvetica');

%sensitivity
% if config==1
%     figure; hold on; box on; xlim([0 1000]); ylim([0 300]);
%     plot(Tt,Sens2_1, 'b--', 'linewidth', 1);
%     plot(Tt,Sens2_2, 'r--', 'linewidth', 1);
%     plot(hthfs_Tavg,hthfs_St1, 'b^', 'linewidth', 1);
%     plot(hthfs_Tavg,hthfs_St2, 'r^', 'linewidth', 1);
%     xlabel('HTHFS Avg. Temperature, {\itT}_{t,avg} (\circC)','FontSize',10,'FontName','↩
    Helvetica','FontWeight','bold')
%     ylabel('HTHFS Sensitivity, {\itS}_t (\muV W^{-1} cm^2)','FontSize',10,'FontName','↩
    Helvetica','FontWeight','bold')
```

```
%     h=legend('Theory (N=2)','Theory (N=3)','Plug02 (N=2)','Plug02 (N=3)',1); legend('boxoff');
%     set(h,'FontSize',10,'FontName','Helvetica');
% elseif config==2
%     figure; hold on; box on; xlim([0 1000]); ylim([0 300]);
%     plot(Tt,Sens2_1, 'b--', 'linewidth', 1);
%     plot(Tt,Sens2_2, 'r--', 'linewidth', 1);
%     plot(hthfs_Tavg,hthfs_St1, 'b^', 'linewidth', 1);
%     plot(hthfs_Tavg,hthfs_St2, 'r^', 'linewidth', 1);
%     xlabel('HTHFS Avg. Temperature, {\itT}_{t,avg} (\circC)','FontSize',10,'FontName','Helvetica','FontWeight','bold')
%     ylabel('HTHFS Sensitivity, {\itS}_t (\muV W^{-1} cm^2)','FontSize',10,'FontName','Helvetica','FontWeight','bold')
%     h=legend('Theory (N=2)','Theory (N=3)','Plug03 (N=2)','Plug03 (N=3)',1); legend('boxoff');
%     set(h,'FontSize',10,'FontName','Helvetica');
% else
% end
%

yzero(1:length(time))=0; %y scale zero - for heat flux plots
%heat flux
figure; hold on; box on;
plot(time,smooth(incident_flux,10), 'k-.', 'linewidth', 2);
plot(time,smooth(thermopile_cal_flux,10), 'b--', 'linewidth', 1);
plot(time,smooth(slug_flux,10), 'r--', 'linewidth', 1);
% plot(time,thermopile_cal_flux+0.5.*abs(slug_flux)', 'c--', 'linewidth', 1);
% plot(time,est_abs, 'g', 'linewidth', 2);
plot(time,smooth(net_flux,10), 'k-', 'linewidth', 2); %xlim([850 1200]);
plot(time,smooth(est_incident,10), 'm', 'linewidth', 1);
plot(time,yzero, 'k:', 'linewidth', 1);
xlabel('Time, t (s)','FontSize',12,'FontName','arial','FontWeight','bold')
ylabel('Heat Flux, q" (W/cm^2)','FontSize',12,'FontName','arial','FontWeight','bold')
h=legend('Incident (Gardon)','Calibrated Thermopile','Slug Calorimeter','HHF Total','Estimated Incident',1); legend('boxoff');
set(h,'FontSize',10,'FontName','arial');

%%heat flux losses
% figure; hold on; box on;
% plot(time,emission, 'r', 'linewidth', 1);
% plot(time,reflection, 'g', 'linewidth', 1);
% plot(time,convection, 'b', 'linewidth', 1);
% xlabel('Time, t (s)','FontSize',10,'FontName','arial','FontWeight','bold')
% ylabel('HTHFS Heat Flux Loss, q" (W/cm^2)','FontSize',10,'FontName','arial','FontWeight','bold')
% h=legend('Emission','Reflection','Convection',2); legend('boxoff');
% set(h,'FontSize',8,'FontName','arial');

%temperatures
figure; hold on; box on;
plot(time,ktc1, 'r', 'linewidth', 1);
plot(time,ktc2, 'b', 'linewidth', 1); %xlim([850 1250]);
xlabel('Time, t (s)','FontSize',10,'FontName','arial','FontWeight','bold')
ylabel('Temperature, T (\circC)','FontSize',10,'FontName','arial','FontWeight','bold')
h=legend('TC1','TC2',1); legend('boxoff');
set(h,'FontSize',8,'FontName','arial');

%expanded uncertainty
figure; hold on; box on; ylim([0 20])
plot(time,abs(200.*uc./net_flux), 'k', 'linewidth', 1);
xlabel('Time, t (s)','FontSize',10,'FontName','arial','FontWeight','bold')
ylabel('Heat Flux Expanded Uncertainty, U(q") (W cm^{-2})','FontSize',10,'FontName','arial','FontWeight','bold')
```

```
%standard uncertainties
figure; hold on; box on;
plot(time,sq(:,1), 'b');
plot(time,sq(:,2),'c');
plot(time,sq(:,3),'g');
plot(time,sq(:,4),'k');
plot(time,sq(:,5),'r');
plot(time,sq(:,6),'m');
plot(time,sq(:,7),'y');
xlabel('Time, t (s)','FontSize',10,'FontName','arial','FontWeight','bold')
ylabel('Uncertainty Components, Sc(x_i)*u(x_i) (W cm^{-2})','FontSize',10,'FontName','arial','FontWeight','bold')
h=legend('V','S','\rho','\delta','C','T','t',1); legend('boxoff');
set(h,'FontSize',8,'FontName','arial');


%% paper figure

if config==2 && testnum==2
    %heat flux
    figure1=figure('Units','Inches','Position',[2 0.3 6.5 7]); hold on;
    sp1=subplot(2,1,1); hold on; box on;
    xlim([0 2000]); %ylim([0 8]);
    set(sp1,'Units','Inches','Position',[.8 3.4 5.2 3.2]);
    plot(time-200,smooth(incident_flux,10), 'k-.', 'linewidth', 2);
    plot(time-200,smooth(thermopile_cal_flux,10), 'b-', 'linewidth', 1);
    plot(time-200,smooth(slug_flux,10), 'r-', 'linewidth', 1);
    plot(time-200,smooth(net_flux,10), 'k-', 'linewidth', 2); %xlim([850 1200]);
    plot(time-200,smooth(est_incident,10), 'm-', 'linewidth', 1);
%     plot(time-200,yzero, 'k--', 'linewidth', 0.5);
    xlabel('Time, {\itt} (s)','FontSize',10,'FontName','Arial','FontWeight','bold')
    ylabel('Heat Flux, {\itq}" (W cm^{-2})','FontSize',10,'FontName','Arial','FontWeight','bold')
    h1=legend('Incident Radiation (Gardon)','HTHFS Differential Response','HTHFS Slug Response',...
        'HHF Hot-Wall Total (HTHFS)','Estimated Incident'); legend('boxoff');
    set(h1,'FontSize',8,'FontName','Arial','Units','Inches','Position',[1 5.6 2 .8])
    annotation(figure1,'textbox',[0.84 0.82 0.05 0.1],'String',{'(a)'},...
        'FontWeight','bold','FontSize',12,'FontName','Arial','LineStyle','none');
    %temperature
    sp2=subplot(2,1,2); hold on; box on;
    set(sp2,'Units','Inches','Position',[.8 .5 5.2 2.2]);
    xlim([0 2000]); %ylim([0 520]);
    plot(time-200,ktc1, 'r', 'linewidth', 1.5);
    plot(time-200,ktc2, 'b', 'linewidth', 1.5);
    xlabel('Time, {\itt} (s)','FontSize',10,'FontName','arial','FontWeight','bold')
    ylabel('Temperature, {\itT} (\circC)','FontSize',10,'FontName','arial','FontWeight','bold')
    h2=legend('{\itT}_1','{\itT}_2',3); legend('boxoff');
    set(h2,'FontSize',10,'FontName','arial','Position',[1 2 .5 .5])
    annotation(figure1,'textbox',[.84 0.26 0.05 0.1],'String',{'(b)'},...
        'FontWeight','bold','FontSize',12,'FontName','Arial','LineStyle','none');
end

clc
```

C.3.2 Function M-Files

HHF.m:

```
function [thermopile_cal_flux,slug_flux,net_flux,hthfs_S,c_hthfs,dT_dt,ds_dT,dc_dT]=...
    HHF(time,rate,room_sensitivity,avg_temp,hthfs_voltage,rho,pc,delta,conversion,...
        weight_const)
%%hybrid heat flux method

%polynomial coefficients for S vs T(deg C)
ps=[1.268788587454231e-015 -4.272354649796778e-012 5.638410957552114e-009 ...
    -3.645081960240481e-006 6.247123059454293e-004 9.881960364544532e-001];
%pc = polynomial coefficients for C vs T(deg C)

c_hthfs=polyval(pc,avg_temp); %[J/(kg K)]
hthfs_S=(room_sensitivity).*polyval(ps,avg_temp); %[uV/W/cm^2]
thermopile_cal_flux=hthfs_voltage./hthfs_S;

dT_dt=gradient(avg_temp)'.*rate; %[deg C/s]

T=0:.1:1200;
s=((room_sensitivity)*10^6).*polyval(ps,T);
dsdT=gradient(s).*10;

c=polyval(pc,T);
dcdT=gradient(c).*10;

n=round(avg_temp.*10);

for i=1:length(time);
    ds_dT(i)=dsdT(n(i));
    dc_dT(i)=dcdT(n(i));
end

dT_dt=dT_dt';
ds_dT=ds_dT';
dc_dT=dc_dT';

slug_flux=(rho*delta*conversion).*(c_hthfs.*dT_dt);
net_flux=thermopile_cal_flux+weight_const.*slug_flux;
```

Test_Info_TG.m:

```
function [ss,std_sens,hthfs_sens,Lpg,eg,lg,wg]=Test_Info_TG(testnum,hf_standard_v,...
    hf_secondary_v)
% test information
% sensor output plot
% sensor_ratio=hf_standard_v./hf_secondary_v;
% figure; hold on; box on; ylim([0 3]);
% plot(sensor_ratio, 'k', 'linewidth', 1);
% xlabel('Time, t (s)','FontSize',10,'FontName','Helvetica','FontWeight','bold')
% ylabel('Sensor Output, V (V)','FontSize',10,'FontName','Helvetica','FontWeight','bold')

%% calibration constants
Gardon64_sensitivity=0.000054594; %V/W/cm^2 (absorbed)
Gardon32_sensitivity=0.000050324; %V/W/cm^2 (absorbed)

vt04_room_sensitivity=.000290; %V/W/cm^2 (sensor broken - recalibration not possible)
gage2_room_sensitivity=.0003420; %V/W/cm^2 (needs recalibration)
% plug01_room_sensitivity_inc=.00008375; %V/W/cm^2
plug01_room_sensitivity_inc=.000168; %V/W/cm^2 lamp bank calibration test#1
% vt03_room_sensitivity=.0002713; %V/W/cm^2  small conduction calibration #8
vt03_room_sensitivity=.0002983; %V/W/cm^2 lamp bank calibration test#1

%% test information
```

```
%Gage2 vs Gardon64
if testnum==3 || testnum==8 || testnum==14 || testnum==30
    hthfs_sens=gage2_room_sensitivity; lg=.275*.0254; wg=0.4*.0254;
    eg=.8; %emissivity - post heating cycles with engine block paint
    std_sens=Gardon64_sensitivity;
    if testnum==3
        Lpg=2.0*.0254; %[m]
        ss(1)=1800; ss(2)=2800;
    elseif testnum==8
        Lpg=1.0*.0254; %[m]
        ss(1)=1400; ss(2)=2000;
    elseif testnum==14
        Lpg=0.5*.0254; %[m]
        ss(1)=400; ss(2)=420; ss(3)=700; ss(4)=840; ss(5)=900; ss(6)=960;
    elseif testnum==30
        eg=0.92;
        Lpg=0.5*.0254; %[m]
        ss(1)=800; ss(2)=1040; ss(3)=1500; ss(4)=1650; ss(5)=2140; ss(6)=2260; ss(7)=2650;...
            ss(8)=2850;
    else
    end
%VT03 vs Gardon64:
elseif testnum==5 || testnum==7 || testnum==15 || testnum==29
    hthfs_sens=vt03_room_sensitivity; lg=.2*.0254; wg=0.4*.0254;
    eg=.8; %vt03 emissivity - post heating cycles with engine block paint
    std_sens=Gardon64_sensitivity;
    if testnum==5
        Lpg=1.0*.0254; %[m]
        ss(1)=700; ss(2)=1000;
    elseif testnum==7
        Lpg=1.0*.0254; %[m]
        ss(1)=1000; ss(2)=1400;
    elseif testnum==15
        Lpg=1.0*.0254; %[m]
        ss(1)=640; ss(2)=680; ss(3)=780; ss(4)=820; ss(5)=1130; ss(6)=1175;
    elseif testnum==29
        Lpg=0.5*.0254; %[m]
        ss(1)=900; ss(2)=1100; ss(3)=1500; ss(4)=1750; ss(5)=2200; ss(6)=2350; ss(7)=2450;...
            ss(8)=2530;
    else
    end
%VT04 vs Gardon64:
elseif testnum==6 || testnum==16
    hthfs_sens=vt04_room_sensitivity; lg=.2*.0254; wg=0.4*.0254;
    eg=.8; %emissivity - post heating cycles with engine block paint
    std_sens=Gardon64_sensitivity;
    if testnum==6
        Lpg=2.0*.0254; %[m]
        ss(1)=1400; ss(2)=2000;
    elseif testnum==16
        Lpg=2.0*.0254; %[m]
        ss(1)=680; ss(2)=770; ss(3)=1750; ss(4)=1840; ss(5)=2850; ss(6)=3000;
    else
    end
%Plug01 vs Gardon32:
elseif testnum==9 || testnum==10 || testnum==17 || testnum==18 || testnum==19 || testnum...
    ==20 || testnum==26 || testnum==28
    eg=.73; %emissivity - oxidized sensor
    hthfs_sens=plug01_room_sensitivity_inc/eg;
    lg=.127*.0254; wg=0.4*.0254;
    std_sens=Gardon32_sensitivity;
    if testnum==9
        Lpg=1.0*.0254; %[m]
        ss(1)=1000; ss(2)=1500;
```

```
    elseif testnum==10
        Lpg=1.0*.0254; %[m]
        ss(1)=800; ss(2)=1600;
    elseif testnum==17
        Lpg=1.0*.0254; %[m]
        ss(1)=1400; ss(2)=1600;
    elseif testnum==18
        Lpg=1.0*.0254; %[m]
        ss(1)=1500; ss(2)=1900;
    elseif testnum==19 %vs Gardon 64
        std_sens=Gardon64_sensitivity;
        Lpg=1.0*.0254; %[m]
        ss(1)=1300; ss(2)=1700; ss(3)=3500; ss(4)=4000;
    elseif testnum==20
        Lpg=0.5*.0254; %[m]
        ss(1)=1400; ss(2)=1500; ss(3)=3350; ss(4)=3750;
    elseif testnum==26
        Lpg=0.5*.0254; %[m]
        ss(1)=1200; ss(2)=1450; ss(3)=1900; ss(4)=2100; ss(5)=2450; ss(6)=2600; ss(7)↩
            =2850; ss(8)=3150;
    elseif testnum==28
        eg=0.92;
        Lpg=0.5*.0254; %[m]
        ss(1)=1700; ss(2)=1900; ss(3)=2400; ss(4)=2650; ss(5)=3400; ss(6)=3600; ss(7)↩
            =5300; ss(8)=5400;
    else
    end
else
end
```

Appendix D

Copyright Permission

This appendix includes copyright permission letters for the material presented in Chapters 2 and 4.

Permission for the material presented in Chapter 2:

ELSEVIER LICENSE
TERMS AND CONDITIONS

May 05, 2011

This is a License Agreement between Clayton A Pullins ("You") and Elsevier ("Elsevier") provided by Copyright Clearance Center ("CCC"). The license consists of your order details, the terms and conditions provided by Elsevier, and the payment terms and conditions.

All payments must be made in full to CCC. For payment instructions, please see information listed at the bottom of this form.

Supplier	Elsevier Limited The Boulevard,Langford Lane Kidlington,Oxford,OX5 1GB,UK
Registered Company Number	1982084
Customer name	Clayton A Pullins
Customer address	210 Heights LN Blacksburg, VA 24060
License number	2662630796164
License date	May 05, 2011
Licensed content publisher	Elsevier
Licensed content publication	International Journal of Heat and Mass Transfer
Licensed content title	In situ High Temperature Heat Flux Sensor Calibration
Licensed content author	Clayton A. Pullins, Tom E. Diller
Licensed content date	August 2010
Licensed content volume number	53
Licensed content issue number	17-18
Number of pages	10
Start Page	3429
End Page	3438
Type of Use	reuse in a thesis/dissertation
Portion	full article
Format	both print and electronic
Are you the author of this Elsevier article?	Yes
Will you be translating?	No
Order reference number	
Title of your thesis/dissertation	High Temperature Heat Flux Measurement: Sensor Design, Calibration, and Applications
Expected completion date	May 2011

Permission for the material presented in Chapter 4:

ELSEVIER LICENSE
TERMS AND CONDITIONS

May 16, 2011

This is a License Agreement between Clayton A Pullins ("You") and Elsevier ("Elsevier") provided by Copyright Clearance Center ("CCC"). The license consists of your order details, the terms and conditions provided by Elsevier, and the payment terms and conditions.

All payments must be made in full to CCC. For payment instructions, please see information listed at the bottom of this form.

Supplier	Elsevier Limited The Boulevard,Langford Lane Kidlington,Oxford,OX5 1GB,UK
Registered Company Number	1982084
Customer name	Clayton A Pullins
Customer address	210 Heights LN Blacksburg, VA 24060
License number	2670861084971
License date	May 16, 2011
Licensed content publisher	Elsevier
Licensed content publication	International Journal of Heat and Mass Transfer
Licensed content title	Adaptation of the in-cavity calibration method for high temperature heat flux sensors
Licensed content author	Clayton A. Pullins, Tom E. Diller
Licensed content date	15 April 2011
Licensed content volume number	n/a
Licensed content issue number	n/a
Number of pages	1
Start Page	
End Page	
Type of Use	reuse in a thesis/dissertation
Intended publisher of new work	other
Portion	full article
Format	both print and electronic
Are you the author of this Elsevier article?	Yes
Will you be translating?	No
Order reference number	
Title of your thesis/dissertation	High Temperature Heat Flux Measurement: Sensor Design, Calibration, and Applications